Jaganathan Jayaprakash
Kok Keong Choong
Mohammed Parvez Anwar   *Editors*

Advances in Construction Materials and Structures

Select Proceedings of ICON 2019

Springer

Lecture Notes in Civil Engineering

Volume 111

Lecture Notes in Civil Engineering (LNCE) publishes the latest developments in Civil Engineering - quickly, informally and in top quality. Though original research reported in proceedings and post-proceedings represents the core of LNCE, edited volumes of exceptionally high quality and interest may also be considered for publication. Volumes published in LNCE embrace all aspects and subfields of, as well as new challenges in, Civil Engineering. Topics in the series include:

- Construction and Structural Mechanics
- Building Materials
- Concrete, Steel and Timber Structures
- Geotechnical Engineering
- Earthquake Engineering
- Coastal Engineering
- Ocean and Offshore Engineering; Ships and Floating Structures
- Hydraulics, Hydrology and Water Resources Engineering
- Environmental Engineering and Sustainability
- Structural Health and Monitoring
- Surveying and Geographical Information Systems
- Indoor Environments
- Transportation and Traffic
- Risk Analysis
- Safety and Security

To submit a proposal or request further information, please contact the appropriate Springer Editor:

- Mr. Pierpaolo Riva at pierpaolo.riva@springer.com (Europe and Americas);
- Ms. Swati Meherishi at swati.meherishi@springer.com (Asia - except China, and Australia, New Zealand);
- Dr. Mengchu Huang at mengchu.huang@springer.com (China).

All books in the series now indexed by Scopus and EI Compendex database!

More information about this series at http://www.springer.com/series/15087

Jaganathan Jayaprakash · Kok Keong Choong ·
Mohammed Parvez Anwar
Editors

Advances in Construction Materials and Structures

Select Proceedings of ICON 2019

Springer

Editors
Jaganathan Jayaprakash
Department of Structural and Geotechnical
Engineering, School of Civil Engineering
Vellore Institute of Technology
Vellore, Tamil Nadu, India

Kok Keong Choong
School of Civil Engineering
Universiti Sains Malaysia
Nibong Tebal, Penang, Malaysia

Mohammed Parvez Anwar
Department of Civil Engineering
Faculty of Engineering
University of Nottingham Malaysia Campus
Semenyih, Selangor Darul Ehsan, Malaysia

Preface

This book comprises selected papers of the International Conference on Recent Trends in Construction Materials and Structures (ICON 2019), which was held in Vellore Institute of Technology, Vellore, India, during 18–20 September 2019. It covers various latest developments in the emerging technologies in areas which include sustainable construction materials, utilization of waste materials in concrete, heritage structures, special concrete, structural dynamics, modelling and simulation in structural engineering, and earthquake engineering. It also offers insights and provides effective and feasible solution to recent problems in sustainable construction materials and structures. The content of this book is invaluable for students, researchers, academia, and practitioners interested in concrete technology and structures.

We wish to express our sincere gratitude to the organizing secretaries Dr. A. Sofi and Dr. T. Meena, Associate Professor, School of Civil Engineering, Vellore Institute of Technology (VIT), Vellore, for their continued support towards this edition. We would also like to express gratitude to the keynote speakers, authors, presenters, various committee members, and session chairs for their participation and valuable contributions towards ICON 2019. Special thanks to convenor and technical committee members of School of Civil Engineering, Vellore Institute of Technology for their priceless contribution in ICON 2019.

Vellore, India   Jaganathan Jayaprakash
Penang, Malaysia   Kok Keong Choong
Semenyih, Malaysia   Mohammed Parvez Anwar

Contents

Contents   ix

About the Editors

Dr. Jaganathan Jayaprakash is a Professor in the Department of Structural and Geotechnical Engineering, School of Civil Engineering, Vellore Institute of Technology, Vellore, India. He obtained his Bachelor of Engineering (B.E.) in Civil and Structural Engineering from Annamalai University followed by Master of Engineering (M.E.) in Structural Engineering at National Institute of Technology, Tiruchirappalli, India. He, afterwards, earned his Ph.D. in Structural Engineering from Universiti Putra Malaysia, Malaysia. He has published over 40 papers in peer reviewed International Journals. He was a recipient of *Teaching Quality* and *Research Publication Awards* from University of Nottingham, Malaysia. His research interests include Repair and Rehabilitation of reinforced concrete structures, strengthening of reinforced concrete members using Fibre Reinforced Polymer (FRP) Composites, Sustainable Construction Materials, Kenaf Fibres, and Fire Engineering.

Dr. Kok Keong Choong is currently a professor at the School of Civil Engineering, Universiti Sains Malaysia, Penang, Malaysia. He obtained his B.Eng. (Civil) from Universiti Teknologi Malaysia, M.Eng. from Gifu University, Japan and D.Eng. from The University of Tokyo, Japan. His major areas of research include computational analysis of shell and spatial structures, structural dynamics, structural stability and computational mechanics. He also collaborates with industry on research study related to precast concrete structures, large span steel structures, and tensioned fabrics structures. He is a Professional Engineer registered with the Board of Engineers Malaysia.

Dr. Mohammed Parvez Anwar is an Associate Professor in the Department of Civil Engineering, University of Nottingham, Malaysia. He received his B.Sc. (Hons) in Civil Engineering from Bangladesh University of Engineering and Technology and Master of Engineering (M.Eng.) in Structural Engineering from National University of Singapore (NUS), Singapore. He has received his D.Eng. in Structural Engineering from Yokohama National University, Japan. He has published more than 30 papers in indexed International Journals. He received *Teaching Quality* and *Research Publication Awards* several times at University of Nottingham, Malaysia. His areas of research are structural dynamics, wind - induced vibration control of long span suspension bridges, earthquake engineering, seismic vulnerability analysis of low and high-rise structures, application of FRP and construction materials.

Eccentric Punching on Edge Waffle Slabs

Dickson Wen Jing Fong, Teck Leong Lau, Wael Elleithy, and Mohammed Parvez Anwar

Abstract This paper presents the test results of six 1/10th scale micro-concrete waffle slabs subjected to eccentric punching at the vicinity of edge columns. It was observed from tests that the punching mechanism of slab having their edge column is located by the free edge to be similar to those having their edge column at the centre of the edge solid region. The punching shear capacity of slabs having their edge column by the free edge was observed to be in average 19% lower than those with column located at the centre of edge solid region. Furthermore, it was also observed that the punching capacity decreased as the moment increased.

Keywords Column's location · Column's eccentricity · Edge · Punching shear · Waffle slabs

1 Introduction

In recent years, increasing popularity has been noted in the use of reinforced concrete waffle slabs due to its economic and structural behaviour. A waffle slab consists of thin topping slabs and narrow ribs spanning in both directions between solid sections (see Fig. 1) which provide a lighter and stiffer solution (presence of ribs provides added strength) than the equivalent flat slab [14].

Similar to reinforced concrete flat slabs, waffle slabs can develop a localised shear failure mechanism known as punching shear failure (see Fig. 2) at columns or under concentrated loads. Punching shear failure is a rupture shear failure mechanism in flat slab floor system, where a solid revolution is formed within the incline shear cracks that are not visible from the surface. At failure, the solid revolution separates normally from the slab and leaving rest of the slab remaining rigid [16]. However, despite the increasing popularity of waffle slabs, only limited amount of research works has been carried out [1, 2, 7, 9, 10, 18]. Therefore, further research is required

D. W. J. Fong · T. L. Lau (✉) · W. Elleithy · M. P. Anwar
Department of Civil Engineering, University of Nottingham, Semenyih, Selangor, Malaysia
e-mail: Teckleong.Lau@nottingham.edu.my
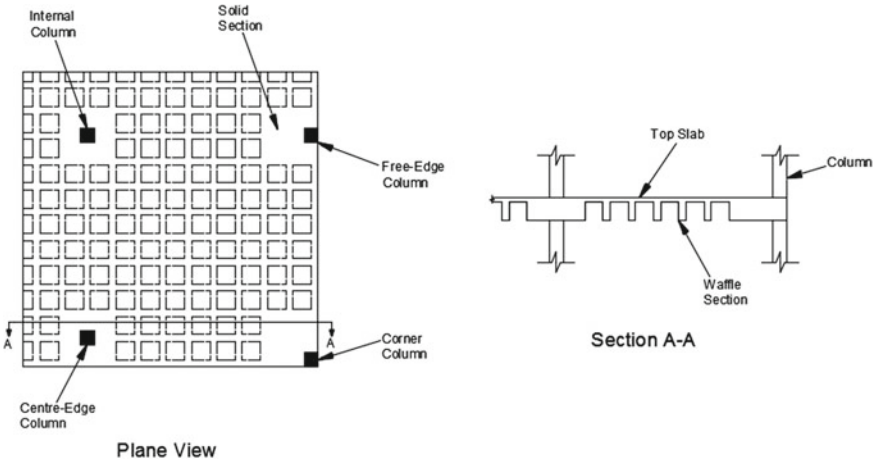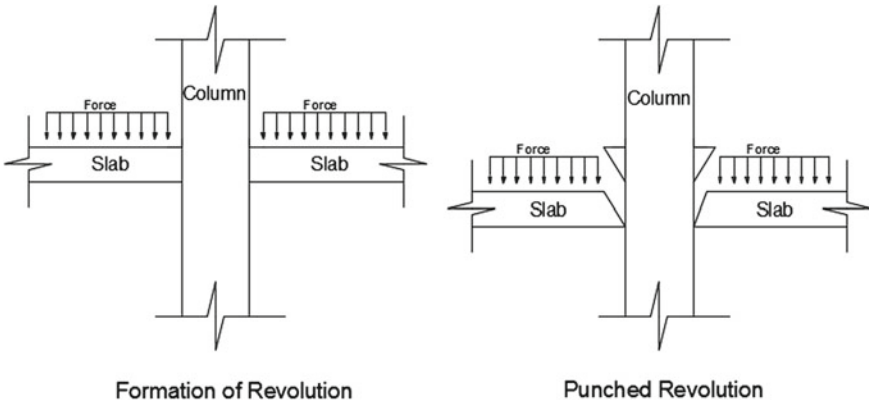
Fig. 1 Waffle slab

Fig. 2 Illustration of punching shear failure

to explore the failure mechanism in the presence of section changes to aid the current understanding on punching shear mechanism of waffle slabs.

2 Methodology

2.1 Specimen Details

Tests were performed on six (1/10th scaled) waffle slab specimens to simulate the edge column waffle slab connections in the presence of moment transfer (via load

eccentricities). Variables considered were the column location, the load eccentricity, and the concrete strength (see Table 1). All slab specimens have an overall depth of 70 mm and a top slab thickness of 20 mm (see Fig. 3). The geometric properties of waffle slab specimens were chosen in accordance with Clause 5.3 of EC2 [4]. All specimens were cast in an upright position so as to simulate the casting position of the prototype but tested in an inverse manner where the tension reinforcement faced downwards and being supported on rollers at three edges. The slab specimens were tested with loads applied through a square column that bolted onto the specimens. Two column locations were studied: centre of solid section and by the edge of solid

Table 1 Slab specimen details

Slab	Size of solid section (mm)	Overall slab height, h (mm)	Column location	Load eccentricity, e (mm)
EWSCE1	200×200	70	Centre	50
EWSCE2	200×200	70	Centre	100
EWSCE3	200×200	70	Centre	150
EWSFE1	200×200	70	Edge	50
EWSFE2	200×200	70	Edge	100
EWSFE3	200×200	70	Edge	150

All columns are square shaped and column size, $c = 100$ mm
*The effective depth of the slab, d = 62 mm
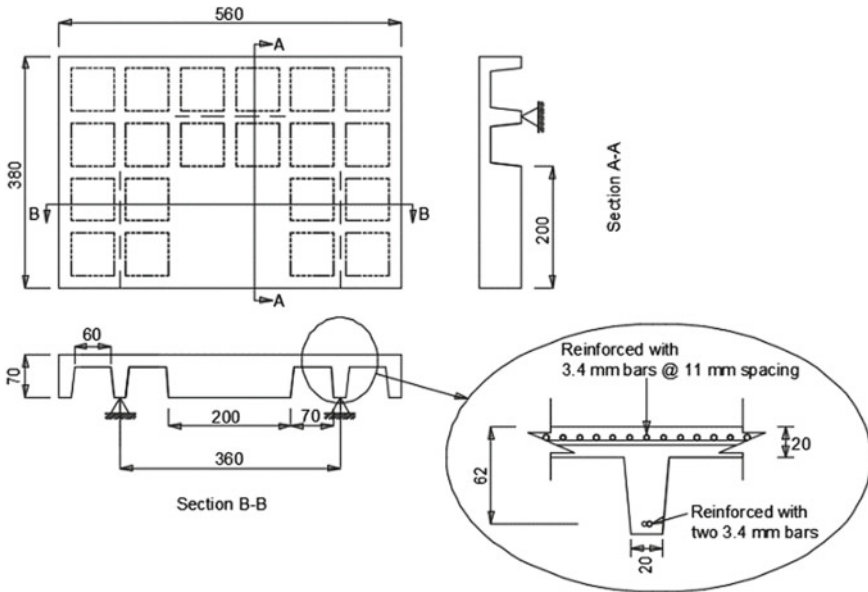
Fig. 3 Slab specimen details
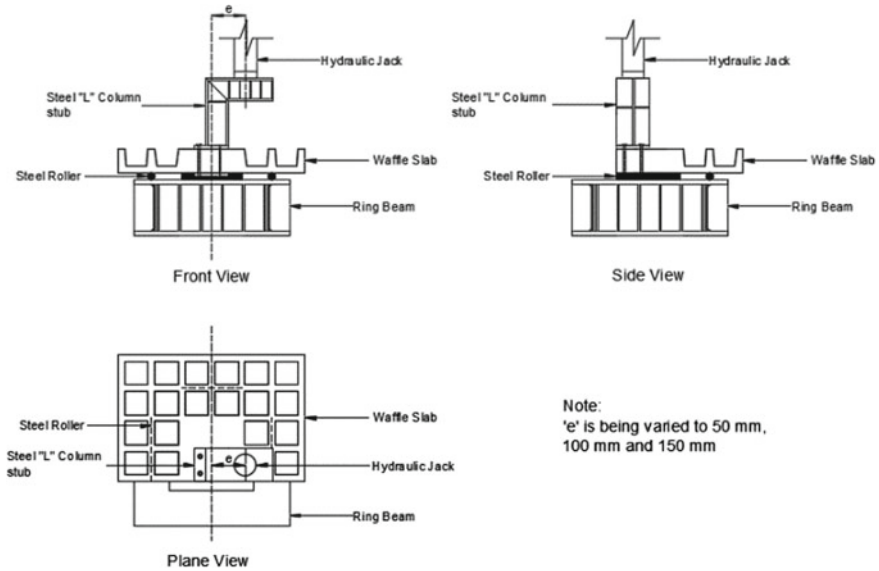
Fig. 4 Schematic diagram of experimental set-up for column positioned at free edge of slab—"EWSFE"

section (see Figs. 4 and 5). Three load eccentricities were studied: 50, 100 and 150 mm.

2.2 Concrete Mix

All specimens were cast from micro-concrete having a maximum aggregate size of 2 mm, Ordinary Portland Cement, water/cement ratio and aggregates/cement ratio at 0.56 and 1.6, respectively [5, 17]. All coarse aggregates were sieved and re-mixed to the required grading distributions (see Table 2) as proposed by Johnson [8].

2.3 Reinforcements

Reinforcements in slab specimens were designed to ensure that flexural failure would not occur during tests. Plain steel bars of 3.4 mm diameter, with yield strength of 440 MPa were used instead of ribbed steel bars as ribbed steel bars were scarce in small diameter. The tension reinforcements were placed at 11 mm spacing across the top slab regions, while the ribs were reinforced with two bars. A cover of 5 mm was adopted in all specimens.
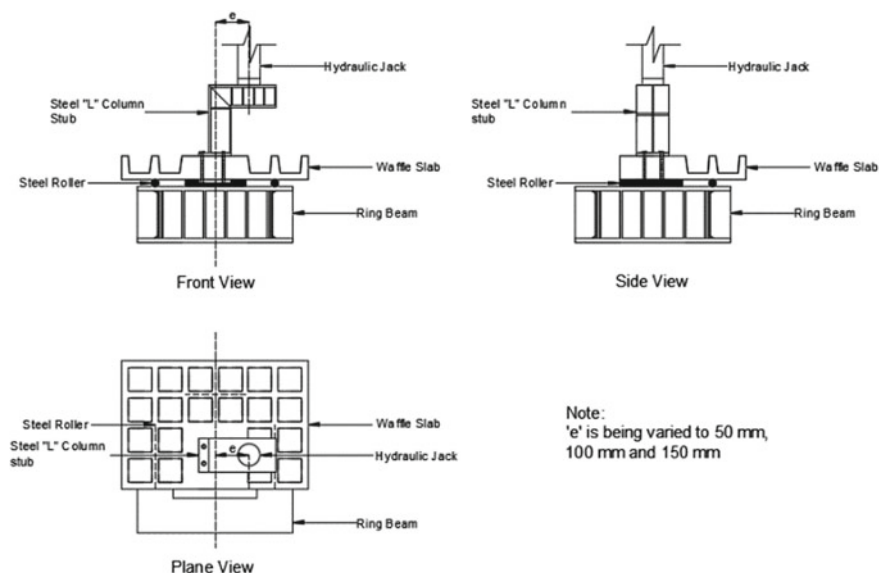
Fig. 5 Schematic diagram of experimental set-up for column positioned at centre edge of slab—"EWSCE"

Table 2 Mix design

Sieve size (mm)	Mass retained (g)	Retained (%)	Passing (%)
2.36	0.00	0.00	100.00
1.18	211.12	42.22	57.78
0.6	57.43	11.49	46.29
0.3	21.67	4.33	41.96
0.15	166.58	33.32	8.64
<0.15	43.20	8.64	0.00

2.4 Test Set-up

All specimens were tested in an inverse manner, that is, the top surface of the specimens faced downwards. All specimens were supported on rollers at three edges and loaded via column stub bolted on the solid section. Two different column locations were tested, that is, free edge of the slab (column positioned at 50 mm from the edge) and centre edge of the slab (column positioned at 100 mm from the edge), as shown in Figs. 4 and 5, respectively. The loads were applied using a hand operated hydraulic jack positioned with the requiring eccentricities (see Table 1) onto a steel L-column stub (see Fig. 7). Central deflections were measured using three digital gauges positioned at the vicinity of the column stub (see Fig. 6). Each specimen was
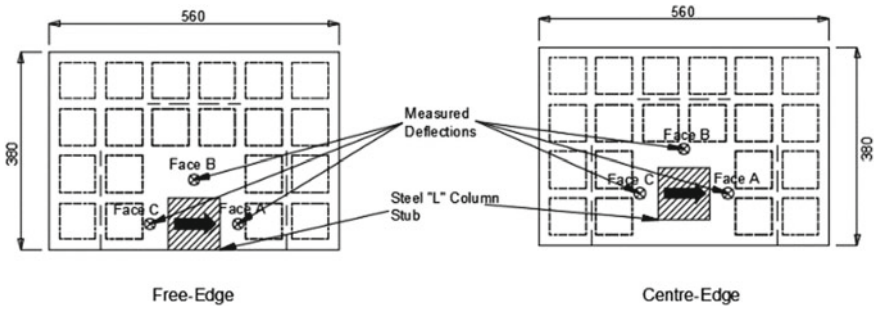
Fig. 6 Locations of digital gauges

Fig. 7 Experimental set-up
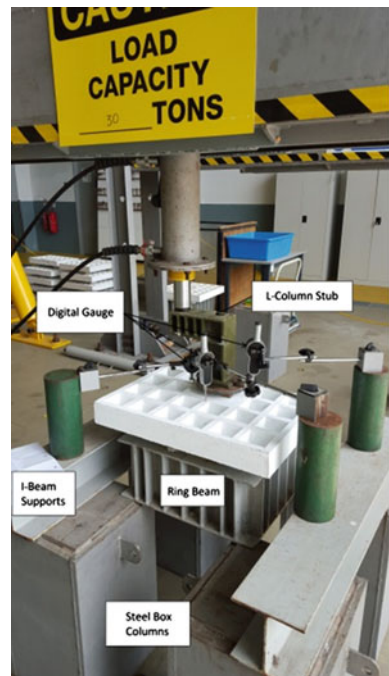
loaded with load increments of 4.21 kN until failure. Deflections were recorded, and cracks were marked after every load interval.

3 Results and Discussions

As expected, it was observed from tests that all the waffle slab specimens failed in a sudden rupture punching failure mechanism similar to that of a flat slab [3, 3]. The

observed punching failure surface was characterised by internal cracks propagated from the heavily loaded sides to the least loaded sides of the column through the slab thickness over the fixed shear span. In plan, a fraction solid revolution of concrete was formed, with the column at its centre, which separated from the main slab vertically leaving the rest of the slab remaining rigid (see Table 5). The punching failure loads are summarised and presented in Tables 3 and 4. As pointed out by Al-bayati [1, 2], the distinct difference between the punching mechanisms in waffle slabs and flat slabs is the reduced solid section at the column vicinity to form the solid revolution of concrete, that is, some of the potential failure surface was lost when it entered the waffle section, thus a lower ultimate punching capacity. The load–deflection curves (see Fig. 8), from the current works, found to agree with previous findings [9, 10]. The load–deflection curves are initiated with a linear elastic behaviour, and later, the rate of deflection increased until failure occurred. As reported by Marzouk and Hussein [12], the first slope represents the stiffness of an uncracked section, while the second slope represents the stiffness of a cracked section. Comparisons between the observed cracking load(s) and the actual cracking load(s) inferred from the load–deflection curve are presented in Tables 3 and 4. The observed cracking load(s) was found to be about 30% higher than the actual cracking load(s) obtained from the load–deflection curve(s) for the specimens with column positioned at the centre of the solid section, while 40% for the specimens with column positioned at the edge of the solid section. This phenomenon is believed to happen due to the formation of micro-cracks within the slab specimen and could not be seen by the naked eye.
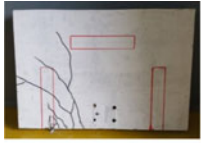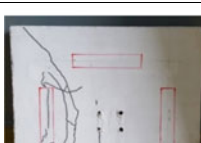
Table 3 Test results for slabs with column positioned at centre of solid section

Slab	f_{cu50} (N/mm^2)	Observed cracking load (kN)	Inferred cracking load (kN)	Failure load (kN)
EWSCE1	40.593	23.16 (56%)	12.63 (31%)	41.05
EWSCE2	40.510	16.84 (47%)	10.53 (29%)	36.84
EWSCE3	42.385	16.84 (53%)	10.53 (33%)	31.58

Table 4 Test results for slabs with column positioned at free edge of solid section

Slab	f_{cu50} (N/mm^2)	Observed cracking load (kN)	Inferred cracking load (kN)	Failure load (kN)
EWSFE1	41.873	18.95 (60%)	12.63 (40%)	31.58
EWSFE2	40.831	14.74 (50%)	10.53 (36%)	29.47
EWSFE3	36.688	14.74 (54%)	10.53 (38%)	27.37

Table 5 Failure patterns

Slab specimen	Top view	Bottom view	Side view
EWSFE1			
EWSFE2			
EWSFE3			
EWSCE1			
EWSCE2			
EWSCE3			

3.1 Effects of Column Location(s)

For ultimate failure loads, test results indicate the punching resistance of waffle specimens with column positioned at centre of the solid section were in average about 19% higher than those with column positioned at free edge of the solid section. For waffle specimens having 50, 100 and 150 mm load eccentricities, the ultimate failure loads were 24, 19 and 13% higher than those with their column positioned at their free edge, respectively. It is believed that these increases derived from the decrease
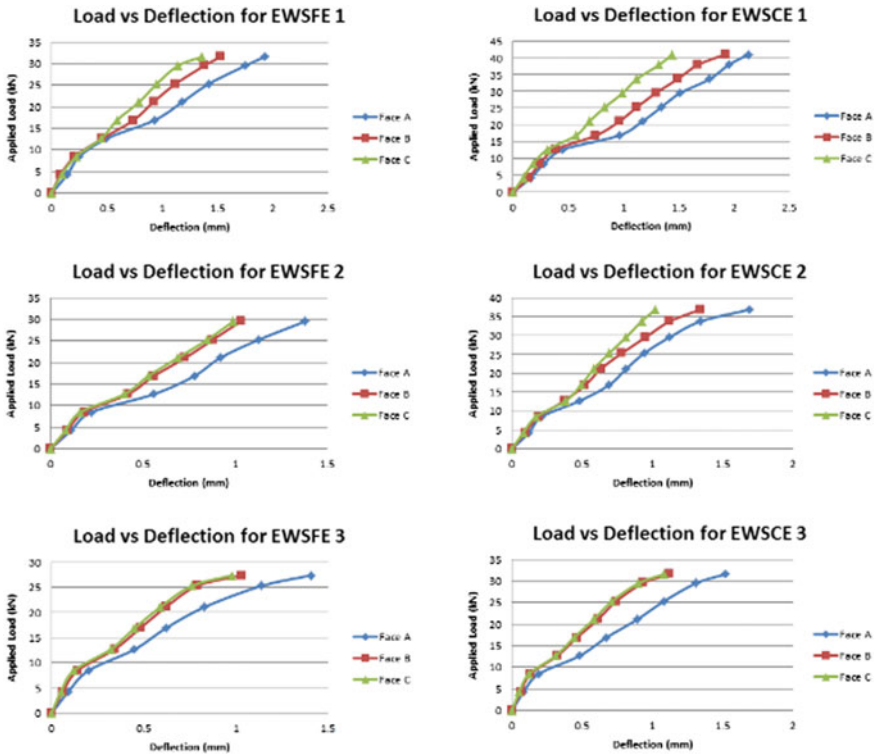
Fig. 8 Load versus deflection curves

in the transverse shear span for specimens loaded with column at centre of the solid section, in direction perpendicular to the free edge, hence, increased the angle of inclination of the shear surface, thus, higher shear strength was mobilised, and as a result, increased the ultimate punching resistance. Similar phenomenon was also noted by the others [6, 13]. The variations observed are derived from the increase in load eccentricities (50, 100 and 150 mm), which in turn decreases the area of shear surface that were associated with the increased angle of inclination. As a result, reductions in the benefits to punching resistance have been noted.

3.2 Effects of Column Eccentricity(s)

It was observed from tests that the punching shear capacities to be inversely related to the column eccentricities are shown in Fig. 9. For waffle specimens with column positioned at the centre of solid section, in comparison with specimen EWSCE 1, loaded with 50 mm eccentricity, specimens EWSCE 2 and EWSCE 3 showed reduction in ultimate failure loads of 10 and 23%, as the eccentricities increased to
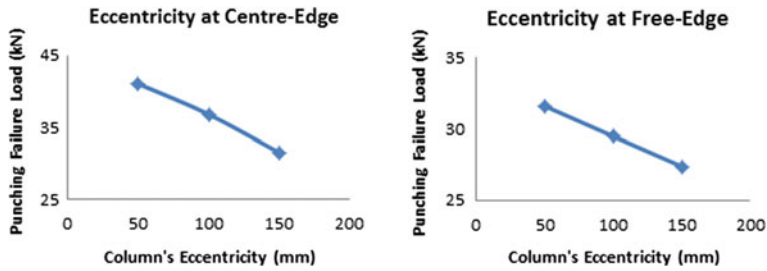
Fig. 9 Load versus eccentricity curves

100 mm and 150 mm, respectively. For waffle specimens with column positioned at the free edge of solid section, in comparison with specimen EWSFE 1, loaded at 50 mm eccentricity, specimens EWSFE 2 and EWSFE 3 showed reduction in failure loads of 7 and 13%, as the eccentricities increased to 100 mm and 150 mm, respectively. As shown in Table 5, specimen loaded with 50 mm eccentricity exhibited the largest shear failure surface area, and the area of failure surface decreases as the load eccentricity increases. In general, it can be noted that the ultimate failure load(s) decreases as the load eccentricity(s) increased (see Tables 3 and 4). These reductions observed may be derived from the decrease in shear failure surface as the load eccentricity increases. That is, for specimens having 50 mm load eccentricity, which exhibited the largest shear failure surface, were observed to have its punching shear failure propagates from the side and front of the column; while specimens with 150 mm load eccentricity having its shear surface propagates mainly from the front of the column (see Table 5). As a result, small shear surfaces were mobilised as the load eccentricity increased thus lower punching resistance(s) were observed [11].

4   Conclusion

The punching shear failure mechanisms of waffle slabs were observed to be very similar in nature between slabs having their column located by the free edge or at the centre edge of the solid region. The punching shear capacities of the waffle slabs with column positioned at the centre of edge solid region were observed to be in average 19% higher than those with column positioned at the free edge. Such increase in punching capacities is derived from the increase in the angle of inclination of the shear failure surface. Furthermore, it was observed that the punching capacities decreased (up to 25%) as the moment (load eccentricities) increased.

References

1. Al-Bayati AF (2013) Punching shear mechanisms of waffle slabs. PhD Thesis, Department of Civil Engineering, The University of Nottingham, Malaysia Campus
2. Al-Bayati A, Leong L, Clark L (2015) Concentric punching shear of waffle slab. ACI Struct J 112(5):533–542
3. CEB-FIB (2001) Punching of structural concrete slabs. Bulletin 12 Lausanne: International Federation for Structural Concrete
4. Eurocode 2 (2004) Design of concrete structures—part I: general rules for building, European pre-standard. ENV 1992–1–1
5. Fong WJ, Lau TL (2015) Effect of aggregate size on punching strength of reinforced concrete slabs. Appl Mech Mater 450–454
6. Gardner NJ (1990) Relationship of the punching shear capacity of reinforced concrete slabs with shear strength. ACI Struct J 87(1):66–71
7. Hussein AF (1994) Punching shear strength at edge columns in ribbed flat slabs. PhD Thesis, Department of Civil Engineering, University of Leeds
8. Johnson RP (1962) Strength tests on scaled-down concrete suitable for models, with a note on mix design. Mag Concr Res 14(40):47–53
9. Lau TL, Clark LA (2007) Shear transfer between ribbed slab and internal column. Mag Concr Res 59(7):507–516
10. Lau TL, Clark LA (2008) Shear transfer between ribbed slab and edge column. Mag Concr Res 60(6):411–419
11. Lovrovich JS, McLean DI (1990) Punching shear behavior of slabs with varying span-depth ratios. ACI Struct J 87(5):507–511
12. Marzouk H, Hussein A (1992) Experimental investigation on the behavior of high-strength concrete slabs. ACI Struct J 88(6):701–713
13. Moehle JP (1988) Strength of slab-column edge connections. ACI Struct J 85(1):89–98
14. MPA The Concrete Centre (2019) Ribbed and waffle slabs [online]. Available at: https://www.concretecentre.com/Building-Elements/Floors/Ribbed-Waffle-Slabs.aspx [Accessed 12 Oct. 2016]
15. Park R, Gamble WL (2000) Reinforced concrete slabs, 2nd edn. Wiley, Danvers, MA
16. Regan P, Braestrup M (1985) Punching shear in reinforced concrete: a state of art report. Lausanne: CEB, Comité Euro-International du Béton
17. William AL, Mario P (1966) Size effects in small-scale models. ACI J Proc 63(11):1191–1204
18. Xiang XZ (1993) Punching shear strength of waffle slabs at internal column. PhD Thesis, Department of Civil Engineering, University of Leeds, UK

A Diagnosis of Potential Creep Settlement of Jacked-In Pile Using Chin Method

W. K. Ng, A. R. bin Zainudin, and Kok Keong Choong

Abstract Pile performance is one of the pile acceptance criteria and depends on the method of pile installation during the construction stage. Jacked-in pile is among the most popular method of pile installation in Malaysia. However, the creep settlement may be encountered on jacked-in pile as its installation causes the plunging force accumulated at the pile tip and push the pile upward when the jacking pressure was released. Therefore, a systematic approach is required to diagnose the condition of jacked-in pile and subsequently identify the suitable type of pile termination criteria. Chin method is the most widely used to diagnose the pile condition such as pile necking and mobilisation of pile load capacity. In this study, it is used to analysis the ultimate capacity and further identifying the potential creep settlement condition on jacked-in pile. Results show that the shaft resistance of jacked-in pile was greater than the driven pile with similar sizes and embedded length. Potential creep settlement on piles also can be identified using Chin method.

Keywords Jacked-in pile · Creep settlement · Chin method · Driven pile · Ultimate pile capacity

1 Introduction

Rapid development in urban city has urged a better piling system which can install pile with lesser disturbance to the surrounding structures or adjacent soils. Jacked-in pile is one of the environmental-friendly piling systems due to the reasons of lesser in vibration and minimum noise pollution during the installation [6]. Jacked-in machine pushes the precast pile into the soil with constant penetration rate. In Malaysia, jacked-in pile method has been adopted since 1990s and the spun pile

W. K. Ng (✉) · A. R. Zainudin
Faculty of Civil Engineering, Cawangan Pulau Pinang, Universiti Teknologi MARA, Penang, Malaysia
e-mail: ngwenkuan321@uitm.edu.my

K. K. Choong
School of Civil Engineering, Universiti Sains Malaysia, Nibong Tebal, Penang, Malaysia

13

Fig. 1 High capacity of jacked-in machine (Google image)

size up to diameter of 600 mm with working capacity of 3000 kN has been installed for high-rise buildings with 45-storeys [2]. A sample of high capacity of jacked-in machine is shown in Fig. 1.

2   Behaviour of Soil During Pile Installation

The deformation characteristics of soil displaced by jacked-in pile are different from the pile installed by impact force. Driven pile is installed by high impacts forces which produced by hammer that hit the pile head and the installation rate is faster as compared to jacked-in method. When the precast pile is driven into the soil, the adjacent soil is displaced to the side and the soil strength is being disturbed. The process leads to high excess pore pressure generated in the surrounding soils. The percussion piling creates noise and ground vibrations that become distraction to the surrounding residents of the construction site. Furthermore, driven pile also may impact the damages of the nearby structures and facilities. As a result, the ultimate capacity of pile may differ due to the pile installation method. Previous study by Yang et al. [5] reported the behaviour of jacked-in and driven piles in sandy soil. The study made a comparison of the capacity and deformation characteristics of jacked-in and

driven pile. Results show that the shaft resistance is generally stronger than driven pile, but the base resistance of jacked-in pile is weaker than driven pile.

Based on the results of the load transfer mechanism, Yang et al. [5] indicated that the change of axial loads along the shaft of driven piles was small and shows that a small shaft resistance was mobilised as compared to jacked-in pile. The difference in load transfer mechanism between jacked-in and driven pile can be seen in Figs. 2 and 3. In this regard, it is explicitly stated that in relatively the mobilised load capacity of the driven piles was evenly distributed between shaft and base, whereas, the shaft resistance of jacked-in piles is higher but lower in tip resistance. This is mainly due to the installation of jacked-in pile was in constant penetration rate. Soils were slowly displaced by jacked-in pile until the pile encountered penetration resistance as per the pre-set jacked-in pressure. The radially displaced soils were found strongly compacted due to the jacked-in process according to Kou [4]. However, it is suspected that creep settlement might be encountered on jacked-in pile caused by the pile bouncing back when the jacking pressure was released. As a result, a diagnosis of creep settlement on jacked-in pile is required to determine the termination criteria of jacked-in pile in order to diminish the effect of creep settlement [5].

Fig. 2 Typical axial load distribution for driven piles [5]
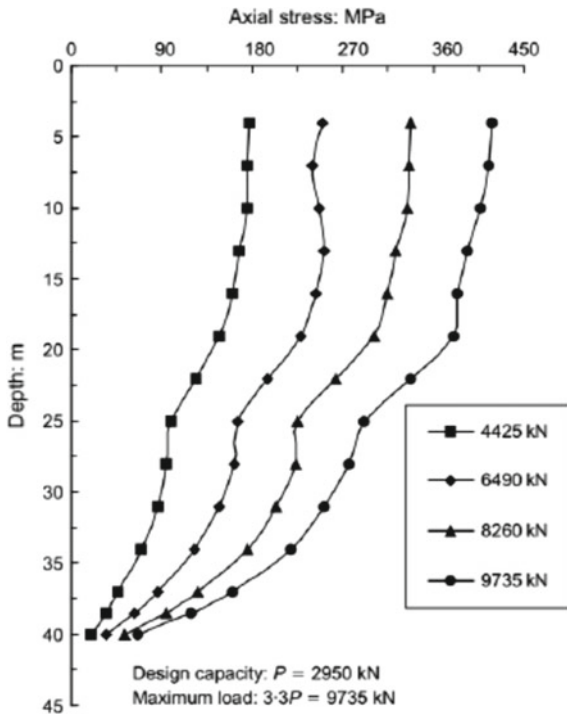
2.1 Chin's Method in Analysing Pile Bearing Capacity

Chin's method is used to obtain shaft friction and end bearing capacity separately
[1]. Chin method assumes that the load–settlement curve is in hyperbolic shape
when the load approaches failure. In this method, each load will be divided by its
corresponding settlement and the result is plotted against the settlement. It produces
a graph of ratio settlement–load, s/Q versus the corresponding settlement, s (Fig. 4).
In many cases, the plot of ratio settlement–load versus the settlement gives a linear
relationship as the pile approaches failure and it produces straight line. The inverse

Fig. 4 Bilinear relationship
of ratio settlement–load, s/Q
vs settlement, s [1]
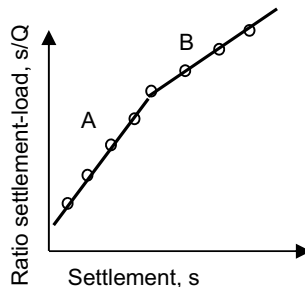
Table 1 Test pile information

Pile ref	Installation method	Pile size (mm)	Pile length (m)	Working load (kN)
DP1	Driven	200 × 200	35.5	400
DP2	Driven	200 × 200	35.5	400
JIP1	Jacked-in	250 × 250	36	450
JIP2	Jacked-in	250 × 250	36	450
JIP3	Jacked-in	250 × 250	36	450
JIP4	Jacked-in	250 × 250	24	450

slope of this line is equal to the ultimate bearing capacity of pile. Chin's method presented two straight lines that intersect were expected to be the combination of shaft friction and end bearing capacity. It has been suggested that the first part (A) would represent shaft resistance and the second part (B) represents total load as the toe resistance needs higher settlement to be mobilised than shaft resistance. Figure 4 presents the bilinear relationship of ratio settlement–load, s/Q versus settlement, s using Chin's plot.

3 Case Studies

A total of six number of pile test results were obtained from a site in Permatang Pauh, Penang. The piles were installed using driving and jacked-in methods. All piles were tested using maintained load test in two cycles of loading. First cycle of loading was loaded to one time working load and second cycle was loaded to two times of the working load. The information of the test piles is tabulated in Table 1. The pile load test results were analysed using Chin's method in order to determine the ultimate pile load capacity and the behaviour of creep settlement in piles. Analysis results of the jacked-in piles (JIP1–JIP4) are compared to the driven pile (DP1 and DP2) to investigate the behaviour of load transfer mechanisms of jacked-in pile as compared to driven pile.

4 Analysis and Discussion

4.1 Ultimate Load Capacity of Piles

The ultimate pile capacity is obtained from the inverse slope of the settlement–load versus settlement graph using Chin's method. Figure 5 shows the typical Chin's plot of jacked-in pile. From the graph, the first slope, M_1 is the shaft capacity, and the second slope, M_2 is the ultimate bearing capacity of the tested pile. The pile capacity

Fig. 5 Typical chin plot of
JIP1
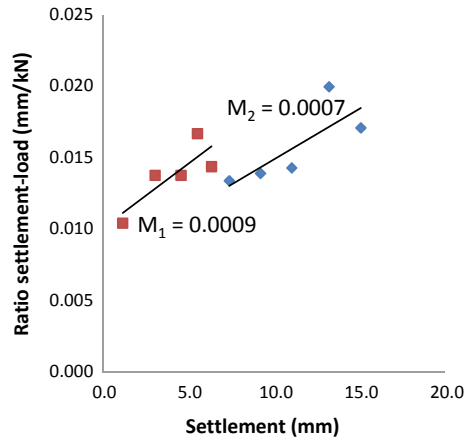
of the pile can be obtained by using the Eq. (1):

$$\text{Pile capacity} = \frac{1}{\text{slope}, M} \tag{1}$$

Figure 6 presents the percentage of the shaft capacity as well as the end bearing of the tested piles. The average percentage of shaft capacity of jacked-in piles (JIP1–JIP4) was about 78% as compared to the ultimate capacities. The findings are justified because jacked-in pile has compacted its surrounding soils in radial direction during installation [4]. However, JIP4 recorded slightly lower in shaft capacity as the pile
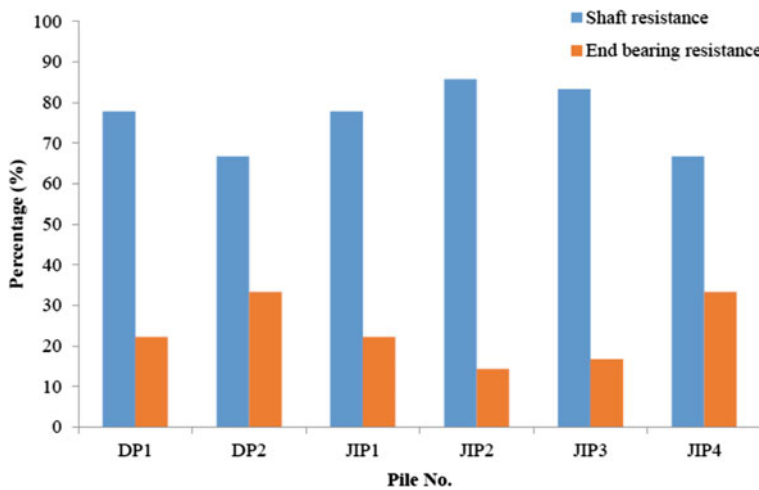
Fig. 6 Percentages of shaft capacity and end bearing resistance of test piles

penetration length is shorter, 24 m as compared to the other jacked-in piles which are 36 m in length.

4.2 Creep Settlement of Jacked-In Pile

The potential creep settlement is detected based on the deviation of the settlement–load from the first slope, M_1. The first slope, M_1 is generated based on the best fitted linear line of the relationship of ratio settlement–load versus the corresponding settlement. When there is any creep settlement or excessive settlement happened during the early loading stage, the corresponded settlement–load shall be deviated from the slope, M_1. In Fig. 7, analysis has identified a potential creep settlement point which has higher settlement–load ratio and deviated from the normal trend of slope M_1.

Table 2 summaries the deviation of the potential creep settlement for all test piles. It was found that the creep settlements of jacked-in piles (JIP1–JIP4) were obviously

Fig. 7 Potential creep settlement in jacked-in pile JIP1
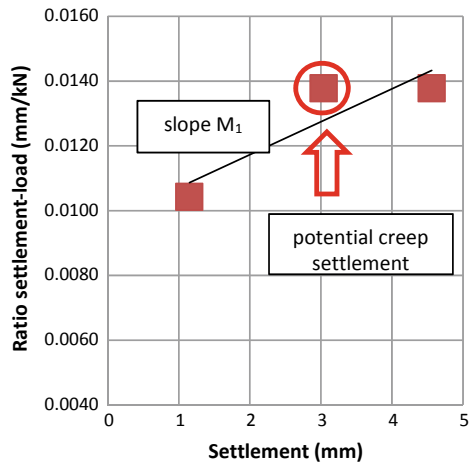
Table 2 Potential creep settlement condition of test piles

Pile ref	Installation method	Creep settlement condition (percentage of deviation from slope M_1, %)
DP1	Driven	1.9
DP2	Driven	3.7
JIP1	Jacked-in	7.0
JIP2	Jacked-in	0.0
JIP3	Jacked-in	8.2
JIP4	Jacked-in	7.9

higher as compared to the driven pile (DP1–DP2). The range of creep settlement on jacked-in piles was 7–8.2% while the driven pile attained lower deviation of 1.9–3.7% only. The reason of driven pile has recorded lower range of creep settlement is mainly due to the uplift movement is resisted by shaft resistance [3] and lower plugging force encountered in the pile tip. The phenomenon of creep settlement is obviously seen in jacked-in piles is mainly due to the bouncing back of the pile when the jacking pressure is released without a proper pile termination procedure. When the subsequence load applied to the same pile, a relatively larger amount of settlement or creep settlement will happen during the early stage of loading. If a proper termination procedure is adopted such as preloading is hold for 30 s before the jacking pressure is released [2]. It may able to diminish the creep settlement such as JIP3 has recorded no creep settlement as shown in Table 2. Despite using pressure holding method, method of pile head tapping to tap on the pile head several times could diminish the creep settlement on jacked-in piles.

5   Conclusion

This study found that Chin's method is a useful tool for pile ultimate capacity estimation without testing the pile to failure. By using Chin' method, the mechanism of load transfer of jacked-in pile can be differentiated from driven pile. The difference is mainly due to the jacked-in pile compressed the surrounding soil in radial direction during the jacking process and subsequently gained higher shaft friction as compared to driven pile. Phenomena of creep settlement on jacked-in pile can be identified using a systematic approach of Chin' plot during the early stage of pile testing. The analysis results of creep settlement could improve the jacked-in pile termination criteria such as the jacked-in pressure holding duration or the tapping numbers on pile head before the jacked-in process is terminated.

References

1. Chin FK (1972) The inverse slope as a prediction of ultimate bearing capacity of piles. In: Proceedings of the third SE Asian conference on soil engineering. The SE Asian Society of Soil Engineering, Hong Kong, pp 83–91
2. Chow CM (2010) Performance of jack-in pile foundation in weathered granite. In: The 17th SE Asian geotechnical conference. SE Asian Geotechnical, Taipei
3. Fei Han MP (2017). Axial resistance of closed-ended steel-pipe piles driven in multilayered soil. J Geotech Geoenviron Eng 3(4)
4. Kou Hai-lei, M-yZ (2015) Shear zone around jacked piles in clay. J Perform Constr Facil 29(6)

5. Yang J, Tham L, Lee P, Chan S, Yu F (2006) Behaviour of jacked and driven piles in sandy soil. Geotechnique 56(4):245–259
6. Yusep MP, Niken SS, Haryanto W (2016) Axial pile capacity prediction obtained from environmental friendly jack-in piling test on clayey soil. Appl Mech Mater 845:70–75

A Review of Seismic Vulnerability and Rehabilitation of Reinforced Concrete Structures

Aw Jia Hao, Mohammed Parvez Anwar, Wael Elleithy, Jaganathan Jayaprakash, Yeong Tuck Wai, and Yap Kian Lim

Abstract Major earthquake events may cause severe fatalities and injuries, resulting in catastrophic damage to structures. However, less emphasis is given regarding earthquake hazard in low seismic regions. Malaysia and Singapore are in a region with low seismic risks; therefore, earthquake resistance designs are not yet included in most of the buildings. Located a few hundred kilometres away from the major earthquake sources, both countries are prone to distant earthquakes, as well as local earthquakes due to the slight change in seismological condition (seismically active period and movement of tectonic plates). This review paper provides some insights into the seismic activity in different places. Research regarding the seismic vulnerability of reinforced concrete (RC) structures is reviewed, with emphasis on non-seismically designed RC buildings. Existing seismic retrofitting methods are also presented through the perspective of level of intervention.

Keywords Earthquake · Seismic hazard · Reinforced concrete · Non-seismically designed · Retrofitting · Rehabilitation

1 Introduction

Earthquake events that occurred in the past centuries had caused severe fatalities and injuries, resulting in catastrophic damage to structures and uncountable loss to the economy of the affected countries. These issues have initiated the research works regarding the seismic behaviour of structures, especially in the recent decades where reinforced concrete (RC) has been widely used in construction industry all over the world. Major research works have been developed in seismic active regions. However, less attention is drawn to regions with low seismic risk, since previous earthquakes

A. J. Hao · M. P. Anwar (✉) · W. Elleithy · Y. T. Wai · Y. K. Lim
Department of Civil Engineering, University of Nottingham Malaysia, Semenyih, Selangor, Malaysia
e-mail: Anwar.Parvez@nottingham.edu.my

J. Jayaprakash (✉)
School of Civil Engineering, Vellore Institute of Technology, Vellore, India
e-mail: jayaprakash.j@vit.ac.in

did not incur severe damage or casualty [9]. For instance in Southeast Asia, many metropolises have been developed in the past few decades due to regional economic growth. Some countries like Malaysia and Singapore are located at regions with low seismic risk. Therefore, earthquake resistance designs are not yet included in most of the buildings, although some earthquake sources surrounding these countries have generated numerous minor earthquakes, whereas some of them had shook high-rise buildings in both Singapore and Kuala Lumpur to a perceptible level [15]. Therefore, the consequences of future earthquake events have become a threat to these cities which are densely populated.

In fact, cities far away from the major earthquake sources are not risk-free, they are also exposed to the risk of being affected by distant earthquakes. In the case of West Malaysia, seismic waves that reached its bedrock are rich in long period waves. These waves are amplified as a result of resonance while they propagate upward through the soft soil layers which have frequency close to the predominant frequency of seismic waves. The resultant amplification waves may also incur resonance to buildings which may affect the comfort of residents [4]. RC framed structures become unsafe or facing high degree of deterioration when subjected to changes in loading and configuration, as well as the occurrence of natural calamities such as earthquakes [16]. Therefore, the issue of seismic hazard should be taken into consideration in order to provide safety to the structures and its occupants. This review aims to provide some insight into the seismic activity in the world, especially in those regions with low seismic hazard but may be affected by earthquakes in future, for example, Malaysia and Singapore in the Southeast Asia region. Research related to seismic vulnerability of RC structures and existing seismic retrofitting methods are also reviewed, while attention is drawn regarding the non-seismically designed RC structures.

2   Seismology

Earthquake is caused by the movements and deformations of tectonic plates. The border between two tectonic plates is named as boundary. The tectonic plates keep moving constantly with a very slow rate but in different directions. Due to this reason, there are different types of inter-plate interactions which give rise to three types of tectonic plate boundaries. They are classified as divergent boundary, convergent boundary and transform boundary. Divergent boundary means two plates are moving apart from each other, while convergent boundary occurs where two plates are pushing towards each other. Transform boundary will occur while two plates are sliding through each other. The faults at highly stressed plate boundaries are usually the locations where earthquakes take place, while the corresponding earthquakes are classified as inter-plate earthquakes. Meanwhile, those earthquakes that occur within plates away from the faults are known as intra-plate earthquakes, where sudden release of energy is expected to take place due to mutual slip of rock beds [6, 7] (Table 1; Fig. 1).

Table 1 Frequency of occurrence of earthquakes based on observations since year 1900 [7]

Description	Magnitude	Average number annually
Great	8.0 and higher	1
Major	7.0–7.9	18
Strong	6.0–6.9	120
Moderate	5.0–5.9	820
Light	4.0–4.9	6200 (estimated)
Minor	3.0–3.9	49,000 (estimated)
Very minor	<3.0	Magnitude 2–3 about 1000 per day Magnitude 1–2 about 8000 per day
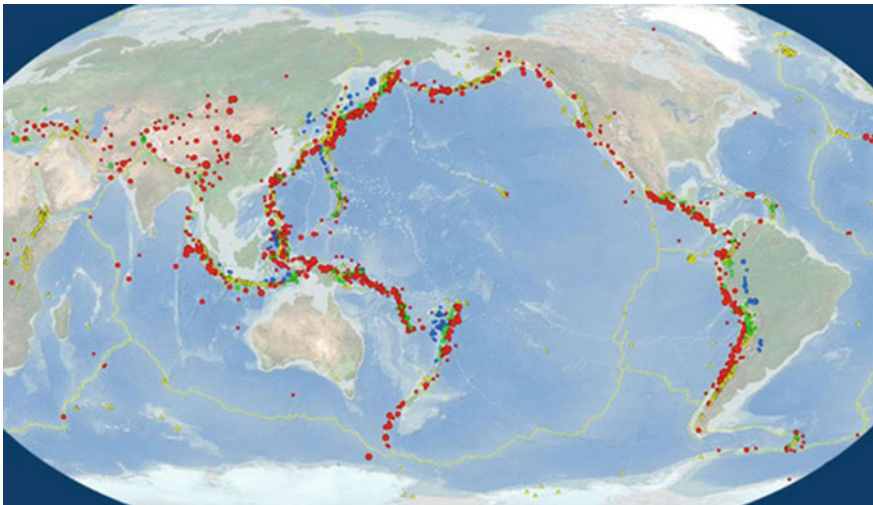
Fig. 1 World seismicity map with global earthquakes from year 1900 to 2013 [24]

2.1 Seismology in Southeast Asia Region

In Southeast Asia, Indonesia and Philippines are the two countries that frequently experience earthquakes and are also directly affected by the consequences of seismicity. Some part of both of these countries is located on or very close to the plate boundaries. The Philippine Sea Plate is bordered by the larger Pacific Plate at the east and Eurasia Plate at the west and northwest side, together with smaller Sunda Plate at southwest direction. The Pacific Plate is subducted into the mantle at south of Japan, which extends more than 3000 km along the eastern margin of the Philippine Sea Plate. The subduction zone consists of rapid plate convergence, hence, high-level
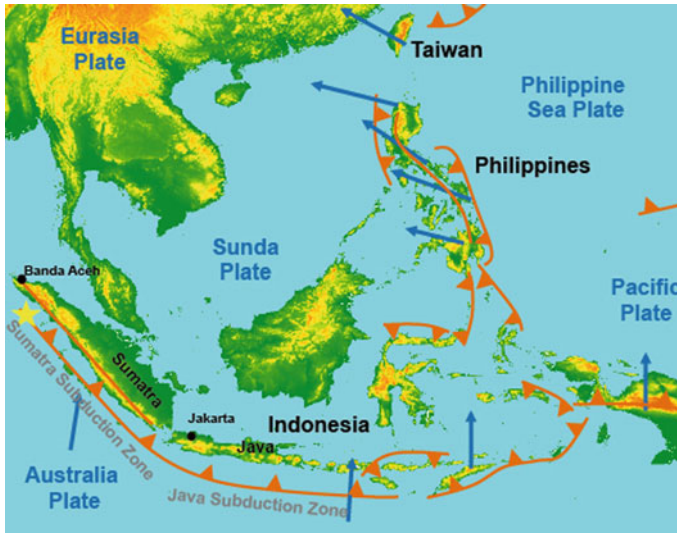
Fig. 2 Seismic hazard map and relative plate motion of Philippine Sea Plate [2]

seismicity extending to depths of over 600 km. The plate interface has been associated with several great magnitude earthquakes in the past. The northwest part of the Philippine Sea Plate is subducting beneath the Eurasia Plate along a convergent zone, which extending from southern Honshu to the northeast coast of Taiwan. The Philippine Sea Plate is attached to a zone of oblique convergence with the Sunda Plate. The highly active convergent plate boundary extends along both sides of Philippine Islands [19]. The seismic hazard map with corresponding plate motion of the Philippine Sea Plate published by United States Geological Survey (USGS) is shown in Fig. 2.

Indonesia experienced the most earthquake events among the countries in Southeast Asia region. The islands of Sumatra and Java are located along the Sumatra subduction zone and Java subduction zone, respectively. These islands are having considerably high population density, especially in Java where the capital Jakarta is located. Hence, an earthquake occurs in Java subduction zone will lead to greater impact than that in Sumatra subduction zone, due to the population as well as robust infrastructure in Java [13].

2.2 Distant Earthquake and Soft Soil Amplification

Malaysia and Singapore are categorised in low seismic region. However, these areas are prone to be influenced by earthquakes originated a few hundred kilometres away. Earthquakes with long epicentral distance to the observing sites are termed as distant earthquakes or far field earthquakes. Mexico City Earthquake in 1985 is a symbolic

example. Mexico City had experienced a tremendous earthquake on 19 September 1985, with a surface wave magnitude (Ms) of 8.1 and Mercalli Intensity of IX. The earthquake had rupture area near the southern coast of Mexico. Severe damages occurred in Mexico City, with more than 4000 people lost their lives [21], although the epicentre of earthquake was approximately 400 km away from Mexico City (1995). The unexpectedly serious damages caused by the distant earthquake were concentrated in area underlain by soft soils, since Mexico City is partially sitting on soft Quaternary deposits. During the earthquake, peak ground acceleration (PGA) recorded on hard rock was about 4% of gravity acceleration (4% g), but the PGA value recorded for soft soil was greater than 20% g. Under this scenario, the earthquake waves which had been attenuated to harmless amplitude due to long distance were then amplified locally by the surface layer of soft soils. Due to the soil amplification, the continuous input of initially insignificant earthquake wave energy had finally caused excitation of surface soil and buildings. The amplified wave had a dominant frequency of 0.5 Hz, therefore, the buildings with natural frequency of 0.5 Hz experienced resonant amplification with ground motion and suffered substantial damages or collapses [21]. Hence, the consequences of distant earthquake should not be ignored even in low seismic region.

The amplitude of incoming earthquake waves is governed by the properties and configurations of the near surface materials. The surface materials consist of different shear wave velocities compared to those of the underlying rock or hard deposits. Normally, shear wave velocities of the surface materials are well below 100 m/s, however, the underlying materials could have values of 2000 m/s or even greater. This difference makes the boundary between soft and hard layers to form a surface of reflection. The incoming wave that has been reflected downwards when hitting ground surface will then be reflected upwards again by the soft-hard boundary. Consequentially, the waves are trapped within the soft surface layer and start to reverberate. The wave will be much stronger under the condition while different reverberating waves in phase with each other [21]. The amplitude of seismograms is smaller for harder materials (such as rock and gravel) compared to some soft materials like clay. The wave energy is transferred to soft clay hence causing significant increase of ground movement. Furthermore, the bedrock motions could be significantly amplified under the condition where natural period of the soft soil is close to predominant natural period of the bedrock motions. Soil amplification can also be enlarged while building is having frequency that is very close to site's frequency [4]. Hence, it is crucial to consider the soil type and corresponding properties of the studied site.

3 Seismic Vulnerability of RC Structures

Reinforced concrete (RC) structures can be categorised into two main types based on their heights: high-rise and low-rise structures. The exact height for which a particular building is defined as high-rise varies with the fire and building codes in particular area or country. Generally, high-rise buildings consist of 12–39 floors

(35–100 m) while low-rise are up to 12 floors (below 35 m) [8]. The conventional design of RC buildings consists of RC frames (foundations, columns, beams and slabs) with masonry infill walls. Nowadays, the modern design applies RC frames with shear wall systems to improve the lateral load resistance. Seismic design is well established for most of the buildings in regions with high seismic risk such as Japan. Seismic isolation systems have been applied to most of the structures, where the application is even extended to high-rise buildings with heights greater than 60 m [5]. Isolation technology can effectively improve the seismic performance of medium-rise and low-rise buildings, but the based-isolated high-rise buildings still in research stage. According to Ma et al. [12], storey drifts and absolute accelerations of a base-isolated high-rise structure could be underestimated if higher modes of superstructure are ignored during structural analysis.

3.1   High-Rise RC Structures

Most of the RC structures in low seismic region are non-seismically designed [9]. Interest may arise whether these buildings can withstand the lateral load imposed by earthquakes up to certain magnitude. Under the scenario, non-seismically designed high-rise and low-rise structures perform differently. Wind load is considered in the structural design for most of the high-rise structures, where lateral load resistance is incorporated to some extent. Adnan and Suradi [1] investigated the performance of medium-rise and high-rise RC buildings using four types of analyses including earthquake and wind load analyses. A comparative study was carried out on the effect of earthquake and wind loads for existing structures in Malaysia. Based on the results obtained from equivalent static analysis (which provided the most critical values), it was found that the studied buildings were generally satisfactory under low intensity earthquake (0.20 g). Inter-storey drifts provided evidences that medium-rise buildings potentially fail at lower storey levels while failures of high-rise buildings potentially take place at higher levels. The indicator showed that only non-structural elements are possibly affected [1]. This indicates that high-rise RC buildings remain stable under low seismic loading.

An irregular high-rise RC building with height of 112.4 m was investigated by Tian et al. [23]. The building had irregular plan and elevation. A 1:20 scaled model was analysed through shaking table test under different earthquake levels, as shown in Fig. 3. The structure did not have significant damage under small earthquake (0.035 g), nevertheless, it encountered significant damages under large earthquake (0.22 g), and however, it was not catastrophic failure. This has proven that deficiencies of structural configurations such as irregular geometry, asymmetric plan, concentration of masses or discontinuity in lateral force resisting system, and weakness of particular storey (e.g. soft storey and weak storey) are not favourable to seismic resistance of structures. However, these designs are very popular in low seismic region; therefore, attraction should be driven to investigate corresponding structural performance under seismic consideration.

Fig. 3 1:20 scaled model of an irregular high-rise RC structure [23]

The failure behaviour of high-rise RC buildings subjected to extreme earthquakes was studied by Lu et al. [11], through finite element modelling which integrated fibre-beam element model, multi-layer shell model and elemental deactivation techniques. A 10-storey simple RC frame, 18-storey and 20-storey frame-core tube systems were studied. For the simple RC frame, collapse occurred at soft storey floors and the floor where discontinuity of column size took place. From the frame-core tube structures, it was noticed that larger ground floor height, changes in column section, changes in shear wall's concrete strength were potentially responsible for the failure and collapse of the entire building under strong earthquakes. The change in structural stiffness is an inhibition for seismic resistance due to the high stress concentration induced, therefore, a special care should be imposed for these structures if seismic provision is necessary. Furthermore, seismic performance of non-seismically designed RC frames with core walls was investigated by Lee et al. [10]. RC structures with core wall in the middle and core wall on the side were studied, and the results showed that most of the non-seismically designed RC frame with core walls, in Korea, fails the life safety level, which did not meet the desired seismic performance criteria, hence, rehabilitations are needed. Similar studies were also conducted by Poovarodom et al. [17] on non-seismically designed high-rise RC structures in Bangkok under soft soil condition. It was observed that the periods of buildings with 15–25 storey heights are close to predominant periods of the amplified ground motion of Bangkok, which shows potential resonance due to distant earthquakes. Vibration mode shapes were identified, meanwhile, general insight was given for the structures in low seismic region, but the structural condition was not well described.

Many existing buildings in Hong Kong are under the same scenario as in Malaysia, where structures were designed according to British Standards [20] with consideration of cyclonic wind loading only. Existing non-seismically designed RC structures

in Hong Kong was studied by Su et al. [20] through the prediction of seismic inter-storey drift. The maximum inter-storey drift demands at deep soil site under rare earthquake events (2% probability of exceedance in 50 years) are recorded at 0.3%, however, this is only applicable for regular buildings. The failure of beam–column RC framed structure or wall structures is also unlikely to happen for buildings less than 45 m high. For the structures with soft storey and torsional irregularity, excessive inter-storey drift and yielding may take place, with moderate damage of non-structural elements. Generally, non-seismically designed RC structures have raised concerns in recent years, such as potential structural performance in projected earthquake scenarios, Su et al. [20], and potential damage caused by soil amplification [4]. Seismic performance of non-seismically designed high-rise RC structures in low seismic region was conducted to some extent, however, the outcomes may vary due to different geotechnical conditions as well as country design codes. High-rise structures are relatively stable under low seismic loading due to the wind load consideration in structural design. Building configurations have significant effects on seismic vulnerability, although only few of them were thoroughly investigated. However, the structures may not be able to resist strong ground motion, especially those with poor configurations which reduce building's lateral load resistance and structural integrity.

4 Seismic Retrofitting of RC Structures

A number of existing buildings have been designed according to old design codes without due consideration of seismic effects. These buildings may have low lateral load resistance, insufficient energy dissipation and may rapidly lose strength during earthquakes. Therefore, interest of research has been focused on such buildings which are non-seismically designed and exhibit deficiencies such as discontinuous load paths and poor detailing. Seismic retrofit or rehabilitation is aimed to provide cost-effective and structurally effective solutions to enhance the structural performance. The conventional retrofitting manners are usually applied through structural strengthening, for instance, adding new structural elements to the system or by strengthening the existing members. The innovative approaches which are most widely used usually incorporate the use of high-performance concrete, steel and composites such as fibre reinforced polymers. The beams and columns, especially beam–column joints are usually the point of interest by researchers, since failure due to seismic action usually occur in these areas. McCafferty and Moody [14] have studied the dynamic characteristics of RC beam–column specimens subjected to dynamic loading. Changes in natural frequencies and damping coefficients were observed which associated to four different cracking conditions (no cracks, minor cracks, intermediate cracks and extensive cracking) and various amounts of transverse reinforcement within beam–column joint region. Cracking within beam region could significantly reduce member's natural frequency, therefore, this issue should be taken care to avoid resonance with the seismic wave frequency.

4.1 Conventional Retrofitting Methods

Steel jacketing or steel cage is used when there is insufficient shear strength and ductility caused by inappropriate reinforcement of structural elements (mostly columns). Steel jacketing refers to the total encasement of column using thin steel plates placed at certain distance from the column surface, while the gaps are filled by non-shrink grout. Steel cage is another alternative, where steel angles are placed at the corners of existing columns, and then transversal steel straps or continuous steel places are welded on the steel angles (Fig. 4). The gap between existing elements and steel plates is filled using on-shrink grout, with shotcrete cover applied when fire protection is required. Deformation capacity is increased with application of steel jacketing, while plate adhesion enhanced shear capacity and flexural strength of local elements [22]. In addition, steel jacketing on columns was used by Ruiz-Pinilla et al. [18] as the seismic strengthening system for RC structures. Full scale beam–column joints with strengthened columns were tested under cyclic loads, while results show that the application of steel jacketing improve the bending strength of columns and increase joint resistant section [18].

Reinforced concrete (RC) jacketing is one of the methods which is commonly used in rehabilitation of concrete members. It possesses global effect to the structure, provided that longitudinal reinforcement placed inside the jacket passes through the existing slabs with new concrete filled in the beam–column joints (Fig. 5). Stiffness, strength and ductility can be enhanced through the global intervention. If the RC jacketing is only applied at a particular floor, it is considered as local intervention to the
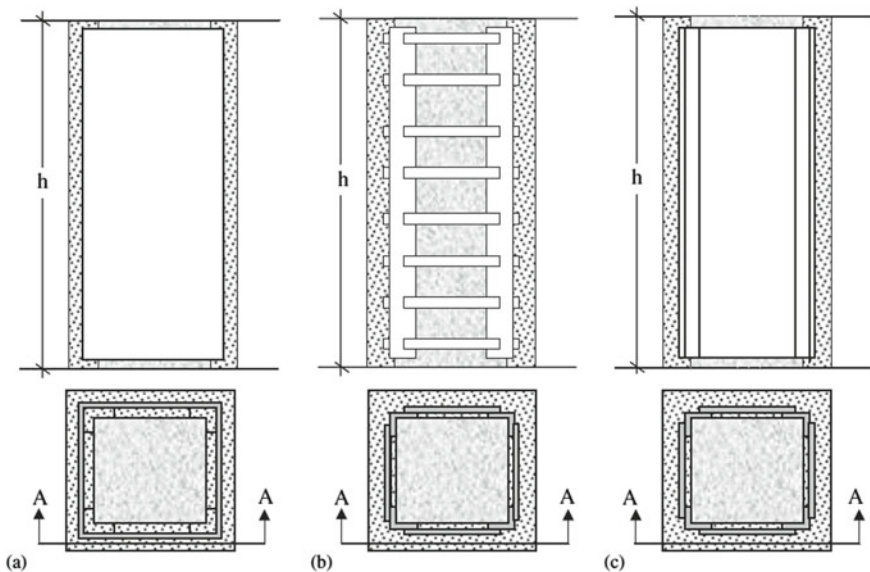
Fig. 4 **a** Steel jacketing, **b** steel cage using transversal steel straps and **c** steel plates [22]

Fig. 5 Reinforced concrete (RC) jacketing applied through several floors [22]

corresponding member, where strength of column is enhanced but flexural strength and the strength of beam–column joints remain unchanged. Additional RC walls or shear walls are another conventional alternative to strengthen existing structures. It is a global intervention approach, whereby global lateral drifts can be controlled through the new shear walls, meanwhile strength and stiffness are enhanced. The distribution of shear walls should be taken into consideration during the design stage (preferably consistent and regular location), to ensure building configurations in both plan and elevation are obeyed and load path to foundations are well integrated. Moreover, foundations might also need to be strengthened to resist the additional overturning moment. Hence, the additional shear walls are only suitable and cost-effective for the existing buildings with adequate foundation system.

Steel bracing is another retrofitting technique which possesses global intervention to the structures. Additional weight of the steel bracings imposed to the structure is minimal, meanwhile, it is able to accommodate openings. Therefore, it involves minimum disruption to the building and occupants. Lateral stiffness and strength of structures can be improved, especially post-tensioned bracings which can significantly alter the distribution of internal forces of existing structures [22]. Badoux and Jirsa [3] have proven that diagonal steel bracing is an effective approach for enhancing lateral strength of existing structures, meanwhile drift control and collapse prevention can be achieved. In practice, there are two types of bracings which are concentric bracing system and eccentric bracing system (Fig. 6). Concentric bracings increase lateral stiffness and natural frequency of RC frame, but decrease the lateral drift. While the bracings decrease the bending moments and shear forces in columns, it enhances axial compression in columns, which is not a problem for RC structures. Eccentric bracings reduce the lateral stiffness of RC frame but improve the energy dissipation capacity [25]. Steel bracings and shear walls are more effective than other techniques such as RC jacketing, due to the reason that they are more cost-effective and have greater familiarity in the construction industry.
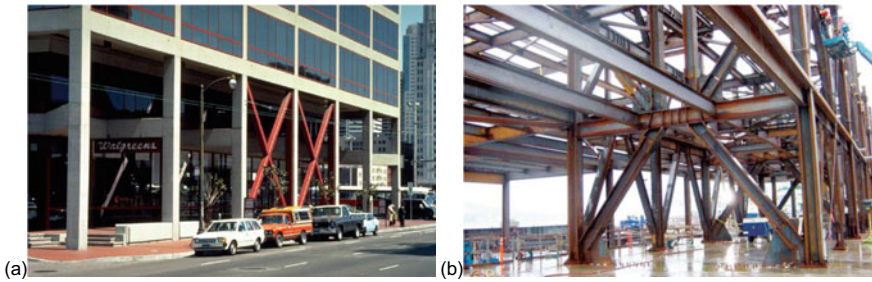
Fig. 6 Steel bracings applied, **a** concentric bracings and **b** eccentric bracings [25]

5 Conclusion

This paper provides insights into global seismic behaviour. Many metropolises have been developed in the past few decades, including those located at regions with low seismic hazard. Most of the buildings in these regions are non-seismically designed; hence, they are exposed to the risk of being affected by distant earthquakes or local earthquakes due to the change in seismological condition in future. Research regarding the seismic vulnerability of RC structures is presented in this paper, especially for the non-seismically designed RC buildings. There could be a need to redefine global seismic hazard through more detailed manners to ensure the safety of existing and future structures and their occupants. The seismic vulnerability assessment should be conducted to a comprehensive level, to enable further action to be taken such as rehabilitation of existing RC structures and improvement in new structural designs to provide sufficient seismic resistance to counterbalance seismic hazard in future. Review of seismic retrofitting approaches available in the field is also presented. The review has not included all techniques, while the more common methods are included. These methods can also be classified using different criteria, however, the level of intervention (global and local intervention) used in this paper is believed to provide clearer pictures regarding the influence of particular approaches to existing RC structures. Combination of conventional retrofitting approaches with advanced materials should be further studied for better understanding and practicable contributions with consideration of cost optimisation to achieve economical solutions.

References

1. Adnan A, Suradi S (2008) Comparison on the effect of earthquake and wind loads on the performance of reinforced concrete buildings. In: The 14th world conference on earthquake engineering, October 12–17, Beijing, China. Available from: https://www.iitk.ac.in/nicee/wcee/article/14_S03-005.PDF. 07 May 2015
2. Annenberg L (2015) Plates & boundaries. https://www.learner.org/interactives/dynamicearth/plate.html. 06 Apr 2015
3. Badoux M, Jirsa JO (1990) Steel bracing of RC frames for seismic retrofitting. J Struct Eng 116(1):55–74
4. Balendra T, Li Z (2008) Seismic hazard of Singapore and Malaysia. Electron J Struct Eng 8:57–63
5. Bangash MYH (2011) Earthquake resistant buildings: dynamic analyses, numerical computations, codified methods, case studies and examples. Springer-Verlag, Berlin Heidelberg
6. Bhattacharya S, Nayak S, Dutta SC (2014) A critical review of retrofitting methods for unreinforced masonry structures. Int J Disaster Risk Reduction 7:51–67
7. Datta TK (2010) Seismic analysis of structures. Wiley (Asia), Singapore
8. Emporis (2015). Multi story building. https://www.emporis.com/building/standard/66/multi-story-building. 24 May 2015
9. Kamarudin AF, Daud ME, Ibrahim A, Ibrahim Z, Koh HB (2014) Dynamic characteristics of site and existing low-rise RC building for seismic vulnerability assessment. Int J Geol 8:28–38. ISSN 1998–4499
10. Lee T-H, Choi K-B, Abu-Lebdeh T (2014) Seismic assessment of non-seismically designed reinforced concrete frames with core walls. Amer J Appl Sci 11(11):1892–1903
11. Lu X, Lu X, Guan H, Ye L (2013) Collapse simulation of reinforced concrete high-rise building induced by extreme earthquakes. Earthq Eng Struct Dynam 42(5):705–723
12. Ma CF, Zhang YH, Tan P, Zhou FL (2014) Seismic response of base-isolated high-rise buildings under fully nonstationary excitation. Shock Vibr 1–11
13. Ma N (2014) "Still risky but better prepared—10 years after the 2004 Sumatra Tsunami. AIR Worldwide Corporation. https://www.air-worldwide.com/Publications/AIR-Currents/2014/Still-Risky-But-Better-Prepared%E2%80%9410-Years-After-the-2004-Sumatra-Tsunami/. 09 Apr 2015
14. McCafferty R, Moody M (1973) Dynamic characteristics of reinforced concrete beam column specimens for various levels of cracking. In: Proceedings of the 5th World conference on earthquake engineering, vol 1, pp 811–814
15. Megawati K, Pan TC, Koketsu K (2005) Response spectral attenuation relationships for Sumatran subduction earthquakes and the seismic hazard implications to Singapore and Kuala Lumpur. Soil Dyn Earthq Eng 25:11–25
16. Mukherjee A, Joshi M (2005) FRPC reinforced concrete beam–column joints under cyclic excitation. Compos Struct 70:185–199
17. Poovarodom N, Warnitchai P, Petcharoen C (2004) Dynamic characteristics of non-seismically designed reinforced concrete buildings with soft soil condition in Bangkok. In: 13th world conference on earthquake engineering, Vancouver, BC, Canada
18. Ruiz-Pinilla JG, Pallarés FJ, Gimenez E, Calderón PA (2014) Experimental tests on retrofitted RC beam–column joints under-designed to seismic loads: general approach. Eng Struct 59:702–714
19. Smoczyk GM, Hayes GP, Hamburger MW, Benz HM, Villaseñor A, Furlong KP (2013) Seismicity of the earth 1900–2012 Philippine sea plate and vicinity. U.S. geological survey, open-file report, no. 2010-1083-M
20. Su RKL, Lam NTK, Tsang HH (2008) Seismic drift demand and capacity of non-seismically designed concrete buildings in Hong Kong. Electron J Struct Eng 8:110–121
21. Sun J, Pan T-C (1995) Seismic characteristics of sumatra and its relevance to peninsular Malaysia and Singapore. J SE Asian Earth Sci 12(1–2):105–111

22. Thermou GE, Elnashai AS (2006) Seismic retrofit schemes for rc structures and local–global consequences. Prog Struct Mat Eng 8(1):1–15
23. Tian C, Liu J, Zhang H, Cao J (2012) Experimental study on seismic behaviour of an irregular high-rise building. In: Proceedings of the 15th world conference on earthquake engineering, Lisbon, Portugal
24. USGS (2015) World Seismicity Map 1900–2013. U.S. geological survey. https://earthquake.usgs.gov/earthquakes/world/seismicity_maps/. 13 Sep 2015
25. Viswanath K, Prakash K, Desai A (2010) Seismic analysis of steel braced reinforced concrete frames. Int J Civ Struct Eng 1(1):114–122

Seismic Analysis of High Rise Steel Structure with Outrigger Braced System

S. Daniel and J. Visuvasam

Abstract Urbanization, increase in population and lack of living space in urban areas lead to development of the high rise structures and this situation is unavoidable in the twenty-first century. The constant evolution of high rise structures is very essential for the development of developing nations like India. However, designing and construction of high rise building is a challenging one because as the height of the structure increases the structural stiffness and resistance of building against lateral loads become the crucial considerations. For high rise structures, the major dominating lateral forces are wind loads and seismic loads. Therefore, minimizing the lateral displacement and inter-storey drift of high rise structures is a demanding factor. There are many lateral load resisting systems available for high rise structures such as shear walls, diagrids, braced frames and outriggers are used in recent decades. In this study, the effectiveness of outrigger system at various locations along the height of the high rise structures in resisting lateral loads is discussed. Time history analysis is carried out on three models of 20 storey steel frame structures for this study such as (1) model with outrigger at 0.3 H and at top floor, (2) model with outrigger at 0.45 H and at top floor and (3) model with outrigger at 0.6 H and at top floor. It is found that the proper location of outrigger especially at 0.6 H and at top floor enhances the seismic performance of the high rise structures.

Keywords High rise structures · Outriggers · Time history analysis · SAP2000 · Steel structures

1 Introduction

Outrigger is a lateral load resisting system used in high rise structures as an effective solution to minimize the lateral deformations such as lateral storey displacement and inter-storey drifts. The conventional outrigger system consists of core at centre and the outer columns at the periphery while the horizontal outrigger trusses/girders

S. Daniel (✉) · J. Visuvasam
School of Civil Engineering, Vellore Institute of Technology, Vellore, India
e-mail: daniel07samuel@gmail.com

connect the outer columns to the central core. The core is either constructed as steel braced frame or reinforced concrete shear wall and also the structural members of outrigger system either are made of steel/concrete/composite. This structural setup of the outrigger acts as a one lateral resisting system which will reduce not only the lateral deformations but also the core overturning moment. As the height of the building increases, the structure will become more slender and therefore it will be exposed to vulnerable lateral loads. At this situation, the design of high rise structure is mainly controlled by the factors such as strength, stiffness, torsional rigidity and serviceability. Among the other lateral load resisting system such as shear wall, braced frames, diagrids and tubular systems, the outrigger is found to be more effective and economic, especially in slender and super tall towers. In addition, belt trusses are often used as additional elements which connect the outer columns at periphery level and they enhance the rigidity of the structure to some extent and it is called as 'virtual outriggers'.

A narrow boat can overturn when it is hit by unexpected waves but with the little span of leverage attached to the boat makes it to float gently thus by avoiding overturn. The principle of outrigger system is inspired from the concept of deep beams and later from concrete walls. When a higher lateral force acts on the high rise structure consisting of outrigger system, the central core tries to tilt its position. The rotational movement at the outrigger level results in the formation of tension–compression couple in the outer columns, acting in opposite to that movement results in restoring movement acting on the core at outrigger level as shown in Fig. 1 [1].

A comparative study of a nonlinear static pushover was performed between five high rise structures of different heights with different bracing systems and conventional moment resisting steel frame to find the seismic effectiveness of braced frames in terms of lateral storey displacement, inter-storey drift and base shear. It was found that the high rise steel braced frame works effectively against lateral loads [10]. A nonlinear static pushover of 4-high rise steel outrigger braced structure of different heights was performed by varying the location of outrigger at different levels to find optimum location of outriggers and effectiveness of structure against lateral loads. From this study, it was observed that the location of outriggers at 0.3–0.6 times height of the building greatly enhances the seismic behaviour of structures. A 50-storey RC
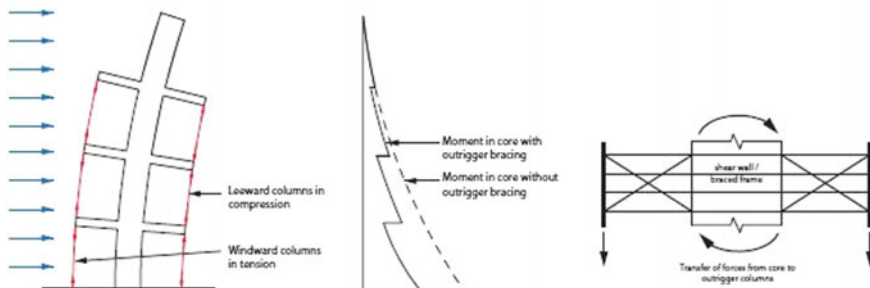
Fig. 1 Interaction of core and outrigger against lateral force [1]

braced frame structure was investigated by varying the location and number of outriggers with three different ground motions to check the seismic behaviour and optimum location of the outriggers. This paper mainly aimed to find the economic design of outriggers under seismic load [3]. A 2D model of high rise steel structure is analysed for wind load alone to find the optimum location of outriggers. It was found that the geometry of the structural system plays a major role in effective seismic design of high rise structures in terms of drift [2]. In this study, three different locations of outrigger are selected such as 0.3, 0.45 and 0.6 H based on previous studies [11] on optimum location of outriggers and time history analysis is carried out to study the effectiveness of outriggers under seismic forces.

2   Modelling and Analysis

2.1   Structure Configuration

A three 20-storey steel framed structures with plan dimensions 16×16 m consist of three bays along both directions are considered for investigation. The plan and elevation of the considered models are shown in Figs. 2 and 3. The typical storey height of the structure is 3.5 m. The structure is symmetric in both the x and y-axes. The structural design of these structures is carried out using [4]. The yield strength of steel material used for beams and columns are 345 MPa and for braces is YSt 310. The sections used for braces are assigned from [5]. The dimensions of structural components are listed in Table 1. Beam to column connections are considered as fully restrained. The model used for investigation is listed in Table 2. The support condition of the structure is assumed to be fixed.

Fig. 2   Plan view of the structure
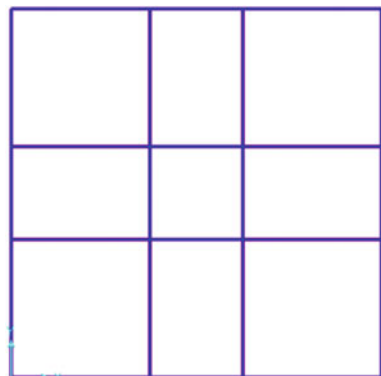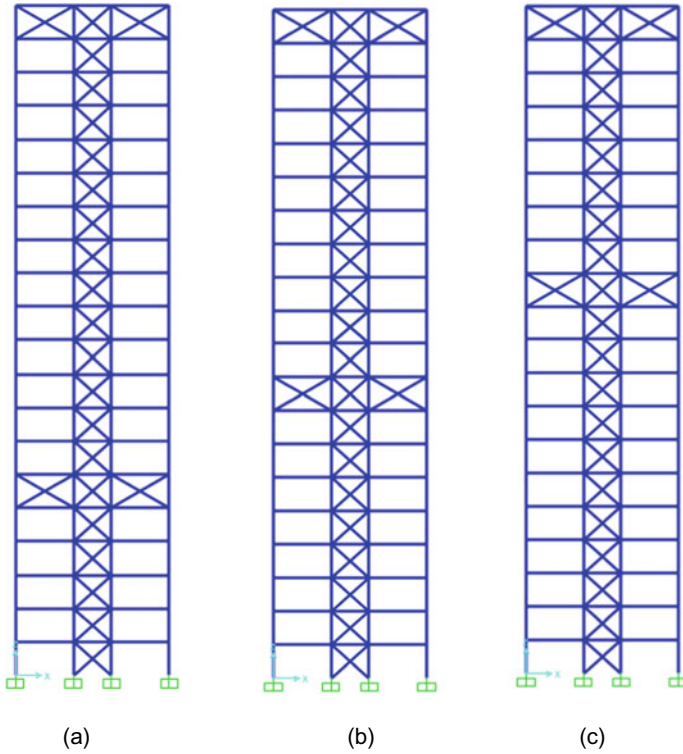
Fig. 3   Position of outriggers **a** 0.3 H and at top, **b** 0.45 H and at top and **c** 0.6 H and at top

Table 1 Details of structural components used

Structural components	Sections/dimensions
Steel braced core	4 × 4 m
Span of an outrigger	6 m
Beams	ISMB500, ISMB450, ISMB400
Columns (fabricated sections)	IF70050W110032, IF50040W90028
Braces	NB300H10

Table 2 Models used for analysis

Model 1	Structure with outrigger position at 0.3 H and at top
Model 2	Structure with outrigger position at 0.45 H and at top
Model 3	Structure with outrigger position at 0.6 H and at top
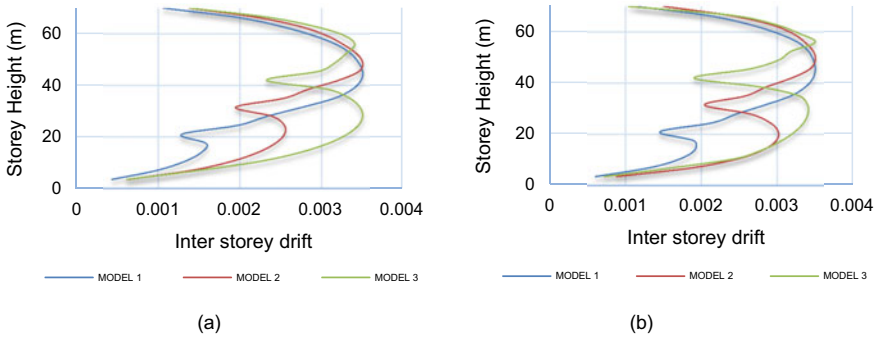
Fig. 4 Inter-storey drift ratio of outrigger systems **a** equivalent static and **b** response spectrum methods

2.2 Loading Configuration

The live [7] and dead loads [6] are given as 4 and 2 kN/m^2 as per Indian Standards. The wind loads are considered as per [8]. Seismic design loads are applied to the structure as per [9].

3 Seismic Analysis

As per [9], it is assumed that the high rise structure is located at Chennai, India. Therefore, seismic zone III is adopted. The type of soil is taken as type III (soft). The importance factor of this structure is considered as 1.5. The response reduction factor for this Ordinary Braced Frame (OBF) building system is adopted as 4.0. Equivalent static and response spectrum analyses are performed for the modelled structure using SAP2000. From the analysis, natural frequency, time period, storey displacement and inter-storey drift value are obtained for all the models. It is observed that the drift for all models with outriggers are reduced to greater extent and it satisfies the drift limitation of 0.4% which is recommended by [9]. The inter-storey drift ratio to the storey levels are plotted in Fig. 4.

4 Time History Analysis

Time history analysis is a dynamic analysis used to evaluate the seismic response of the structure under earthquake loads which may vary according to the specified time. The ground motions used in this study are obtained from the Seismomatch ground motion database. The four ground motions with different PGA values are used for the analysis are shown in Fig. 5.
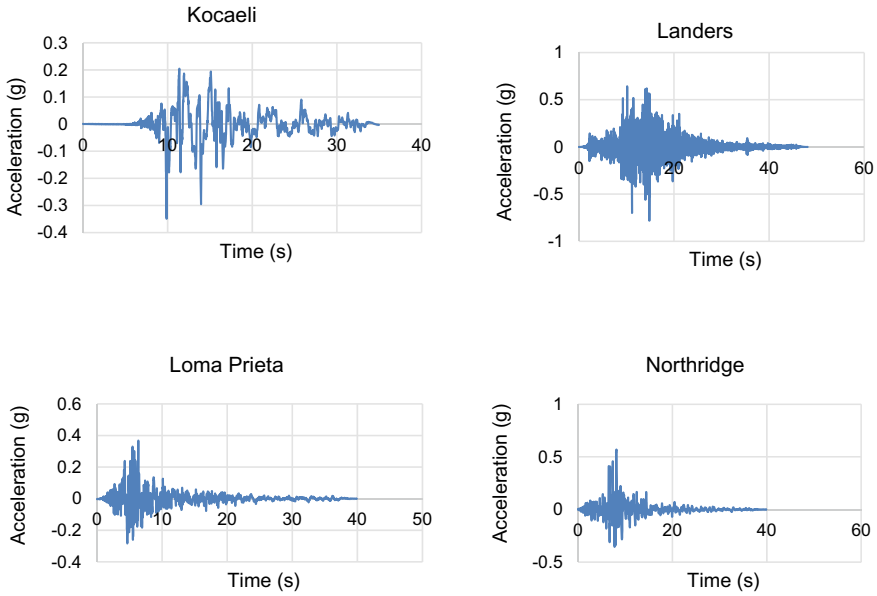
Fig. 5 Selected unscaled ground motions for time history analysis

The response spectrum of these selected ground motions is scaled to match the design spectrum recommended by [9]. The scaling of ground motions is carried out using Seismomatch by considering the factors of time period, tolerance of convergent and scale factor. The natural time periods of the outrigger structures with models 1, 2 and 3 are 2.07 s, 2.34 s and 1.61 s, respectively. Therefore, the time period of the selected ground motions is fixed between 0.5 and 3.5 s and the tolerance for scaling is maintained to be less than 25%. The scale factor used for scaling of ground motions and other considered factors is given in Table 3. The matched response spectrum of ground motions with IS 1893:2016 recommended design spectrum is shown in Fig. 6. Then, the time history analysis was performed by applying the scaled ground motions to all models.

Table 3 Details of selected ground motions

Ground motion	PGA	Tmin	Tmax	Tolerance	Scale factor
Kocaeli	0.261	0.2	3.5	14.7	1.1
Landers	0.778	0.5	3.5	14.8	1.0
Loma prieta	0.306	0.5	3.5	13.8	1.0
Northridge	0.356	0.5	3.5	15	0.8
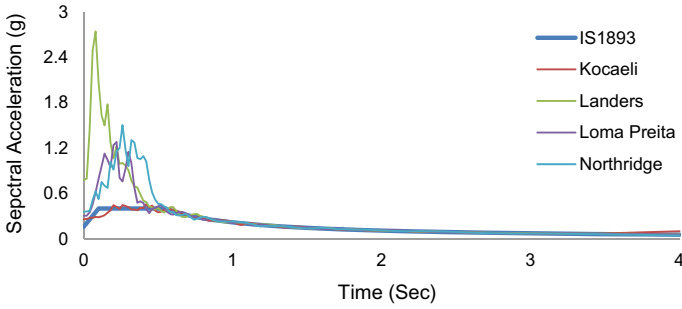
Fig. 6 Scaled response spectra of ground motions

5 Results and Discussion

The linear modal time history analysis is performed on models 1, 2 and 3. After analysis, the storey displacements at every floor levels of all models are considered and average storey displacements of all structure due to the various ground motions are recorded and compared. Figure 7a shows the storey displacement of model 2 over building height for selected ground motions. The maximum storey displacements of model 2 are obtained to be 142 mm, 121 mm, 163 mm and 183 mm for Kocaeli,

(a)   (b)
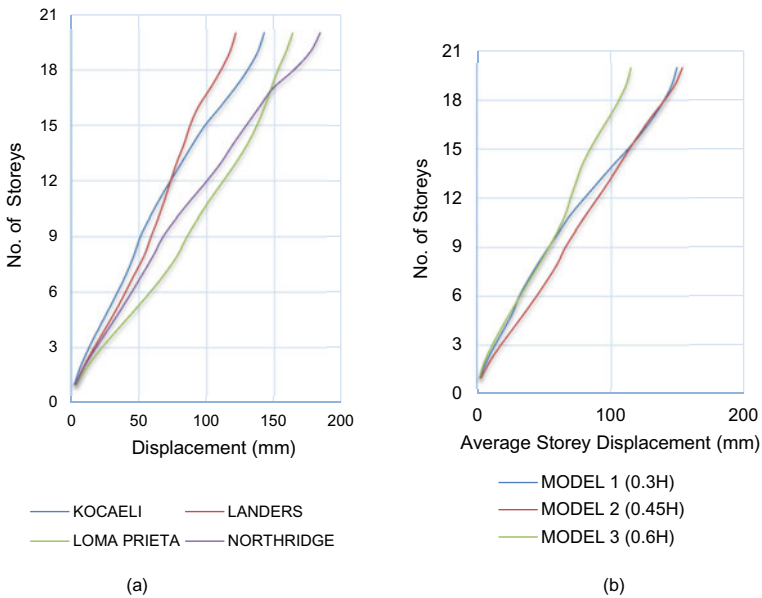
Fig. 7 Comparison of storey displacement of outrigger structures **a** various ground motions on model 2 and **b** average displacement of various outrigger systems

Landers, Loma Prieta and Northridge, respectively. It clearly shows that the response of a structure is different from one ground motion to the other. It may be because of characteristics of ground motions which alter the response of structure.

Similarly, the average lateral storey displacements of models 1, 2 and 3 are compared and shown in Fig. 7b. The average lateral displacement values at roof level of model 1, model 2 and model 3 are obtained to be 148 mm, 152 mm and 114 mm, respectively. Moreover, it can be observed from Fig. 7b that model 2 experiences higher storey displacement as compared to other models.

Inter-storey drift is the relative displacement of the successive storey levels per storey height. As per Indian standards, the value of inter-storey drift is limited to 0.4%. The inter-storey drift values of model 2 under four scaled ground motions are shown in Fig. 8a. The maximum values of inter-storey drift of model 2 are observed to be 0.32%, 0.25%, 0.34%, 0.44% for Kocaeli, Landers, Loma Prieta and Northridge, respectively. The maximum values of the other two models such as model 1, model 3 are 0.41% for Landers and 0.27% for Northridge. It is very apparent that model 1 experiences a maximum inter-storey drift and model 3 experiences a minimum inter-storey drift values for different ground motions. It can also be seen that all models experience the maximum values at upper storey levels.

Similarly, the comparison of average inter-storey drift over the height of the building for all models is shown in Fig. 8b. It is found that model 3 provides more lateral resistance against seismic forces compared to other two models. The maximum average inter-storey drift values of these models are estimated to be 0.35%, 0.25% and 0.21% for model 1, model 2 and model 3, respectively. Furthermore, model 1 experiences maximum drift at upper storey levels, whereas model 2 experiences the same at lower storey levels. Thus, it is very clear that outrigger can be provided at 0.6H to reduce the drift effectively.
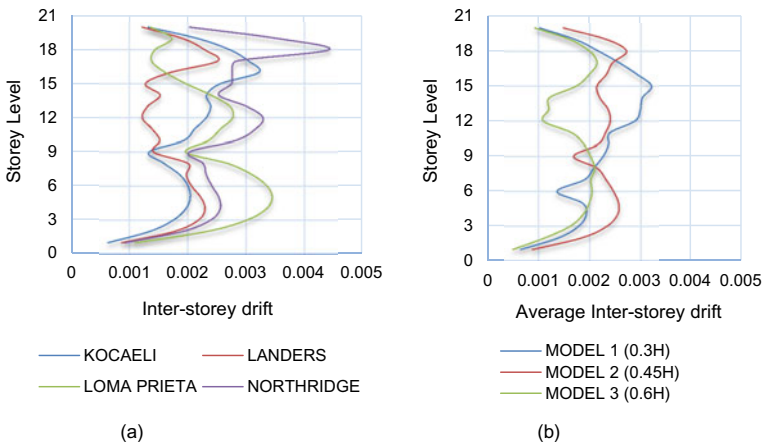
Fig. 8 Comparison of inter-storey drifts **a** various ground motions on model 2 and **b** average displacement of various outrigger systems

6 Conclusion

Three models consisting of outriggers at 0.3, 0.45 and 0.6 H were considered for linear modal time history analysis. Four ground motions are selected and scaled to match the target response spectra specified as per Indian Standards. The results in terms of storey lateral displacement and inter-storey drifts are estimated and discussed. It is concluded from the results that by providing outriggers at 0.6 H, the storey displacement and inter-drift can be reduced significantly. It is also observed that model with outrigger at 0.3 H experiences maximum drift at upper storey levels and model 2 with outrigger at 0.45 H experiences the same at lower storey levels. It could cause the collapse of structure due to the inelastic deformation at these storey levels. Thus, providing outrigger at 0.6 H, the maximum resistance against lateral forces can be achieved.

References

1. Choi HS, Ho G, Joseph L, Mathias N (2017) Outrigger design for high-rise buildings. The Images Publishing Group Pty Ltd., Victoria, Australia
2. Gerasimidis S, Efthymiou E, Baniotopoulos CC (2009) Optimum outrigger locations of high-rise steel buildings for wind loading. In: Proceedings of 5th European and African conference on wind engineering EACWE 5, Florence, Italy
3. Herath N, Haritos N, Ngo T, Mendis P (2009). Behaviour of outrigger beams in high rise Buildings under earthquake loads. In: Proceedings of Australian Earthquake Engineering Society Conference, Australia
4. IS 800 (2007) General construction in steel—code of practice (third revision). Bureau of Indian Standards, New Delhi, India
5. IS 1161 (1998) Steel tubes for structural purposes—specification (fourth revision). Bureau of Indian Standards, New Delhi, India
6. IS 875-Part 1 (1987) Code of practice for design loads (other than earthquake) for buildings and structures—dead loads—unit weights of building materials and stored materials (second revision). Bureau of Indian Standards, New Delhi, India
7. IS 875-Part 2 (1987) Code of practice for design loads (other than earthquake) for buildings and structures: imposed loads (second revision). Bureau of Indian Standards, New Delhi, India
8. IS 875-Part 3 (2015) Code of practice for design loads (other than earthquake) for buildings and structures: wind loads (second revision). Bureau of Indian Standards, New Delhi, India
9. IS 1893-Part 1 (2016) Criteria for earthquake resistant design of structures: general provisions and buildings (sixth revision). Bureau of Indian Standards, New Delhi, India
10. Patil DM, Sangle KK (2015) Seismic behaviour of different bracing systems in high rise 2-D steel buildings. Structures 3:282–305
11. Patil DM, Sangle KK (2016) Seismic behaviour of outrigger braced systems in high rise 2-D steel buildings. Structures 8:1–16

Performance of Cantilever Structure Inspired by Tree Patterns

Yap Kian Lim, Mohammed Parvez Anwar, Jaganathan Jayaprakash, Wael Elleithy, Teck Leong Lau, and Jing Ying Wong

Abstract Nature designs have inspired many architectural works and technological advancements in today's world. Trees are one of nature's pattern and share similar mechanics as in civil engineering structures (e.g. buildings). From literature, trees are able to transfer load efficiently. To identify the effectiveness of having a triangular profile similar to nature, a set of cantilever beams with various geometrical projection are analysed under transverse loading. Standard triangle (ST) cantilever beam was the best overall design. However, it was also found that the method of tensile triangles (MTT) cantilever beam was able to improve cantilever designs if the projection remains small. Thus, demonstrating why buttresses do not exist along with its entire tree height. The results obtained do not discard its potential as it may be more suitable in other civil engineering applications.

Keywords Cantilever · Nature · Vertical loading · Static · Steel · Triangular projection

1 Introduction

Geometry plays a pivotal role in the stability of any kind of structures, and for solid mechanics, it is often related to its shape and size. Hence, the geometrical design of a structure is often associated with the amplification effects of a loading condition on the structure. Geometrical patterns can often be found in nature, and its pattern may sometimes be modelled and explained mathematically. Trees are one of the known natural patterns. The development of tree buttresses and branches in the tree has sparked many research interests [5, 11]. Mattheck's [7] study in trees has led to the development of a graphical optimisation method that resembles the shape of

Y. K. Lim · M. P. Anwar (✉) · W. Elleithy · T. L. Lau · J. Y. Wong
Department of Civil Engineering, University of Nottingham Malaysia, Semenyih, Selangor, Malaysia
e-mail: Anwar.Parvez@nottingham.edu.my

J. Jayaprakash (✉)
School of Civil Engineering, Vellore Institute of Technology, Vellore, India
e-mail: jayaprakash.j@vit.ac.in

Fig. 1 MTT shape profile follows closely to the shape profile in buttresses

a tree buttress known as the method of tensile triangles (MTT) as shown in Fig. 1. The shape profile has led to a better notch design that reduces or eliminate localised stress concentration in between joints [8]. Although there are other graphical optimisation methods or natural occurring curves like, for example, Grodzinski's curve [3, 4] and Baud's curve [1, 6], Mattheck's design were a practical choice due to its simplicity and construction considerations [10]. By applying this design in structures, the study hopes to create a better connection/joint design. To eliminate factors other than geometry, a simple linear elastic isotropic purely fixed cantilever beam is the natural choice to understand and to determine the advantages and disadvantages of different cantilever beam geometries. Hence, a parametric study on the various steel cantilever beam geometries was conducted to identify the performance and feasibility of introducing a projection that follows the shape profile of MTT.

2 Simulation of Cantilever Beam Geometries

The study was conducted through the finite element method (FEM) package to identify and capture the general behaviour of the various cantilever beam geometries. The geometry of cantilever beams is varied by the projection beneath or the bottom face of the beam. Its performance can be quantified through the comparison of typical/traditional cantilever geometry with regards to its deflection resistance and amount of material required. Other aspects, like the total depth of cantilever and stress profile, are also reviewed. A total of 134 different sizings of cantilever beam geometries were modelled, producing a total of 1474 specimen variations. Using ANSYS, the cantilever beams were analysed under a 2D plane stress, isotropic, linear elastic and a programmed controlled medium coarse mesh. The cantilever beam geometries are modelled as a solid steel cantilever section with a Young's modulus of 200 GPa and a Poisson's ratio of 0.3. Since the displacement value in the x-direction is small and negligible, the displacement value defined in this study is the total displacement (x and y).

There are three rectangular cantilever base models (a.k.a. standard) with a length of 200 and 1 mm thick defined in this analysis, and they are varied by their depth of 20, 30 and 40 mm with an aspect ratio of 1/10, 3/20 and 1/5, respectively. The cantilever beams were analysed under five separate loading conditions, as shown in Fig. 2, 1000 N single point load top face downwards (STD), 1000 N single point load bottom face downwards (SBD), 1000 N single point load top face upwards (STU), 1000 N single point load bottom face upwards (SBU) and 5 MPa triangular pressure top face downwards with the maximum at its free end (TTD). The loading condition of a single point load at its free end is used to simulate the behaviour of a cantilever beam with the maximum amount of deflection on whereas the triangular pressure with its maximum at its free end is to simulate the worst distributed loading condition on a cantilever beam. A total of five cantilever beam geometries were analysed, as shown in Fig. 3, standard (base model), cantilever beam with increased depth (ID), cantilever beam with a tapering triangle (ST), cantilever beam with a triangular projection following the method of tensile triangles rule of thumb (MTTR) and cantilever beam
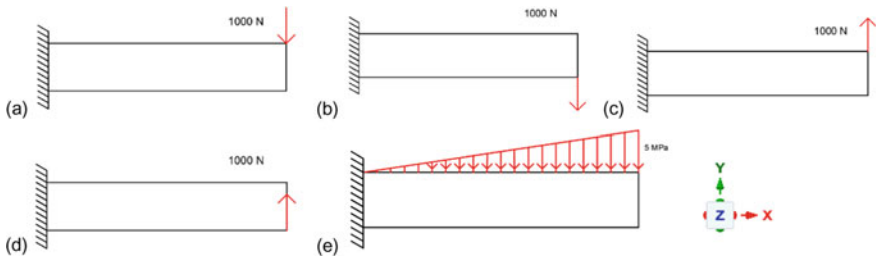
Fig. 2 Separate loading conditions on the cantilever beam. **a** 1000 N single point load top face downwards (STD); **b** 1000 N single point load bottom face downwards (SBD); **c** 1000 N single point load top face upwards (STU); **d** 1000 N single point load bottom face upwards (SBU); **e** 5 MPa triangular pressure top face downwards with the maximum at its free end (TTD)
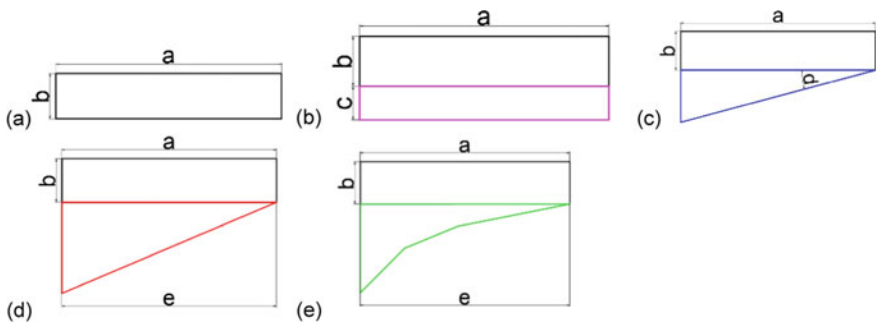
Fig. 3 Various cantilever beam geometries. **a** standard (base model), **b** cantilever beam with increased depth (CID), **c** cantilever beam with a tapering triangle (ST), **d** cantilever beam with a triangular projection following the method of tensile triangles rule of thumb (MTTR), **e** cantilever beam with a triangular projection following the method of tensile triangles (MTT)

Table 1 Deflection performance comparison of the cantilever beam geometries under STD, STU and SBD

Cantilever beam	DT versus UT (average difference %)	Volume range (mm^3)	DT versus DB (average difference %)	Volume range (mm^3)
MTT	2.62	4003–4665	2.07	4772–9418
ST	1.97	4350–4700	5.3	5050–12,900
MTTR	2.7	4005–4525	2.88	4632.5–12,500

with a triangular projection following the method of tensile triangles (MTT). The parameter analysed in this study for "a" is fixed all cantilever models, "b" varies from 20 to 40 mm, "c" varies from 0 to 27 mm, "d" varies from 1 to 26° and "e" varies from 5 to 200 mm. Due to the page limit, a focused set of results will be discussed. Geometrical dimensions are rounded to the next integer in the analysis.

3 Deflection Resistance of Various Cantilever Beam Geometries and Its Loading Condition

3.1 Comparison of Four Single Point Loading Conditions

The results discussed only encompass the 20 mm cantilever beam geometries as it will result in a higher asymmetry design while emphasising the performance of the triangular projection. All cantilever beam geometries performed the worst under STD loading condition. The ID cantilever beams as expected does not differ with the different loading location and direction as their geometry is symmetrical. The remaining three cantilever beam geometries display better performance under STU loading condition at lower volumes while performing better under SBD loading conditions at higher volumes. The results are summarised in Table 1. Since STD resulted in the worst loading condition, the STD and TTD loading conditions will be further discussed in this paper.

3.2 Deflection Limit

In this academic exercise, the base models chosen have a deflection limit greater than L/180 (as defined in the National Annex 2.23 Clause 7.2.1(1) B) to determine the performance of each cantilever beam geometry [2]. For a cantilever beam span of 200 mm, the deflection limit is 1.1111 mm. Hence, for example, a cantilever beam of 40 mm depth under STD loading condition is 136.14% or 1.6238 mm higher than the deflection limit, whereas for a TTD loading condition of a similar depth is 35.44%

or 0.39378 mm lower than the deflection limit. Due to the distributed load in TTD, the cantilever beam is only expected to exceed the deflection limit of 1.1111 mm with depths less than 35 mm. The ST cantilever beam performs the best among the other geometries under STD loading condition. MTT and MTTR cantilever beams show a similar performance under STD but perform better under TTD condition at 30 mm depth. The ID cantilever beam performed the worst under all conditions. The design details and the results for STD and TTD loading conditions are summarised in Tables 2 and 3. Their relative sizing is shown in Fig. 4.

Table 2 Design details for deflection less than 1.11 mm for STD loading condition

Cantilever beam	Additional depth (mm)	Difference (%)	Displacement (mm)	Difference (%)	Total volume (mm^3)	Difference (%)
Base (20 mm)	**0**		**20.31**		**4000**	
ID	35	175% more	1.06	94.77% less	11,000	175% more
ST	57.3	286.5% more	1.01	95.02% less	9730	143.25% more
MTTR	72	360% more	1.08	94.69% less	10,120	153% more
Base (30 mm)	**0**		**6.09**		**6000**	
ID	25	83.33% more	1.06	82.55% less	11,000	83.33% more
MTT	74	246.67% more	1.04	82.96% less	10,197	69.95% more
ST	38.9	129.67% more	0.99	83.59% less	9890	64.83% more
MTTR	59	196.67% more	1.06	82.59% less	10,130	68.83% more
Base (40 mm)	**0**		**2.62**		**8000**	
ID	15	37.5% more	1.06	59.49% less	11,000	37.5% more
MTT	53	132.5% more	1.09	58.28% less	10,135	26.69% more
ST	21	52.5% more	1.06	59.49% less	10,100	26.25% more
MTTR	42	105% more	1.10	57.97% less	10,100	26.25% more

Table 3 Design details for deflection less than 1.11 mm for TTD loading condition

Cantilever beam	Additional depth (mm)	Difference (%)	Displacement (mm)	Difference (%)	Total volume (mm^3)	Difference (%)
Base (20 mm)	**0**		**5.54**		**4000**	
ID	15	75% more	1.06	80.89% less	7000	75% more
MTT	53	265% more	1.10	80.21% less	6135	53.38% more
ST	21	105% more	1.00	81.89% less	6100	52.5% more
MTTR	45	225% more	1.03	81.47% less	6362.5	59.06% more
Base (30 mm)	**0**		**1.67**		**6000**	
ID	5	16.67% more	1.06	36.46% less	7000	16.67% more
MTT	28	93.33% more	1.05	37.17% less	6584.5	9.74% more
ST	7	23.33% more	1.02	38.7% less	6700	11.67% more
MTTR	21	70% more	1.09	34.49% less	6525	8.75% more
Base (40 mm)	**0**		**0.72**		**8000**	
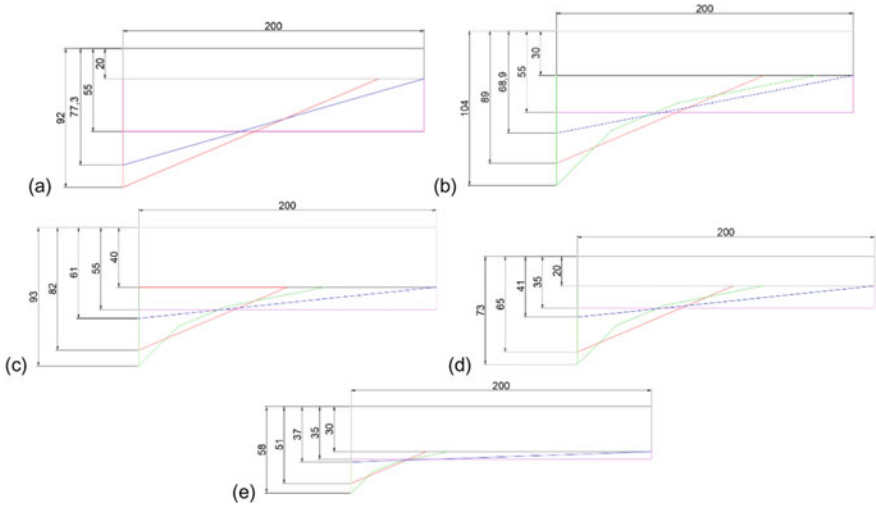
Fig. 4 Relative cantilever beam dimension. **a** 20 mm STD, **b** 30 mm STD, **c** 40 mm STD, **d** 20 mm TTD, **e** 30 mm TTD

3.3 Combined Result of Each Cantilever Geometry

As expected, the ID cantilever shows a single continuous curved line as there are not any discontinuity between the different depths. For the other three cantilever beam geometries, three separate curves are visible and consistent for each of the geometry types at different depths. This is due to the discontinuity in the shape and size of their respective cantilever beam geometries that affect its load path. Between the three cantilever beam geometries, the ST cantilever beam has the most significant effect in the variation of the cantilever beam depth. The graph in Fig. 5 shows that ST cantilever beam will perform better through a well-defined triangular projection than a deeper cantilever beam. Nevertheless, all three cantilever beam geometries show better displacement resistance across higher volume at the same depth than a deeper beam with lower volume. This is mainly due to the angle of the triangular projection that leads to a different load path, whereas for cantilever beam geometries MTT and MTTR, they both show lesser geometrical benefits in reducing the displacement variation between the different depths. Thus, the triangular projection in both MTT and MTTR cantilever beam geometries has a smaller effect on the performance of the cantilever beam. The 30 mm depth MTTR cantilever beam under STD loading shows some inconsistency when compared to the other models. This may be due to the load transfer between the load and the support.

For the TTD loading condition, all three cantilever beam geometries other than the ID cantilever beam show higher displacement variation between various depths when compared to the STD condition. It suggests that the triangular projection would perform more effectively than the STD loading condition, and this is expected. The combined results are shown in Fig. 6.
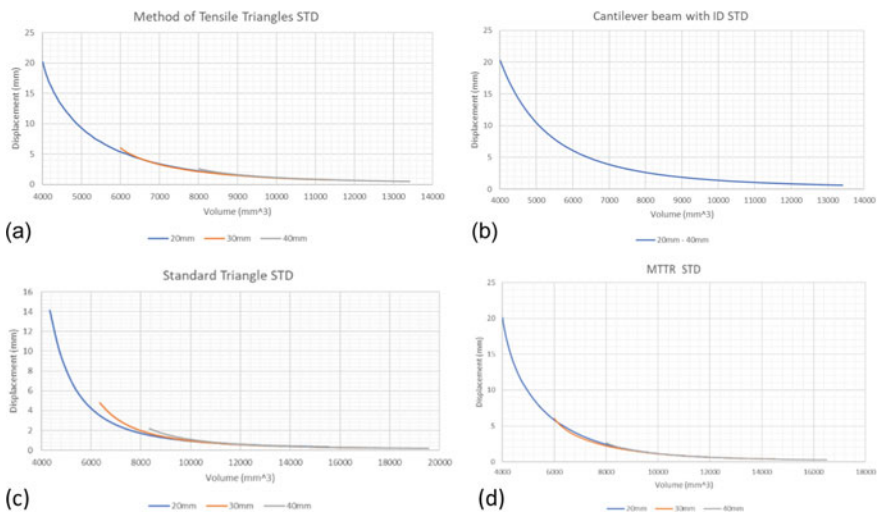
Fig. 5 Combined results under STD loading condition
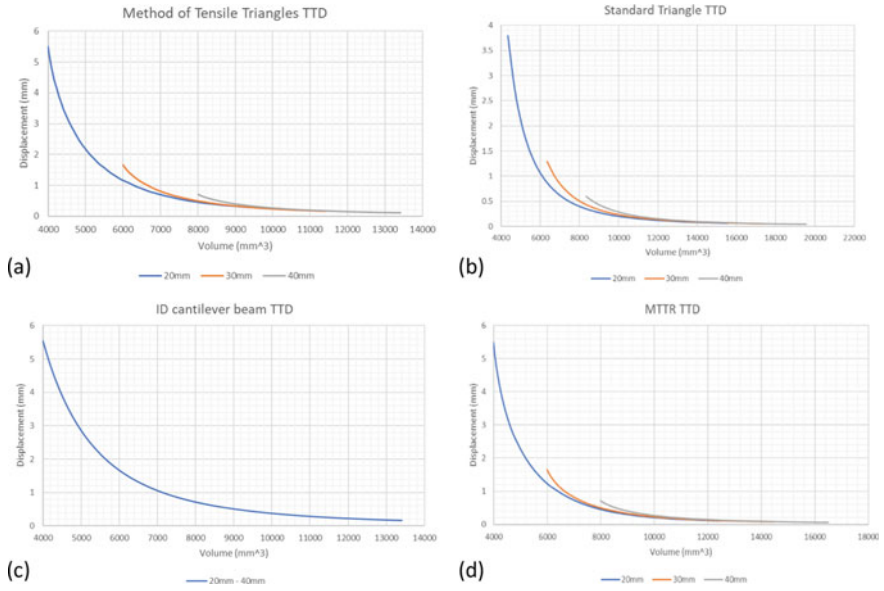
Fig. 6 Combined results under TTD loading condition

3.4 Variation in Depth of Cantilever Beam

As expected, the ID cantilever beam performed the worst among the other cantilever geometries under all loading conditions, as shown in Fig. 7. ST cantilever beam is the best overall design under STD loading. Under STD, the ST cantilever beam performed the best across all volumes for the 20 mm cantilever beam. For 30 and 40 mm cantilever beam, the ST cantilever beam performed best at higher volumes. In this case, MTT and MTTR cantilever beams are seen to perform better at lower volumes. Under the 30 and 40 mm STD loading condition, MTT performs better than the ST cantilever beam with volumes less than 6485.5 mm^3 and 8750 mm^3, respectively, while for MTTR, volumes less than 6427.5 mm^3. MTTR can achieve similar performance as the ST cantilever beam at volumes above 14,000 mm^3 and 15,215 mm^3, respectively. MTT and MTTR cantilever beams are better supported when the cantilever beam has sufficient depth, thus, as expected performing poorer towards shallower cantilever beam depth. The MTT cantilever beam performs better than the MTTR at lower volumes across all cantilever beam depths under STD.

Whereas under TTD loading condition, the ST cantilever beam performed best at higher volumes for 20 mm cantilever beam depth. Both MTT and MTTR cantilever beams performed better at lower volumes as in the STD loading condition for the 20 mm cantilever beam depth (with an extended volume range). For depths of 20, 30 and 40 mm under TTD loading conditions, MTT perform better than the ST cantilever beam with volumes less than 4584.5 mm^3, 8338 mm^3 and 11,269 mm^3, respectively, whereas for MTTR under 20 mm TTD loading condition, it performs better than
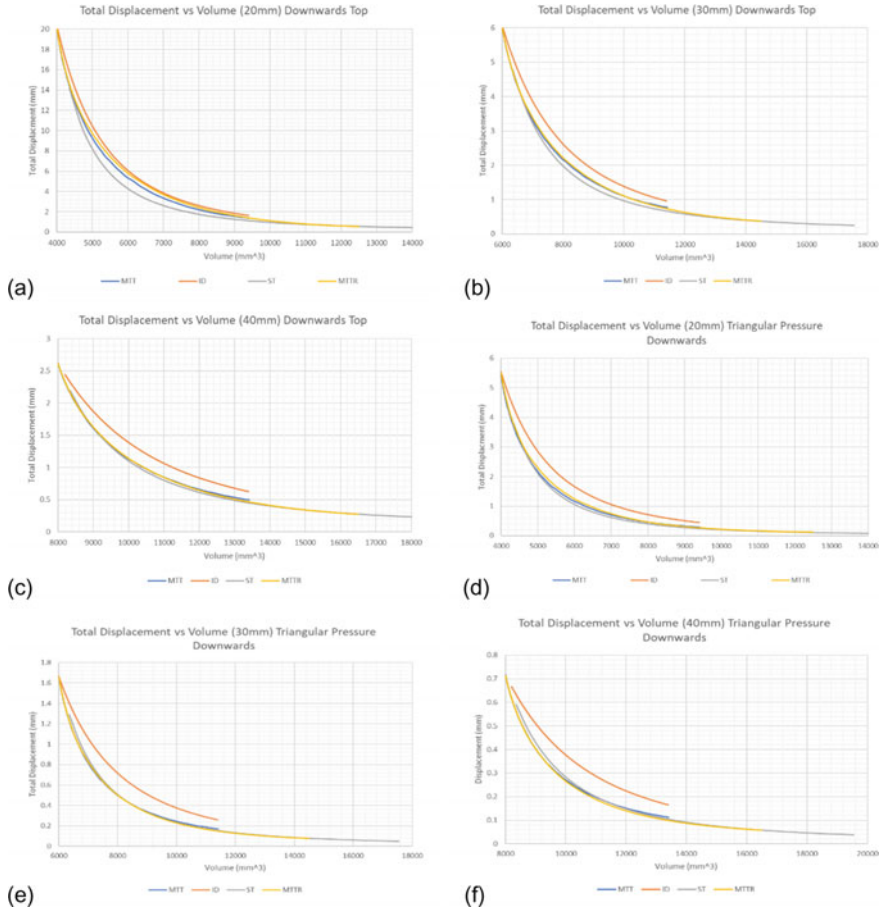
Fig. 7 Displacement under different cantilever depth

the ST cantilever beam with volumes less than 4525 mm^3. MTTR cantilever beam consistently outperforms the ST cantilever beam across all volume range for beam depth of 30 and 40 mm. MTTR shares similar performance with ST cantilever beam at volumes above 9600 mm^3, 8460 mm^3 and 15215 mm^3, respectively. The MTT cantilever beam performs better than the MTTR at lower volumes across all cantilever beam depths. Towards the higher volume range for both loading conditions, the MTTR cantilever beam has similar performance with the ST cantilever beam. Thus, showing the design to be very comparable.

3.5   Displacement Performance for Volume up to 50%

The graphs shown in Fig. 8 is the displacement performance plotted against volume in terms of percentage. The two best cantilever beam geometries cantilever are compared to their respective base cantilever model in each graph set. For the 20 mm STD, the ST cantilever beam has about 7–11% better displacement performance than the ID cantilever beam. Whereas, the MTT cantilever beam is 6% better than the ID cantilever beam. For the 30 mm STD displacement performance, ST cantilever beam has a maximum difference of 11% while the MTT cantilever beam has a maximum difference of 10% when compared to an ID cantilever beam. In the case of the 40 mm STD, the ST cantilever beam and the MTT cantilever beam achieve 10% displacement resistance at a different volume range 35% volume and 27% volume, respectively.

Whereas for TTD, the MTT cantilever beam achieves a maximum difference of 10% at 11% volume while the ST cantilever achieves a maximum difference of 12%
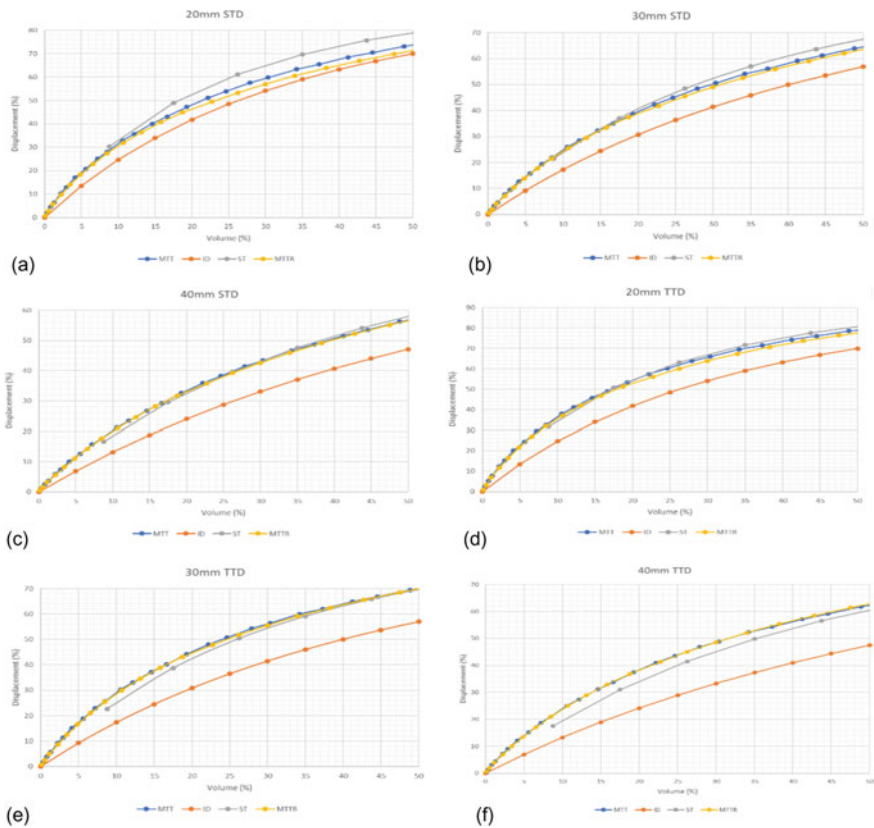
Fig. 8   Displacement performance for a volume of up to 50%

at 17.5% volume for the 20 mm beam depth. For the 30 mm beam depth, MTT cantilever beam achieves 14% difference at a volume of around 19% while the ST cantilever beam achieves a 12% difference at 24% volume. For the 40 mm beam depth, the MTT cantilever beam achieves 15% difference at 34% volume while the ST cantilever beam achieves only 12% difference at 35% volume. It clearly shows that the MTT cantilever beam generally performs well under the lower volume range.

4 Discussion

The study shows that the ST cantilever beam has the best overall performance across the higher volume. The ST cantilever performs better through the incremental inclination angle of the triangle projection as opposed to increasing the depth of the beam. As expected, the ID cantilever performed the worst when compared to the other cantilever beam geometries. This is mainly due to the moment induced on the structure. Hence, it can be concluded that a triangular-shaped projection is more suited for a cantilever structure. However, it is not a single solution that is appropriate for all cantilever beam designs (aspect ratio) and loading conditions.

The MTT cantilever beam performed better than the ID cantilever but performed poorer than the ST cantilever beam. For cantilever beam depth of 20 mm, the MTT cantilever beam was not able to show any benefits across all volume range of the ST cantilever beam under STD. However, the MTT cantilever beam clearly performs better than the ST cantilever beam across the lower volume range under STD and TTD loading conditions when the cantilever beam has sufficient depth (e.g. 40 mm). The MTT cantilever beam performed better than the ST cantilever beam under TTD loading conditions at lower volume range. Although the MTT cantilever beam may not display the intended outcome in this numerical example, the displacement resistance was close to the ST cantilever beam.

For cantilever beam depth of 20 mm, the MTTR cantilever beam did not display any improvement over the MTT cantilever beam under STD. It shows a poorer deflection resistance than the MTT cantilever beam. As the cantilever beam deepens towards the 30 and 40 mm depth, the MTTR cantilever beam under STD loading condition was found to perform better than the MTT cantilever at the higher volume range. For both STD and TTD at all different cantilever beam depths, MTT cantilever beam performs slightly better than MTTR cantilever across the lower volume range and inversely MTT performing poorer across higher volume range. MTTR cantilever beam performs better than the ST cantilever beam consistently under TTD loading condition for the 30 and 40 mm cantilever beam depth. The results demonstrated in both MTT and MTTR show that the triangular projections have reduced efficiency in reducing displacements across the increasing size of the projection. This is likely due to the difference in the distribution of internal forces affected by its geometry. Aside from its displacement performance, the relative sizing of the various cantilever beam geometries plays an important factor.

The ST cantilever beam provides a more consistent ceiling height (e.g. in buildings) but does not provide the benefits of additional height at the free end as in the MTT cantilever beam. The design disadvantage of MTT cantilever beam is a triangular projection towards its support that requires a large amount of space. The triangular projection support for ST cantilever beam is much smaller than the support size of the MTT cantilever beam. The MTT triangular projection may be better suited in a multistorey design as the MTT cantilever beam performs best when the triangular projection is small. Hence, its design may be appropriate in haunches or knee braces between joints as they are often small projections. The analysis confirms the study conducted by other researchers in the review paper [9]. Nevertheless, further studies are still required.

5   Conclusion

The paper presents a parametric study on the various cantilever beam geometries to identify the feasibility and performance of introducing nature's design in civil engineering structures. The study demonstrates the standard triangular projection designed by many engineers to be the best overall design. The MTT cantilever beam performed best when the additional volume is small. It may also suggest the reason why tree buttresses appear as small projections instead of its entire length. MTT cantilever beam offers a different design with better height requirement towards the free end but suffers height and space towards its support. MTTR cantilever beam may be an alternative when considering its sizing and performance. Both MTT and MTTR cantilever beam geometrical projections benefited with deeper beam depth, displaying more displacement resistance with minimal increase in volume. Although the MTT and MTTR geometrical projections do not show significant improvement over the ST cantilever beam, its nature suggests that it might be more suitable for multistorey design. Still, it also does not eliminate the application on other civil engineering structures. Further studies are still required.

References

1. Baud RV (1934) Fillet profiles for constant stress. Prod Eng 5(4):133–134
2. British Standards Institution (2005). National annex to CYS EN 1993–1–1:2005+A1:2014+AC:2009 Eurocode 3: design of steel structures Part 1–1: general rules and rules for buildings
3. De Albuquerque Simões D, de Castro JTP, Meggiolaro MA (2011) On the improved notch shape. In: 21st Brazilian congress of mechanical engineering. Natal, RN, Brazil

4. De Castro J, de Albuquerque SD, de Menezes I, Meggiolaro M, Martha L (2016) A note on notch shape optimisation to minimise stress concentration effects. Theoret Appl Fract Mech 84:72–85
5. Eslami R (2017) A novel micro-mechanical model for prediction of multiaxial high cycle fatigue at small scales. Karlsruher Institut für Technologie (KIT)
6. Mattheck C (1990) Engineering components grow like trees. Mater Sci Eng Technol 21(4):143–168
7. Mattheck C (2006) Teacher tree: the evolution of notch shape optimisation from complex to simple. Eng Fract Mech 73(12):1732–1742
8. Mattheck C (2007) Secret design rules of nature (optimum shapes without computers). Forschungszentrum Karlsruhe
9. Yap KL, Mohammed Parvez A, Jayaprakash J, Elleithy W, Lau TL, Yeong TW (2019) Feasibility of replication and optimisation of nature's design shapes in civil engineering structures to enhance performance and efficiency: a review. Int J Innovative Technol Exploring Eng 8(6S3):2278–3075
10. Yap KL, Mohammed Parvez A, Jayaprakash J, Elleithy W, Lau TL (2018) Feasibility study on replicating tree design structure in trusses subjected to lateral loading. Int J Eng Technol 7(3.36):84–89
11. Zajączkowska U, Kucharski S, Guzek D (2015) Are trichomes involved in the biomechanical systems of Cucurbita leaf petioles? Planta 242(6):1453–1465

Thermal Performance of Reinforced Concrete Column with Different Loading Conditions

N. Parthasarathi and K. S. Satyanarayanan

Abstract Design and development of fire resistant building structure is essential to prevent the building from the fire accident. Thus, in recent decade, researchers have intend to analysis thermal resistance of the reinforced concrete. In this sense, this paper presented an investigation to analysis the thermal performance of reinforced concrete. The steel is used as the reinforced material, and the concrete column is modelled. The concreated column is initially modelled using ABAQUS software and its analytical performance is evaluated. Then, three real sample specimens are prepared for the experimental investigation. In order to evaluate the thermal performance the temperature is varied up to 1200 °C and processed for two hours at three ultimate load conditions as 40, 50 and 60%. The internal temperature in the specimen was calculated using the k-type thermocouple and the deformation for the column was measured at every 10 min. The performance of the analytical and experimental results in terms of temperature and deformation is compared. Eventually, the performance analysis suggests that the increase in temperature influence the deformation in the concrete column.

Keywords High temperature · Finite element analysis · Reinforced concrete column · Deformation analysis

1 Introduction

Major accidents in World Trade Centre, USA on 11 September 2001 and Taj Hotel, India on November 2011, have made the engineers to focus on fire safety in building design [13]. The fire accidents in building may extend based on the structural element conduct. Thus, the fire accidents in the building could easily collapse the entire building [17]. Rodrigues et al. [15] and Neves et al. [11] have pointed out that the structural column tends to elongate, when it is subjected to high temperatures. They have also stated that the elongated temperature could be distributed to the adjacent

N. Parthasarathi (✉) · K. S. Satyanarayanan
Department of Civil Engineering, College of Engineering and Technology, SRM Institute of Science and Technology, SRM Nagar, Kattankulathur, Tamilnadu 603203, India
e-mail: nrnpartha@gmail.com

columns. At high temperatures, the concrete failure may occurs, moreover the failure may depends on the fire conditions, type of loading, and materials used and type of building. The failures in reinforced concrete buildings may also occur due to the reduction in tensile strength of steel, shear loss and changes in compressive strength of concrete. Moreover, at high temperature, the strength and material properties of reinforcement and concrete get reduced. One of the major reasons of structural failure is the distribution of temperature is not uniform inside the concrete, it leads uneven strength degradation [3, 6, 7].

Chinthapalli and Agarwal [2] have studied the role of confining reinforcement on the compression behaviour of axially loaded RC columns at elevated temperatures. The experimentation is conducted to analysis the behaviour of columns at high temperatures. They have prepared RC square columns and heated at the middle for a desired duration and then loaded concentrically in compression until failure. The results based on the experimentation suggested that the increase in amount of confining reinforcement significantly improves the axial load carrying capacity of RC columns at elevated temperatures. Michel and Ferrier [10] have investigated the effect of temperature and curing conditions of the glass transition temperature of the epoxy polymer used for externally bonded strengthening system applied by wet lay-up methods. This investigation shows that the thermal properties are considerably enhanced while curing at a high temperature.

Shen et al. [16] have proposed a discrete hygro-thermal model of concrete at high temperature called DTemPor3. They have performed a full coupling scheme between DTemPor3 and the lattice discrete particle model. They have conducted a numerical simulations, which demonstrated that the spalling phenomenon was successfully reduced, only when the effect of thermal stresses was taken in account along with the effect of pore pressure on crack initiation. Wang et al. [18] have analysed the distribution of the thermal field of a prestressed concrete containment vessel (PCCV) at different times under a loss of coolant accident (LOCA). In order to reveal the failure mechanism and mode of failure the structure, they have investigated the mechanical behaviour of the PCCV under the coupling effect of thermal load and internal pressure. The investigation shown that the structure fails with a large deformation near the largest hole and evident expansion at the dome considering the thermal load. At last, the results found that the deformation develops deficiently under the high temperature of the LOCA. Nguyen et al. [12] have introduced a hybrid method to evaluate the fire performance of carbon fibre reinforced polymer (CFRP) reinforced concrete structure over a small scale laminate. The laminated CFRP reinforced concrete specimen was capable to evaluate fire performance of more general CFRP reinforced concrete structures.

Form the literature review, it if found that few recent researches are discussed, which are concentrated to evaluate the thermal performance of the reinforced concrete. Most of these researches have presented the analytical simulation. However, in some of research investigations, the fibre materials are used for reinforcement. Therefore, this paper aims to investigate the thermal performance of the steel reinforced concrete with different load conditions.

2   Modelling Using ABAQUS

In order to evaluate the thermal performance of reinforced concrete column, the column specimens were modelled using the ABAQUS simulation software. These specimens were subjected to evaluate the thermal performance with different loading conditions. The geometry of the column specimens was $100 \times 130 \times 1200$ mm. The cross section of the column was 100×130 mm and 1200 mm length. The longitudinal reinforcement of 4 numbers of 8 mm diameter with a tensile strength of 358 N/mm^2 and 6 mm diameter transverse reinforcement at 100 mm c/c with tensile strength of 353 N/mm^2 was used. The cover of concrete is 20 mm from the reinforcement and the grade of concrete M30 was used with a compressive strength of 36.2 N/mm^2 at 28 days of curing. In this simulation-based analysis, the column specimen was modelled and reused for the various analysis. The specimen is created using ABAQUS, so single model is created and used for the various analysis. The specimens were kept in transient state condition with respect to time and subjected to axial loading of 40, 50 and 60% of ultimate load of the reinforced concrete column. All the specimens were tested after 28 days curing and also to replicate the moisture condition of the real columns. In the finite element analysis, the support is pinned condition with vertical and horizontal reaction takes place. The column is maintained in a room temperature of 29 °C in all testing conditions has shown in Fig. 1.

In the finite element method, the hexahedron type of mesh is used in the specimen and surface to surface interactions are used between the steel and concrete. Material properties for concrete and steel at different temperatures, like the elastic modulus, thermal conductivity, specific heat, expansion, are taken from euro code EN 1992–1-2 and EN 1993–1-2 [4, 5]. The reinforcement and mesh type for the analytical model as shown in Fig. 2.

Fig. 1 Reinforcement details of modelled column
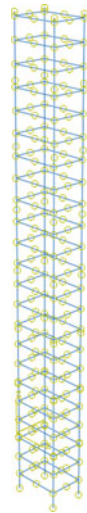
Fig. 2 Mesh details

The model is studied to study the structural behaviour of RC column under high temperatures based on the real time scenario. The RC model for one-third of prototype model also analysed and compared with experimental model. The transient state analysis was used in this model. In steady-state condition, constant temperature will be maintain with the interval of room temperature 29–600 °C and the load will be gradually increased until failure. But, in transient state, the load is subjected to 40, 50 and 60% of ultimate load will give in the column and temperature will be gradually increased until collapse. The Failure column specimen under temperature with loading as shown in Fig. 3.

3   Experimental Test Setup and Procedure

The reinforced concrete column specimens were tested under axial loading in Structural Engineering Laboratory, SRM institute of Science and Technology, India. The prepared column was placed in the self-straining two-dimensional frame with a capacity of 100 tonnes and was heated in vertical direction using the electric furnace. The furnace was of 600 mm height and 500 mm outer diameter and inner dimension of 150 × 150 mm size and capable to heat up to 1200 column specimens were prepared for analysing the three conditions. The specimen was heated in accordance with fire curve of ISO and ASTM standards [1]. Figure 4 shows the test setup of specimen exposed to elevated temperature. Test specimen was heated according to the [8] of standard fire curve. The k-type thermocouple is fixed in middle of specimen to measure the internal temperature of the cross section. The proving ring is attached on top of the specimen with capacity of 50 T(C). The column specimen was loaded to 40, 50 and 60% of ultimate load and the corresponding load of 78 kN, 97.5 kN

Fig. 3 Sample specimens

and 117 kN, respectively. The four digital dial gauges were used for measuring the deformation in both linear and lateral direction (D).

4 Results and Discussion

The performance measured from the experimental and simulation analysis is discussed. The performance analysis is measured based on the temperature rating and deformation.

4.1 Temperature Rating in RC Column

The properties of concrete and steel include specific heat, thermal conductivity, coefficient of thermal expansion, type of reinforcement, boundary conditions, aggregate type and cover thickness and strength of concrete have significant effect when there is a change in temperature rating in RC structural columns [9]. The rating of temperature determined based on two aspects, i.e. thermal and strength criteria. The thermal rule is taken as the temperature of steel bar surpassing the basic temperature, which is 593 °C and quality criteria is the point at which the column could not resist the working load [14]. During testing of column specimen, the internal and surface temperatures were measured. Figure 5 shows the comparison of experimental results

Fig. 4 Test setup for column
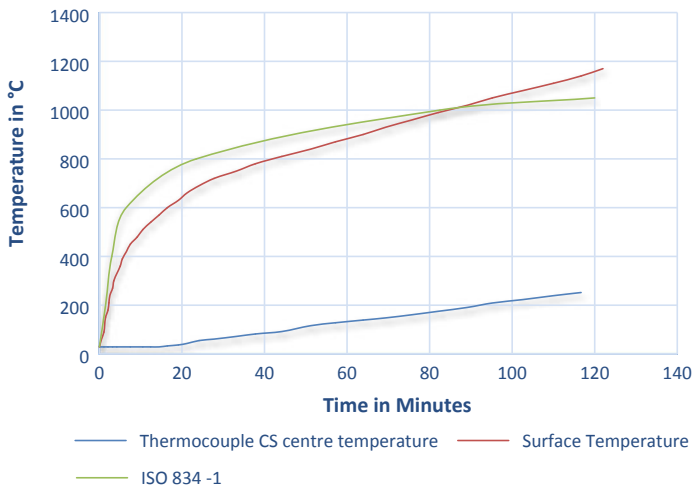
Fig. 5 Furnace temperature with respect to time
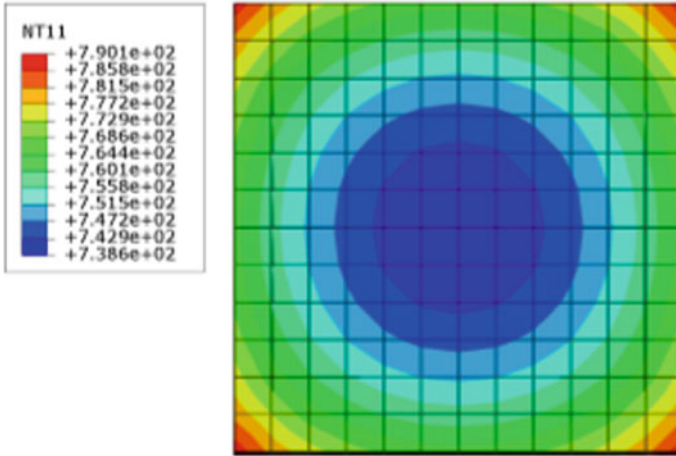
Fig. 6 Temperature distribution in cross section of column from FE analysis

of internal and surface temperature distribution for transient state condition for 2 h and standard curve of ISO 834-1.

Figure 5 shows the furnace temperature with respect to time. In this comparison, the standard curve of ISO 834-1 is compared with the surface temperature and thermocouple CS centre temperature. From the comparison, it proves that the surface and thermocouple CS centre temperature got increased up to 1000 °C while the ISO 834-1 has 180 °C at 80 min. The temperature distribution in the column cross section in finite element method is shown in Fig. 6. From Fig. 6, it can be seen that the surface temperature was very high compared to internal temperature. This indicates that the transfer of temperature inside the column was very less due to the thermal conductivity and specific heat condition.

4.2 Deformation in Column

The axial deformation of column specimen of 40% ultimate load was relatively lesser than the specimen of 50 and 60% of ultimate load. This was due to physical changes like spalling and dehydration of cement. The percentage of deformation was increased from experimental to analytical in the 40% of ultimate load is 21%. Similarly, the FE results of columns with 40, and 60% of ultimate load were also 19.2 and 26% greater than experimental results. It shows that while increasing the percentage of ultimate load with temperature conditions, the column deformation was increased and tends to fail immediately. The time vs displacement curve at various loads is shown in Fig. 7. From Fig. 7, it is clear that the displacement get increased with respect to ultimate load percentage and time.
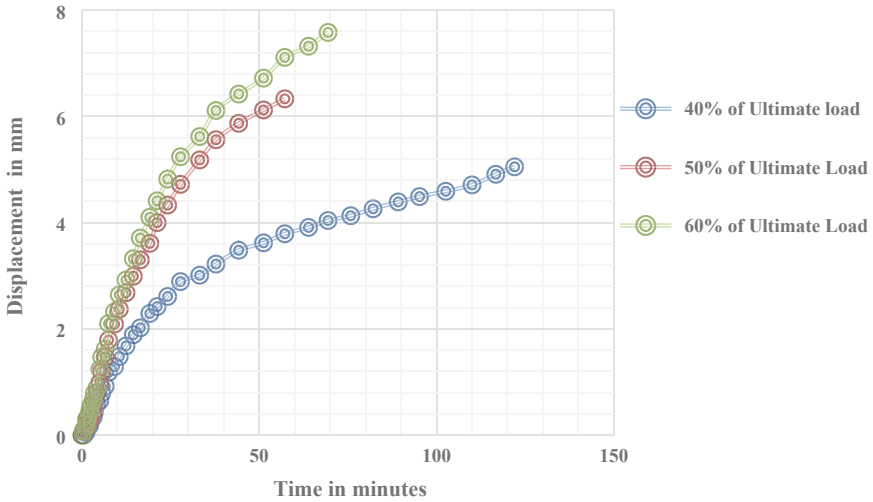
Fig. 7 Time versus displacement curve

From Fig. 8, temperature versus displacement, it shows that the displacement also increases with respect to temperature and load. The deformation is increased from 3.8 to 9.73 mm after the column reaches the maximum temperature. The final cracks are measured using the microscope. The displacement or the width of crack gets increases, when the temperature increases from room temperature to peak temperature. The width of crack increased from 0.52 to 1.2 mm in the centre of the column
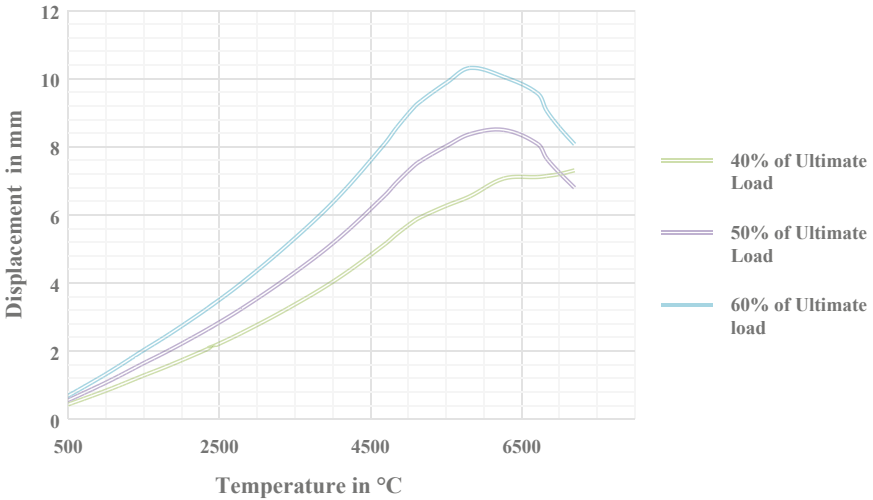
Fig. 8 Temperature versus displacement curve

as well as the column length is reduced due to axial load. Moreover due to temperature the column tends to elongate. Then, the results measured from the experimental analysis are compared with these analytical values, which is plotted in Fig. 9. The results from the experimental analysis are measured manually. The ultimate load deformation also increased in experimental work from 3.63 to 5.05 mm compared to analytical work. The observation is made in the reinforced concrete column under high temperature. While increasing the temperatures, the cracks were observed on the surface of concrete column. In addition to the crack, the high temperature creates some other problems like spalling of concrete, concrete moisture and porosity. The tested samples with crack are given in Fig. 10.

Fig. 9 Axial displacement at column
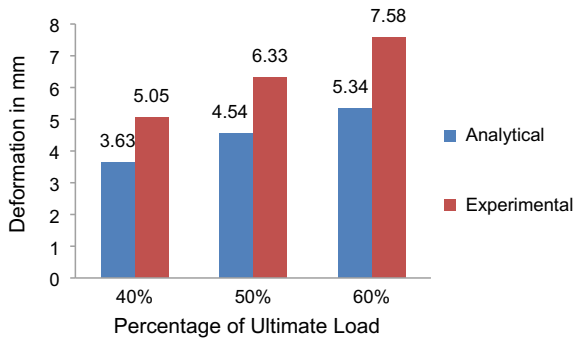
Fig. 10 Samples of failure pattern for column

Figure 10 shows the failed samples after testing. It shows that the three samples tested at three conditions, such as 40%, 50% and 60% ultimate load, respectively. From the figure, we can visually realize the damage, at heavy load condition the damage is severe.

This study analysed the thermal performance of reinforced concrete columns at various load conditions. The reinforced concrete is modelled using ABAQUS software and analytical performances are extracted. Then, the real concrete column is created for the evaluation of experimental analysis. Then, both the performances are compared with each other, based on the analysis, it is observed that the displacement of crack get increase with respect to temperature, time and load.

5 Conclusion

The thermal performance of reinforced concrete at various load condition is investigated in this paper. The reinforced concrete column under high temperature at transient state condition using analytical and experimentation was studied. The RC specimens are subjected to under different loading like 40, 50 and 60% of ultimate load under high temperature of 1200 °C with respect to time up to 120 min. At high temperature, the steel and concrete expand and thus results in formation of crack and leads to failure. The cracks are formed more in maximum load with increase in temperature and also the stiffness is reduced with respect to time. The performances of analytical and experimental result are compared. The result shows that 15–20% of the difference in deformation.

References

1. ASTM: D7205, 7205M (2006) Standard test method for tensile properties of fiber reinforced polymer matrix composite bars. ASTM International, USA
2. Chinthapalli HK, Agarwal A (2020) Effect of confining reinforcement on fire behavior of reinforced concrete columns: experimental and numerical study. J Struct Eng 146(6):04020084
3. Dotreppe JC, Franssen JM, Bruls A, Baus R, Vandevelde P, Minne R, Lambotte H (1997) Experimental research on the determination of the main parameters affecting the behaviour of reinforced concrete columns under fire conditions. Mag Concr Res 49(179):117–127
4. EN 1993-1–2 (2005) Eurocode 3: design of steel structures–Part 1–2: general rules–structural fire design. British Standards Institution
5. EN 1992- 1–2 (2004) Eurocode 2: design of concrete structures-Part 1–2: general rules-structural fire design. European Standards, London
6. Gruz CR (1966) Elastic properties of concrete at high temperature. J PCA Res Dev Lab 8(1):37–45
7. Hosny H, Abo E (1994) Fire of reinforced concrete structures. Dar El Nasher for Egyptian University
8. ISO 834-1:1999 (E) International Standard ISO 834-1. First edition. 1999–09–15. Fire-resistance tests-Elements of building construction

9. Lie TT, Denham EMA (1993) Factors affecting the fire resistance of circular hollow steel columns filled with bar-reinforced concrete columns. Struct Concr 10(2):73–86
10. Michel M, Ferrier E (2020) Effect of curing temperature conditions on glass transition temperature values of epoxy polymer used for wet lay-up applications. Constr Build Mater 231:117206
11. Neves CI, Valente JC, Rodrigues CJP (2002) Thermal restraint and fire resistance of columns. Fire Saf J 37(1):753–771
12. Nguyen PL, Vu XH, Ferrier E (2020) Numerical modeling of thermo-mechanical performance of small-scale CFRP reinforced concrete specimen using near surface mounted reinforcement method. In: CIGOS 2019, innovation for sustainable infrastructure, Singapore, pp 239–244
13. Parthasarathi N, Satyanarayanan KS, Thamilarasu V (2020) Performance of reinforced concrete beam column joint under high temperature. Mater Today Proc 2020. https://doi.org/10.1016/j.matpr.2020.03.497
14. Raut N, Kodur V (2012) Behaviour of circular reinforced concrete columns under fire conditions. J Struct Fire Eng 3(1):37–55
15. Rodrigues CJP, Cabrita Neves I, Valente JC (2000) Experimental research on the critical temperature of compressed steel elements with restrained thermal elongation. Fire Saf J 35(1):77–98
16. Shen L, Li W, Zhou X, Feng J, Di Luzio G, Ren Q, Cusatis G (2020) Multiphysics lattice discrete particle model for the simulation of concrete thermal spalling. Cem Concr Compos 106:103457
17. Usmani AS, Rotter JM, Lamont S, Sanad AM, Gillie M (2001) Fundamental principles of structural behaviour under thermal effects. Fire Saf J 36(1):721–744
18. Wang Z, Yan J, Lin Y, Fang T, Ma J (2020) Study on failure mechanism of prestressed concrete containments following a loss of coolant accident. Eng Struct 202:109860

A Simple Approach for Topological Optimization of Concrete Beams

M. P. Salaimanimagudam, G. Murali, and C. R. Suribabu

Abstract Recently, a numerous topology optimization technique has been reported by the earlier researchers. Within most techniques, a design domain with applied boundary conditions and load case is well defined and used by the design engineers. The design problems in formal optimization problem are rigorously solved using a mathematical program. To the judicious understanding of authors, an optimization through a density-based approach is still in infancy and there only exists limited literature. In this study, a density-based topology-optimized design of plain concrete hammerhead beams was investigated using Autodesk Fusion 360. For this intention, the design example from the literature has been used for topology optimization. Imposing stress limits on the design problem considered in this work is found to create solutions that require significant levels of post-processing prior to construction. The results revealed that the size lessening without affecting its functionality led to saving in building materials within the built world. Also, an interactive density-based topology optimization of concrete beams resulted in new shapes and topology of beams for use in the bridge construction industry.

Keywords Optimization · Stress · Autodesk fusion 360 · Density · Volume

1 Introduction

The topology optimization is the utmost amenable type of structural optimization which helps the structural engineers to create improved designs and modify existing shapes of target members. This enables the targeted structural member lighter and more efficient by eradicating inessential material in a particular zone. Topology optimization can be effectively used for adding and subtracting the part of the structural elements that leads to a reduction in element size. Several researchers have

M. P. Salaimanimagudam · G. Murali (✉) · C. R. Suribabu (✉)
School of Civil Engineering, SASTRA Deemed to be University, Thanjavur, India
e-mail: murali@civil.sastra.edu

C. R. Suribabu
e-mail: suribabu@civil.sastra.edu

proposed the algorithm for the topology optimization for the strut-and-tie models based approach. Many researchers have suggested different methods like truss optimization [1], a density-based approach [2]. The author [3] adopted three different cases in topology optimization, compliance, high tension, and low tension.

The pre-processing and post-processing can be minimized by 3D printing, and the difficult topology-optimized structural components can be created using additive manufacturing method by selective deposition for ultra-high performance concrete; hence, the density constraint can reduce and lesser dimension can be achieved by additive manufacturing [4, 5]. In the present study, the topology optimization has been carried out using Autodesk Fusion 360 software. A hammerhead beam with a four-point load and with necessary boundary conditions, constraints and dimensions of the beam have been taken from the literature [3]. The density-based approach is used to minimize the volume and mass of the structure, which automatically increases the stiffness of the optimized structural element. The design process started with different initial volume fractions, mesh densities and resulted in different designs. The optimization algorithm available in the software searches for better topology and helps to reach the local minimum with consideration of multiple constraints.

2 Topology Optimization Framework

The topology optimization of the beam has been carried out according to the principle of solid isotropic material penalization (SIMP). The SIMP method occasionally called a density method that works with fixed finite element discretization. Each finite element is then accompanying with a density function X_e. The density function values are binary. A zero ($X_e = 0$) denotes void and ($C = 1$) denotes a solid (Siva Rama [6]). The values between 0 and 1 are called intermediate densities which can be taken as a material meso-structure with holes [7]. The structural volume V_o can act as vital factor and solved in contextual of the CAD-based topology optimization.

$$V(X) = \sum_{e=1}^{NE} X_e V_o \tag{1}$$

The topology optimization framework is more advantage while comparing with the traditional finite element analysis (FEA) approach that gives the response to the optimization engine, which provides optimal topology to the element, according to the defined design variables and constraints. The implementation procedure of the proposed frame is illustrated in Fig. 1.

Standard pre-processing of the Fusion 360 bulk data file includes specific optimization objectives, constraints, and parameters. Additional pre-processing of optimization-specific data such as adjacency, distances, manufacturing constraint dependency, and initial volume fraction are considered in the analysis. In the design process of topological optimization, iteration starts with calculating stiffness
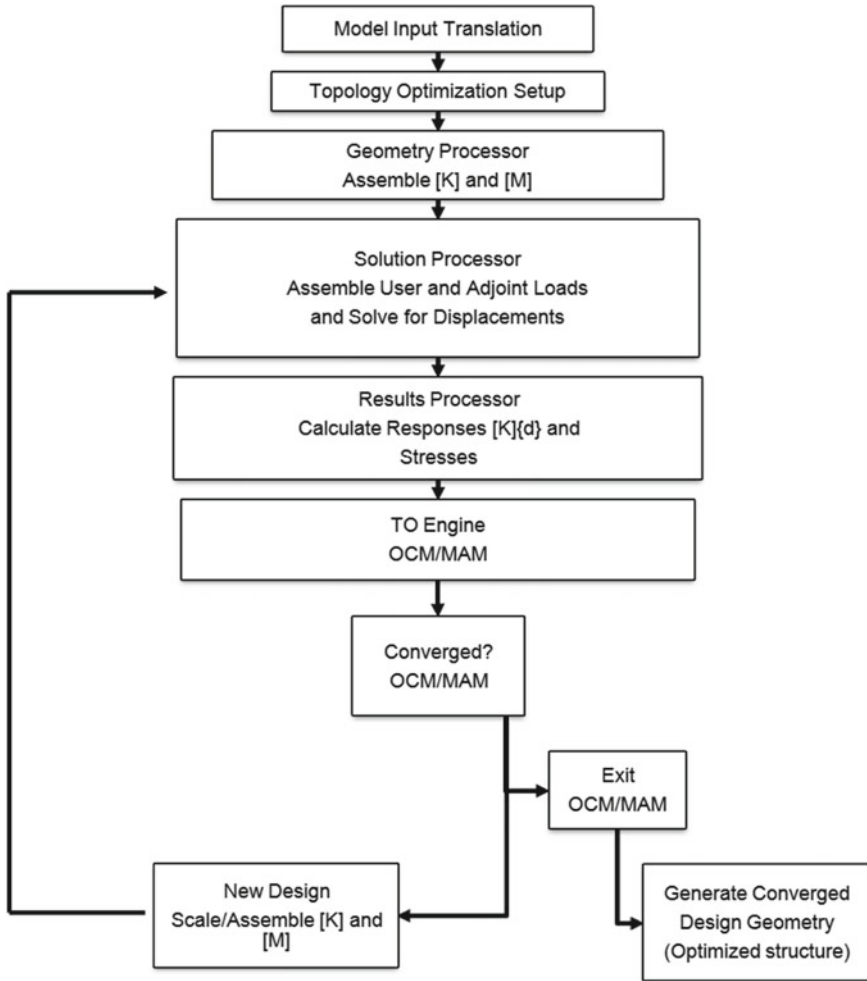
Fig. 1 Topology optimization framework

followed by mass matrixes and all subsequent are scaled. The optimization engine simply decides new design variables (scaled stiffness and mass) and determines until the stopping criteria satisfied.

Additional pre-processing of specific data optimization such as adjacency, distances, manufacturing constraint dependency and initial volume fraction, the first iteration calculates stiffness and mass matrixes and all subsequent are scaled. Optimization engine simply decides new design variables (scaled stiffness and mass) and determines if to continue or stop.

2.1   Optimality Criteria Method (OCM)

OCM is used for large structural components with many constraints and design variables. The OCM provides an optimal design for small and large structures under displacement and frequency constraints. This is adequate for structures with a minimum number of design variables, even in the presence of stress constraints. OCM can be fully utilized when stress constraints dominated the design [8]. The new type of optimality criteria method is proposed by [9]. OCM works effectively and gives good performances even for lower system capacity because of its store minimum information from the previous iteration. OCM works well with the single and multiple constraints which are mostly used with compliance objectives and volume fraction constrains.

2.2   Moving Method Asymptotes

Method of moving asymptotes can easily handle multiple constraints. Hessian information is not needed to be stored it requires less space to store information. The internal parameter can be controlled by many users that need to tune these parameters for fast convergence and stability. The different parameters can be applied within a single model. Researchers [10] proposed the topology optimization for pre-stressed concrete beams. This method is most suitable for structural topology optimization cases, and it can handle any form of optimization issues. MMA is the most convenient optimization method for any type of objective function and any number of constraints equations and also reaches the optimum solution with minimum run time. Using the method of moving asymptotes, it is easy to control the convergence, stability, and speed of the optimization process. It is worth raising the number of elements, the range of asymptotes should be increased to save much time [11].

3   Methodology

Figure 2 illustrates the density-based approach procedure adopted in the topology optimization of the beam for the hammerhead pier using Autodesk Fusion 360 software. The design problem, geometry, and loading have been taken from the earlier literature [3]. Length of the model $L = 36''$ (0.91 m), height $H = 9''$ (0.23 m) and depth $D = 3''$ (0.076 m) with four-point load $P = 2.2$ kN at a spacing of L/3 and the fixed structural boundary condition used at the bottom center of the section with L/6 ratio.

Fig. 2 Methodology for generating topology optimization
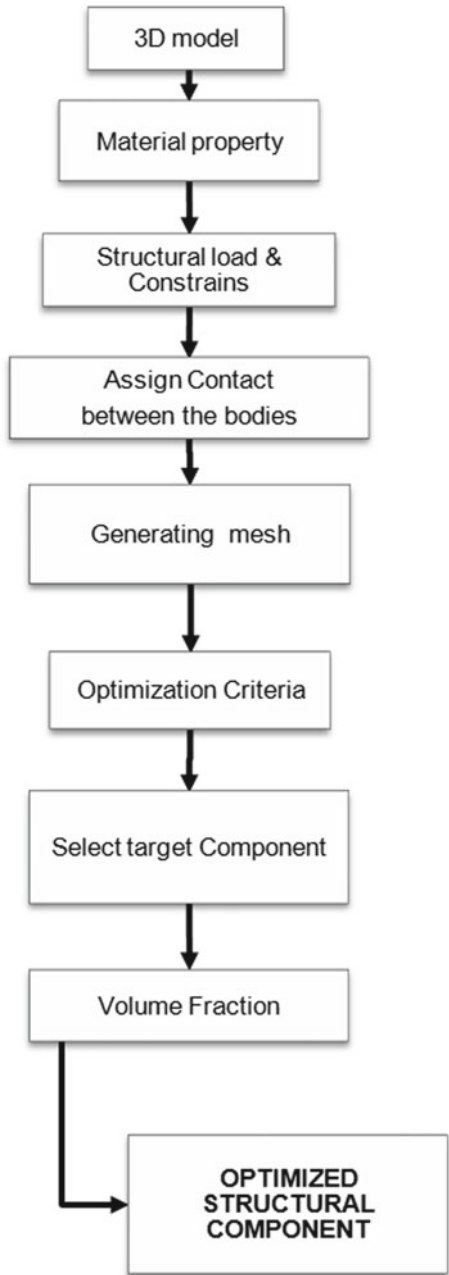
Fig. 3 3D model
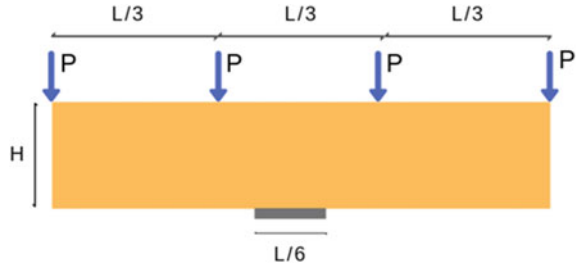
3.1 3D Model

The 2D sketch is created and converted into a 3D workspace with top four load transfer plates with a dimension of 2″ × 2″ × 0.3″ thickness at a spacing of *L*/3 and design load (*P* = 2.2 kN) is applied over a four plate and bottom plate of 6″ × 2″ × 0.3″ with structural fixed constraints (Fig. 3).

3.2 Material Properties

The material properties assigned for the different components of the beam, M30 grade of concrete was used and three cases with different compression and tension as mentioned in [3]. The stress bounds are frequently executed using corresponding stress measures, for example, von Mises stress (Fig. 4). Nevertheless, a von Mises stress condition is only applicable to the material which has equal strength in both tension and compression. Consequently, a Drucker–Prager stress condition is ideal since it allows for different strength levels [12]. In the case of concrete is stronger in

Fig. 4 Von Mises and Drucker–Prager yield principles
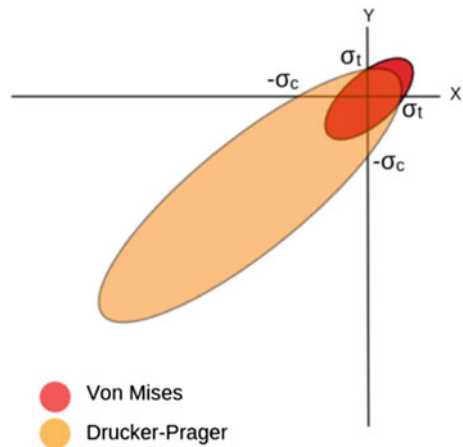
Table 1 Material properties used in design cases

Design	Model	Volume fraction in %	σ_c (MPa)	σ_t (MPa)
Compliance	C′	51.3	–	–
	C	50.2		
	C1	53.4		
High tension	H′	50.9	34.5	3.9
	H	51.2		
Low tension	L′	56.3	34.5	2.9
	L	49.6		

compression and weaker in tension, hence von Mises yield criteria cannot be used so it changes to Drucker–Prager in advanced properties [13]. Table 1 demonstrates the assigned material property used in this investigation.

3.3 Constraints and Assigning a Contact

The structural constraints of topology optimization can be classified into two types: design constraints and manufacturing constraints. In design constraints, a specific limit on results such as stress, displacement at the point, temperature, etc. In the manufacturing constraints, d_{min} is the factor controlling the minimum dimension of the model. In the case of concrete 3D printing d_{min}, the value will be smaller and it reduces the post-processing while comparing with conventional casting. The contact between the components such as load plate, concrete beam, and base plate are bonded together to act as a monolithic structure. This contact plays a major role in topology optimization, and hence, it has to be assigned carefully.

3.4 Generating Mesh

In topology optimization, adaptive meshes are refined and coarsened based on our requirements. In order to reduce error, generate adaptive meshing for different components, i.e., compliance, stress, and strain. In the design mesh, refinement increases the resolution of the material stress distribution resulting in a more accurate evaluation of the structural limit. Local modification alleviates the calculation timing and the cost of both analysis and optimization by insertion of less degree of freedoms and fewer design variables in great void regions [14], In our design, the 3% of adaptive meshing is used for the model where it can be controlled from 1 to 10%.
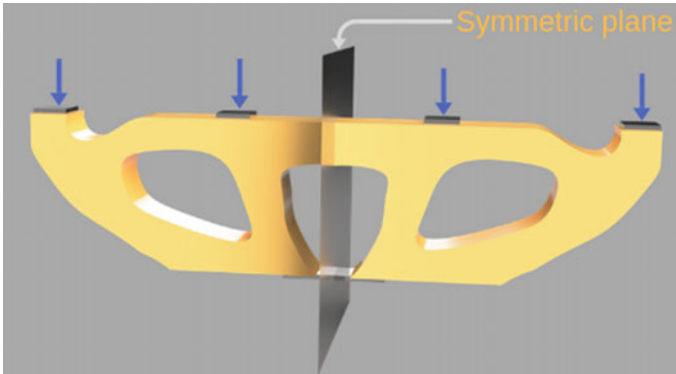
Fig. 5 Symmetric about YZ plane

3.5 Optimization Criteria

In optimization criteria, several works are needed to be carried out, and they are classified into two types, namely (1). global objectives: (a) stiffness (b) target body; and (2) global constraints: (a) symmetrical plane and (b) volume fraction. Works which involves (i) selection of target body for that object to be optimized, (ii) the main aim is to maximize the stiffness and to minimize the compliance, (iii) selection of symmetrical Y-axis (Fig. 5), and (iv) expressing the volume fraction with minimum member size d_{min} as $>$ OR $= 50$ mm.

3.5.1 Selecting a Target Component

The design domain needs to be selected in the structure as the target component to carried out the topology optimization process. The target components are 3D printed concrete beam then d_{min} can be taken as $2''$ in the present model. Global objectives and global constraints are defined, and a symmetric plane is used to achieve the symmetric design to reduce the complexity in manufacturing.

3.5.2 Volume Fraction

The percentage of volume fraction is maintained in the range of 45–60% with consideration of effect due to post-processing. Inverse compliance is used in this study as a scalar measure of stiffness [15], The compliance minimization problem also has been discussed by [16] when global objectives and global constraints are defined. Table 2 demonstrates the volume fraction and mass for design cases.

Table 2 Volume fraction and mass for design cases

Design case	Volume fraction in %	Mass after optimized (Kg)
C'	51.3	19.97
C	50.2	19.54
C_1	53.4	20.78
H'	50.9	19.81
H	51.2	19.93
L'	56.3	21.91
L	49.6	19.3

4 Result and Discussion

Optimized structure results are based on volume fraction and mass. The pre-processing and post-processing are reduced by converting it into the model and purely based on stress and density-based approach. Density-based topology optimization is applied effectively in conditions with a nonlinear material. The comprehensive finite element operation of the linear analysis with distinct properties (tensile and compressive) are discussed in [17]. Compliance [C] 50.2% exhibited the best performance while comparing the other model which has high stiffness and low compliance. The typical stress distribution of the structural member is illustrated in Fig. 6 with the deformation scale (1.5 × Actual) for visualizing the stress path and the deformation.

In the case of optimization of nonlinear elements using density-based methods, the arithmetical uncertainties are resolved to low-density elements [18]

The beams are modeled, and topology optimization was executed using Fusion 360 software as shown in Figs. 7 and 8. The static stress results compared with [3] algorithm-based model.

Figure 8a shows the compliance model of [3], and other two compliance models Fig. 8b 50.3% and Fig. 8c 53.4% were optimized using Autodesk Fusion 360. The static stress analysis comparisons were made between all three compliance models which behave elastically under the design load. Figure 8b, c shows the models obtained from Fusion 360 for three different cases considered according to [3].
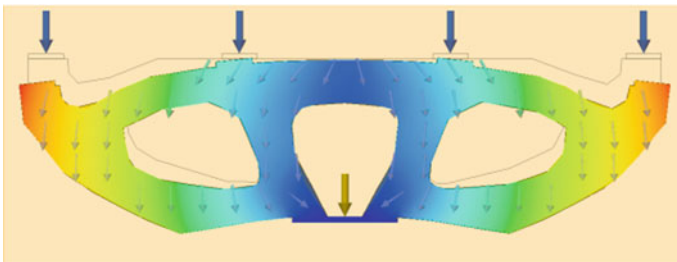
Fig. 6 Stress distribution
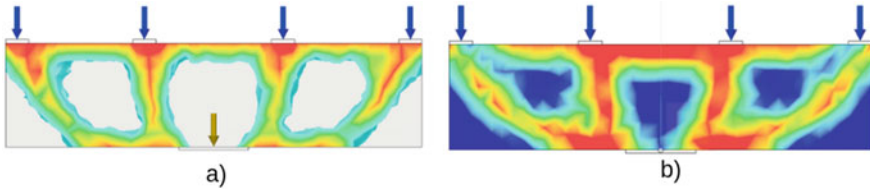
Fig. 7 Topology optimization, **a** density based, **b** stress based
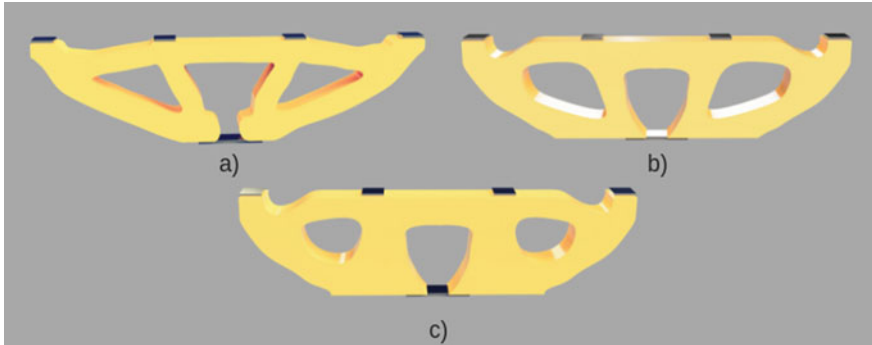
Fig. 8 Compliance model, **a** [C′] is 51.3% designed by [3], **b** [C] is 50.2% and **c** [C₁] is 53.4% designed in fusion 360

From Fig. 9, it can be seen that among the obtained models, model [C_1] exhibited a minimum deflection due to low stiffness of that design and it led to low yield capacity as compared with other models. From this, it is clear that volume fraction and shape of the models are important factors while considering yield capacity of the structural element. Model C of 50.3% has high yielding with optimum volume fraction, and it having high stiffness and low compliance geometrical property of the

Fig. 9 Static stress analysis result of compliance model with [C_1] **53.4%**, [C] **50.2%**, [C′]**51.3%**
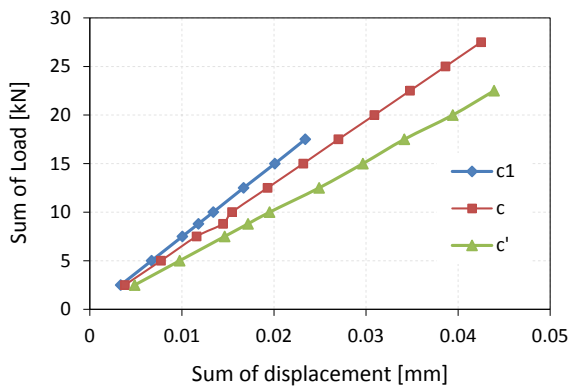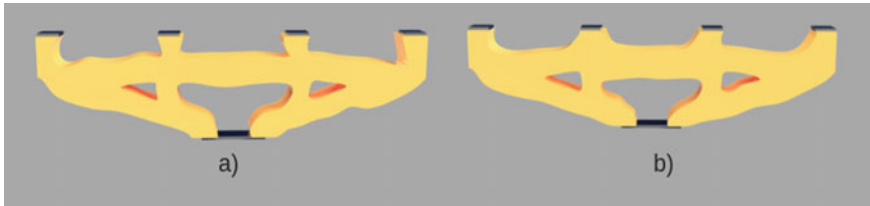
Fig. 10 High tension **a** [H′] **50.9%** designed by [3], **b** [H] **51.2%** designed using fusion 360

model C increasing load caring capacity and raises the factor of safety. The result from Fig. 9 helps to find the local minima for compliance design where model [C] have high yielding capacity and minimum deflection, but in case of model [C_1] with high volume fraction, it have low deflection and less yielding capacity. The result clear shows the local minima lies in between the model [C_1] and model [C′], which helps to find model [C] as a the optimum compliance design.

In Fig. 11, high tension models are pre-processed and minimum member density is altered by minimizing the manufacturing constraint instead of using concrete casting using additive manufacturing with the algorithmic model [3]. The volume fraction of 50.9% was used for [H′] model developed by [3], and Model (b) [H] increased to 51.2% by adding the extra support at the top cord of the model to encounter the tension over a top cord. The load can be transmitted effectively by adding 0.3% which gives the more stiffness to the top tensile cord of the member and the deflection has been reduced to a minimum (Fig. 10).

Low-tension pre-processing carried out to decrease the compliance by altering and use of effective topology by extending the manufacturing constraints are shown in Fig. 12. The post-processing in optimization causes the dramatic alteration over a result its discussed in [3]. The post-processing needs to be avoided to get optimal design. In real life, it can be achieved by extending the manufacturing limits by using concrete 3D printing. Figure 11a [L′] is optimized by the algorithm and its post-processed due to the manufacturing limits. In conversational concrete casting have some difficulties during the critical shapes, may affect the optimality of the design. To overcome those constraints Fig. 11b [L] modeled for 3D concrete printing which has minimum manufacturing constraints while comparing with the model (a) due to post-processing. Model (a) [L′] volume fraction drastically increased from 52 to 56.3%, but in the model (b) [L] archives the at 49.6% with the better performance due to zero post-processing it can be observed in Fig. 12.

The result comparison shows that based on the compliance design model [C] of 50.2% for a boundary condition and loading exhibited lesser displacement with maximum yield capacity while compared with the other designs. The local minima have lower volume fraction with lower displacement in the case of low tension because [L] 49.6% have lower displacement compare with [L'] 56.3%. The optimality is only dependent upon the compliance of the model, volume fraction only affects the displacement, and it does not play a role in yielding capacity. But in the stress-based design, such as high tension and low tension, the volume fraction only alters the
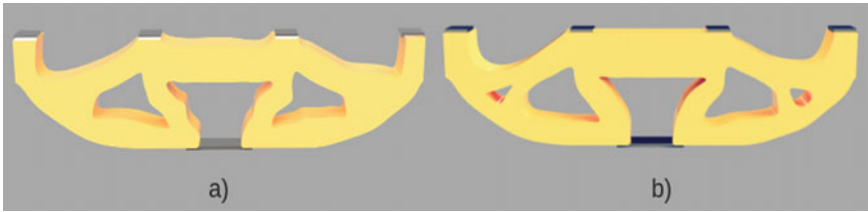
Fig. 11 Static stress analysis comparison of all the six cases

Fig. 12 Static stress analysis comparison of all the six cases
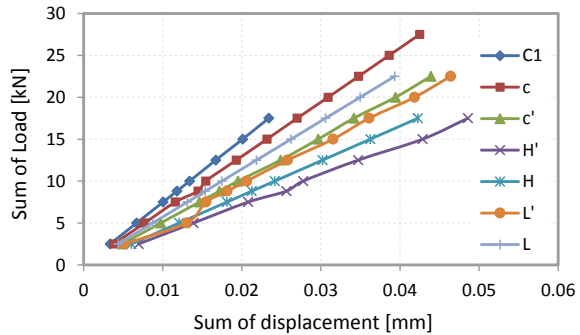
deflection and It does not affect the yielding capacity of the model. It is worth to state from the load–displacement curve that the sum of ultimate load for the C_1, C, C', H', H, L' and models were 17.5, 27.5, 22.5, 17.5, 17.5 and 22.5 kN, respectively, and the corresponding displacements were 0.023, 0.042, 0.043, 0.048, 0.042, 0.046, and 0.039 mm, respectively. Model [C] is the local minimal design in compliance, model [L] is a local minimum for low tension, and model [H] is local minima for the high tension model. While comparing the local minima of all those cases, the model [C] is an absolute local minimal design.

5   Conclusion

The paper has been focused on topology optimization achieved by a simple approach using Autodesk Fusion 360. The best local optimum member can be achieved in all the cases, and it is easy to export the model to additive manufacturing and also reduce the effect of pre-processing. Additionally, a study aimed to design a framework, generating a rigid structural design with a fixed amount of material and aiming at creating a lightweight beam in which the stress field is constrained. The enhanced performance in topology optimization could save building material within the built world. It is worth highlighting that the pattern detected for these properties might

not be deployable to all design areas. The Interactive density-based topology optimization of concrete beams resulted in new shapes and topology of beams for use in the bridge construction industry.

References

1. Kumar P (1978) Optimal Force Transmission in Reinforced Concrete Deep Beams. Comput Struct 8(2):223–229
2. Bruggi M (2010) On the automatic generation of strut and tie patterns under multiple load cases with application to the aseismic design of concrete structures. Adv Struct Eng 13(6):1167–1181
3. Jewett JL, Carstensen JV (2019) Topology-optimized design, construction and experimental evaluation of concrete beams. Autom Constr 102:59–67
4. Gosselin C, Duballet R (2016) Large-scale 3D printing of ultra-high performance concrete—a new processing route for architects and builders. Mater Des 100:102–109
5. Liew A, López (2017) Design, fabrication, and testing of a prototype, thin-vaulted, unreinforced concrete floor. Eng Struct 137:323–335
6. Krishna SR, Mahesh L, Sateesh N (2017) Topology optimization using solid isotropic material with penalization technique for additive manufacturing. Mater Today: Proc 4(2):1414–1422
7. Rozvany GIN (2009) A critical review of established methods of structural topology optimization. Struct Multidiscipl Optim 37(3):217–237
8. Patnaik SN (1995) Merits and limitations of optimality criteria method for structural optimization. Int J Numer Meth Eng 38(18):3087–3120
9. Lógó J (2007) New type of optimality criteria method in case of probabilistic loading conditions. Mech Based Des Struct Mach 35(2):147–162
10. Amir O, Shakour E (2018) Simultaneous shape and topology optimization of prestressed concrete beams. Struct Multidiscipl Optim 57(5):1831–1843
11. Svanberg K (1987) The method of moving asymptotes—a new method for structural optimization. Int J Numer Meth Eng 24(2):359–373
12. Prager D, Drucker C (1952) Soil mechanics and plastic analysis or limit design. Q Appl Mathem x(2):157–165
13. Amir O, Bogomolny M (2012) Conceptual design of reinforced concrete structures using topology optimization with elastoplastic material modeling. Int J Numer Methods Eng 90(13). https://doi.org/10.1002/nme.4253
14. Lambe AB, Czekanski A (2017) Topology optimization using a continuous density field and adaptive mesh refinement. Int J Numer Meth Eng 113(3):357–373
15. Guest JK, Igusa T (2008) Structural optimization under uncertain loads and nodal locations. Comput Methods Appl Mech Eng 198(1):116–124
16. Xu S, Cai Y, Cheng G (2010) Volume preserving nonlinear density filter based on heaviside functions. Struct Multidiscipl Optim 41(4):495–505
17. Liu S, Qiao H (2011) Topology optimization of continuum structures with different tensile and compressive properties in bridge layout design. Struct Multidiscipl Optim 43(3):369–380
18. Deaton JD, Grandhi RV (2014) A survey of structural and multidisciplinary continuum topology optimization: post 2000. Struct Multidisc Optim 49(1):1–38

Advanced Signal Processing Techniques for Damage Detection in Reinforced Concrete Beams

S. Kavitha, K. Sumangala, R. Joseph Daniel, and S. Rajakumar

Abstract Structural health monitoring (SHM) using non-destructive testing (NDT) generally involves measurement of shift in natural frequency of the monitored structure. Vibration sensors play a crucial role in such SHM systems and the present-day SHM systems use commercially available off-the-shelf (COTS) micro-electro mechanical system (MEMS) accelerometers. Reduction in natural frequency indicates the degradation of stiffness and consequential damage of the concrete structures. This paper presents the damage detection of reinforced concrete beams using COT MEMS accelerometer. For this work, four reinforced concrete beams of size 125 × 250 × 3200 mm were cast. Two of them were considered as control and two as damaged beams. Damage was inducted to the beams after 28 days of curing using accelerated corrosion set up. All the four beams were subjected to both static and dynamic tests. The maximum load carrying capacity was determined using the static test, and the signals from vibration test of the beams were taken using COTS MEMS accelerometer. The instrumentation of dynamic test includes data acquisition system with signal conditioning circuit, DAQ measurement hardware and a computer with programmable software and multi storage oscilloscope. The vibration signals acquired from the dynamic test is then analysed using signal processing techniques like fast Fourier transform (FFT) and Morlet wavelet transforms and are compared. From the study, it is concluded that the time–frequency contour map helps to identify the damage in a more effective way than that of FFT analysis.

Keywords Structural health monitoring · MEMS accelerometer · Vibration · Wireless sensor · Damage assessment · Natural frequency

S. Kavitha · R. Joseph Daniel (✉)
Department of Electronics and Instrumentation Engineering, Annamalai University, Chidambaram, India
e-mail: josuma.au@gmail.com

K. Sumangala
Department of Civil and Structural Engineering, Government College of Engineering, Tirunelveli, India

S. Rajakumar
Department of Manufacturing Engineering, Annamalai University, Chidambaram, India

87

1 Introduction

SHM has been extensively used in civil structural systems to monitor the performance of degradation due to ageing of materials, improper maintenance, and various types of hazardous events [1]. SHM system evaluates online statistic of a structure so that the warnings of structural distress can be detected at early stages. Various sensors that are commercially available for evaluating the structural response information can be used for identifying structural safety conditions [1]. In the past decades, the wired sensors are replaced by wireless sensors which are considered as a possible alternate, although it offers a nominal appreciable cost approach for vibration detection from the structure.

Even among the wireless sensors being established, the MEMS-based accelerometers are starting to play a key role since the sensing, signal conditioning and data transmission are often integrated as single chip. Lynch et al. [1] have conducted investigation on SHM integrating COTS accelerometers for detecting the.vibration and wireless communication equipment for transmission of acquired vibration data to explore the benefits of wireless SHM systems. To date, the standard practice in the SHM community has been to adopt sensing technologies like MEMS accelerometer to the particular proof-of-concept experiment in recent years. MEMS vibration sensor is fabricated through micro-fabrication techniques and therefore electromechanical transduction mechanisms can be combined with micro-circuitry for signal processing and computation. The acquired signal from vibration sensors, thus attained are then processed using computational technique to extract information on the fundamental frequency components and therefore the condition of the structure can be monitored. Fast Fourier transforms (FFT) may be a widely used approach to realize these fundamental components of the structure.

A drawback of FFT is the frequency components that can only be extracted from the complete duration of a signal. The frequency components are attained from an average over the whole length of the signal. Therefore, it is not a suitable tool for a non-stationary signal such as the impulse response of cracked beams, vibration generated by damage taking place in a concrete beam. These types of problems associated with FFT could be reduced using wavelet analysis. Consequently, the wavelet analysis has recently been used for damage detection in civil infrastructures. It provides a powerful tool to characterize the local features of a signal. Unlike the Fourier transform, where the function used as the basis of decomposition is always a sinusoidal wave, other basis functions can be selected for wavelet shape according to the features of the signal.

This paper presents the damage detection of undamaged and damaged reinforced concrete using FFT and wavelet transform analysis tools. Wavelet evaluation can be considered as an extension of the conventional Fourier transform with flexible window size and location. The merits of wavelet evaluation lie in its capacity to observe local data with a "zoom lens having an adjustable recognition of focus" to provide multiple tiers of information and approximations of the original signal. Therefore, transient behaviour of the data can be retained. This paper also employs

the use of Morlet wavelet transform. Epp and Cha [2] described the parameters used for the wavelet dictate which features in the signal the wavelet will be sensitive to. Knowledge of the nature of the spectral data is therefore important, as the parameters set for the wavelet determine the effectiveness for the given application. When the frequencies embedded in a signal are unknown, the use of FFT to determine the spectral makeup of a signal prior to the application of wavelet transforms is a beneficial coupling of the two processing methods. Recent developments in mathematical theory of wavelets and their applications were addressed by several researchers Lotfollahi-Yaghin and Hesari [3], Abbasnia and Farsaei [4], Kanarachos et al. [5], Jiang et al. [6], Safari and Gholizad [7].

2 Overall Scheme of Experimental Investigation

The beams used in this investigation were of uniform cross section, i.e. 125 250 3200 mm, as shown in Fig. 1. The longitudinal reinforcement consists of 3HYSD bars of 12 mm diameter at bottom and 2 numbers of 10 mm rods at top. The stirrups were made using mild steel bars of 6 mm diameter and were provided with a spacing of 150 mm. Reinforcement details were kept same for all the beams.

2.1 Induction of Damage in Test Beams

The extent of damage by uniform corrosion is defined as percentage mass loss of the metal. In order to obtain the metal loss, a constant direct current is applied to the reinforcement for a predetermined time. The time and magnitude of the current injected to achieve a particular damage level is obtained through the preliminary experiment conducted. A prior corrosion study had been conducted with 12 mm
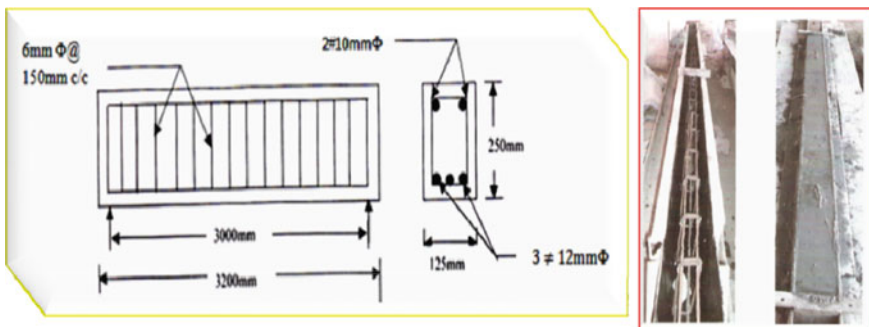
Fig. 1 Reinforcement fabrication and casting details of the beam

diameter main reinforcement and evaluated the electrochemical equivalent to be 0.9 g/A-h.

After 28 days of curing, the beams were subjected to uniform corrosion for a predetermined duration, using an accelerated electro-chemical corrosion process with a constant power source. An electric current was passed through the main longitudinal bottom reinforcing bars corresponding to an approximate current density of 0.87 mA/cm^2. Stainless steel plate was used as a cathode, and these set up were placed in 3.5% NaCl solution for two weeks to get approximately 10% corrosion..

All these beams were tested under static and dynamic load conditions. The test results of only two beams are presented here. The major goal of this paper is to study the effectiveness of general-purpose MEMS accelerometers in picking up the vibration signals from the concrete beam specimens under static and dynamic loadings. This is important because the sensors used for SHM applications need to pick up low magnitude and low-frequency vibration signals under noisy conditions.

Figure 2 shows the experimental investigation involves various tasks include fabrication of reinforcement, casting and curing of reinforced concrete beam, process of inducing corrosion, mounting of MEMS accelerometers, implementation of electronics and instrumentation design, acquiring data using necessary instrumentation in the concrete beam specimen and prediction/condition diagnosis of structures using FFT and wavelet analyses (from tasks 1–6).

3   Instrumentation for SHM

The various types of components of the instrumentation used in SHM system is shown in Fig. 3. It consists of a host computer, sensor excitation hardware, an integrated system of sensors, software, and communication hardware. The host computer performs the task of controlling data acquisition and interpretation hardware in addition to storing recorded data in its hard disc, analysing the data, and communicating with the computers. The sensor excitation and data interpretation hardware provides the link between the sensors and the host computer for analysis. In this study, the ADXL 203 dual axis MEMS accelerometer sensors; namely, S_1 and S_2 were mounted on top and front sides of the concrete beam specimen, respectively. The impact on the concrete beam specimen was achieved with a hammer. Subsequently, the undamaged and damaged beams were subjected to static and dynamic load tests. During these tests, the vibration signals were picked up using the fabricated kit and then these signals were recorded with an Agilent MSO digital oscilloscope. These signals were fed to a personal computer for FFT and wavelet analyses.

Task 1: Casting of concrete beam specimen

Task 2:Induction of corrosion / Accelerated corrosion process
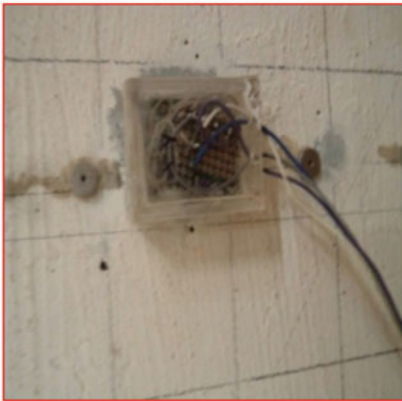
Task3: Mounted MEMS accelerometer on concrete beam
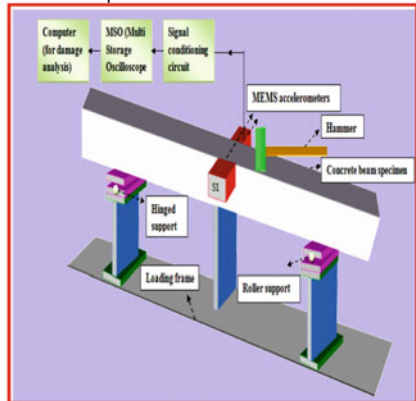
Task 4: Implementation of electronics and instrumentation design

Task 5: Acquire information using necessary instrumentation in the concrete beam specimen and Data Acquisition
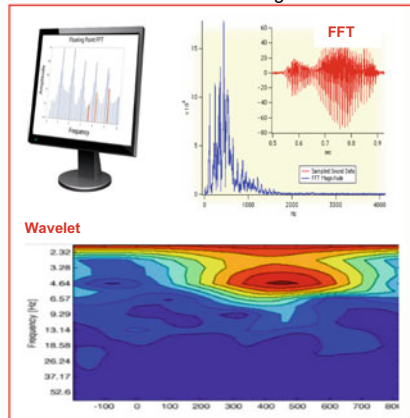
Task 6: Prediction/Condition diagnosis of structures using FFT and wavelet analyses

Fig. 2 Methodology of experimental Investigation
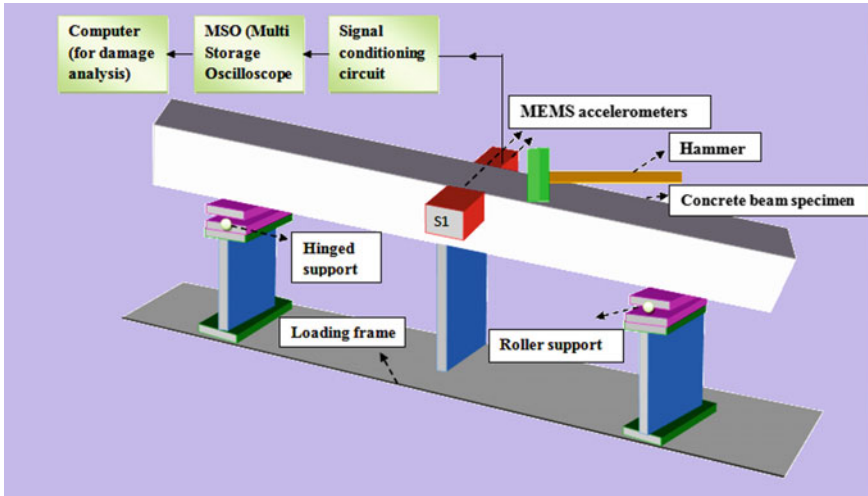
Fig. 3 Instrumentation system in SHM

4 Testing of Beams

In this study, four beams were fabricated and tested under static and dynamic load-ings. Beams in Group A and B consisted of control beam (CB1 and CB2) and damaged beam (DB1 and DB2). The test results of only two beams (CB1 and DB1) are presented in this paper.

4.1 Static Load Test

The reinforced concrete beams were tested under four point bending system. The load was applied using hydraulic jack at equal intervals till failure. Three dial gauges (DG1, DG2, and DG3) having a least count of 0.01 mm were used to record the deflections at one-third points and at mid span. The experimental setup is shown in Fig. 4.

The beams were loaded till the failure load is reached. Deflections and strains were measured for each increment of load of 2.5 kN up to failure. The static tests were conducted for determining the moment–curvature, load–deflection variations with loading in addition to the evaluation of ultimate load carrying capacity of the test beams. The load–deflection curve for the CB1 and DB1 at each loading stage is shown in Fig. 5. From the graph, it was observed that the observed deflection in beams was similar in the elastic region.

Fig. 4 Experimental setup for beam under static loading
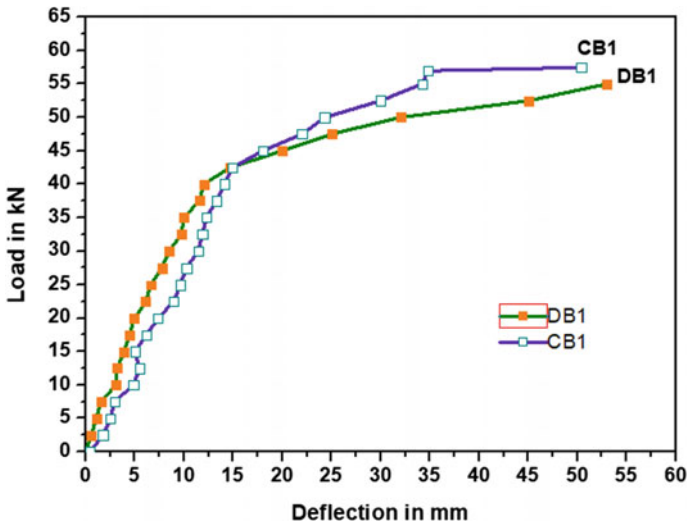
Fig. 5 Load versus deflection behaviour of control and damaged beams

4.2   Dynamic Test and Data Acquisition

Reduction in natural frequency indicates the degradation of stiffness and consequential damage, and hence, the natural frequency was experimentally estimated for the beams CB1 and DB1 using dynamic test at different load levels. The experimental setup used for dynamic test is shown in Fig. 6. MEMS accelerometer mounted on one surface of the concrete beam was used to pick up the vibration signals from which the natural frequency is extracted. After setting the beam in position, with the same type of boundary conditions adopted for static test, the dynamic response of the test beams in virgin state was first obtained. A free hammer hit was given at mid span of the beam to excite the beam. The dynamic response of the beam in the form of displacement time history was picked up by MEMS-based accelerometer sensor and acquired by the data acquisition system, and it was recorded in computer through multi-storage oscilloscope (MSO). This test was conducted at every 10 kN load interval after four cycles of static load application. Finally, the time history records were analysed using the FFT and wavelet transforms tools for obtaining the natural frequencies.
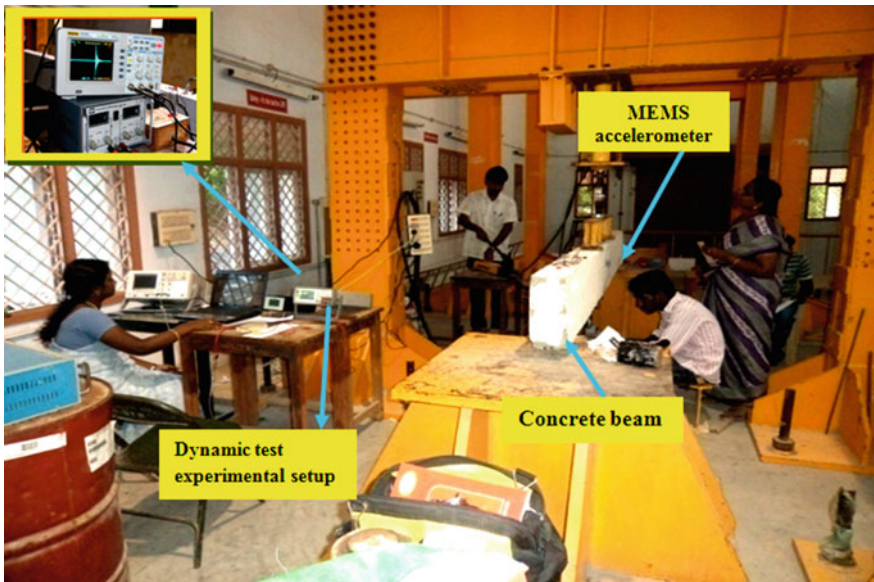
Fig. 6   Dynamic test experimental setup of concrete beam specimen

5 Condition Diagnosis of Concrete Beam Structures

Wavelet analysis permits the use of long time intervals in more precise low-frequency information and shorter regions where it requires high-frequency information. It is found from the literature that the four different wavelets such as Morlet, Mexican Hat, Discrete Meyer and Gaussian wavelets were initially examined for their performance in SHM [8]. The best performance was obtained from the complex Morlet wavelet although the Gaussian wavelet also generated good results during the analysis. Therefore, in this study complex Morlet wavelet transform has been used for damage detection and generated all the results based on the scalogram of complex Morlet wavelet transform.

5.1 Condition Diagnosis of Group-A Beams

In order to gain a clear understanding of the captured signals, the FFT and Morlet wavelet transform were applied to the signals. The signal is captured after four cycles of each static load say 0, 10, 20, 30, 40 kN at an interval of 2.5 kN. These signals are analysed for effective damage detection of concrete beams using FFT and wavelet transforms. Wavelet tool is used to generate the frequency spectrum, power spectral density, contour plot to view the spectral information, scalogram graph and maximum wavelet coefficients in the 3D plot.

5.1.1 Analysis of CB1

The signal captured in beam CB1 during dynamic test at virgin state and the signals captured when the beam was subjected to four cycles of loading up to 57.5 kN have been shown here with the analysed results (Fig. 7). The time–frequency contour is used to distinguish and classify.

Figures 7a, a_1 represent the FFT response for CB1 at 0 N and 57.5 kN and obtained natural frequencies are 48.1 Hz and 35.89 Hz, respectively. Figures 7b, b_1 represent the power spectral density analysis of wavelet for CB1 and produced frequencies are 47.88 Hz at 0 kN and 35.16 Hz at 57.5 kN, respectively. Figures 7c, c_1, d, d_1 show the corresponding table of scales and frequencies and maxima of energy in the scalogram analyses of wavelet for CB1 at 0 kN and 57.5 kN respectively and both the analysis produced the same natural frequency as in FFT and power spectral density analyses. Figures 7e, e_1 shows the time versus scale contour map calculated using wavelet transform which shows the line connects the maxima of energy are detected at scales 17 and 23 (Figs. 7c, c_1), which corresponds to frequencies 48 Hz and 37.6 Hz respectively as shown by pink colour dotted lines, and Figs. 7f, f_1 shows the scalogram images of Figs. 7e, e_1. This is one of the methods used to obtain the natural frequency using wavelet analysis and this analysis produced the same scale as
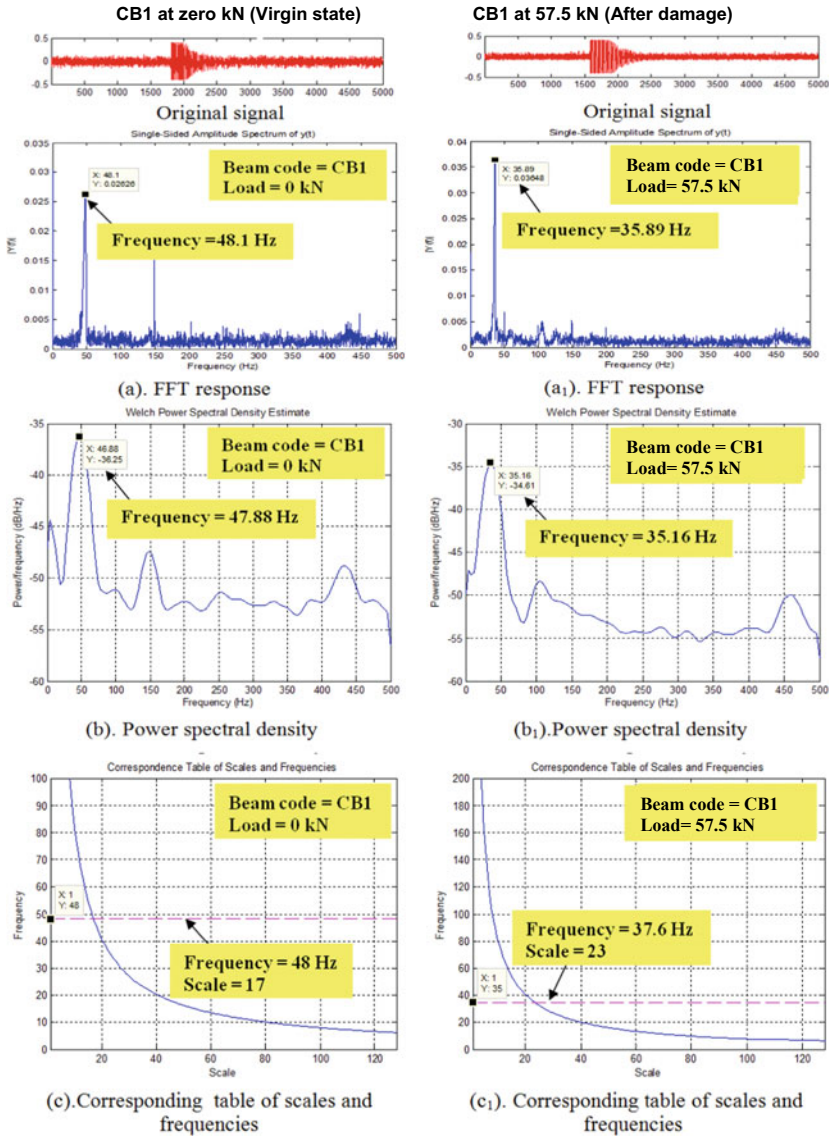
Fig. 7 Impact responses of CB1

in contour and scalogram analyses. Figures 7g, g_1 shows the three-dimensional plots which contain the time, frequency and coefficients information. From the above figures, the frequency at which peaks are seen in FFT spectrums, contour plots and three dimensional plots. The results of the control beam are given in Table 1. These proposed approaches are herein applied to extract the natural frequency of the concrete beams to identify the damage more effectively.

(d). Maxima of energy in the scalogram

(d₁). Maxima of energy in the scalogram

(e). Contour plot to view the spectral information

(e₁). Contour plot to view the spectral information

(f). Scalogram graph

(f₁). Scalogram graph

Fig. 7 (continued)

(g). 3D-view of wavelet coefficient graph   (g₁). 3D-view of wavelet coefficient graph
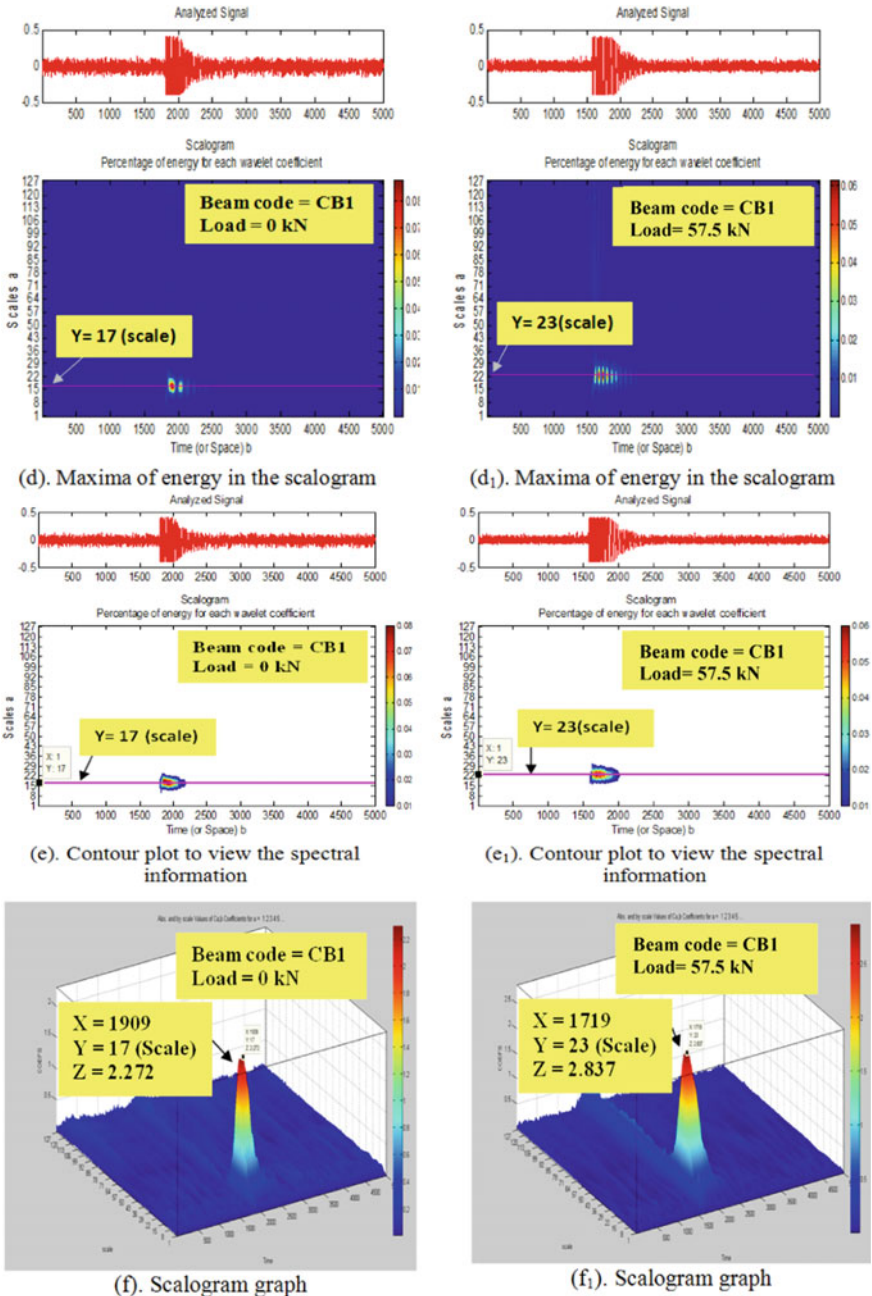
a, b, c, d, e, f, g : Beam CB1at virgin state condition
a₁, b₁, c₁, d₁, e₁, f₁, g₁: Beam CB1 after 57.5 kN load
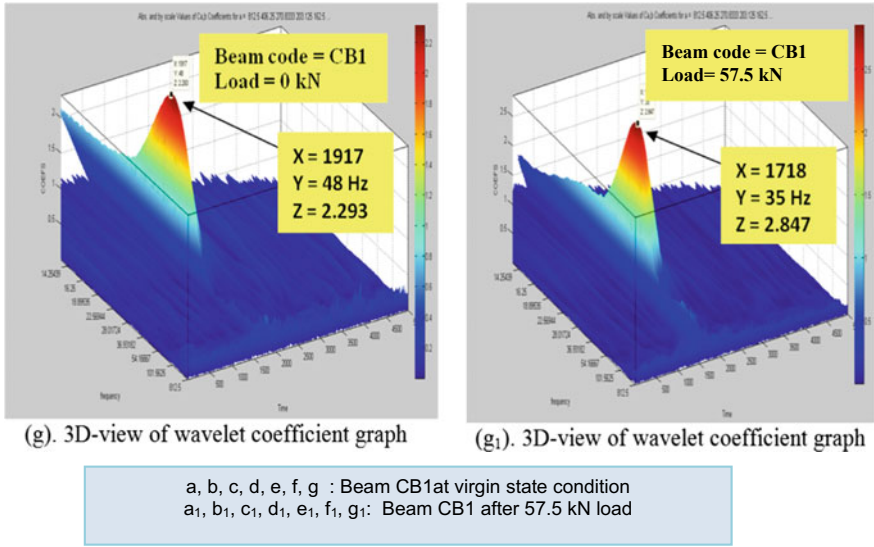
Fig. 7 (continued)

Table 1 Summary of FFT natural frequency, scale/frequency and frequency at 3D wavelet coefficient graph results of control beam CB1

Parameters	CB1 frequency in (Hz)	
	Virgin	After 57.5 kN
FFT natural frequency	48.1	35.89
Natural frequency from power spectral density	47.88	35.16
Scale/frequency from scalogram	17/48	23/37.6
Frequency at which 3D wavelet coefficient graph	48	35

From the above analysis, it was concluded that almost same natural frequency was obtained through all the analyses such as FFT, natural frequency from power spectral density, natural frequency from scalogram and frequency at which 3D wavelet coefficient. Further, it was observed that the natural frequency has dropped to 35 from 48 Hz after cyclic loading at 57.5 kN.

5.2   Analysis of DB1

The signal captured from the damaged beam during the dynamic test before applying static load and the signal captured when the beam was subjected to four cycles of 55 kN loading have been considered, and analysis was performed. These signals are analysed using the same procedure adopted for CB1 as explained in Sect. 5.1.1, and

Table 2 Summary of FFT natural frequency, scale/frequency and frequency at 3D wavelet coefficient graph results of damaged beam DB1

Parameters	DB1 frequency in (Hz)	
	Virgin	After 55 kN
FFT natural frequency	46	34
Natural frequency from power spectral density	46.88	33.16
Scale/frequency	18/46	21/33.2
Frequency at which 3D wavelet coefficient graph	46	33

the results are shown in Table 2. The damaged beam DB1 natural frequency has dropped to 33 from 46 Hz after cyclic loading at 55 kN.

From the analysis of DB1, it was concluded that almost the same natural frequency was obtained through all the analyses such as FFT natural frequency, natural frequency from power spectral density, natural frequency from scalogram and frequency at which 3D wavelet coefficient. Further, it was observed that the natural frequency has dropped to 33 from 46 Hz after cyclic loading at 55 kN.

From the above analyses of CB1 and DB1, the natural frequencies were obtained at various stages of loading for both control and damaged beams which are plotted as shown in Fig. 8. It is clearly seen that the natural frequency for the damaged beam decreased with the increase in the damage's intensity.
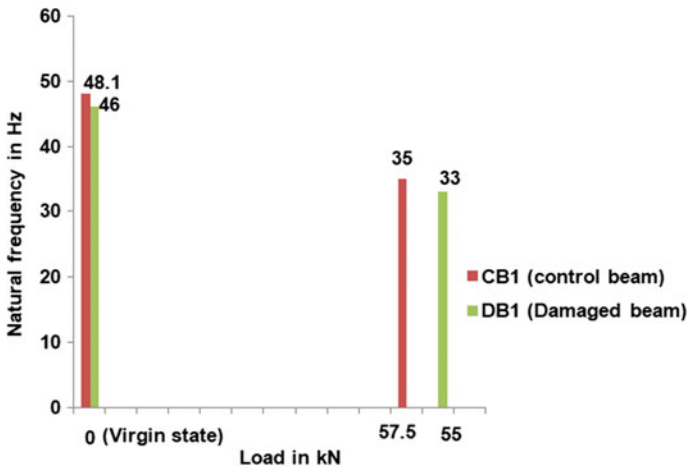
Fig. 8 Natural frequency versus load response

6 Conclusion

The researcher has conducted experimental studies to assess the capabilities of general-purpose COTS MEMS accelerometer sensors for damage detection of reinforced concrete beams using SHM applications. Based on the results of the laboratory test implementation, it can be concluded that the extent of damage is clearly identified by shift in frequency in the FFT and scalogram contour image of Morelet wavelet transform. Furthermore, a relationship between the extent of damage and the maximum wavelet coefficient is established which enables the evaluation of the severity of the damage of reinforced concrete beams. The proposed signal analysis method using wavelet transform has proven to be an applicable and convincing non-destructive damage detection method in SHM. With the aid of the presented damage detection method, the state and the performance of the structure can be continuously observed and evaluated. This technique can be extended to any infrastructure systems such as dam, machinery, residential and commercial buildings.

References

1. Lynch JP, Wang P, Loh KJ, Yi JH, Yun CB (2006) Performance monitoring of the Geumdang Bridge using a dense network of high-resolution wireless sensors. Smart Mater Struct 15:1561–1575
2. Epp T, Cha Y-J (2017) Air-coupled impact-echo damage detection in reinforced concrete using wavelet transforms. Smart Mater Struct 26(2):025018
3. Lotfollahi-Yaghin AM, Hesari MA (2008) Using wavelet analysis in crack detection at the arch concrete dam under frequency analysis with FEM. World Appl Sci J 3(4):691–704
4. Abbasnia R, Farsaei A (2013) Corrosion detection of reinforced concrete beams with wavelet. Int J Civil Eng Trans A Civil Eng 11(3):160–169
5. Kanarachos S, Christopoulos S-R, Chroneos A, Fitzpatrick ME (2017) Detecting anomalies in time series data via a deep learning algorithm combining wavelets, neural networks and Hilbert transform. Expert Syst Appl 85:292–304
6. Jiang T, Kong QH, DevendraPatil ZL, Huo L, Song GB (2017) Detection of debonding between fiber reinforced polymer bar and concrete structure using piezoceramic transducers and wavelet packet analysis. IEEE Sens J 17(7):1992–1998
7. Safari H, Gholizad A (2018) Application of finite element model updating for damage assessment of space structure using charged system search algorithm. Int J Optim Civil Eng 8(2):275–293
8. Nair K, Kiremidjian K, Anne S (2009) A damage detection algorithm using the Morlet wavelet transform. Feb 14

Experimental and Analytical Investigations of Flexural Behaviour of Self-compacting Concrete Rectangular Beams

R. Manju, J. Anu Barkavi, and J. Helen Jai Snahe Swathy

Abstract The primary objective of the present study is to carry out the experimental and analytical investigations on flexural behaviour of rectangular reinforced self-compacting concrete (SCC) beams of size 100 mm × 175 mm × 1500 mm with five different mix proportions, containing various percentages of filler materials like limestone powder (LP) and marble powder (MP), along with the mineral admixtures like fly ash (FA) and silica fume (SF). Finite element modelling (FEM) is carried out for all the five types of rectangular SCC beams using the ANSYS14.5 software and analysed for their performance under two-point loading. The analytical results obtained through FEM analysis are validated with the experimental results. From the experimental and analytical study, it is observed that the SCC mix with equal proportions FA (10%), SF (10%), LP (10%) and MP (10%), exhibit better performance than the control and thus it is concluded that the addition of mineral admixtures and filler materials have pivotal role in the development of strength of SCC.

Keywords Self-compacting concrete · Filler material · Mineral admixtures · FEM

1 Introduction

One of the major environmental concerns faced today is disposal or recycling of the waste materials produced from various industries. Recycling of waste material can reduce virgin products which indirectly save costs [1]. The waste materials such as limestone powder (LP), fly ash (FA), silica fume (SF) and granulated blast furnace slag (GBFS) and alternatives or recycled materials such as marble powder (MP), dolomite powder (DP), Crump rubber (CR), recycled aggregate (RA) and rice husk ash (RHA) are obtained as a by-product from various industries in greater quantity which are hazardous to the environment. When lime stone powder is used as a fine aggregate in the presence of marble powder, the concrete has enhanced performance over their fresh and hardened properties [2].

R. Manju · J. Anu Barkavi (✉) · J. Helen Jai Snahe Swathy
Department of Civil Engineering, Kumaraguru College of Technology, Coimbatore, India
e-mail: anubarkavijagan@gmail.com

The conversion of industrial waste materials to useful applications in the construction field will provide an effective alternative for the engineers to select the most suitable concrete replacement material for different environment. These factors have led to the thought of reduction of cement consumption and to the intensification of research in exploring the possibility of enhancing strength and durability through the use of mineral admixtures and filler materials. The usage of mineral admixtures, in general, has significantly enhanced the fresh properties of SCC [3]. A well-established mix design methodology needs to be developed for SCC with high-volume supplementary cementitious materials. The economic and environmental advantages of SCC with high-volume supplementary cementitious materials need to be embodied in more detail [4]. Without the utilization of class F fly ash and natural pozzolana, durable SCC can be produced without the utilization of viscosity modifying agent [5]. It has also been added that the inclusion of waste materials in SCC has led to the sustainable economy [6]. In addition to the improved mechanical properties of SCC, the high-volume fly ash SCC mixes showed lower chloride ion permeability than SCC without fly ash. The developed SCC has good segregation resistant property [7].

The objectives of the study are to arrive at the mix proportion for M30 grade of SCC with the combination of mineral admixtures and filler materials, thereby carrying out the experimental study on the flexural behaviour of simply supported rectangular-reinforced SCC beams with various mix proportions. Further to provide experimental data on the response of rectangular-reinforced concrete SCC beams in flexure, five numbers of RC beams of size 100 mm × 175 mm × 1500 mm are cast and tested to study their flexural behaviour. Finally, results must be analysed and validated using Ansys software.

2   Materials and Mix Proportions

The basic components of the mix composition of SCC are the same as used in conventional concrete. However, to achieve the required rheological properties in fresh state, a higher proportion of fine materials and the incorporation of Super plasticizers (SP) are needed.

2.1   Materials

The materials used to prepare SCC are ordinary Portland cement (OPC), fly ash (FA), fine aggregate (FA), coarse aggregate (CA), water, super plasticizer (Glenium B 233), mineral admixtures and filler materials. The binder materials used in this study are shown in Fig. 1.

Fig. 1 Filler materials used in SCC

2.1.1 Mineral Admixtures.

Fly ash is a fine residue resulting from the burning of powdered coal at high temperatures. The most common sources of fly ash are electric power-generating stations. Fly ash has become the predominant pozzolan in use throughout the world due to its performance and economic factors. Researchers have extensively investigated the effects of fly ash in both fresh and hardened concrete. It mainly consists of silicon dioxide (SiO_2), aluminium oxide (Al_2O_3), ferrous oxide (Fe_2O_3), calcium oxide (CaO) and some impurities. According to ASTM C618, fly ash belongs to Class F if ($SiO_2 + Al_2O_3 + Fe_2O_3$) $\geq$ 70% and belongs to Class C if 69% > ($SiO_2 + Al_2O_3 + Fe_2O_3$) $\geq$ 50%. Generally, Class F fly ash has a low content of CaO and exhibits pozzolanic properties; however, Class C fly ash contains up to 20% CaO and exhibits cementitious as well as pozzolanic properties [8]. This study used Class F fly ash obtained from Mettur Thermal Power Plant, Tamilnadu, conforming to IS: 3812–2013.

Silica fume (SF) is a by-product in the manufacture of silicon metals and ferrosilicon alloys. This finely divided, glassy powder results from the condensation of silicon oxide gas. Silica fume is composed primarily of silicon dioxide (SiO2), and it is a very reactive pozzolanic material. Adding SF in concrete improves the durability of the concrete by reinforcing the microstructure through filler effect and reduces segregation and bleeding. It also helps in achieving high early strength of the concrete mix. Silica fume of specific gravity 2.32 was used as one of the mineral admixtures in this study.

2.1.2 Filler Materials

Filler is a very finely ground material which has the same fineness of Portland cement. It has a beneficial effect on some properties of concrete such as workability, density, permeability, capillarity, bleeding and segregation. Fillers are usually chemically inert, but there is no disadvantage if they have some hydraulic properties or if they enter into detrimental reactions with the products of reactions in the hydrated cement paste. Limestone powder (LP) and marble powder (MP) are used as filler materials in the present experimental investigation. Finely crushed limestone powder and marble powders which have been brought from local market with specific gravity of 2.89 and 2.6, respectively, were used in the concrete mixes after passing a 75 µm sieve (No. 200).

2.1.3 Physical and Chemical Analysis of Binder Materials

The specific surface area of OPC, FA, SF, LP and MP was obtained using Blaine's air permeability test as per IS 4031 (Part 2)—1999. Physical properties include specific gravity, specific surface area of OPC, FA, SF, LP and MP were determined as per IS 1727–1995. A mineralogical analysis was carried out on OPC, FA, SF, LP and MP by x-ray diffraction (XRD) analysis. The physical properties and chemical composition of binder materials are given in Tables 1 and 2 respectively.

Table 1 Physical properties of binder materials

Description	OPC	FA	SF	LP	MP
Specific gravity	3.09	2.75	2.32	2.89	2.6
Specific surface area (Blaine Fineness) (m^2/kg)	320.437	306.160	1357.152	547.286	789.181

Table 2 Chemical composition of binder materials

Chemical Compounds	% by weight				
	OPC	FA	SF	LP	MP
SiO_2	20–25	52.54	90–96	04.32	02.08
Al_2O_3	4–8	23.59	0.5–0.8	01.47	–
MgO	0.1–3	02.62	0.5–1.5	00.80	00.86
Fe_2O_3	0.5–0.6	2.36	0.2–0.8	01.16	00.74
CaO	64.89	3.78	0.1–0.5	41.65	41.48
Na_2O	0.1–0.5	00.44	0.2–0.7	–	–
K_2O	0.4–1.3	00.49	0.4–1.0	–	–

2.2 Mix Proportion

The initial mix proportion was determined in accordance with IS 10,262: 2009 for M30 grade of concrete, and the modifications were made as per European Guideline for SCC [9] to achieve the desired properties of self-consolidating concrete. Different trial mixes were prepared in the laboratory to obtain a SCC mix which gives the required fresh and hardened properties.

ASTM C595 defines two blended cement products, in which fly ash has been added to Portland–Pozzolan cement (Type IP) containing 15–40% Pozzolana. By considering this fact, fly ash content is restricted to a maximum of 40% to OPC in the present work. For SCC incorporating fly ash only possess required fresh properties but the mechanical and durability characteristics, fly ash content in the mix may be limited to 40% [10].

A total of five concrete mixes were designed having a constant water/binder ratio of 0.35, fine aggregate content of 1000 kg/m^3, coarse aggregate content of 790 kg/m^3 and total binder content of 520 kg/m^3. As the specific surface area of different binders varies, the water requirements in SCC were not be same for all types of binders [11]. Therefore, the requirement of superplasticizer (SP) varied from 2.25 to 3.0% of total binder content was adopted to improve the workability of SCC.

Table 3 shows the composition of binder contents and labelling of the SCC mixes. From Table 3, the mixes are labelled such that the ingredients are identifiable from their mix IDs. For example, the mix 10SF contained 10% replacement of SF; and the mix 10SFLPMP contained 10% replacement of F, SF, LP and MP each.

3 Mechanical Properties of SCC Mixes

The strength tests were conducted on the SCC specimens of standard size as per IS 516–1959 to investigate the strength-related properties such as cube compressive strength, splitting tensile strength and flexural strength of various mixes. The specimens were tested as per the standards, and the average value was reported for each mix. The mechanical properties of SCC mixes are given in Table 4.

Table 3 Binder contents used in the mixes of SC

No.	Mix ID	Binder contents in %					w/b ratio
		OPC	F	SF	LP	MP	
1	CM	60	40	–	–	–	0.35
2	10SF	60	30	10	–	–	0.35
3	10LP	60	30	–	10	–	0.35
4	10MP	60	30	–	–	10	0.35
5	10SFMPLP	60	10	10	10	10	0.35

Table 4 Mechanical properties of SCC mixes

Mix ID	Cube compressive strength N/mm^2	Split tensile strength N/mm^2	Flexural strength N/mm^2	% increase in compressive strength	% increase in Split tensile strength	% increase in flexural strength
CM	37.54	2.58	6.33	–	–	–
10SF	49.76	3.15	6.99	25.92	22.09	10.43
10LP	30.67	2.22	5.12	−18.30	−13.95	−19.12
10MP	32.40	2.25	5.73	−13.69	−12.79	−9.48
10SFLPMP	55.02	3.99	8.43	46.56	54.65	33.18

4 Experimental Investigations on Behaviour of SCC Beams in Flexure

4.1 Dimensions and Reinforcement Details of Beams

A series of five numbers of reinforced concrete SCC beams of size 1500 mm × 100 mm × 175 mm were cast, out of which one was control beam (60% OPC and 40% fly ash) and four SCC beams were with various combinations of SF, LP and MP as given in Table 3. The beams were designed as under-reinforced beams and reinforced with two numbers of 10 mm diameter bars as longitudinal reinforcement at bottom, two numbers of 8 mm diameter bars at top as hanger bars and 2-legged 8 mm diameter stirrups at a spacing of 100 mm c/c as shear reinforcement. The reinforcement cage was kept at a clear cover of 20 mm from the bottom surface of the mould.

4.2 Experimental Test Set-Up

The beams were simply supported with effective span of 1.4 m and tested under two-point loading as shown in Fig. 2. The beams were tested under symmetrical 2-point loading on simply supported span of 1.4 m. The beam was placed on hinged support at the left end and with the roller support at the right end. The test was performed with a loading frame of 100 tonnes capacity. The load was gradually applied under 2-point loading under controlled deflection, and the propagation of cracks was carefully marked. The dial gauges of 0.001 mm least count were used for measuring the deflection of beams. The deflections of the beams at the midspan, and one third span was measured at every 2.5 kN interval of loading using dial gauges. The deflections were recorded for respective load increment until failure. The experimental test set-up is shown in Fig. 2. The first crack load, yield load and ultimate load were recorded for all the tested specimens.
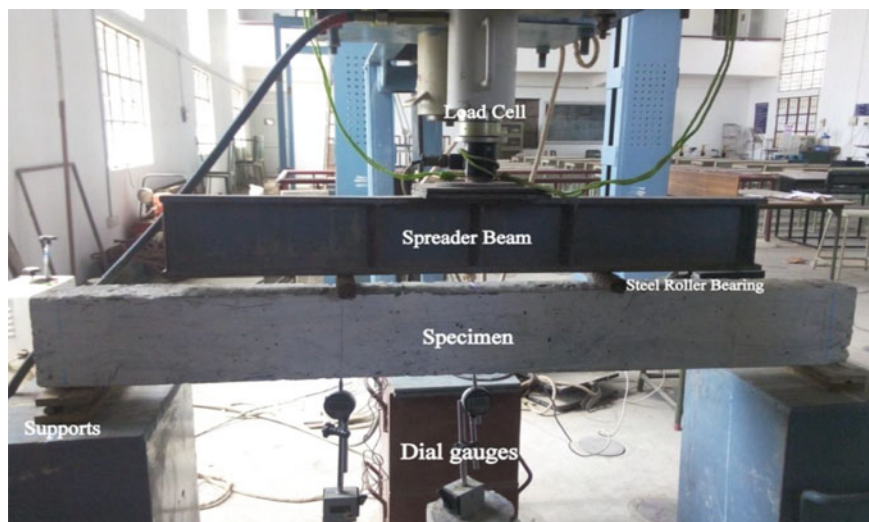
Fig. 2 Experimental set-up of the beam

5 Analytical Study on Behaviour of SCC Beams in Flexure

An eight nodded SOLID 65 element was used to model the concrete which had three translational degrees of freedom in the nodal x-, y- and z-directions at each node and was capable of simulating the linear and nonlinear behaviour of concrete material, and LINK 180 element was used to model steel reinforcement. This element is a 3D spar element, and it has two nodes with three degrees of freedom—translations in the nodal x-, y- and z-directions. The rectangular beam was modelled with a dimension of 1500 mm × 100 mm × 175 mm. The material properties of concrete which are obtained from the experimental investigations according to the replacement of additives added are adopted in finite element modelling of beams. The boundary conditions were adopted to ensure that the models act in the same way as in the experimental investigation. Loads were applied to the flexure beam in the same way as that of experimental study.

6   Results and Discussion

6.1   Experimental Investigation

6.1.1   Load Carrying Capacity of Beams

The test results of beams from each mix tested for flexure at the age of 28 days are presented in Table 5. The moment at first crack and the ultimate load capacity of the tested beams are given in Table 6.

It os observed from that the first crack loads were almost similar in all the mixes of beams. The ultimate load carrying capacity of SCC beam with mix 10SF, 10LF and 10MP is found to be increased by 26.85%, 6.71% and 2.31%, respectively, when compared to that of the beam with mix CM (Table 5). The ultimate moment capacity of the beam with 10SFLPMP is found to be increased by 15.56% than that of the beam with mix CM. The beam (10SFLPMP) with LP and MP in combination with mineral admixtures such as FA and SF in equal percentage is found to be optimum which increased the ultimate moment capacity by 15.56% with that of the control beam. Therefore, it, from the test results, is found that the addition of filler materials increases the flexural strength in combination with mineral admixtures such as FA and SF.

Table 5   Results of beam specimens tested for flexure

No.	Mix ID	First crack load (kN)	Yield load (kN)	Ultimate load (kN)	Deflection (mm)	
					Mid span	One third span
1	CM	20.0	30.0	43.20	24.43	18.66
2	10SF	25.0	35.0	54.80	27.27	22.46
3	10LP	20.0	30.0	46.10	22.12	22.97
4	10MP	22.5	32.5	44.20	21.45	19.22
5	10SFMPLP	25.0	35.0	49.92	23.32	20.27

Table 6   Moments at first crack and ultimate moment capacity

No.	Mix ID	Moment at first crack (kNm)	Yield load (kN)	% increase in ultimate moment capacity
1	CM	4.67	10.1	–
2	10SF	5.83	12.8	26.85
3	10LP	4.67	10.8	6.71
4	10MP	5.25	10.3	2.31
5	10SFMPLP	5.83	11.6	15.56

6.1.2 Load–Deflection Behaviour of Beams

The deflection of reinforced SCC beams was measured along the beam at L/2 and L/3 points at each increment of load. The deflected shape of control and 10SFLPMP beams is shown in Figs. 3 and 4, respectively. The plot comparing the load–deflection for all five different beams at L/2 and L/3 distances are shown in Figs. 5 and 6, respectively. A considerable decrease in the deflection was observed at the midspan

Fig. 3 Deflected shape of control beam

Fig. 4 Deflected shape of 10SLFPMP beam
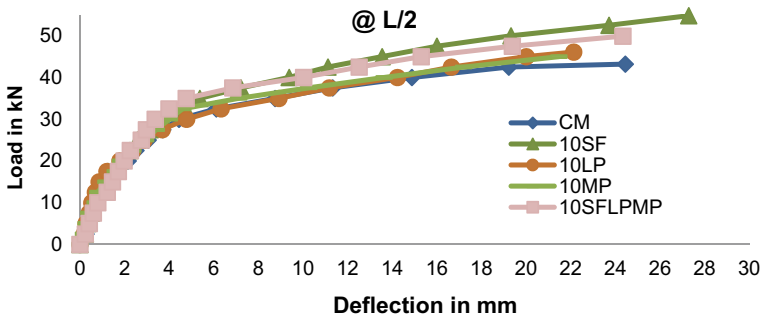
Fig. 5 Comparison of load–deflection plot for all five beams in L/2 span
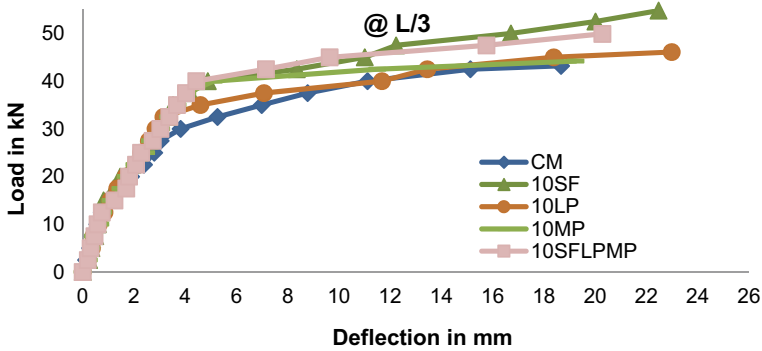
Fig. 6 Comparison of load–deflection plot for all five beams in L/3 span

of the beam with 10SFLPMP when compared to that of the beam with CM (Table 5). The beam 10SFLPMP showed less deflection compared to control beam due to the effective dispersion of cement particles and cohesiveness of concrete, pozzolanic and filler effect of binders. Even though, the other mixes show considerable decrease in deflection, the ultimate load taken by 10SFLPMP was high compared to other mixes.

6.1.3 Crack Pattern

During testing of SCC beams, similar crack patterns were observed in all the beams tested. Initially, hair-line cracks were formed at the first crack load in the pure bending zone. As the load increased, new cracks developed and the existing cracks expanded further and then it propagated from the bottom tension zone to the top compression zone. As the load increased further, the number of cracks was increased in the pure bending zone and they propagated towards the compression zone and the spalling of concrete was observed in the compression zone. At ultimate load, the width of the cracks was increased to a greater extent. The crack patterns of the CM and 10SFLPMP beams at ultimate loads are shown in Fig. 7.

6.2 Analytical Results of Beams

The nonlinear analysis was performed by dividing the load into a series of load increments called load steps. The deflections were recorded at each load step, and the results obtained from the analytical investigations of beams with five different mixes are listed in Table 7. Figures 8 and 9 depict the deflection plot of CM and 10SFLPMP beams respectively.

Fig. 7 Crack pattern of beams
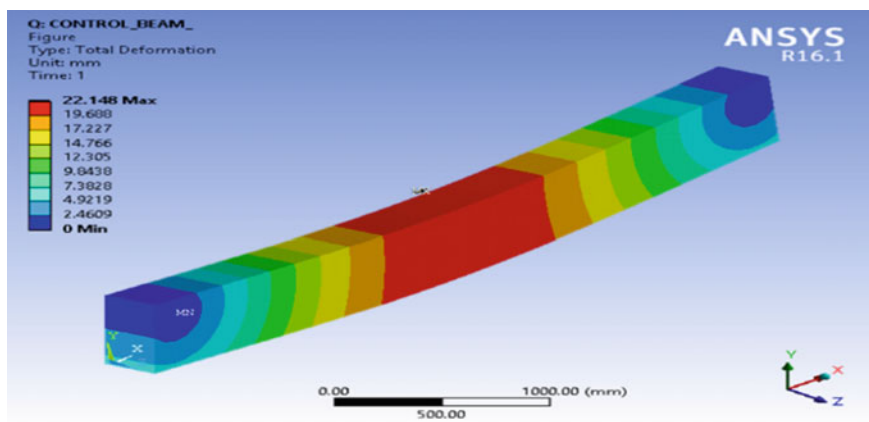
Fig. 8 Deflection plot of control beam
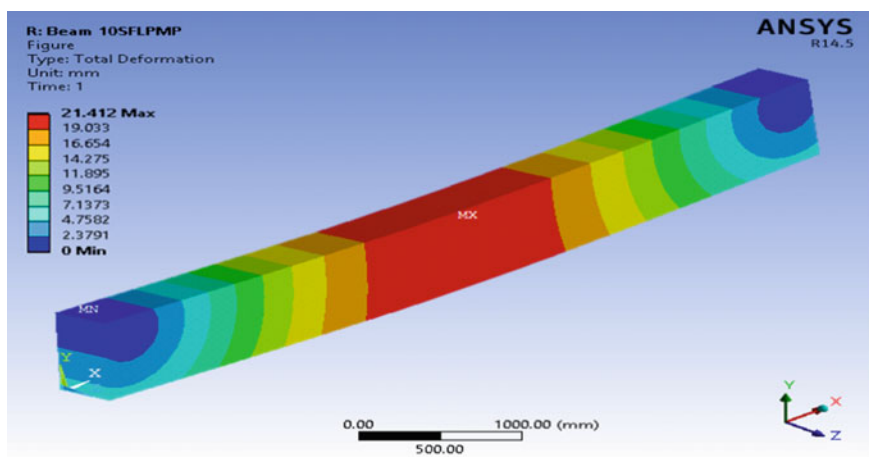
Fig. 9 Deflection plot of 10SFLPMP beam

Table 7 ANSYS test results

No	Mix ID	First crack load (kN)	Ultimate load (kN)	Deflection (mm)
1	CM	27.0	42.1	22.15
2	10SF	29.7	53.4	25.97
3	10LP	27.3	43.7	19.67
4	10MP	28.8	42.2	20.54
5	10SFMPLP	29.7	49.5	21.41

Table. 8 Comparison of experimental and ANSYS results

Mix ID	Ultimate load (kN)		Midspan deflection (mm)		% difference in load	% difference in deflection
	EXP	ANSYS	EXP	ANSYS		
CM	43.2	42.1	24.43	22.15	2.55	9.33
10SF	54.8	53.6	27.27	25.97	2.19	4.77
10LP	46.1	43.7	22.12	19.67	5.21	11.08
10MP	44.2	42.2	21.45	20.54	4.52	4.24
10SFMPLP	49.92	49.5	23.32	21.41	0.84	8.19

6.3 Comparison of Experimental and ANSYS Results

The comparison of loads at first crack, ultimate loads and deflections obtained from the experimental study and ANSYS modelling under flexure are presented in Table 7. The comparison of ultimate load is shown in Table 8. It is evident that the ultimate loads obtained from the ANSYS modelling shows good agreement with that of the experimental results. The percentage difference in ultimate load and midspan deflection obtained from experimental and analytical investigations is varied from 0.84% to 5.21% and 4.24% to 11.08%, respectively. The plot showing comparison of load–deflection for control beam and 10SFLPMP beams for experimental and analytical results is shown in Fig. 10.
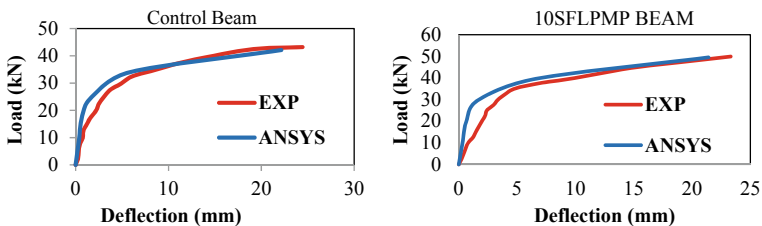
Fig. 10 Comparison of load-deflection plot for control beam and 10SFLPMP beam
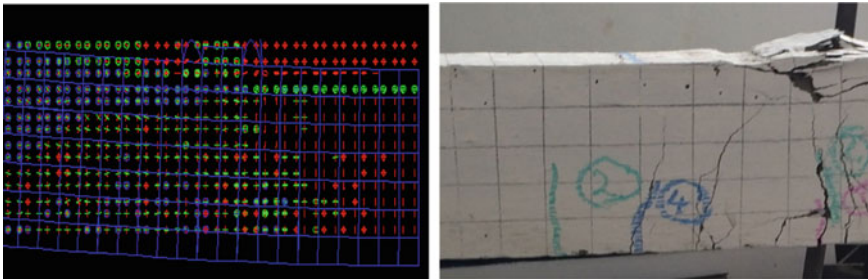
Fig. 11 Comparison of crack pattern for 10SFLPMP beam
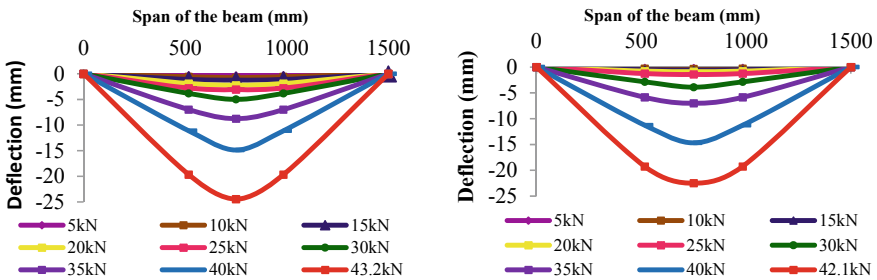
Fig. 12 Comparison of deflection profile of control beam from experimental and analytical results

Figure 11 depicts the comparison of crack pattern obtained from the experimental and ANSYS results under flexure. The comparison of deflection profile of control beam from experimental and analytical study is shown in Fig. 12.

Similar crack patterns were observed for all the beams tested under flexure from both experimental and analytical investigations. From Fig. 12, it was observed that the vertical cracks developed in the flexure zone during testing were propagated towards the compression zone and cause flexure failure.

7   Conclusions

From the experimental investigations and the results of the five numbers of different mixes of SCC with F, SF, LP and MP, the following conclusions are drawn.

- From the flexural test conducted on reinforced SCC beams, the maximum load carrying capacity is observed in the beam with the 10SF mix of SCC, which is 26.85% higher than that of the control beam. But same-sized material shows poor fresh concrete properties.
- The load carrying capacity is increased by 15.56% in the beam cast with the mix 10SFLPMP with equal percentage of mineral admixtures and filler materials

when compared to that of the control beam. In this, all different-sized materials place a major role in pore filling and enhance fresh properties of concrete.

• Finite element modelling of rectangular-reinforced SCC beams studied using ANSYS 14.5 software and analysed under flexure, the analytical results are validated with that of the experimental results. It is observed that the difference in ultimate load and midspan deflection of analytical and experimental results varies less than 5.5 and 11.08%. Thus, it is concluded that analytical results was effective.

References

1. David A, Thangavel YD, Sankriti R (2019) Recover, recycle and reuse an efficient way to reduce the waste. Int J Mech Prod Eng Res Dev (IJMPERD) 9(3):2249–6890
2. Omar OM, Abd Elhameed GD, Sherif MA, Mohamadien HA (2012) Influence of limestone waste as partial replacement material for sand and marble powder in concrete properties. HBRC J 8(3):193–203
3. Mithra M, Ramanathan P, Muthupriya P, Venkatasubramani R (2012) Flexural behavior of reinforced self compacting concrete containing GGBFS. Int J Eng Innov Tech 1(4):124–129
4. Güneyisi E, Gesoğlu M, Algin Z (2013) Performance of self-compacting concrete (SCC) with high-volume supplementary cementitious materials (SCMs). Eco-effi Conc 198–217
5. Celik K, Meral C, Mancio M, Mehta PK, Monteiro PJ (2014) A comparative study of self-consolidating concretes incorporating high-volume natural pozzolan or high-volume fly ash. Constr Build Mater 67:14–19
6. Hameed MS, Sekar A, Balamurugan L, Saraswathy V (2012) Self-compacting concrete using marble sludge powder and crushed rock dust. KSCE J Civil Eng 16(6):980–988
7. Siddique R (2011) Properties of self-compacting concrete containing class F fly ash. Mater Des 32(3):1501–1507
8. Oner A, Akyuz S, Yildiz R (2005) An experimental study on strength development of concrete containing fly ash and optimum usage of fly ash in concrete. Cem Concr Res 35(6):1165–1171
9. EFNARC (2005) The European guidelines for self-compacting concrete specification, production and use. EFNARC pp 1–63
10. Liu M (2010) Self-compacting concrete with different levels of pulverized fuel ash. Constr Build Mater 24(7):1245–1252
11. Alyamaç KE, Ince R (2009) A preliminary concrete mix design for SCC with marble powders. Constr Build Mater 23(3):1201–1210

Behaviour of Beam–Column Joints Under Cyclic Loading

K. Ravichandran and A. K. Prsadkrishnan

Abstract Various structures built during the early 1950s through 1970s lack the strength and ductility required to withstand earthquake excitations. The beam–column joint plays a very crucial role for the structural performance under cyclic loading. Several strengthening or retrofitting schemes have been adopted over the years to improve the seismic resistance. Many structures in India and other countries need retrofitting in order to improve the performance of existing old building, which lack adequate lateral reinforcement and ductility. Four full scale beam–column joint specimens were cast and designed for column and beam shear failure. Out of four specimens, two beam–column joints were strong column–weak beam, and the other two beam–column joints were weak column strong beam specimen. All the specimens were tested up to failure under reversed cyclic loading. The hysteretic curves of the specimen were then plotted. The results show that the strong column–weak beam–column joint exhibits increased strength, stiffness, energy dissipation and composite action until failure.

1 Introduction

Many older reinforced concrete (RC) buildings or frames generally known as non-ductile RC frames designed during the 1950s through 1970s in many parts of the world do not satisfy the current seismic design requirements set forth by many standards such as ACI 318–05 [1], NZS3101-95 [2] and IS:13920 [3]. These framed structures were designed to resist only gravity loads or gravity and routine live loads or moderate wind loads. The older buildings generally do not possess enough ductility to withstand seismic loadings as the detailing of reinforcement was not adopted as per the requirements. The rebars may not have adequate embedment or

K. Ravichandran (✉) · A. K. Prsadkrishnan
Department of Civil and Structural Engineering, Annamalai University, Chidambaram, India
e-mail: krcrithish@gmail.com

splice lengths long enough for full development of the tensile strength of the bars. These issues are very important when RC beam–column joints are considered for the overall response of the structures. During the late 1970s and early 1980s, the seismic design standards introduced capacity design and detailing procedures for adequate ductility. In capacity design, the designer chooses the most desirable mechanism for the structures to achieve the required displacement ductility factor in the post-elastic range during a major earthquake, normally by flexural yielding at selected plastic hinge locations. All other parts of the structure are made strong enough to ensure post-elastic deformations occurring only at the selected locations. Due to this, the failure due to shear and loss of reinforcement anchorage is avoided. The capacity design ensures appropriate balance of flexural strength between the selected plastic hinge regions and other modes of failure. The detailing reinforcement is specified in order to ensure adequate ductility and shear strength in the joint during cyclic loading. The ductility of such structures is inadequate to resist lateral forces caused by severe earthquake excitations. Under load reversals, due to earthquake excitations, the structures should possess enough ductility to allow loads to redistribute and prevent catastrophic failure. Many strengthening schemes are being adopted to bring the performance levels of the deteriorated structures to its full or partial capacity depending on the requirement and importance of the building. Bringing the performance level of deteriorated structures to a required degree is referred to be repair, rehabilitation, retrofitting and upgradation. The shear failure of beam–column joints is identified as the primary cause of collapse of many moment-resisting frame buildings during the earthquakes. The effective and economical rehabilitation techniques for the upgradation of the joint shear resistance capacity in existing structures are needed. The main reasons for beam–column joint shear failure are (i) inadequate transverse reinforcement in the joint and (ii) weak column/strong beam design. Joint shear failures lead to sudden or non-ductile failures of RC moment-resisting frames.

Strengthening of interior beam–column joints by concrete jacketing was carried out by Alcocer and Jirsa [4]. The exterior joints are more vulnerable than interior joints, which were partially confined by beams attached to four sides of the joint and contribute to core confinement. Biddah et al. [5] have conducted investigation on the effectiveness of upgrading the non-ductile reinforced concrete (RC) exterior corrugated steel jacketing. The rehabilitation technique proposed by them can be used in case of connections with floor slab and transverse beams. From the experimental results, they proved that, corrugated steel jacketing was the effective upgrading system. Geng et al. [6], from the experiments conducted, showed that carbon fibre reinforced polymer retrofitted to column-to-beam connection was effective in increasing ductility and strength of the specimens under cyclic loading. Mosallam et al. [7] have conducted tests on six half-scale on interior beam–column joints retrofitted using glass/epoxy and carbon/epoxy composites and concluded that the glass/epoxy composites increased the ductility compared to carbon/epoxy composites. An investigation on the seismic rehabilitation of exterior RC beam–column joints by glass fibre reinforced polymer (GFRP) sheets/laminates was carried out by El-Amoury and Ghobarah [8] and Ghobarah and Said [9]. The proposed rehabilitation scheme using GFRP composite on beam–column joint was found to be

effective in increasing ductility and energy dissipation. The strengthening scheme suggested by the authors was not applicable in the presence of beams and transverse beams, and they could be the real situation in the field. The authors anchored GFRP sheets using steel plates. Wonggpakdee and Leelataviwat [10] have conducted an experiment on strong column–weak beam, indicates the structural response and beam-to-column joint demand strongly depend on the column strength and stiffness. Hu and Kundu [11] have carried out investigation on the seismic performance of interior and exterior beam–column joints recycled aggregate concrete frames. They found that the specimens attained an increase in shear strength and stiffness of joint. Surana et al. [12] investigated the effect of strong column–weak beam design provision on the seismic fragility of RC frame building. Based on the analysis, the strong column–weak beam design criterion leads to significant reduction in collapse probability in case of mid rise building. From the literature review, very limited investigation is available on the behaviour of beam–column joint. Retrofitting scheme is critical only in exterior beam–column joints. The behaviour of beam–column joints without retrofitting must be studied before selecting a suitable retrofitting scheme. The objective of this investigation is to study the effectiveness of strong column–weak beam and strong beam–weak column joints under cyclic loading. It can be achieved by casting and testing of four beam–column joints with various configurations.

2 Experimental Investigation

Beam–column joint is an important part for earthquake resistant design of reinforced concrete moment-resisting frames. Beams-to-column joints should have sufficient stiffness and strength to resist and sustain the load induced from adjacent beams and columns. Four numbers of beam–column joint specimens were cast, out of which two beam–column joint specimens were based on strong column–weak beam and the remaining two beam–column joint specimens were based on weak column strong beam. All the beam–column joint specimen was prepared with concrete grade of 30 MPa. Beam and column with different cross sections were used. The cross section and internal reinforcement details are shown in Table 1, and the experimental setup is shown in Fig. 1a. The reinforcement details are shown in Fig. 1b, c. The joint assemblages were subjected to axial load and reverse cyclic loading. A 500 kN hydraulic jack mounted vertically to the loading frame was used for simulating the axial gravity load on the column. A constant axial load of 100 kN, which is about 20% of the axial capacity of the column, was applied to the columns for holding the specimen in position and to simulate column axial load. Two ends of the column were given an external axial hinge support, in addition to the two lateral hinge supports provided at the bottom and top of the column. Another 500 kN capacity hydraulic push and pull jack was used to apply reverse cyclic load to the beam portion of the beam–column joint The point of application of the cyclic load was at 50 mm from the free end of the beam. The test was displacement controlled, and the specimen was subjected to an increasing cyclic displacement up to the failure. The displacement

Table 1 Internal reinforcement and cross section details of beam–column joint specimens

Specimen	Column size	Beam size	Column reinforcement	Beam reinforcement
SCWB-A1	200 × 200 mm	150 × 200 mm	4.Nos 12 mm dia, 8 mm dia 150 mm c/c	4.Nos 10 mm dia, 8 mm dia 150 mm c/c
SCWB-A2	230 × 230 mm	200 × 200 mm	4.Nos 12 mm dia, 8 mm dia 150 mm c/c	4.Nos 12 mm dia, 8 mm dia 150 mm c/c
SBWC-B1	200 × 200 mm	200 × 250 mm	4.Nos 12 mm dia, 8 mm dia 150 mm c/c	4.Nos 12 mm dia, 8 mm dia 150 mm c/c
SBWC-B2	200 × 200 mm	200 × 250 mm	4.Nos 12 mm dia, 8 mm dia 150 mm c/c	4.Nos 10 mm dia, 8 mm dia 150 mm c/c
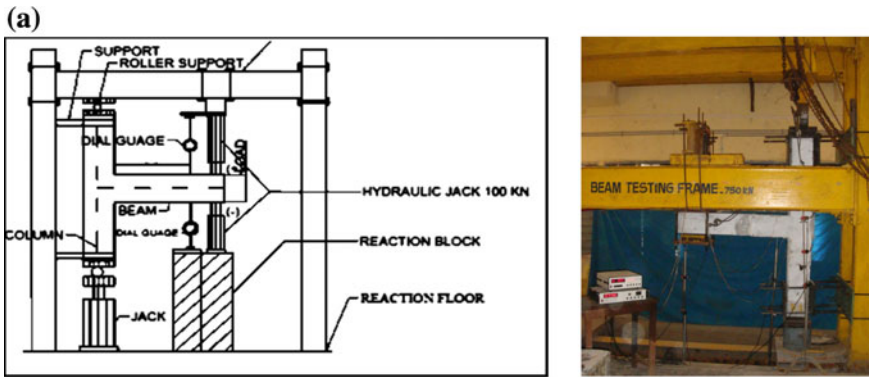
Fig. 1 **a** Test setup with instrumentations, **b** details for strong column–weak beam, **c** details for strong beam–weak column

increment was of 5 mm, for push and pull for the test specimen. The specimens were instrumented with linear variable differential transducer having range ±75 mm to measure the displacement at loading point.

3 Strong Column–Weak Beam

The hysteresis behaviour of strong column–weak beam specimen is shown in Figs. 2 and 3. The maximum load obtained for specimen SCWB-A1 was 50.4 kN in push and 46.8 kN in pull, respectively, at a displacement of 25 mm. The maximum load obtained for SCWB-B1 was 57.4 kN in push and 55.4 kN in pull, respectively, at a displacement of 25 mm. The maximum displacement obtained was of 50 mm. The energy dissipation and stiffness values are given in Table 2.

Based on the hysteresis behaviour, the energy dissipation and stiffness degradation per cycle were worked out and presented. The total cumulative energy dissipation observed for SCWB-A1 was 1636.84 kN mm and for SCWB-B1 was 2184 kN mm,
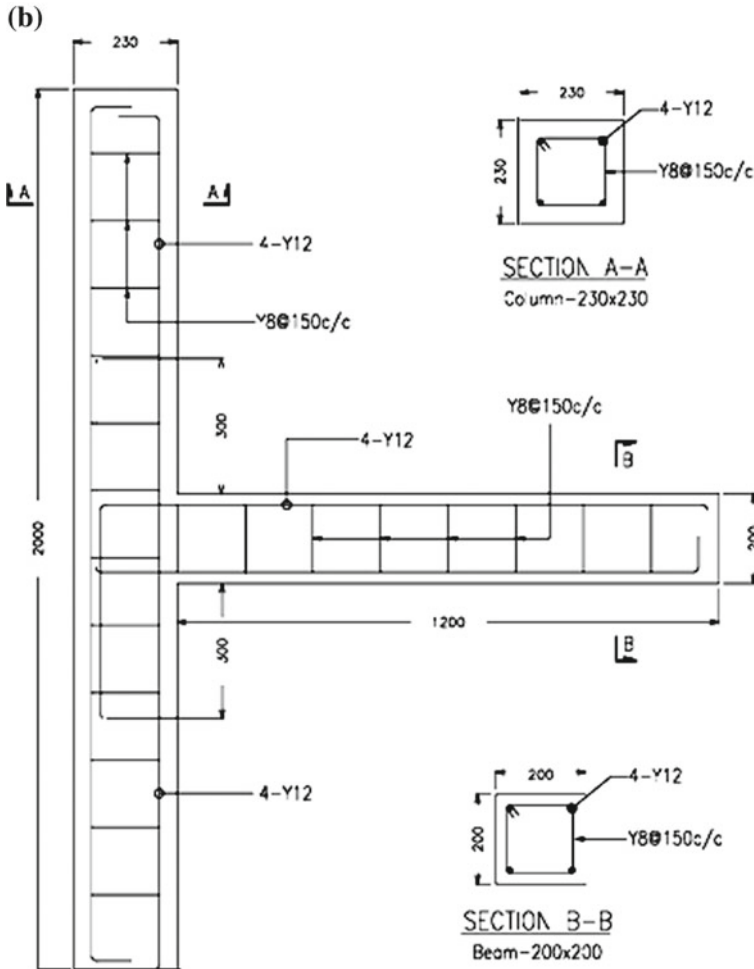
Fig. 1 (continued)

respectively. The stiffness values were degraded for SCWB-A1 from 3.78 kN/mm to 0.81 kN/mm and for SCWB-B1 from 4.90 to 1.03 kN/mm. The initial stiffness values obtained were 3.78 and 4.9 kN/mm and at a displacement of 5 mm. The energy dissipation and stiffness are shown in Fig. 4. The crack pattern for strong column–weak beam is shown in Fig. 5.
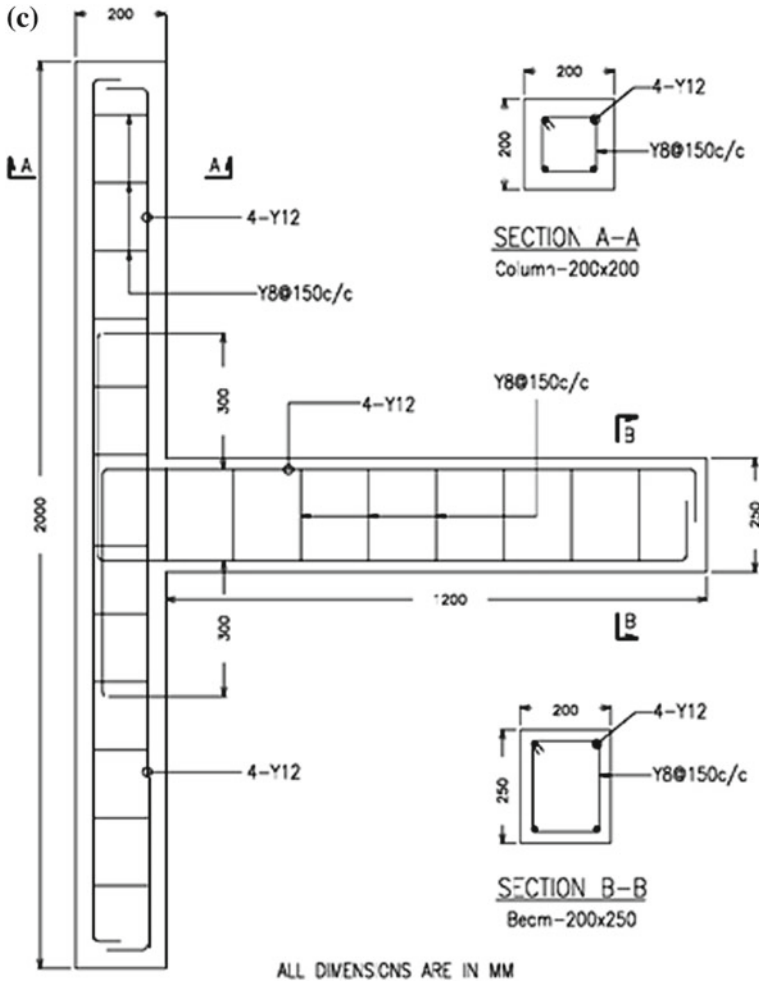
Fig. 1 (continued)

4 Strong Beam–Weak Column

The hysteresis behaviour of strong beam–weak column specimen is shown in Figs. 6 and 7. The maximum load obtained for SBWC-A2 was 75.3 kN in push and 46.8 kN in pull, respectively, at a displacement of 20 mm. The maximum load obtained for SBWC-B2 was 65.30 kN in push and 60.50 kN in pull, respectively, at a displacement of 15 mm. The maximum displacement obtained was of 50 mm. The energy dissipation and stiffness values are given in Table 3.

Based on the hysteresis behaviour, energy dissipation and stiffness degradation per cycle were worked out and presented. The total cumulative energy dissipation
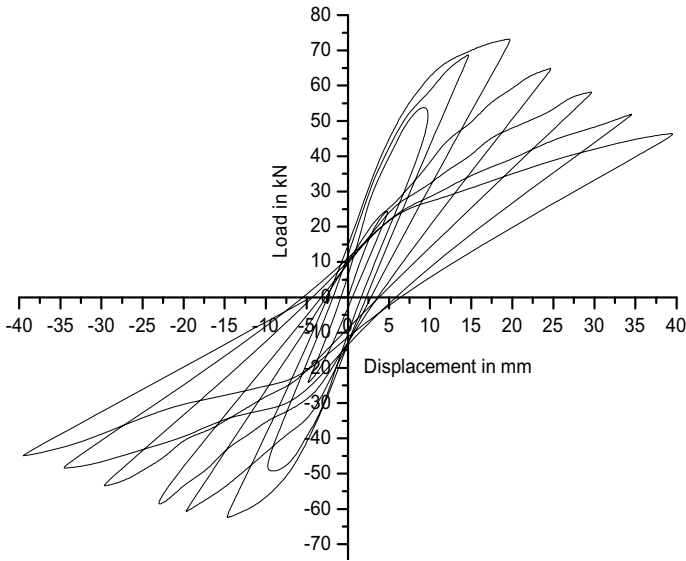
Fig. 2 Hysteresis behaviour of strong column–weak beam specimen (SCWB-A1)
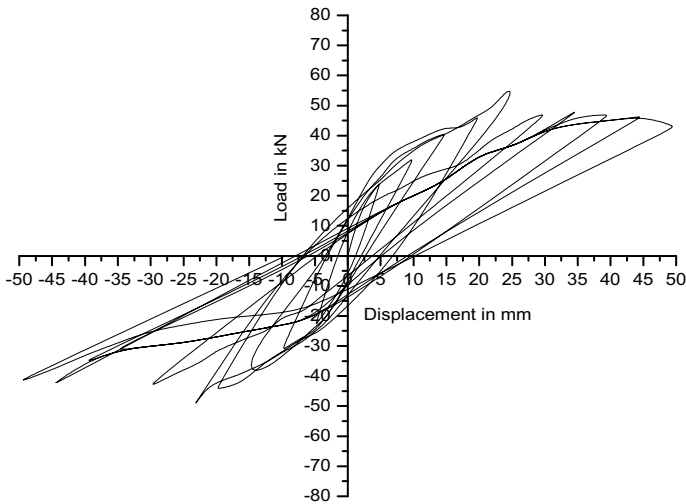
Fig. 3 Hysteresis behaviour of strong column–weak beam specimen (SCWB-B1)

observed for SBWC-A2 was 1572.36 kN mm and for SBWC-B2 was 1837.00 kN mm The stiffness degraded for SBWC-A2 from 5.67 to 1.17 kN/mm and for SBWC-B2 from 4.90 to 1.32 kN/mm. The initial stiffness value obtained was 5.67 and 4.9 kN/mm and at a displacement of 5 mm. The energy dissipation and stiffness are shown in Fig. 8. The crack pattern for strong beam–weak column is shown in Figs. 9.

Table 2 Energy dissipation and stiffness for strong column–weak beam specimen

Displacement (mm)	Energy dissipation (kN mm)		Stiffness (kN/mm)	
	SCWB-A1	SCWB-B1	SCWB-A1	SCWB-B1
5	61.82	72.36	3.78	4.9
10	186.28	203.84	3.15	3.27
15	432.84	452.75	2.52	2.72
20	692.86	712.86	2.21	2.32
25	1023.72	1124.68	2.02	2.10
30	1318.68	1420.60	1.26	1.58
35	1512.83	1640	0.98	1.38
40	1636.84	1842	0.81	1.14
45		2184		1.03

Fig. 4 Energy dissipation and stiffness for strong column–weak beam specimen
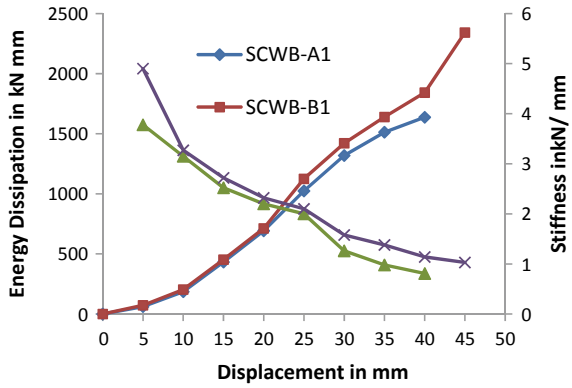
Fig. 5 Cracking pattern of beam–column joint SCWB
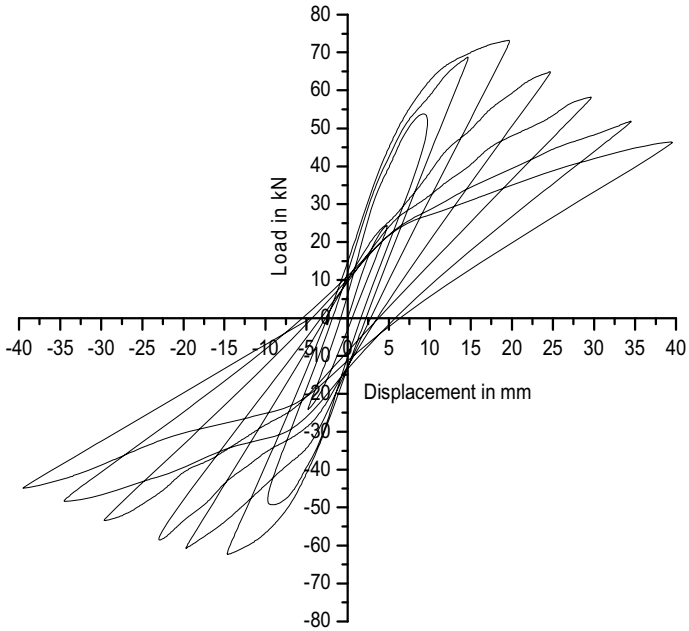
Fig. 6 Hysteresis behaviour of strong beam–weak column specimen (SBWC-B1)
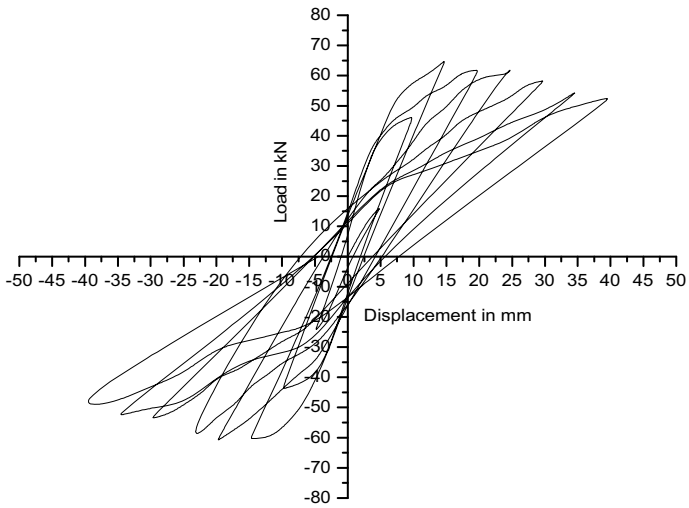
Fig. 7 Hysteresis behaviour of strong beam–weak column specimen (SBWC-B2)

Table 3 Energy dissipation and stiffness for strong beam–weak column specimen

Displacement (mm)	Energy dissipation (kN mm)		Stiffness (kN/mm)	
	SBWC-A2	SBWC-B2	SBWC-A2	SBWC-B2
5	58.25	68.54	5.67	4.9
10	182.6	192.62	5.01	4.6
15	402.78	438.6	4.62	3.8
20	685.72	710.6	3.67	3.1
25	986.24	1158.67	2.60	2.4
30	1286.32	1357.6	1.94	1.93
35	1462.86	1552.8	1.49	1.57
40	1572.36	1837	1.17	1.32

Fig. 8 Energy dissipation and stiffness for strong beam–weak column specimen
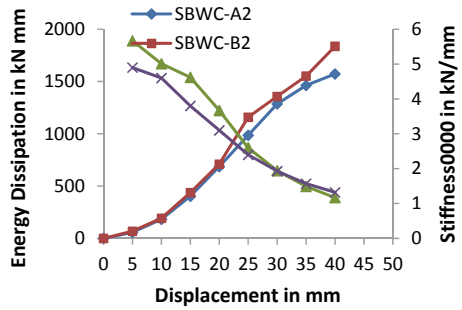
Fig. 9 Cracking pattern of beam–column joint SBWC

5 Conclusion

The simulation of beam–column joint through experimental work represented by the load–deflection plots at free end of beam shows good for strong column and weak beam. The total shear resistance at the critical section for the SCWB specimen was higher than SBWC. The increase in energy dissipation of strong column–weak beam was 4% greater as compared with the strong beam–weak column. From the observation, it can be seen that the increase in energy dissipation capacity of strong column weak beam to enhance the ductility capacity.

References

1. ACI Committee 318 (1995) Building code requirements for structural concrete (ACI 318–05) and community. American Concrete Institute, Farmington Hills, Mich, p 369
2. NZS3101 (1995) Part I Code of practice for the design of concrete structure. St. Assn of N. Z, Wellington
3. IS 13920 (1993) Indian Standard Ductile of reinforced concrete structures subjected to seismic forces (Bureau of Indian Standard), New Delhi
4. Alcocer SM, Jirsa JO (1993) Strength of reinforced concrete connections rehabilitated by jacketing. ACI Struct J 90(3):249–261
5. Biddah A, Ghobarah A, Aziz TS (1997) Upgrading of non-ductile reinforced concrete frame connections. J Struct Eng 123(8):1001–1010
6. Geng Z, Chajes MJ, Chou T, Pan DY (1998) The retrofitting of reinforced concrete column-to-beam connections. Compos Sci Tech 58(8):1297–1305
7. Mosallam A, Chakrabarti P, Lau E, Ibrahiem M, Elsanadedy E (2000) Application of polymer composites in seismic repair and rehabilitation of reinforced concrete connections, ACUN-2 international composites conference. Australia, Sydney
8. El-Amoury T, and Ghobarah A (2002) Seismic rehabilitation of beam-column joint using GFRP sheets. Eng Struct 24(11):1397–1407
9. Ghobarah A, Said A (2002) Shear strengthening of beam-column joints. Eng Struct 24(7):881–888
10. Wonggpakdee N, Leelataviwat S (2019) Influence of column strength and stiffness on the inelastic behavior of strong–column-weak-beam frames. ASCE J Struct Eng 145(9),04017124:1–12
11. Hu B, Kundu T (2019) Seismic performance of interior and exterior beam-column joints in recycled aggregate concrete frames. ASCE J Struct Eng 145(3), 04018262:1–16
12. Surana MI, Yogendra Singh I, Lang DH (2018) Effect of strong-column weak-beam design provision on the seismic fragility of RC frame buildings. Int J Adv Struct Eng 10:131–141

Seismic Appraisement of Building with Silt Floor Using Composite Column

Abhishek D. Chaudhari, Pravin D. Dhake, Sudhanshu Pathak, and Vaishnavi Battul

Abstract This paper investigates the effects of providing steel–concrete composite column at soft-storey level in place of a reinforced concrete column. The main parameters include the storey displacement and drift, base shear, axial force, shear force and bending moment. The linear and nonlinear analysis are used to assess the seismic response of the building using steel–concrete composite columns at the soft-storey level. For linear analysis, the response spectra method (RSA) is used, and for nonlinear analysis, time history method (THA) is used. The analytical work was conducted by considering the three different analytical models and modelling infill walls as an equivalent strut approach. The analysis is performed using finite element software SAP2000. The results obtained indicate that the replacement of soft-storey reinforced concrete columns with steel–concrete composite columns is possible because of higher strength and efficiency of a steel–concrete composite column. It is strongly recommended to provide steel–concrete composite column at the level of soft-storey to increase the performance of the silt floor.

Keywords Steel–concrete composite column · Soft storey · Non-linear analysis

A. D. Chaudhari (✉)
Applied Mechanics Department, Sardar Vallabhbhai National Institute of Technology, Surat, Gujarat, India
e-mail: ac2565@gmail.com

P. D. Dhake
Civil Engineering Department, K. K. Wagh Institute of Engineering Education and Research, Nashik, Maharashtra, India

S. Pathak
Department of Civil Engineering, D Y Patil College of Engineering, Akurdi, Pune, Maharashtra, India

V. Battul
Department of Civil Engineering, D Y Patil Institute of Engineering Management and Research, Akurdi, Pune, Maharashtra, India

1   Introduction

From the last few years, steel–concrete composite column sections are widely used in buildings. The main reason for providing such composite column is due to the rigidity as well as stiffness of concrete, in addition to that, the strength and ductility of steel composite column classified into two categories namely steel embedded in concrete section and concrete filled in hollow steel tube. The first type of section is considered for this study. Due to the composite action, there will be a reduction in the cross-sectional area of column. The cross-section of column becomes an important consideration while analysis and design of the silt floor. A silt floor which is also termed as a soft-storey is a storey in a building that has substantially less stiffness than the stories above or below. Also in accordance, it has less shear resistance or ductility, i.e. energy absorption capacity to resist the stresses induced by the earthquake. Indian seismic code IS 1893 [1] defines the soft-storey as storey in which the lateral stiffness is less than that the storey above. The storey lateral stiffness is the total stiffness of all seismic force resisting elements resisting lateral earthquake shaking effects in the considered direction. Such buildings are most common in India especially in residential apartment schemes which are constructed at metro cities. The main reason for the formation of soft-storey is due to the irregularity in stiffness of storey above and below the ground floor.

Banerjee et al. [2] have analysed the different response parameters such as displacement and drift of storey and base shear using nonlinear analysis program IDARC 2D and concluded roof displacement and maximum drift reduced by considering infill wall effect as compared with a bare frame. However, in case of ground storey consideration, the purpose of parking construction of infill was difficult. Dande and Kodag [3] studied the behavior of reinforced concrete frame by modifying the provisions of soft-storey. Providing the strength and stiffness of the building frame in two ways, first with stiff column and second with adjacent infill wall panels at each corner of the building frame, and concluded that the provision of a stiff column for the required capacities is difficult. Arlekar et al. [4] studied on nine different building models using ETABS and concluded buildings having silt floor exhibit poor performance during earthquake and proposed that solution for this problem is by increasing the stiffness of silt floor. One of the approaches to increase this stiffness is by providing large size columns at ground floor. But it is not feasible to provide large size column at first level due to the increase in space requirement at that level. To solve this problem, it is proposed to provide steel–concrete composite columns at ground floor level only which may be more efficient and required less cross-sectional area. The configuration for the rest of the structure is regular RCC frame. The connection for RCC and steel–concrete composite column can be achieved by the proper detailing of the joint. As most of the available literature is focused on seismic behavior of reinforced concrete frame with silt floor considering the effect of infill wall panel, the shear wall, by providing large size column, but very little information is available on seismic appraisement of building with silt floor using composite column. In this work, it is intended to study the performance of soft-storey using composite column.

2 Methodology

In this paper, it is aimed to study the response characteristics of steel–concrete composite columns and stiffened columns. Increasing the stiffness is one of the measures which is adopted for control over storey drift irregularity; however, the increase in stiffness could lead to attract more forces. Therefore, after analysis of different sizes of columns and their respective storey drift as shown in Fig. 1, the following three analytical models are prepared and studied:

- **Model CM (650 mm × 650 mm)**: This model is a control model representing the soft-storey at ground level.
- **Model M1 (900 mm × 900 mm)**: Model with large size silt floor columns. The size of the columns is deliberately increased till it neutralized the effect of stiffness variation and hence the irregularity in storey drift. To reach a specific size of the column, firstly, the control model (CM) is designed, and then, the cross section is decided based on the load combinations for limit state of strength. Then, by increasing the size of the column and simultaneously observing drift graph till it gives regularity in drift for the storey above and below the soft-storey. The design size evaluated for control model was 650 mm × 650 mm. Figure 1 shows the graphical representation of storey drifts with increasing sizes of ground floor columns. In the graph, it shows the storey drift for first three stories only. It is clear that the effective size of the column would be 900 mm × 900 mm. Hence, for model M1, the design size evaluated was 900 mm × 900 mm.
- **Model M2 (Composite 650 mm × 650 mm)**: In this model, the steel–concrete composite columns are considered for response verification. The sizes of soft-storey columns are kept same as that for the control model, i.e. 650 mm × 650 mm and ISMB-450 steel section was embedded in a concrete column, and the column is modelled as a steel–concrete composite column. The percentage of reinforcement is kept equal to 0.8%. The effective flexural stiffness is worked out using the guidelines provided by INSDAG [5, 6] as mentioned in Table 1.

i) Column size 650mmx650mm   ii) Column size 800mmx800mm   iii) Column size 900mmx900mm
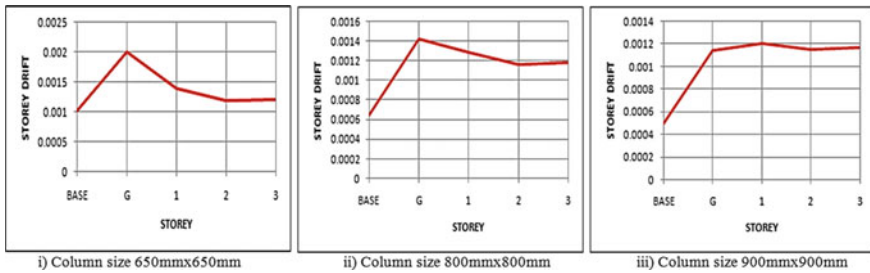
Fig. 1 Storey drifts for various sizes of columns

Table. 1. Effective flexural stiffness

Considered axis	Properties of RCC section		Properties of composite section	
	Area (mm^2)	Effective flexural rigidity (N-mm^2)	Area (mm^2)	Effective flexural rigidity (N-mm^2)
About 3–3 (major)	422.5×10^3	4.7040×10^{14}	422.5×10^3	4.2417×10^{14}
About 2–2 (minor)	422.5×10^3	4.7040×10^{14}	422.5×10^3	3.7136×10^{14}

3 Modelling and Analysis

Modelling of the structure is carried out using SAP2000 nonlinear software tool. The effect of infill wall is considered by assigning a diagonal strut having the properties of brick masonry. The diagonal lengths and thicknesses of the struts are same as that of brick walls, only width of the struts is derived according to formulae suggested by Mainstone [7]. The section designer tool was used for modelling of the composite column. The properties of the composite section are calculated based on the guidelines provided by INSDAG [5, 6]. Typical cross sections of composite column considered for this study with fully concrete encased steel section are illustrated in Fig. 2. For modelling of composite section, 'E' and 'I' are calculated separately for the considered section. The 'E' is modelled in the material property where as 'I' is modelled using property modifier for moment of inertia in particular direction.

The equivalent flexural stiffness of composite section is given by Eq. (1)

Fig. 2 Typical cross sections of fully concrete encased composite column
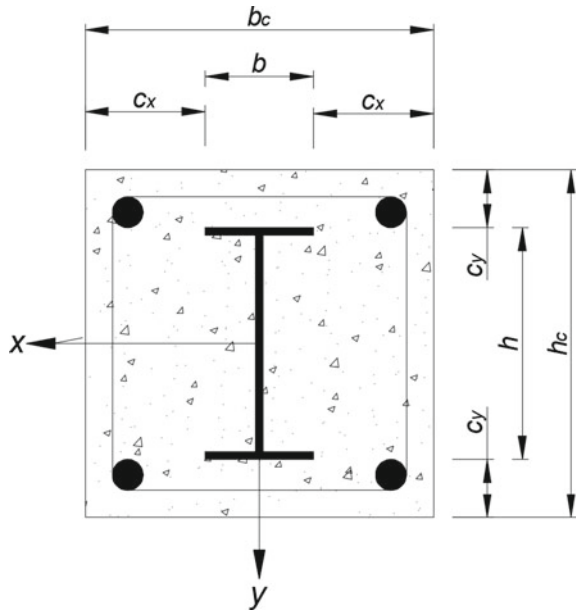
$$(EI)_{\text{ex}} = E_a I_{\text{ax}} + 0.8 E_{\text{cd}} I_{\text{cx}} + E_s I_{\text{sx}} \qquad (1)$$

where E_a is Young's modulus of elasticity for steel, I_{ax} is moment of inertia of steel section (ISMB) about the considered axis, E_{cd} is $E_{\text{cm}}/1.35$, E_{cm} is second modulus of concrete, E_s is Young's modulus of elasticity of structural steel and I_{sx} is moment of inertia of reinforcement about the considered axis of bending.

The calculated properties of the selected section are shown in Table 1. It has been observed that there is not much variation in effective flexural stiffness compared to the original RCC column. This is because that the only around 59% of 'E' is considered for the calculation of effective flexural stiffness and it will reflect in our analysis results. The equivalent static analysis (ESA), response spectra analysis (RSA) and nonlinear time history analysis (THA) were carried out on the above three considered models. Based on the base shear values obtained from static and dynamic analysis, all response quantities are multiplied by a factor stated in IS 1893 [1].

For an inner portion of the frame, infill walls are considered at alternate panels along each of the principal direction as shown in Fig. 3b, and the building plan considered for this study is shown in Fig. 3c.

Manually analysing a building with lateral forces is a very tedious process and almost practically impossible. There are various finite element software tools available which have a capacity to simulate the exact behaviour of building subjected to different loadings including lateral load. One of the finite element software tool was SAP which has a capacity to analyse a three-dimensional model of a building subjected to various loading. The software has various elements such as line element, shell element, membrane elements which can be used to model various structural elements in the building. All elements have got their local axis, and results are obtained with respect to local axis. The software has a capacity to perform linear as well as nonlinear analysis. While analysing the building frame, the dead load of the brick infill wall is directly applied on the beams in the form of uniformly distributed load. This will ignore the stiffness contribution of wall and affect the analysis results. The actual building has first storey open, and hence to model this effect, stiffness of infill walls needs to be modelled. This effect can be modelled using various methods, and one of the methods of modelling infill wall is to model an equivalent diagonal

(a) Periphery of building   (b) Inner region of building   (c) Building plan
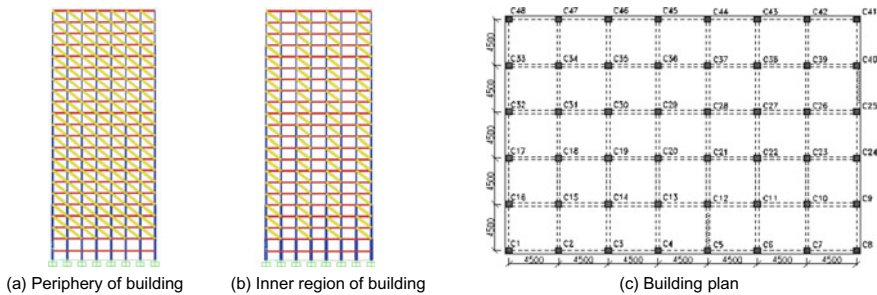
Fig. 3 Arrangement of infill wall panels and building plan considered for analysis

strut which will simulate the behaviour of infill wall. This strut is modelled in such a way that it will not contribute for resisting any bending moment but will certainly contribute the stiffness of wall. There are various imperial formulae available to calculate the properties of strut based on the properties of infill wall.

The relative infill to frame stiffness shall be evaluated by using Eq. (2).

$$\lambda_1 h = \left[\frac{E_m t \sin 2\theta}{4 E_c I col h} \right]^{\left(\frac{1}{4}\right)} \tag{2}$$

$$\theta = \tan^{-1}\left(\frac{h}{l}\right) \tag{3}$$

$$a = 0.175 D (\lambda_1 h)^{-0.4} \tag{4}$$

where A is equivalent width of strut, $\lambda_1 h$ is relative infill to frame stiffness, E_m is Young's modulus of elasticity for masonry and E_c is Young's modulus of elasticity for concrete.

The effect of infill wall is considered by assigning a diagonal strut having the properties of brick masonry. The diagonal lengths and thicknesses of the struts are same as that of brick walls, and only width of the struts is derived according to formulae suggested by Mainstone [7]. The equivalent strut width 'a' as shown in Fig. 4 depends on a relative flexural stiffness of the infill to that of the column of the confining frame. Data considered for analysis is presented in Table 2.

Fig. 4 Equivalent width of strut
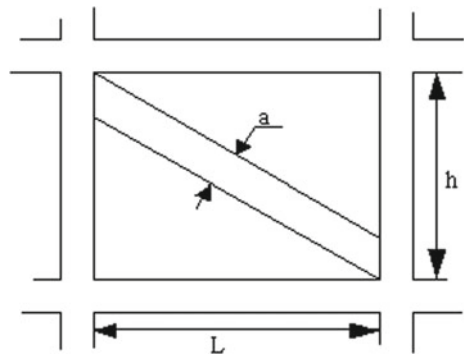
Table 2 Data considered for analysis

Frame type	OMRF	Thickness of external wall	230 mm
Building	G + 20	Thickness of internal wall	115 mm
Storey height	3.2 m	Height of parapet	1.0 m
Depth of foundation	2.0 m	Seismic zone	IV
Plan dimension	31.5 m × 22.5 m	Zone factor (Z)	0.24
Unit weight of RCC	25 kN/m^2	Importance factor (I)	1.5
Unit weight of masonry	18 kN/m^2	Repose reduction factor (R)	8
Live load intensity on floor	3.0 kN/m^2	Soil type	Medium
Live load intensity on roof	3.0 kN/m^2	Grade of concrete	M40
Weight of floor finish	1.5 kN/m^2	Grade of steel	Fe500
Waterproofing load on roof	2.0 kN/m^2	% of steel for composite column	0.8%

4   Results and Discussion

4.1   Response Spectra Analysis

The results obtained from the RSA are presented in terms of displacement, drift and column forces. The column forces are presented for two columns, one at the periphery of building and one at the interior level, designated as column C1 and C19 shown in Fig. 3c. The response spectra analysis is performed using the spectra given in IS 1893 [1]. The code required that the results obtained from response spectra analysis shall be scaled to a value equal to that obtained from the fundamental period of the building.

From Fig. 5 which represents the displacement in transverse as well as longitudinal direction for the respective level, it has been observed that the displacement reduced by 2.6% with composite column and 7.4% with stiffened column. For the model displacement, CM was found to be maximum with compared to the all models, and model M1 is found to be a minimum of all.

As observed from Fig. 6 which is representation of the storey drift in transverse as well as in longitudinal direction for the respective floor, the drift profile is reduced
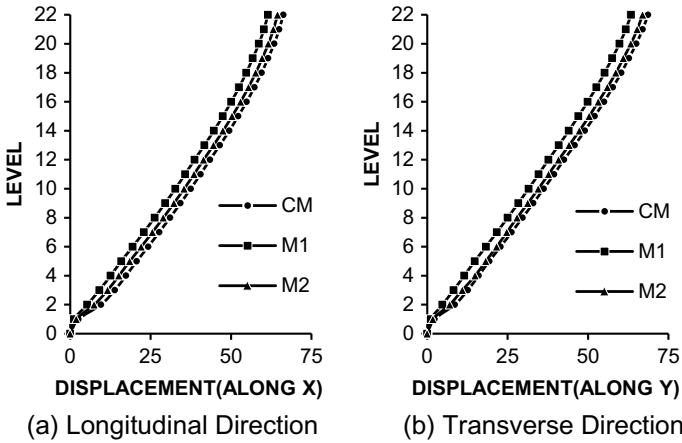
Fig. 5 Maximum storey displacement
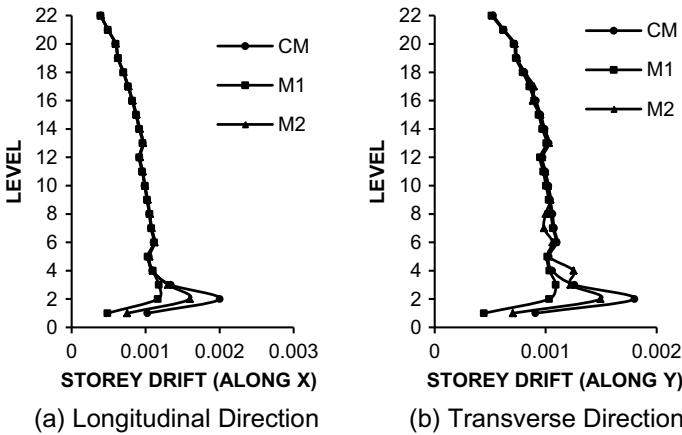
Fig. 6 Maximum storey drift

by 20% with composite column and 42% with stiffened column. Additionally, it is found that the composite column significantly improves the performance of silt floor in both the principal direction (i.e. in longitudinal and transverse direction). However, again, it will not completely neutralize the effect as in the case of model M1.

From Fig. 7 which highlights the base shear in both the directions for the considered model (i.e. CM, M1 and M2), it has been observed that the base shear is increased by 1.2% with composite column and 1.3% with stiffened column. As the base shear is function of seismic weight of building due to which base shear is more in case of stiffened column as compared to composite column.

(a) Longitudinal Direction

(b) Transverse Direction
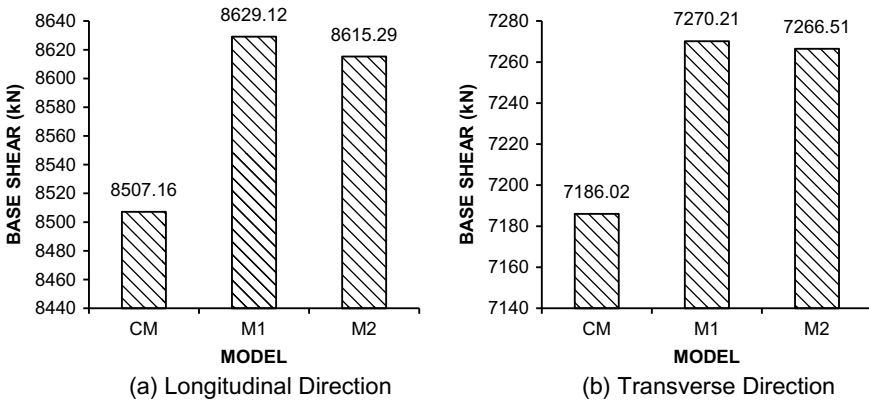
Fig. 7 Base shear in longitudinal and transverse directions

To compare axial and shear force as well as bending and torsional moment, one exterior column (C1) is biaxially loaded and subjected to biaxial bending, and one interior column (C19) is axially loaded.

As shown in Fig. 8 which represents the axial force for respective columns (i.e. C1 and C19) in both the directions, it has been observed that for column C1 axial force increased by 0.7% with composite column and 0.6% with stiffened column, while for C19, it is increased by 1.6% with composite column and 4.1% with stiffened column.

As shown in Fig. 9 which represents the shear force for respective columns (i.e. C1 and C19) in both the directions, it has been observed that for column C1 shear force increased by 2.0% with composite column and 5.7% with stiffened column,

	ALONG X	ALONG Y
CM	1620.34	1565.48
M1	1643.40	1561.84
M2	1634.78	1573.23

Exterior Column (C1)

	ALONG X	ALONG Y
CM	543.49	479.7
M1	567.34	498.29
M2	551.74	486.31

Interior Column (C19)
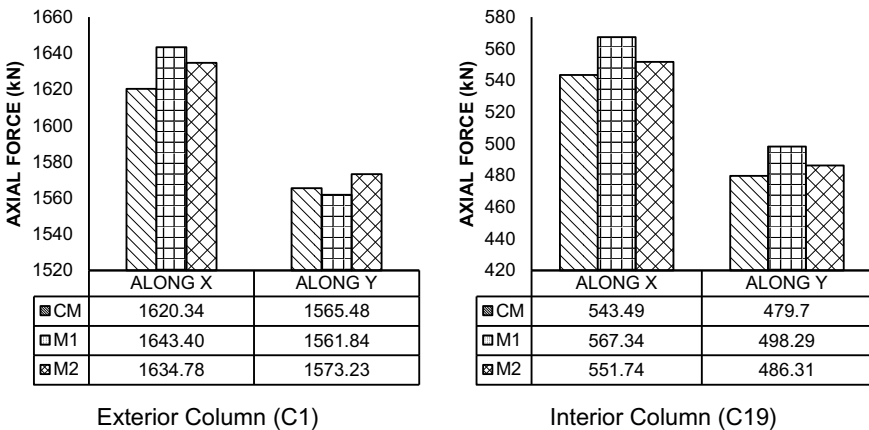
Fig. 8 Maximum axial force (kN)
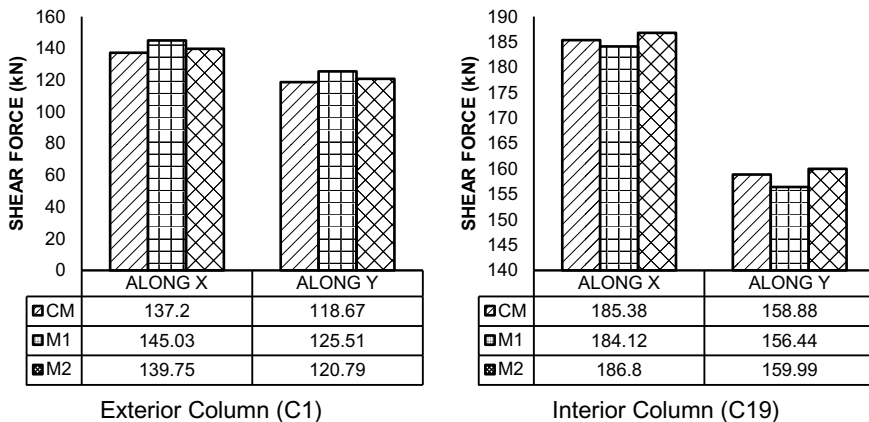
Fig. 9 Maximum shear force (kN)

while for C19, it is increased by 0.7% with composite column and reduced by 0.9% with stiffened column.

From Fig. 10 which represents the bending moment carried by respective column (i.e. C1 and C19) in both the directions, it has been observed that for column C1, bending moment increased by 21.1% with composite column and 68.2% with stiffened column, while for C19, it is increased by 11.5% with composite column and increased by 41.8% with stiffened column. As the bending moment is function of moment of inertia $\left(\text{i.e.} M = EI \int \frac{d^2 y}{dx^2}\right)$, there is a large increase in the moment, and torsional forces were observed for model M1; however, there is a slight increase in forces for composite columns (as moment of inertia for stiffened column is 5.47×10^{10} mm^4, while for composite column, it is 1.49×10^{10} mm^4).
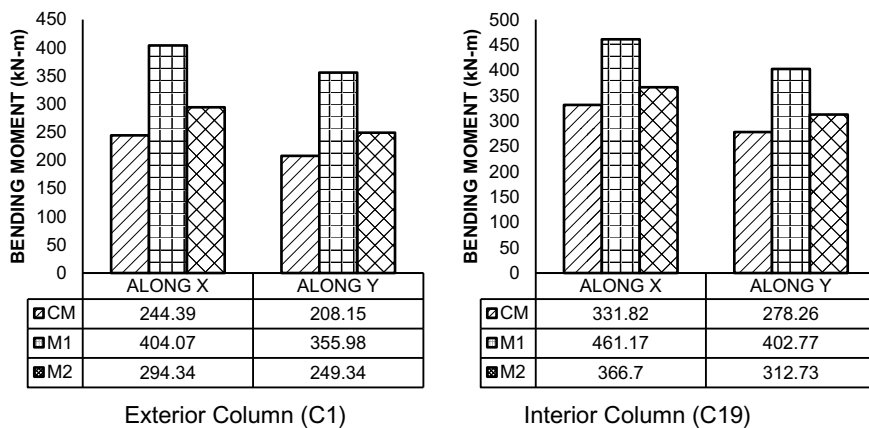
Fig. 10 Maximum bending moment (kN-m)

☑CM	ALONG X	ALONG Y
☑CM	3.14	2.65
☐M1	5.96	4.97
☒M2	3.4	2.86

Exterior Column (C1)

	ALONG X	ALONG Y
☑CM	2.07	1.65
☐M1	3.83	2.91
☒M2	2.13	1.65

Interior Column (C19)
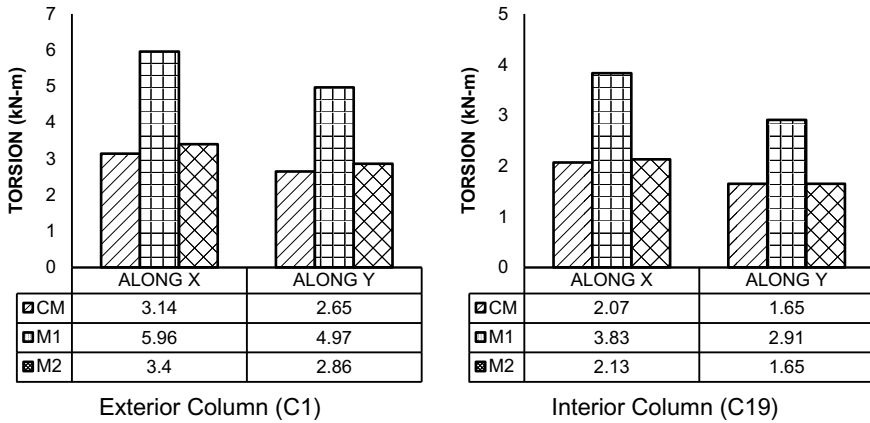
Fig. 11 Torsional moment of interior and exterior column

Like bending moment, there is increased in torsional moment, for column C1, torsional moment increased by 7.81% with composite column and 88.67% with stiffened column, while for C19, it is increased by 1.5% with composite column and increased by 80.69% with stiffened column as shown in Fig. 11. As again in case of torsional moment because of modulus of rigidity, there is huge increment was observed for torsional moment with stiffened column. The increase in these forces in composite columns may be tackled by the additional strength due to composite action. Undoubtedly, it is one of the alternatives for improving the behavior of soft-storey by providing composite columns. The stiff columns attract more forces and also lead to the reduced space in the soft-storey. Hence, it is proposed to keep the column size minimum possible and to increase the stiffness by using composite action.

4.2 Time History Analysis

The results obtained using RSA are now verified through nonlinear analysis as well. The nonlinear analysis is performed using El Centro time history. The details of time history data are mentioned in Table 3.

The results obtained from time history analysis are represented in Figs. 12 and 13. Figure 12 represents the absolute displacement for the considered column models (i.e. CM, M1 and M2) in both directions, while Fig. 13 represents the maximum base shear for the considered column models in both directions. It has been observed that the results obtained for displacement from the time history analysis are in line with the response spectra analysis. The maximum displacement is found to be for model CM (i.e. 252.13 mm) and minimum for model M1 (i.e. 204.01 mm). For model M1,

Table 3 Details of time history data

Earthquake	El Centro	Station	Imperial valley
Hypocentral distance	12.12 km	Date and time	18/05/1940
Peak acceleration	341.69 cm/s/s	Earthquake component	N 75 E
Scale factor for SAP	9.81	Unit	g
No. of acceleration data points recorded	1559	Magnitude	6.9

(a) Longitudinal direction   (b) Transverse direction
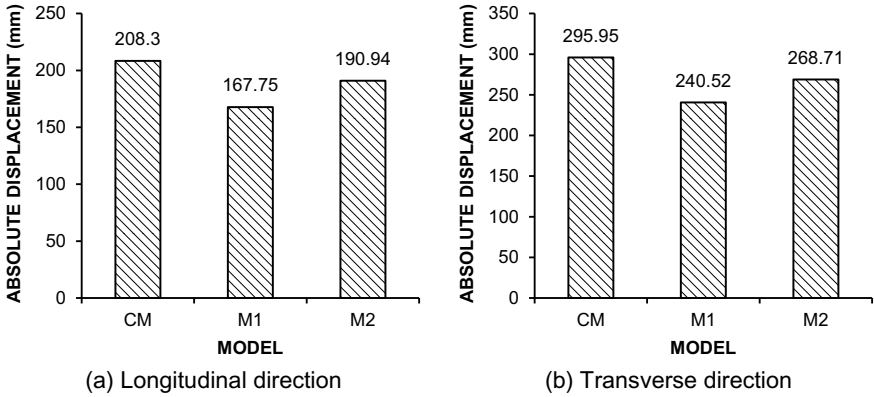
Fig. 12 Absolute roof displacement in longitudinal and transverse directions

	CM	M1	M2
MAX. NEGATIVE	-31210.41	-25505.48	-27027.51
MAX. POSITIVE	30193.34	32395.58	31087.77

	CM	M1	M2
MAX. NEGATIVE	-40286.64	-35015.01	-39035.32
MAX. POSITIVE	38400.229	35503.2	37563.34

(a) Longitudinal direction   (b) Transverse direction
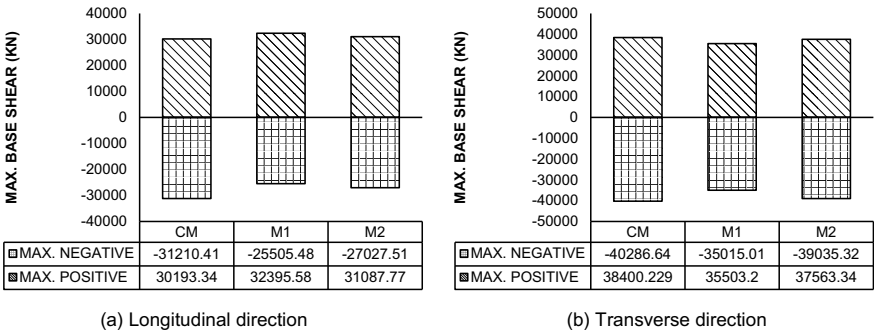
Fig. 13 Base shear for longitudinal and transverse directions

base shear is found to be maximum, for model M2 and model CM, it gives maximum displacement in other direction.

5 Conclusion

The following conclusions are drawn from this study:

- The stiffening of columns is highly effective but due to increase in cross-sectional area and subsequently the stiffness of storey, leads to attract additional forces for these columns.
- It is highly recommended to go for composite columns at the level of the silt floor as there will be very less space consumed compared to stiff columns which will be having more area.
- The composite column attracts more forces than RCC column, but due to the composite action, the strength of these columns will also be more and hence can be designed easily for this increase in forces. Due cares shall be taken while working out the connections for these columns.
- The use of composite columns at the level of soft-storey will lead to reduction in soft-storey effect as well as there will be very less space consumed at ground level. The composite column will prove to be equally stiff as that of the stiffened column of larger cross-sectional area.
- No guidelines are available in Indian Standards for analysis and design of composite structure.

References

1. IS:1893 Part-I (2002) Criteria for earthquake resistant design of structures. Bureau of Indian Standards, India
2. Banerjee S, Patro SK, Rao P (2014) Inelastic seismic analysis of reinforced concrete frame building with soft storey. Int J Civil Eng Res 5(4):373–378
3. Dande PS, Kodag PB (2013) Influence of provision of soft storey in RC frame building for earthquake resistance design. Int J Eng Res Appl 3(4):461–468
4. Arlekar JN, Jain SK, Murty CVR (1997) Seismic response of RC frame buildings with soft first storeys. In: Proceedings of the CBRI Golden Jubilee Conference on Natural Hazards in Urban Habitat, New Delhi, pp 13–24
5. INSDAG: Chapter 25 (2003) Steel-concrete composite columns-I. Institute of Steel Development & Growth, India
6. INSDAG: Chapter 26 (2003) Steel-concrete composite columns-II. Institute of Steel Development & Growth, India
7. Mainstone RJ (1971) On the stiffnesses and strengths of infilled frames. In: Proceedings of the institution of civil engineers supplement, pp 57–90

Theoretical and Experimental Study on the Behaviour of Deep Beams Reinforced Internally Using Hybrid Fibre-Reinforced Polymer Rebars with and Without Web Openings

P. Swaminathan and G. Kumaran

Abstract The use of non-corrosive reinforcements in the place of steel reinforcements has therefore been focused as an alternative to improve the life span of the concrete structures. Fibre-reinforced polymer (FRP) reinforcements offer many advantages over steel reinforcements including resistance to electrochemical corrosion, high strength to weight ratio and easy in fabrication and electromagnetic insulating properties. The use of hybrid FRP reinforcements in lieu of conventional steel reinforcements requires better understanding under different parametric conditions. Therefore, the present study deals mainly with the behaviour of deep beams with and without openings reinforced internally with hybrid-type FRP reinforcements under static loading condition. In this study, two types of grades of beams, viz., normal and high strengths concrete deep beams with and without web openings are investigated. Among the sixteen beams, eight beams are reinforced internally using conventional reinforcements with and without web openings, and eight beams are reinforced internally using hybrid FRP reinforcements with and without web openings. Different parameters like normal strength concrete, high strength concrete, web opening positions (Top, Middle and Bottom), and span sprinkled FRP hybrid reinforcements are considered. Based on this study, the static load carrying capacities and their modes of failures of deep beams reinforced internally with FRP hybrid type reinforcements for various web openings positions are compared with the existing theories for better understandings. A good agreement exists between the theoretical and experimental results. Based on the experimental and theoretical work, the final conclusions of the present study are derived.

Keywords Fibre-reinforced polymer hybrid reinforcements · Deep beams · Static loading · Web openings · Shear span to depth ratio

P. Swaminathan (✉) · G. Kumaran
Department of Civil and Structural Engineering, Annamalai University, Chidambaram, India
e-mail: sam7586@gmail.com

1 Introduction

Fibre matrix composites made of different proportions of fibres and resins are now commercially utilized as reinforcing agents in place of conventional ferrous reinforcements for conventional concrete structures. The advantages of fibrous reinforcements, when compared with metallic reinforcements, give a better strength and serviceability (ACI 440.1R-01 [1]; ACI 440.XR [2, 3]). The application of non-metallic reinforcements gains its use both in reinforced concrete and pre-stressed concrete works all over the world. Most of the study techniques specially within the early years had been directed closer to behaviour of concrete deep beams reinforced with conventional reinforcements [4].

However, the application of hybrid non-metallic reinforcements in concrete deep beams with and without web openings in concrete structures, their behaviours under different positions of web openings [5–7] and the formulation of rational design specifications are not well explored with regard to Indian standards [8]. The non-metallic reinforcements, few decades, have received much attention in structural applications including bridge structures. Despite their successful introduction into the construction industry, the widespread acceptance of non-metallic reinforcements by the engineering industry depends on timely development of design guidelines and specifications. Hence, the present work has been proposed to study the behaviour of concrete deep beams reinforced with non-metallic reinforcements with and without web openings and their suitability for codal recommendations [9–13, 21]. Although an extensive research has been carried out on the behaviour of FRP-reinforced structural elements in other countries, very limited studies have been carried out in India. There is a need for modelling and experimental study that accounts for the fundamental issue related to the hybrid FRP reinforcements and their interaction with the concrete under static loading conditions with and without web openings [12, 14, 15, 21].

2 Material Properties

2.1 Concrete

Normal strength concrete (NSC) of grade M30 and high strength concrete (HSC) of grade M60 are used to cast the deep beam specimens [16]. The strength of concrete under uni-axial compression is determined by loading 'standard test cubes' to failure in a compression testing machine, as per IS 516–1959. Each series of test specimens is tested after 28 days, and their corresponding cube strength values are given in Table 1.

Table 1 Properties of concrete

Material/m^3	M30 grade of concrete	Ratio	M60 grade of concrete	Ratio
Cement	368.42 kg	1:1.87:3.50	466.67 kg	1:1.36:2.70
Fine aggregate	690.04 kg		629.16 kg	
Coarse aggregate	1290.98 kg		1263.55 kg	
Water/cement ratio	0.38		0.30	
Average compressive strength of concrete cubes	42.00 MPa		76.00 MPa	

Table 2 Tensile properties of reinforcements

Properties	Sand-coated hybrid FRP rebar (H_f)	Steel Fe 500 rebar (Fe)
Tensile strength (MPa)	1052.04	520
Longitudinal elastic modulus (GPa)	64.70	210
Strain (@max stress level)	0.012	0.002
Poisson's ratio	0.236	0.3

2.2 Reinforcement

The reinforcements used in the study are conventional steel and hybrid FRP reinforcements. Hybrid FRP reinforcements are manufactured using pultrusion process with the E-glass fibre volume approximately 60% and carbon fibres volume 40% and are reinforced with epoxy resins. The hybrid reinforcements and with surface indentations, namely sand-coated-type. The mechanical properties of hybrid FRP reinforcements are obtained from the tests prescribed as per ASTM Standards (ASTM-D 3916-84). Table 2 summarizes the mechanical properties of all hybrid FRP and conventional steel reinforcements.

3 Analytical Investigation

3.1 Proposed Design Equation from Kong and Sharp [18]

Noting the inadequacy of the literatures on deep beam with web openings, Kong and Sharp [18] tested 24 reinforced lightweight concrete deep beams with web openings. The results indicated that web reinforcement did not have any effect on the failure

Fig. 1 Parameters involved in deep beam with web openings
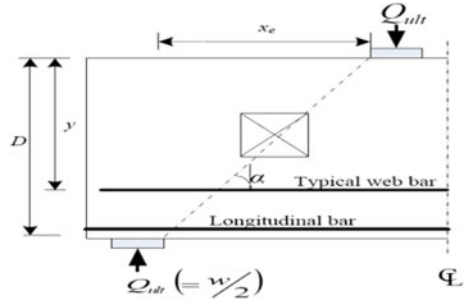
mode of these beams, and the failure mode was more dependent on the location and size of opening. The location and size of the web openings, particularly if intercepting the load path, also had an effect on the load carrying capacity of the deep beams. Where the opening is clear or reasonably clear the load path, the strength of deep beams was comparable to solid deep beams [19]. From this study, two design equations for these beams were proposed. When the opening is reasonably clear of the load path joining the support with the bearing plate, the beam may be considered as not having an opening, therefore, the ultimate load capacity is as given in Eq. (1):

$$V_u = c_1 \left(1 - 0.35 \frac{x}{D}\right) f_t b D + c_2 \Sigma A \frac{y}{D} \sin^2 \alpha \tag{1}$$

Various parameters involved in Eq. (1) are explained in Fig. 1.

3.2 Proposed Design Equation from Kong and Sharp [18]

The proposed design equation is based on the equations recommended by Kong and Sharp [18]. The present study focuses on identifying the effect of opening especially location and effect of hybrid FRP reinforcements on the behaviour of deep beams with web openings. The equation regarding main steel and/or web reinforcement is adopted from the proposal of Kong and Sharp [18].

$$V = V_C + V_S \tag{2}$$

where V is the ultimate strength of deep beams with openings, V_C and V_S are, respectively, the ultimate strength of concrete and steel. The ultimate strength of concrete V_C by Kong [17] is given:

$$V_C = C_1.\lambda c.D.b.ft \tag{3}$$

where C_1 is a parameter for high strength concrete, λ_C is a parameter of opening location and size, D is the overall depth of the deep beam, b is the thickness of deep
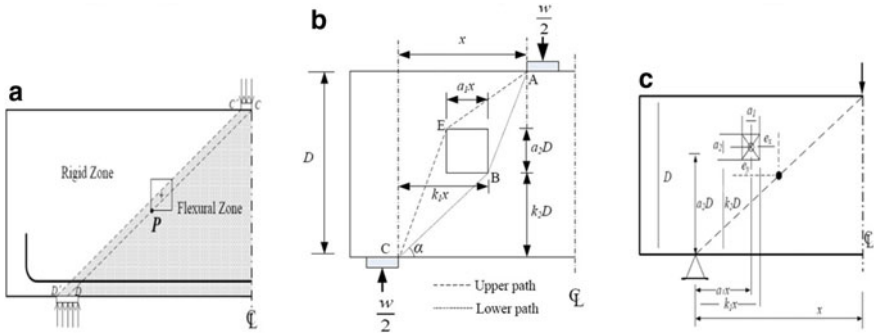
Fig. 2 a Zone identification in deep beams by diagonal strut, **b** load paths in deep beam with web opening, **c** various parameters involved deep beams with web openings

beam and f_t is the calculated tensile strength (Fig. 2).

$$\lambda_c = (1 - m) \tag{4}$$

where $m = $ ratio of strength reduction of opening location and size $\frac{\Psi_x}{\Psi_y}$ multiplied by shear span to depth ratio $\left(\frac{x}{D}\right)$.

$$\lambda_c = 1 - \frac{\Psi_x}{\Psi_y} \frac{x}{D} \tag{5}$$

where Ψ_x is the strength reduction ratio of opening location and size in the horizontal direction and Ψ_y is that in the vertical direction.

$$\Psi_x = 1 - \frac{e_x}{x} \tag{6}$$

$$e_x = 1 - (2k_1 - t_3 a_1)x$$

$$e_x = 1 - 2k_1 x - t_3 a_1 x \tag{7}$$

Similarly,

$$\Psi_y = 1 - \frac{e_y}{D} \tag{8}$$

where the eccentricity of opening in vertical direction,

$$e_y = 1 - (2k_2 - t_4 a_2)D$$

$$e_y = 1 - 2k_2D - t_4a_2D \tag{9}$$

Substituting the Eqs. 6, 7, 8 and 9 in Eq. 5, we get

$$\lambda_C = 1 - t_2\frac{(2k_1 - t_2a_1)}{(2k_2 - t_4a_2)}\left(\frac{x}{D}\right) \tag{10}$$

Thus, we get,

$$V_C = C_1\left(1 - t_2\frac{(2k_1 - t_2a_1)}{(2k_2 - t_4a_2)}\frac{x}{D}\right)f_tbk_2 \tag{11}$$

The ultimate strength related to steel is given by

$$V_S = C_2\Sigma\lambda\frac{Ay_1}{D}\sin^2 \tag{12}$$

The coefficients of parameters (C_1, t_2, t_3 and t_4) are obtained by linear analysis based on least square method using parametric study results for best fit. This yields for rigid zone, $C_1 = 1.4$, $t_2 = 0.7$, $t_3 = -0.6$ and $t_4 = 0.4$ and for flexure zone, $C_1 = 1.3$, $t_2 = 0.15$, $t_3 = -0.1$ and $t_4 = 0.9$. Thus, the proposed design equation for high strength concrete deep beams with web openings is expressed as

$$V_u = C_1\left(1 - t_2\frac{(2k_1 - t_2a_1)}{(2k_2 - t_4a_2)}\frac{x}{D}f_tbk_2D\right) + C_2\Sigma\lambda\frac{Ay_1}{D}\sin^2\theta \tag{13}$$

For opening located in flexural zone, the equation is expressed as

$$V_u = 1.3\left(1 - t_2\frac{(2k_1 - t_2a_1)}{(2k_2 - t_4a_2)}\frac{x}{D}f_tbk_2D\right) + C_2\Sigma\lambda\frac{Ay_1}{D}\sin^2\theta \tag{14}$$

For opening located in rigid zone, the equation is expressed as

$$V_u = 1.4\left(1 - t_2\frac{(2k_1 - t_2a_1)}{(2k_2 - t_4a_2)}\frac{x}{D}f_tbk_2D\right) + C_2\Sigma\lambda\frac{Ay_1}{D}\sin^2\theta \tag{15}$$

To verify the proposed design equation, a comparison of the proposed equation and other existing equations is made utilizing the experimental results.

4 Experimental Investigation

The experimental shear strength of the deep beams is determined using the tensile strength parameters of the specimens. Unlike shallow beams, deep beams transfer

shear forces to support through shear stresses rather than bending stresses. The diagonal cracks in deep beams eliminate the inclined principal tensile stresses required for beam action, and these result in a redistribution of internal stresses, in order that the beam acts as a tied arch. The most important conducted parametric study can be summarized as follows (Fig. 3; Tables 3 and 4):

- The model validation with experimental work from literature has shown that the model is capable of capturing reasonably.
- The web openings crossing the anticipated compression struts evolved among the weight and the supports motive approximately about 14% for M30 grade of concrete 32% for M60 grade of concrete and reduction in the load carrying capacity in all the web opening positions, and therefore, it must be considered while doing layout.
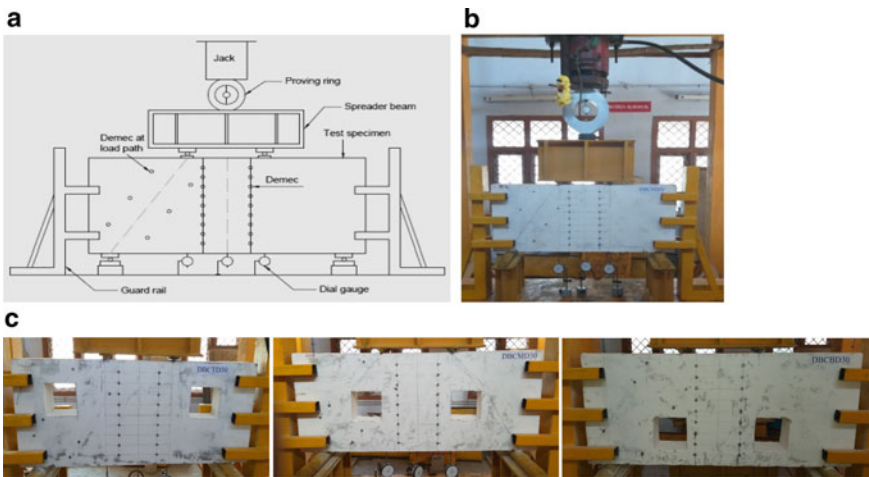
Fig. 3 a Schematic diagram of test set-up, **b** experimental setup for deep beam without web openings, **c** experimental set-up for deep beam with web openings (top, middle, bottom)

Table 3 Various parameters used in deep beams

Parameters	Description	Designation
Type of reinforcements	Hybrid FRP	H
	Conventional steel	C
Grades of concrete	M30	30
	M60	60
Positions of duct	No duct	ND
	Middle	MD
	Top	TD
	Bottom	BD

Table 4 Experimental test results

No.	Designation of beams	Initial crack load (kN)	Ultimate load Vu (kN)	Ultimate deflection, Δu (mm)	Failure mode
1	DBCND30	130	350	4.68	Shear
2	DBHND30	80	250	4.50	Combined flexural and shear
3	DBCND60	190	470	3.35	Shear
4	DBHND60	110	440	3.00	Flexural
5	DBCTD30	110	240	3.38	Shear compression
6	DBHTD30	70	210	3.05	Shear
7	DBCTD60	130	460	2.92	Shear
8	DBHTD60	80	278	2.56	Shear
9	DBCMD30	90	260	4.00	Shear compression
10	DBHMD30	70	220	2.25	Shear
11	DBCMD60	120	400	2.75	Shear compression
12	DBHMD60	90	310	2.59	Shear
13	DBCBD30	80	340	3.81	Shear
14	DBHBD30	90	270	3.74	Shear
15	DBCBD60	100	520	3.47	Combined flexural and shear
16	DBHBD60	110	400	3.24	Combined flexural and shear

- If the web opening does no longer intervene with the load route(beam with bottom web opening) or compression struts, the observed growth in the load carrying potential ranged from 6% to 8% for M30 grade of concrete (normal strength concrete) depending on the position of openings. For better grade concrete (M60), the observed reduction in the load carrying capacity ranged from 6 to 8%.
- The intensity of the opening is the most crucial parameter influencing load carrying capacity of beam. Hence for an overall reduction in the beam's capacity not exceeding 10% of the capacity the beam without web opening, the depth of the opening should not exceed 20% of the beam overall depth (0.2d).
- For beam with and without web opening, the reduction in the beam capacity is about 14–32% for normal and higher strength concrete beams if the depth of the opening is about 30% of the beam usual depth (0.3d).

- The effect of reinforcement distribution on the beam capacity is not studied, but it is adopted in the range of 0.1–0.2H for simply supported deep beams.
- The load–deflection response of the simply supported deep beams under 4-points bending shows the presence of web openings crossing the compression struts developed between the load and the supports (DBCTD30, DBHTD30, DBCMD30, DBHMD30, DBCTD60, DBHTD60, DBCMD60, DBHMD60) resulted in a substantial reduction in the beam load carrying capacity of 33%. However, while the web openings were located outside the expected line of action of compression struts, the reduction in the failure load is from 33% (DBCBD30, DBHBD30, DBCBD60, DBHBD60). In order to study the effect of the position of web opening on the beam's overall capacity, three different web openings were considered. The web opening width to beam length is in the ratio of 0.125L and web opening depth to total depth of beam is in the ratio of 0.3H.

In deep beams, the major portion of load is transferred to support directly through compression struts formed between the load and support points. This mechanism of transferring load leads to the type of failure that is most common in deep beams [20]. The deep beams fail by widening of diagonal shear cracks and crushing of concrete. The failure of beams DBCND30 and DBHTD60 is initiated by diagonal cracks which appear along compression strut trajectories from support to the load points. The shear and diagonal cracks emerged between 40 and 80% of failure load. These cracks appeared only between load and support points. It has an angle of $\theta = \mathrm{Tan}^{-1}(h/a_v)$ where h is the effective depth and a_v is shear span. In all cases of tested beams, the load corresponding to inclined cracks is in close proximity. The appearance of these cracks is independent of tensile bar or web bar percentages. It depends on concrete compressive strength.

These cracks can be observed upon increasing the load; inclined cracks appear at the end of vertical cracks. These cracks are directed towards the load points. These cracks seldom appeared as failure crack at ultimate load. The failure of beam DBHND30 shows that diagonal crack appears perpendicular to the strut compression trajectory which causes failing of support. Diagonal cracks rarely develop within the exterior shear span. Beam DBHND30 shows two diagonal cracks in this region. After the emergence of these cracks at support, the beam abruptly fails in shear. The combined shear and flexural cracks appear inside 25% of pure bending zone from load point to centre of beam. This sort of failure is observed in DBCND30. To overcome this failure mode, the high compressive stress should be distributed over an area using bearing plates at support and load points. This failure is identified as a premature failure which is not desirable always acceptable. This type of failure occurs when the stress exceeds the allowable compression stress of concrete.

Table 5 Theoretical and experimental results of deep beams

Beam	Vu (kN)			$\frac{Vu(\text{Exp})}{Vu(\text{Theo})}$
	Exp	Theo [18]	Theo [17]	[17, 18]
DBCND30	350	328	–	1.06
DBHND30	250	210.5	–	1.18
DBCND60	470	451	–	1.04
DBHND60	440	404	–	1.09
DBCTD30	240	–	227	1.05
DBHTD30	210	–	182	1.15
DBCTD60	460	–	407	1.13
DBHTD60	270	–	223.5	1.20
DBCMD30	260	–	187.5	1.38
DBHMD30	220	–	212	1.03
DBCMD60	400	–	365	1.09
DBHMD60	310	–	292.5	1.05
DBCBD30	340	–	300	1.13
DBHBD30	270	–	255.5	1.05
DBCBD60	520	–	450	1.15
DBHBD60	400	–	359	1.11

4.1 Load Versus Deflection Response

In the case of conventional beams, the yielding of reinforcement leads to a larger increase in deflection with little change in load, whereas hybrid FRP-reinforced beams show no yielding of reinforcements and the deflection continues to increase with the increase in load due to lower elastic modulus, thereby exhibiting some ductility despite the brittle nature of hybrid FRP reinforcements. Hybrid FRP reinforcements are elastic and brittle with no yield point. The linear elastic behaviour is considered at all stress levels. Load–deflection response under static loading shows a greater reduction in stiffness in the case of hybrid FRP-reinforced beams than the conventional beams (Fig. 4).

The concrete surface strains are observed through demec gauges. Nine sets of demec pellets are placed at centre across the depth below the load point, and another three sets of demec pellets are also placed along the diagonal load path. The demec gauge readings are measured at every load increment. The strain distributions across the depth and along load path are then captured for various beam parameters and are presented in the form of graphs. Two sets of graphs are presented, viz., one at the first crack stage across the depth and strut path and another set corresponds to ultimate stage across the depth and strut path. The strain distributions for various beam parameters are presented in the form of graphs (Fig. 5).
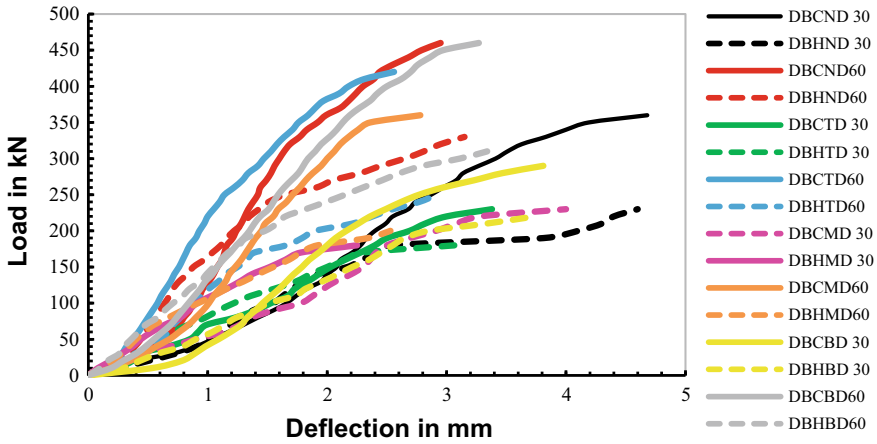
Fig. 4 Load versus deflection curve for tested deep beams

(a) At first crack   (b) At ultimate state
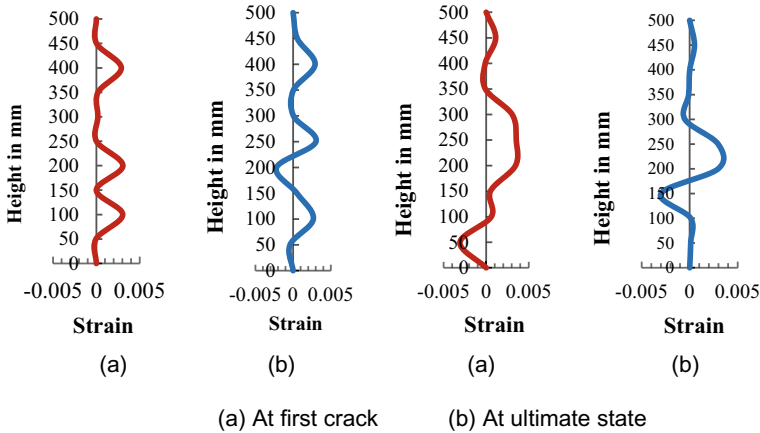
Fig. 5 Surface concrete strains (DBCND30 and DBHND30)

The Euler–Bernoulli plane section hypothesis cannot be used since the number of neutral axis is more than one as load reaches ultimate stage. Deep beam shows predominant compression load along the strut path. The two-dimensional state of stress and their strain distributions are nonlinear. It is observed that nearly 30–60% strains across the depth of deep beam at mid-span are under tension. The strain distributions for all parametric beams are observed and few are shown in Fig. 5. The maximum strain measured experimentally at mid-span and along the compression strut is presented in Table 6.

The residual strains are at mid-span and along the strut path for hybrid specimens than the conventional specimens. Hybrid specimens show the increased deflections,

Table 6 Theoretical and experimental results of deep beams

No.	Designation of beams	Strain at the mid-span	Strain along the strut line
1	DBCND30	0.00335	0.00059
2	DBHND30	0.00305	0.00290
3	DBCND60	0.00297	0.00292
4	DBHND60	0.00307	0.00285
5	DBCTD30	0.00302	0.00057
6	DBHTD30	0.00303	0.00292
7	DBCTD60	0.00300	0.00296
8	DBHTD60	0.00294	0.00144
9	DBCMD30	0.00304	0.00296
10	DBHMD30	0.00232	0.00058
11	DBCMD60	0.00294	0.00304
12	DBHMD60	0.00291	0.00300
13	DBCBD30	0.00312	0.00288
14	DBHBD30	0.00322	0.00196
15	DBCBD60	0.00290	0.00197
16	DBHBD60	0.00284	0.00155

larger crack widths, linear strain curve at all stress levels with no definite yielding. Design of such hybrid FRP reinforced concrete beams requires the serviceability design consideration rather than strength.

5 Conclusion

The specimens which is reinforced internally with conventional reinforcements, have shown higher strength than that of hybrid reinforced specimens. It is primarily due to the fact that hybrid FRP reinforcements reach their ultimate tensile strength without exhibiting strain hardening of material. Unlike steel, the tensile strength of hybrid FRP reinforcements show milder slope in the strain hardening region. The specimens inferably show the ultimate deflection at the mid-span, lower than that of specimens with hybrid reinforced. This is primarily due to the fact that the modulus of elasticity of hybrid FRP reinforcements is approximately 25–30% that of steel. The concrete surface strains are observed through demec gauges. The strain distributions for various beam parameters are observed. The Euler–Bernoulli plane section hypothesis cannot be used since the number of neutral axis is more than one as load reaches ultimate stage. Deep beam shows predominant compression load along the strut path. The two-dimensional state of stress and their strain distributions are nonlinear. It is observed that nearly 30–60% strains across the depth of deep beam

at mid-span are under tension. The maximum strain is measured experimentally at mid-span and along the compression strut.

From the experimental, it is seen that the effect of the concrete strength on the deflection and crack spacing is not much dependent. The crack spacing and deflections are much dependent on the type of reinforcements. Hybrid specimens show a good bond performance in terms of deflections and spacing of crack. Hybrid specimens experience more number of cracks, larger crack spacing and higher deflections than conventionally reinforced beams. The existing theoretical load based on Kong and Sharp model for various parametrics of deep beams with and without web openings is utilized for hybrid FRP reinforced concrete deep beams. The predicted results using the proposed equations show good agreement with experimental results. The predicted equations for steel/hybrid FRP-reinforced deep beams with and without web openings show a closer and almost similar range when compared to the experimental data.

References

1. ACI 440.1R-01 (2001) Guide for the design and construction of concrete reinforced with FRP bars. ACI Committee 440
2. ACI 440.XR (2007) Report on fiber-reinforced polymer (FRP) reinforcement of concrete. American Concrete Institute
3. Zhang N, Tan KH (2007) Direct strut-and-tie model for single span and continuous deep. Eng Struct 29:2987–3001
4. Jian L, Mihaylov BL (2016) A comparative study of models for shear strength of reinforced concrete deep beams. Eng Struct (41):81–89
5. Mohamed AR, Shoukry MS, Saeed JM (2014) Prediction of the behavior of reinforced concrete deep beams with web openings using the finite element method. Alexandria Eng J 53(2):329–339
6. Campione G, Minafo G (2012) Behaviour of concrete deep beams with openings and low shear span-to-depth ratio. Eng Struct 41:294–306
7. Yang EH, Chung H (2006) The influence of web openings on the structural behavior of reinforced high-strength concrete deep beams. Eng Struct 1825–1834
8. IS 456: 2000, Indian standard plain and reinforced concrete. Bureau of Indian Standards, New Delhi
9. Dae-JK, Junbok L, Young HL (2014) Effectiveness factor of strut-and-tie model for concrete deep beams reinforced with FRP bars. Composites: part B (56):117–125
10. Saravanan J, Kumaran G (2012) Strut and tie model for the analysis of RC beam-column joints reinforced with non-metallic reinforcements. J Struct Eng, SERC, India, 2012–2029
11. Shanmugam NE, Swaddiwudhipong S (1988) Strength of fibre reinforced concrete beams containing openings. Int J Cement Compos Lightweight Concr 10(1):53–60
12. Saleh HA (1998) Flexural behaviour of concrete beams reinforced with GFRP bars. Cement Concr Compos 20:1–11

13. El Maaddawy T, Sherif S (2009) FRP composites for shear strengthening of reinforced concrete deep beams with openings. Compos Struct 89:60–69
14. Yang KH, Chung HS, Lee ET, Eun HC (2003) Shear characteristics of high-strength concrete deep beams without shear reinforcements. Eng Struct (25):1343–1352
15. Sachan AK, Kameswara Rao CVS (1990) Behaviour of fibre reinforced concrete deep beams. Cement Concr Compos 12:211–218
16. Mohammadhassani M, Jumaat MZ, Ashour A (2011) Failure modes and serviceability of high strength self-compacting concrete deep beams. Eng Fail Anal 18:2272–2281
17. Kong FK (1990) Reinforced concrete deep beams. Van Nostrand Reinhold (3rd edn), New York
18. Kong FK, Sharp GR (1973) Shear strength of lightweight reinforced concrete deep beams with web openings. Struct Eng 51(8):267–275
19. Kong FK, Sharp GR (1977) Structural idealization for deep beams with web openings. Magaz Concr Res 29(99):81–91
20. Kim HS, Lee MS, Shin YS (2011) Structural behavior of RC deep beams under combined axial and bending force. College of Engineering, Ewha Womens Univeristy, South korea
21. Suzan A, Mustafa A, Hassan HA (2018) Behavior of concrete beams reinforced with hybrid steel and FRP composites. HBRC J (14):300–308

Progressive Collapse Analysis of Reinforced Concrete Asymmetrical Vertical Frames

M. Prakash, K. S. Satyanarayanan, and V. Thamilarasu

Abstract This paper presents the correlation behaviour of a two-dimensional, two-bay five-storey vertical asymmetrical prototype building frame under a corner and middle column removal at the ground floor level using finite element software. This study analysed four different asymmetrical configurations (i.e. Configuration-I, Configuration-II, Configuration-III, and Configuration-IV), where each case is examined under three different load cases. The demand capacity ratio (DCR) of axial force, bending moment and shear force and deflection were studied. The study shows that the maximum negative shear force DCR of 6.55 at Configuration-IV asymmetrical bare frame with wall load under the corner column is more prone to progressive collapse. It is also observed that the less vertical deflection and DCR for column and beam are within the permissible limits in infilled frame with cement mortar (IFCM).

Keywords Progressive collapse · Asymmetrical · Demand capacity ratio · Deflection · Axial force · Bending moment and shear force

1 Introduction

Progressive collapse is a phenomenon that is widespread propagation of structural member failures in which the resulting damage is disproportionate to the actual case. When there is a failure in the primary load-bearing fundamental element in the structure, it causes overloading to the adjacent members. The local failure leads to global failure of the structure, and this partial collapse is known as progressive collapse. In USA, the General Service Administration (GSA) [1] and Department of Defence [2] had furnished detailed information and guidelines regarding the methodologies to resist the progressive collapse of the buildings. Progressive failure occurs due to fires such as sudden impact, vehicle collision, bomb explosion, and gas. For instance, unprecedented temperature, effects, tremor, blasts, and impact. Few examples of the progressive collapse are Ronan Point Apartment, World Trade Centre, Sampoong

M. Prakash (✉) · K. S. Satyanarayanan · V. Thamilarasu
Department of Civil Engineering, College of Engineering and Technology, SRM Institute of Science and Technology, SRM Nagar, Kattankulathur 603203, Tamilnadu, India
e-mail: prakashm17@gmail.com

155

Tower, Alfred Murrah Building, etc. Fu [3] studied two, three-dimensional, 20 storeys RC building to perform the nonlinear dynamic progressive collapse analysis by ABAQUS. Two different types of buildings were analysed, one building provided with RC shear wall and other buildings with structural cross bracings, and five different column removal cases on both ground and 14th floor. The models incorporate both nonlinear material and nonlinear geometric properties. It was found that all the structural members at the possible column removal level should be designed at least twice the static axial force obtained and also, at the beam to column connection at the column removal level should be designed to have at least twice the static axial effect connecting the (1.0DL + 0.25LL) load combination. The maximum vertical displacement was observed at higher column removal than a column removal at ground level. Sun et al. [4] have investigated the progressive collapse of the two-dimensional brace and unbraced steel frame under fire. The combined static and dynamic procedure was developed in the study. It also includes the influence of load ratio, beam section and bracing systems. The results show that for unbraced frame, the different loading ratio and beam section could generate different collapse mechanisms. The lower loading ratio and more significant beam section could give higher failure temperature in which the global collapse of the frame happened. However, the higher loading ratio and smaller beam section can more quickly generate localized destruction. The bracing system helps preventing the frame from progressive failure. Sezen and Song [5] carried out an analytical and experimental study on progressive collapse of the existing three-storey steel frame structure under four-column removal cases and analysed 2D and 3D models by using SAP 2000. Most of the structural members exceeded the DCR limits once the second column is removed. However, the building did not experience a collapse during the field test. When compared to 2D DCR results, the lower DCR was observed in 3D models. Li et al. [6] have carried out the analytical and experimental investigation that was conducted into the progressive collapse of a steel frame under middle column removal. The progressive collapse test was conducted on three two-storey four-bay 2D frames. The finite element model result shows good agreement with the experimental results, and they found a dynamic amplification factor which was found to be in a range of 1.10–1.34. Bae et al. [7] have carried out a progressive collapse analysis of a prototype army barracks, a three-storey cold-formed steel frame structure. Linear static analysis is carried out using SAP 2000. Two-column removal scenarios were taken exterior l and corner stud column removal. The result shows the use of a built-up section. The structure is safe under progressive collapse, both exterior and corner column removal. Kim et al. [8] investigated the progressive collapse analysis for steel moment frame; the present study has taken a three-storey building, six-storey building, and a fifteen-storey building under the corner and middle column removal. Linear static, nonlinear static, linear dynamic, and nonlinear dynamic analyses were carried out. The frame was designed for lateral as well as gravity load turned out to be less vulnerable for progressive collapse. When compared to the corner column, the middle column structure shows less vulnerable. Marjanishvili and Agnew [9] studied three-dimensional G + 8 storey RC building under middle column removal using SAP [10]. This study was carried out to compare different types of analysis, linear static, nonlinear static, and linear

a) Beam Element (b) Plane Stress Element
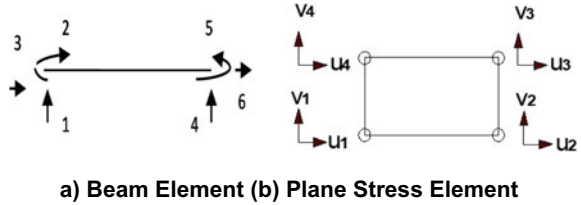
dynamic and nonlinear dynamic analysis procedures for the progressive collapse of RC structure. The maximum vertical displacement results show in nonlinear dynamic analysis compared to the other three types of analysis. The primary goal of this paper is carried out the two-dimensional asymmetrical (vertical irregularity) frame, under three different loading conditions (i) bare frame with or without wall load (ii) bare frame with wall load and (iii) infilled frame with cement mortar (IFCM) under a corner and middle column removal at the ground floor level.

2 Model Description

Different aspects are used in the mathematical model to represent various structural components like a beam, column, and infill. Frame members (beam and column) are modelled as line elements, while infill modelled as plane stress area elements. The frame members are shaped as beam elements with three degrees of freedom per node, as shown in Fig. 1a, and the infill is modelled as four-noded plane stress elements, as shown in Fig. 1b with two degrees of freedom per node and with similar masonry properties. The prototype structure of the analysis model is a two-bay five-storey building, as shown in Fig. 2, where the bay width is 2.5 m, and storey heights are 3 m. The structure is designed with dead and live loads of 3 kN/m^2, floor finish of 1 kN/m^2, wall load of 14.7 kN/m^2, and slab load of 2.5 kN/m^2. Table 1 shows the dimensions and reinforcement details for beams and columns. The entire frame is designed as per IS 456:2000 [11]. M30 grade concrete and Fe415 steel are used. Brick masonry of 1:6 is used. The beams and columns are designed based on IS 456:2000. The cross-sectional area and reinforcement for beams are taken the same in all cases of the 2D bare frame; the sizes of the main bar and stirrups are given in Table 1. In this present study, linear static analysis is carried out using an SAP 2000 version 20.

3 Linear Static Analysis

According to GSA rules, the DCR is calculated using the equation given below:

Configuration - I   Configuration -II   Configuration -III   Configuration - IV

(a) Bare Frame without wall load

Configuration - I   Configuration -II   Configuration -III   Configuration - IV

(b) Bare Frame with wall load

Configuration - I   Configuration -II   Configuration -III   Configuration - IV

(c) Infilled Frame with cement Mortar (IFCM)
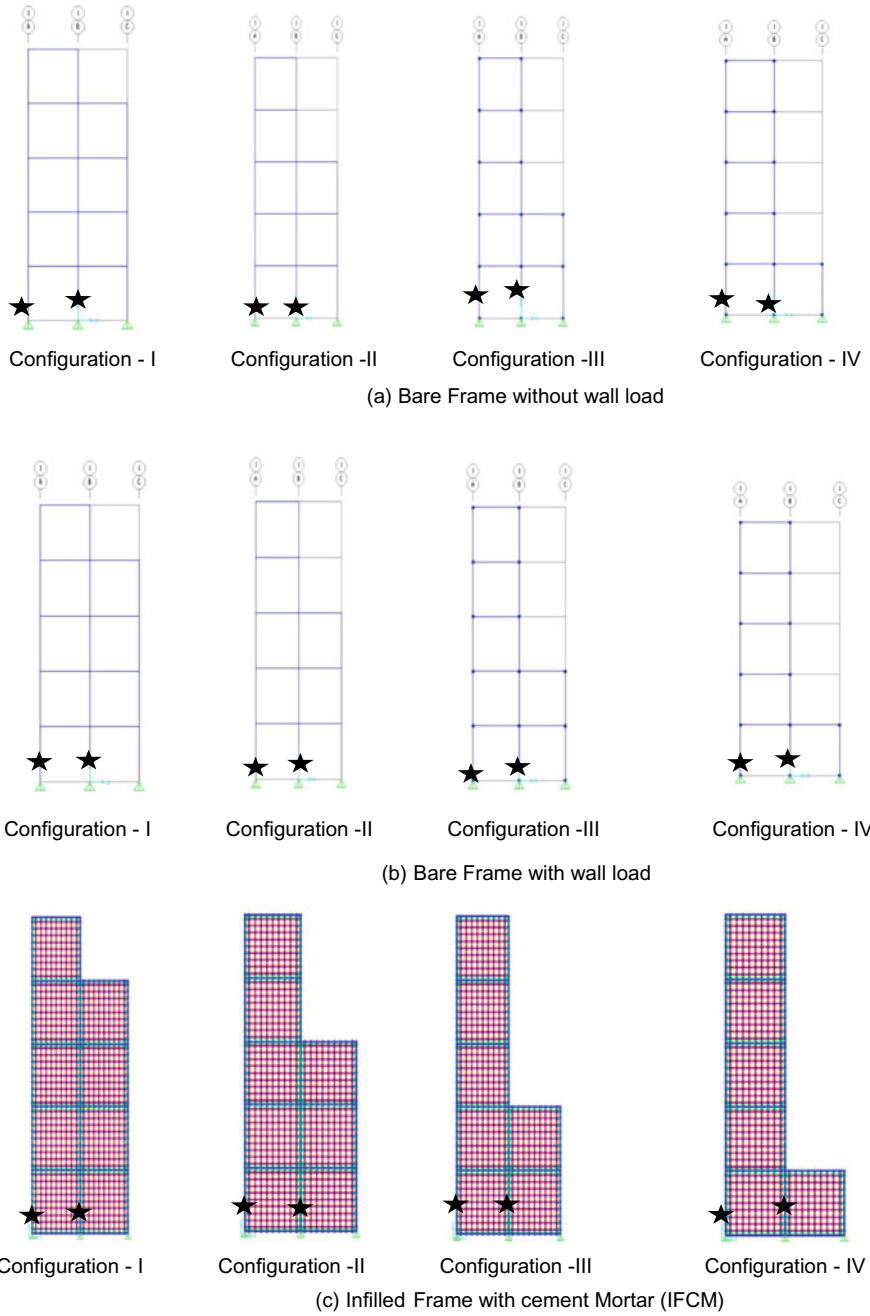
Fig. 2 Two-bay five-storey asymmetric vertical configuration for three different load cases (corner and middle column removal)

Table 1 Dimensions and reinforcement provided for structural elements

Member	Dimensions (mm)	Clear cover (mm)	Size of main steel bars	Size of stirrups
Beam	230 × 300	25	4 nos. 16 mm	8 mm @ 210 mm c/c
Column	400 × 230	40	4 nos. 16 mm	8 mm @ 190 mm c/c

$$\mathrm{DCR} = \frac{Q_{\mathrm{UD}}}{Q_{\mathrm{CE}}} \tag{1}$$

where

Q_{UD} = Acting force obtained in member (axial force, bending moment, shear force) (SAP 2000 Values)

Q_{CE} = Expected ultimate capacity of the structural member (axial force, bending moment, shear force) or theoretical calculated axial, moment and shear values

The permissible demand capacity ratio values are:

DCR less than equal to 2.0 for symmetrical structural geometry

DCR less than equal to 1.5 for asymmetrical structural geometry

4 Analysis of Vertical Deflection of Two-Bay Five-Storey Two-Dimensional Frame

In this study, four different configurations of each beam removed as shown in Fig. 2a through 2c. All the configuration analysed with three different load cases like a bare frame without wall load, bare frame with wall load and IFCM, and the corner of each case, and the middle column removed. The results of the two-dimensional asymmetrical vertical configuration study are shown for (i) vertical displacement (ii) maximum DCR values of various forces (axial force, bending moment and shear force)

4.1 Analysis of Vertical Displacement of Frames

The results of vertical displacement for bare frame with wall load under corner and middle column removal are presented in Table 2. The maximum vertical displacement is observed at CF-IV 363.48 mm at the fifth floor level under corner column removal which is shown in Fig. 3. From the above values, the maximum vertical displacement is increased by (363.48/1.34) = 271 times. Similarly, the frames CF-I, CF-II, and CF-III increased by 29, 37, and 107 times when compared to before column removal. IFCM shows the less displacement as compared to all three cases. The frame displacement, like both lateral and vertical displacement, is determined

Table 2 Configuration-IV vertical displacement for bare frame with wall load under corner and middle column removal

No of Storeys	Configuration-IV displacement before corner column removal (mm)	Configuration-IV displacement after corner column removal (mm)	Configuration-IV displacement before middle column removal (mm)	Configuration-IV displacement after middle column removal (mm)
1	0.46	361.99	0.52	85.73
2	0.82	362.51	0.89	86.34
3	1.09	362.99	1.16	86.85
4	1.26	363.33	1.33	87.19
5	1.34	363.48	1.40	87.34
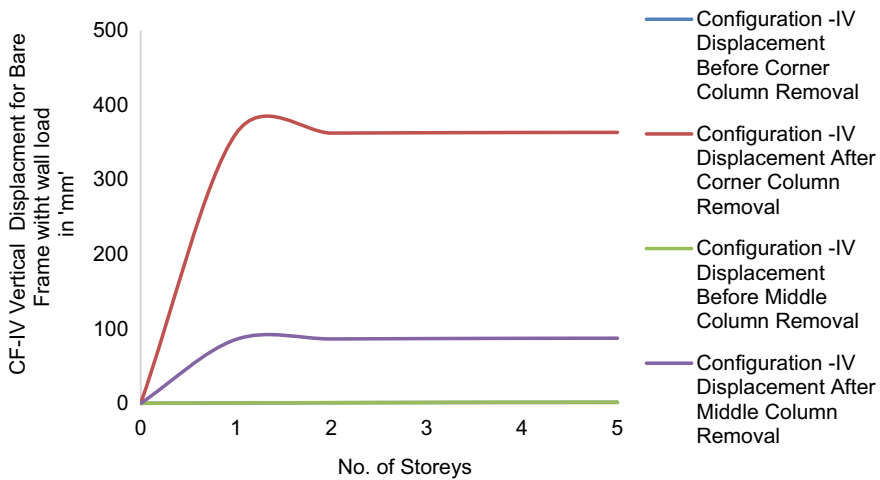
Fig. 3 Vertical displacement for bare frame with wall load under four different configurations

when the frame moved towards to the column removal direction. The maximum value is observed in the top storey level of the affected bay.

4.2 Results for Internal Forces in Two-Dimensional Asymmetrical Frame

The internal forces in the frame, such as maximum DCR value for various effects, are given in this section.

Axial Force DCR: The maximum axial DCR value for two-dimensional asymmetrical RC bare frame with wall load under corner and middle column removal

is shown in Table 3. The maximum value of axial force DCR observed at CF-I bare frame with wall load under corner column removal is 2.01 and [(2663.05-1169.29)/2663.05] X100 = 56%. Similarly, the increase in the axial force of CF-II, CF-III, and CF-IV is 58%, 60%, and 62%, respectively. The results show that the bare frame with wall load observed an increase in axial force after corner column removal by (12663.05/1169.29) = 2.3 times. Similarly, the increase in axial force CF-II, CF-III, and CF-IV is 2.4, 2.5, and 2.6 times, respectively. Figure 4 shows the maximum axial force DCR values for bare frame with wall load under corner and middle column removal. Based on the GSA guidelines, the bare frame with wall load under corner column removal exceed the permissible limit of 1.5. The bare frame without wall load and infilled frames, both corner and middle columns, are within the allowable limit of 1.5.

Bending Moment DCR: The maximum support bending moment DCR for two-dimensional asymmetrical RC bare frame with wall load under corner and middle column removal is shown in Table 4. The maximum value of support bending moment DCR observed at CF-IV is 5.89 and [(1391.97 − 24.46)/1391.97] X 100 = 81%. Similarly, in CF-I, CF-II, and CF-III, the span bending moment is increased by 78, 79, and 80%. It indicates that the bare frame with wall load increased in support bending moment after corner column removal by (1391.97/24.46) = 57 times. Similarly, in CF-I, CF-II, and CF-III, the increase in span bending moment is 15, 21, and 31 times, respectively. Figure 5. shows the maximum support bending moment DCR for bare frame with wall load under corner and middle column removal. When compared to bare frame without wall load and infilled frame, both the values of span and support bending moment DCR are lesser values than bare frame with wall load.

Shear Force (Positive and Negative): The maximum negative shear force DCR for bare frame with wall load under the corner and middle column removal is shown in Table 5. The maximum negative shear force DCR values for both corner and middle column are 6.55 and 3.24. From Table 5, the bare frame with wall load under corner column shows the maximum amount of negative shear force DCR observed at CF-IV is 6.55 and [(833.99 − 50.03)/833.99] × 100 = 94% and same CF-I, CF-II, and CF-III the negative shear force is increased by 84, 87, and 90%. It shows that the bare frame with wall load negative shear force is increased after corner column removal by (833.99/50.03) = 17 times of before column removal. Similarly, it was observed that CF-I, CF-II, and CF-III had an increase in negative shear force by 6.2, 7.8, and 10 times, respectively. Figure 6 shows the maximum support DCR for bare frame with wall load. When compared to bare frame without wall load DCR for infilled frame DCR values are lesser than the bare frame with wall load.

5   Conclusion

The following conclusions can be made from the outcome of the study:

Table 3 Maximum axial DCR values for bare frame with wall load

Description	Axial force bare frame with wall load in (kN) (Q_{UD})				Ult. capacity (Q_{CE}) (kN)	Axial force DCR for bare frame with wall load, DCR = (Q_{UD}/Q_{CE})			
	CF-I	CF-II	CF-III	CF-IV		CF-I	CF-II	CF-III	CF-IV
Before corner column removal	1169.29	1085.26	997.55	910.63	1328	0.88	0.82	0.75	0.69
After corner column removal	2663.05	2568.21	2473.3	2378.5	1328	2.01	1.93	1.86	1.79
Before middle column removal	813.11	807.70	804.13	800.16	1328	0.61	0.61	0.61	0.60
After middle column removal	1364.64	1317.21	1269.7	1222.3	1328	1.03	1.0	0.96	0.92
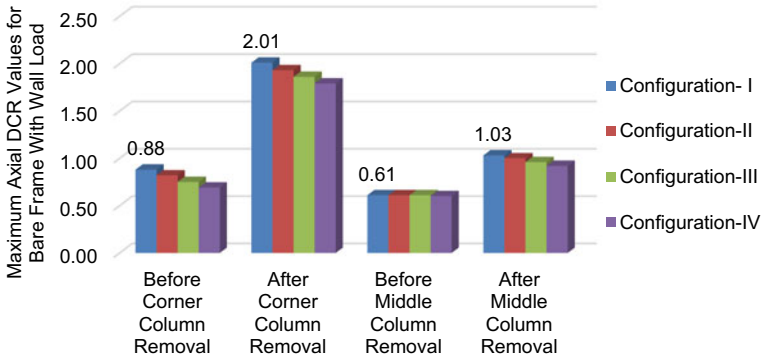
Fig. 4 Maximum axial force DCR for bare frame with wall load

- From the analytical result, the bare frame with wall load, the maximum vertical deflection is observed in Configuration—IV with a value of 363.48 mm at corner column removal.
- The maximum axial DCR of bare frame with wall load observed in Configuration—I under corner column removal is 2.01. Based on GSA guidelines, the Configurations—I, II, III, and IV with bare frame with wall load under the corner column show that all Configurations—I, II, III, and IV exceed the permissible limit of 1.5. The bare frame without wall load and infilled frames are within the allowable limits.
- The maximum span and support bending moment DCR observed at bare frame with wall load found in Configuration—IV under corner column removal is 3.5 and 5.89, respectively. In bare frame without wall load, the span moment under the corner and middle column removal and in support bending moment DCR corner column exceeds the permissible limits of 1.5. However, in span and support bending moment, the infilled frames are within the allowable limits.
- The maximum positive and negative shear force DCR observed at bare frame with wall load found at Configuration—IV under corner column removal is 5.18 and 6.55. In infilled frame, both positive and negative shear forces are within the permissible limit of 1.5.

Table 4 Maximum support bending moment DCR values for bare frame with wall load

Description	Maximum support bending moment values for bare frame with wall load in kN m (Q_{UD})				Ult. capacity (Q_{CE}) (kN m)	Support bending moment DCR = (Q_{UD}/Q_{CE})			
	CF-I	CF-II	CF-III	CF-IV		CF-I	CF-II	CF-III	CF-IV
Before corner column removal	23.34	21.19	21.19	24.46	236	0.10	0.09	0.09	0.10
After corner column removal	350.96	448.41	664.16	1391.97	236	1.49	1.90	2.81	5.89
Before middle column removal	26.10	25.19	21.97	16.66	236	0.11	0.11	0.09	0.07
After middle column removal	256.59	311.02	388.82	541.79	236	1.09	1.32	1.65	2.30
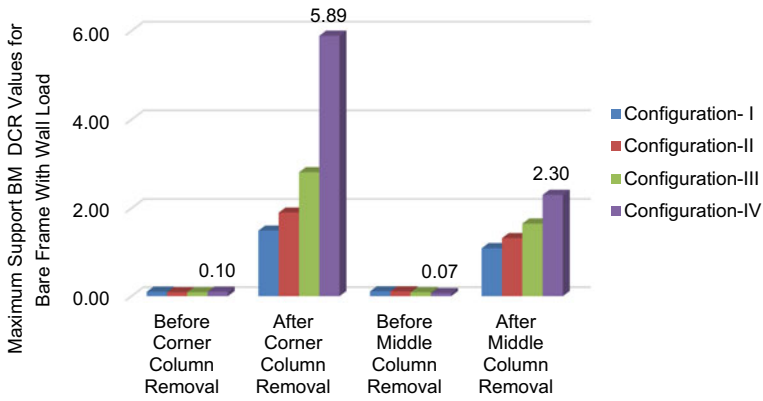
Fig. 5 Maximum support bending moment DCR for bare frame with wall load
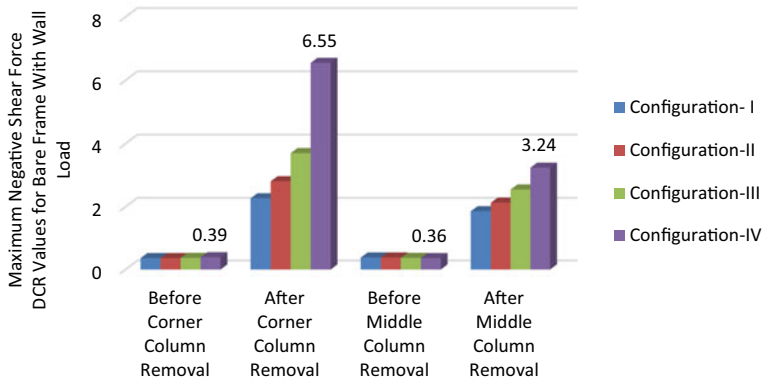
Fig. 6 Maximum negative shear force DCR for bare frame with wall load

Table 5 Maximum negative shear force DCR values for bare frame with wall load

Description	Max. negative shear force values for bare frame with wall load in (kN) (Q_{UD})				Ult. capacity (Q_{CE}) (kN)	Negative shear force DCR = (Q_{UD}/Q_{CE})			
	CF-I	CF-II	CF-III	CF-IV		CF-I	CF-II	CF-III	CF-IV
Before corner column removal	46.31	46.09	47.41	50.03	127.43	0.36	0.36	0.37	0.39
After corner column removal	288.89	358.15	471.49	833.99	127.43	2.27	2.81	3.70	6.55
Before middle column removal	48.54	49.03	47.43	45.44	127.43	0.38	0.38	0.37	0.36
After middle column removal	237.05	270.99	324.39	413.48	127.43	1.86	2.13	2.55	3.24

References

1. GSA, General Service Administration (2013) Alternate path analysis and design guidelines for progressive collapse resistance, 1–143. Washington DC, USA
2. Department of Defence (2005) Design of building to resist progressive collapse, Washington DC, USA
3. Fu F (2009) Progressive collapse analysis of high-rise building with 3-D finite element modelling method. J Constr Steel Res 65:269–278
4. Sun R, Huang Z, Burgess IW (2012) Progressive collapse analysis of steel structures under fire conditions. Eng Struct 34:400–413
5. Song BI, Sezen H (2013) Experimental and analytical progressive collapse assessment of a steel frame building. Eng Struct 56:664–672
6. Li L-L, Li G-Q, Jiang B, Lu Y (2018) Analysis of robustness of steel frames against progressive collapse. J Constr Steel Res 143:264–278
7. Sang-Wook Bae, LaBoube Roger A, Belarbi Abdeldjelil, Ayoub Ashraf (2008) Progressive collapse of cold-formed steel frame structures. Thin-Walled Struct 46:706–719
8. Taewan Kim, Kim JinKoo, Park Junhee (2009) Investigation of progressive collapse capability of steel moment frames using pushdown analysis. J Perform Constr Facil 23:327–335
9. Marjanishvili S, Agnew E (2006) Comparison of various procedures for progressive collapse analysis. J Perform Constr Facil 20:365–374
10. SAP, Integrated software for structural analysis and design, computers and structures, 2000 Berkeley, California
11. IS 456: 2000 Plain and reinforcement concrete code of practice. Bureau of Indian Standards, New Delhi

Structural Behaviour of Reinforced Geopolymer Concrete Frame Under Lateral Loading

Dhavamani Doss Sakthidoss and Thirugnanasambandam Senniappan

Abstract The main intent of this research is to replace the conventional concrete frame with geopolymer concrete frame under lateral loading condition and to study the structural parameters such as ductility factor, energy absorption capacity, load carrying capacity and stiffness. The activator solution is used in the preparation of geopolymer concrete. The dimension of prototype frames components include beams and columns are 230 mm × 350 mm and 300 × 300 mm, respectively. The characteristic strength of geopolymer concrete is 40.45 N/mm^2 and the elasticity modulus of geopolymer concrete is 3.35×10^4 N/mm^2. The size of beams and columns of the ¼ reduced scaled model frame i.e. 170 mm × 120 mm and 200 mm × 120 mm, respectively and the length and height of the frame are 1400 mm and 2340 mm, respectively. The frame was tested under push and pull lateral loading condition. The experimental results are compared with analytical results using finite element analysis. The stiffness, ductility factor and energy absorption capacity of reinforced geopolymer concrete frame for the first storey are 2.61 and 2.01 kN/mm; 6.23 and 5.97; 1542.82 and 1291.80 kN mm respectively and for the second storey, the stiffness, ductility factor and energy absorption capacity values are 1.47 and 1.41 kN/mm; 6.724 and 6.29; 2732.5 and 1837.44 kN mm, respectively. The reinforced geopolymer concrete frame, thus, exhibits better performance against horizontal loading circumstances, which makes geopolymer concrete suitable for construction sectors.

Keywords Alkaline solution · Ductility factor · Energy absorption capacity · Geopolymer concrete frame · Structural · Behaviour · Lateral displacements

D. D. Sakthidoss (✉) · T. Senniappan
Department of Civil and Structural Engineering, Annamalai University, Chidambaram, India
e-mail: dhavamanidossphd@gmail.com

169

1 Introduction

The most common three major problems, in the construction industry, are the increased probability of lateral loads on the structures, the availability of source materials for constructions and the global warming of the earth due to pollution. Firstly, due to the increase of urbanisation throughout the world and for safety purposes, the structural engineers preferred to go for the construction of framed structures for their efficiency in strength and stability from structural point of view. Secondly, the use of concrete is used more than any other materials in the world next to water [1]. For the production of concrete, it requires a lot of resource materials such as cement, sand and blue metals. Therefore, there is a need for finding alternative materials for these resource materials. Thirdly, global warming is a major problem throughout the world today. This is due to high emission of greenhouse gases into the atmosphere. The main concern of the entire planet earth is eagerly turned towards the control of pollution. This initiative is mainly started to control the rate of increase of global warming day by day. At current scenario, the whole nations are in a critical situation to control the global warming. The temperature today is not the same as before a decade. The rate of temperature keeps on increasing rapidly. To control this, usage of greenhouse gas emitting materials need to be reduced. Among the greenhouse gases, carbon dioxide (CO_2) is more vulnerable to the atmosphere since it could increase the rate of global warming. The construction industry, especially cement industry plays a significant role by producing 7% of total CO_2 gas emission into the atmosphere [2]. It is concluded that the rate of CO_2 gas emission by the cement industry will further increase in future, Malhotra [3]. Cement is a binder material, which is considered as the backbone of construction industry. Therefore, the usage of cement will increase significantly due to vast development of infrastructure around the globe. As a result, the emission of CO_2 gas will be increase. The cement causes the environment impact by utilising the natural resource materials such as lime and clay for the production process with a huge amount of energy. High efficient of energy is required to burn the lime at high temperature to get cement. On the other hand, water is highly used for curing of concrete. The availability of the natural raw materials for the construction use is also a concern since the natural raw materials are becoming shortage. Due to the innovations in the field of construction industry, the engineers and the architects are keen to construct different types of strong and durable structures. The usage of reinforced concrete framed structures is widely adopted for construction of multi-storey buildings. Concrete is emerged as an unavoidable material in the construction, which will lead to the increase of the above said problems regarding global warming. To find a remedy for these problems, a thought of replacing cement by other supplementary materials are discussed by scientist and researchers. The thought is developed and several approaches have been taken to use the industrial waste by-product materials as replacement for cement as a binder material [4, 5]. This study mainly deals on finding a proper alternative to reduce the above-mentioned problems. The cement is completely replaced by waste by-product material which is highly available in India and around the globe. A combination of two materials

are used in this study to replace the cement as a binder. The two materials used are fly ash and Ground Granulated Blast Furnace slag (GGBS). In India, the fly ash is dumped in abundant quantity in the land and created land pollution. Fly ash is finer than the cement particle. Therefore, it can be easily spread through the medium of air. It is very harmful and will cause health disorder if it is not disposed safely. This fly ash can be utilised in the production of concrete as a partial replacement of cement. GGBS can be also use as binder, since the strength is a main parameter which will affect the concrete [6]. Fly ash and GGBS are mixed to form a binder material which will need an activator solution to initiate and enhance the binding of concrete. The production of concrete using fly ash and GGBS is referred as geopolymer concrete.

Geopolymer concrete is made by using materials rich in silica and aluminium. The materials such as kaolin, metakaolin, fly ash, rice husk ash, dolomite are used for making geopolymer concrete. Geopolymer was first invented by a French scientist Joseph Davidovits in 1978 [7, 8]. Geopolymer is a green and sustainable material for making concrete, sometimes it is known as alkali-activated binder where, the hazardous harmful materials are turned into strong and durable construction material [9–13]. Geopolymers materials are used in bricks, sealents, ceramics, fire protection, foundry equipment', heat composite fibres and etc. Hardjito and Rangan [14]. The alkaline solution used in making geopolymer concrete is combination of sodium/potassium hydroxide solution and sodium/potassium silicate solution. Sodium based alkaline solution is widely used due to its easy availability in Tamil Nadu. The chemistry behind the geopolymers are different from that of the cement chemistry. The hardening of cement occurs through hydration process but the hardening of geopolymer occurs through polycondensation of sodium oligo-(sialate-siloxo) into sodium poly-(sialate-siloxo). The polycondensation mechanism is three-dimensional polymerisation mechanism. The complete polymerisation process is shown in Eqs. 1 and 2.

$$
\begin{aligned}
&n(Si_2O_5, Al_2O_2) + 2nSiO_2 + 4nH_2O + NaOH \ \rightarrow Na^+ + n(OH)_3 - Si - O - Al^- - O - Si - (OH)_3 \\
&\text{(Si-Al Materials)} \qquad\qquad\qquad\qquad\qquad\qquad\qquad\qquad\qquad\qquad\quad |\\
&\qquad\qquad\qquad\qquad\qquad\qquad\qquad\qquad\qquad\qquad\qquad\qquad\quad (OH)_2 \\
&\qquad\qquad\qquad\qquad\qquad\qquad\qquad\qquad (Geopolymer\ Precursor) \rightarrow
\end{aligned}
\tag{1}
$$

$$
\begin{aligned}
&n(OH)_3 - Si - O - Al^- - O - Si - (OH)_3 + NaOH \rightarrow Na^+ \ -(-\overset{|}{Si} - O \ - \overset{|}{Al^-} - O - \overset{|}{Si} - O -) + 4nH_2O \\
&\qquad\qquad\ |\\
&\qquad\quad (OH)_2 \\
&\qquad\qquad\qquad\qquad\qquad\qquad\qquad\qquad\qquad\qquad (Geopolymer\ Backbone) \rightarrow
\end{aligned}
\tag{2}
$$
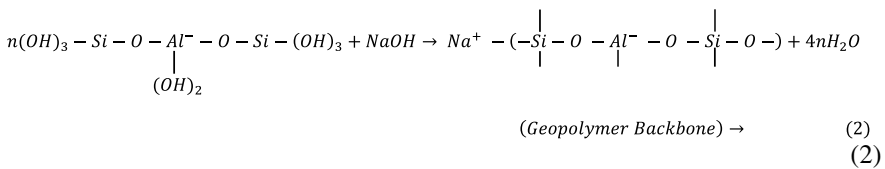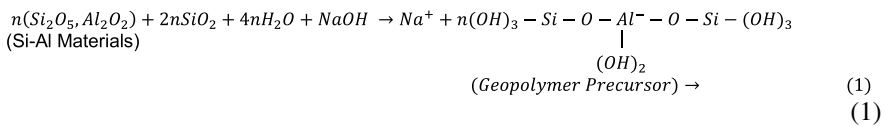
2 Materials and Proportions for Geopolymer Concrete

Geopolymer concrete process is similar to control concrete process except the binder and solution used for mixing of concrete. In geopolymer concrete, the fly ash and GGBS are the by-products obtained from thermal power plant and steel plant, respectively used as replacement for cement in a ratio of 50:50. Water was replaced by alkaline solution during the mixing of geopolymer concrete. The ratio of sodium silicate to sodium hydroxide is 2.5 and the ratio of alkaline solution to binder materials is chosen as 0.45. The concentration of the alkaline solution is 8 molarity. The strength of the geopolymer concrete is mainly influenced by the molar concentration of the solution. The mix proportion used for M30 geopolymer concrete was 1:2.11:3.37. River sand and blue metal were used as fine and coarse aggregates, respectively. The specific gravity of fly ash, GGBS, sand and coarse aggregate are 2.15, 2.65, 2.67 and 2.7, respectively. Poly Carboxylic Ether (PCE) based Super Plasticizer (SP) were used to enhanced the workability and setting time of geopolymer concrete. The percentage of SP used was 1.5%. In geopolymer concrete, the preparation of alkaline solution is an important factor. The alkaline solution should made 24 h prior to production of concrete. The sodium hydroxide pellets were dissolved in required water. For obtaining 1000 ml of sodium hydroxide solution, 320 g of sodium hydroxide pellets and 680 ml of water are required. Subsequently, the sodium silicate solution was added and both the solutions were mixed thoroughly. Geopolymer concrete cubes of 100 mm × 100 mm × 100 mm were used using steel moulds. The aggregates were well saturated before mixing. The binding materials and aggregates were dry mixed for 2–3 min. Then, the alkaline solution was poured into dry mix and finally SP with extra water is poured into the concrete. The concrete matrix was mixed for 3–5 min and the cube specimens and the frame specimens were cast. The workability of fresh geopolymer concrete was 110 mm after 30 min. The materials used for making geopolymer concrete are shown in Figs. 1 through 6. The workability of fresh geopolymer concrete is shown in Fig. 7. The casting process of reinforced

Fig. 1 Fly ash

Fig. 2 GGBS

Fig. 3 River sand

geopolymer frame is shown in Figs. 8 through 10 (Figs. 1, 2, 3, 4, 5, 6, 7, 8, 9 and 10).

3 Setup and Loading Pattern for Testing Reinforced Geopolymer Concrete Frame

A proper arrangement was made for testing the Reinforced Geopolymer Concrete Frame (RGPCF) under lateral loading condition. A foundation block was made to ensure the rigid connection for the frame. The frame and the foundation block were connected properly to avoid any base movement of frame due to the application of

Fig. 4 Blue metal

Fig. 5 Sodium hydroxide pellets

lateral load. The loading pattern applied to the frame was incremental type load. The two-storey single bay frame was subjected to lateral loads at the nodal points of the beam column joints. The horizontal load was applied using a 25 kN capacity jack. The jack was fixed horizontally to testing steel frames and arranged to apply lateral load for push and pull conditions. The incremental lateral loads of 15, 30, 45, 60, 75 and 90 kN for push direction and 12, 24, 36, 48, 60 and 72 kN for pull direction were applied. The corresponding displacement is measured using Linear Variation Differential Transducers (LVDT) [15, 16]. The LVDT is fixed on the beam column joint of both the storey. The least count for the LVDT is 0.01 mm. Figure 11 shows the Reinforced Geopolymer Concrete Frame (RGPCF) setup for testing. Figure 12 shows the testing of RGPCF under lateral loads. The RGPCF after testing is shown in Figs. 13 and 14. The LVDT measurement for displacements were recorded using a

Fig. 6 Sodium silicate solution
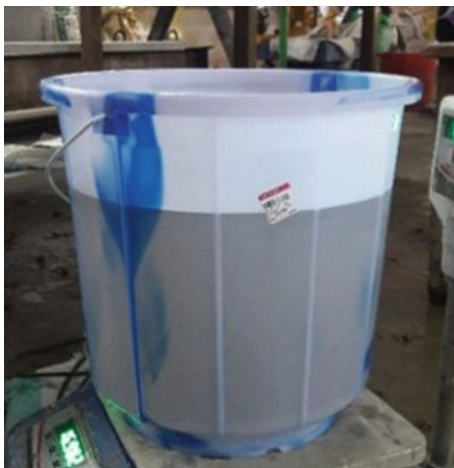
Fig. 7 Slump test

Fig. 8 Mould with reinforcement

Fig. 9 Preparation of frame

Fig. 10 Frame after demoulding the formwork

digital electrical strain indicator. When the RGPCF was subjected to lateral load, the displacement values corresponding to that particular load can be directly measured from the electrical strain indicator.

4 Analytical Modelling of Reinforced Geopolymer Concrete

The reinforced geopolymer frame was modelled using finite element method software, SAP 2000.v20. The dimensions of the beams and columns are 230 × 350 mm and 300 × 300 mm, respectively. Fixed support condition was chosen for the two-storey single bay bare frame. The material properties of geopolymer concrete (GPC) was used. The seventh day compressive strength of GPC cured under ambient curing
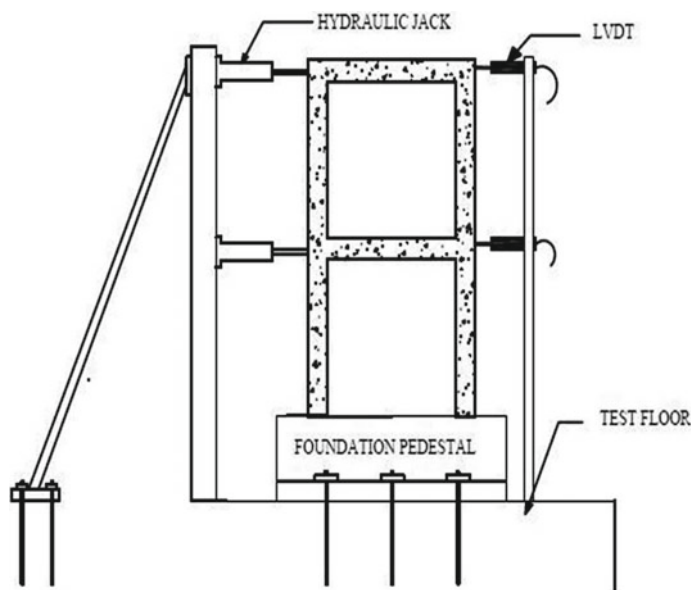
Fig. 11 Schematic testing arrangement for frame

Fig. 12 Loading arrangement for testing frame

Fig. 13 Frame after testing (push)

was 40.45 N/mm^2. The modulus of elasticity of geopolymer concrete was 3.35×10^4 N/mm^2. The poisson ratio was 0.17. The frame model was created using SAP 2000 and incremental loading pattern as experimental model was applied. The model was created by using the grid data option. By using edit grid option, the size and shape of model was created. Subsequently, the sectional and material properties of beam and column elements were applied using define option. Then load cases were given and the frame was analysed. The displacement values for the corresponding loads were found and tabulated in Table 1. Figures 15, 16, 17 and 18 indicate the application of load (both push and pull direction) and displacements of reinforced geopolymer concrete frame model in SAP 2000.

The reinforced geopolymer concrete frame analysis in SAP 2000 is carried out for determining the displacement against lateral incremental loads. Initially the frame is loaded with 15 kN and gradually loaded up to 90 kN for forward push loading. The frame model is loaded with 12 kN and gradually increased up to 72 kN for reverse pull loading. The load—displacement curve for the analytical frame are shown in Figs. 19, 20, 21 and 22.

Fig. 14 Frame after testing (pull)

Table 1 Load—deflection values for analytical model

No.	Load (kN)		Deflection (mm)			
	Forward push	Reverse pull	First storey		Second storey	
			Push	Pull	Push	Pull
1	0	0	0	0	0	0
2	15	12	5.355	−4.284	9.837	−7.878
3	30	24	10.710	−8.568	19.696	−15.757
4	45	36	16.064	−12.851	29.544	−23.635
5	60	48	21.419	−17.140	39.391	−31.513
6	75	60	26.774	−25.700	49.240	−47.27
7	90	72	32.129	−28.650	59.087	−53.24

5 Testing of Reinforced Geopolymer Concrete Frame

The reinforced geopolymer concrete frame was tested with proper arrangements for ensuring the rigid support conditions. Horizontal load was applied to the frame at beam column joint. The load was applied along the axis of beam column joint,

Fig. 15 Application of
lateral load on frame model
(push)
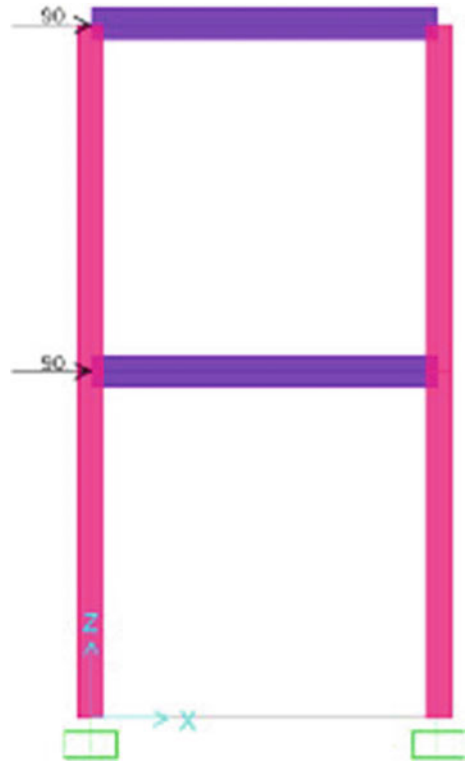
Jayaramappa [17]. Table 2 shows the load—displacement values of the reinforced
geopolymer concrete frames. The load—displacement curves for the experimental
frame are shown in Figs. 23, 24, 25 and 26.

6 Results and Discussions

From the experimental and analytical investigations, following results were obtained
and discussed. From the results, the structural behaviour of reinforced geopolymer
concrete such as stiffness, ductility factor and energy absorption capacity are deter-
mined. It was observed that there is no significance change in these parameters for
analytical and experimental model. The results are demonstrated in Figs. 27, 28, 29,
30, 31 and 32 which indicate the structural behaviour parameters. By comparing
the analytical and experimental results, the obtained experimental results are almost
in the same range. The experimental results show that the reinforced geopolymer
concrete frame performs well in stiffness, ductility and energy absorption capacity.
The slope of the load—deflection curve attributes the stiffness parameter. The area
under the load—deflection curve shows the energy absorption capacity of structure

Fig. 16 Application of
lateral load on frame model
(pull)
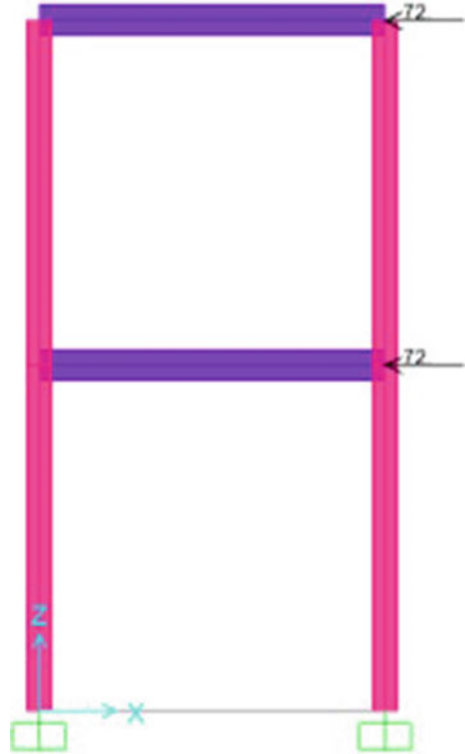
[18]. The ductility factor of the structure is calculated from the ratio of ultimate displacement to yield displacement (Figs. 27, 28, 29, 30, 31 and 32).

7   Conclusion

The load—deflection curve for the reinforced geopolymer concrete frame through experimental investigations and analytical investigations are studied. From the results obtained, the following conclusions have been made:

- The compressive strength and the elastic modulus of geopolymer concrete is 40.45 N/mm^2 and 3.35 $\times$ 10^4 N/mm^2, respectively.
- The stiffness based on the analytical model for the first and second storey are 2.80, 2.533 kN/mm under push and 1.523, 1.372 kN/mm under pull.
- The stiffness based on the experimental model for the first and second storey are 2.61, 2.01 kN/mm under push and 1.47, 1.41 kN/mm under pull.
- The ductility factor based on the analytical model for the first and second storey are 5.99, 6.007 under push and 6.687, 6.76 under pull.

Fig. 17 Deformed shape of reinforced geopolymer concrete subjected to lateral push load
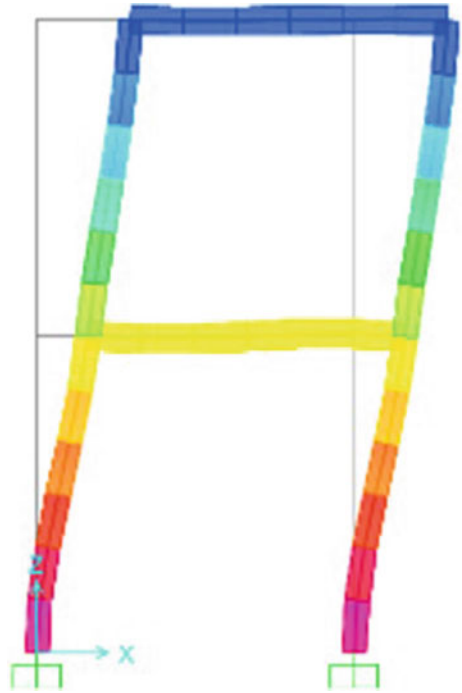
- The ductility factor based on the experimental model for the first and second storey are 6.23, 6.724 under push and 5.97, 6.29 under pull.
- The energy absorption capacity based on the analytical model for the first and second storey are 1445, 2585 kN mm under push and 994.416, 1832.076 kN mm under pull.
- The energy absorption capacity based on the experimental model for the first and second storey are 1542.825, 2732.5 kN mm under push and 1291.8, 1837.44 kN mm under pull.

Fig. 18 Deformed shape of reinforced geopolymer concrete subjected to lateral pull load
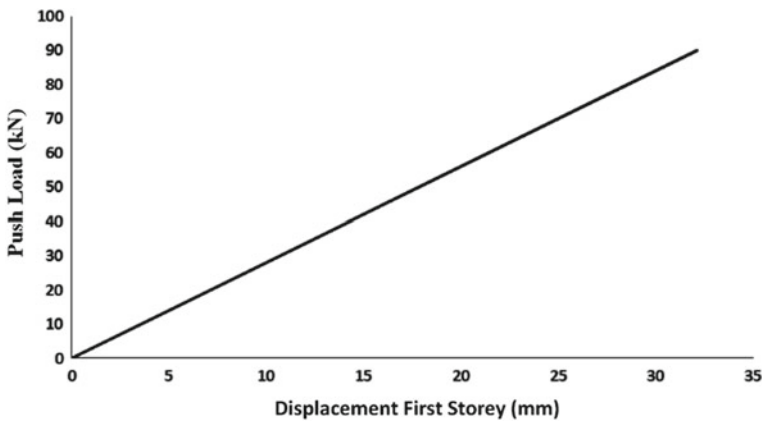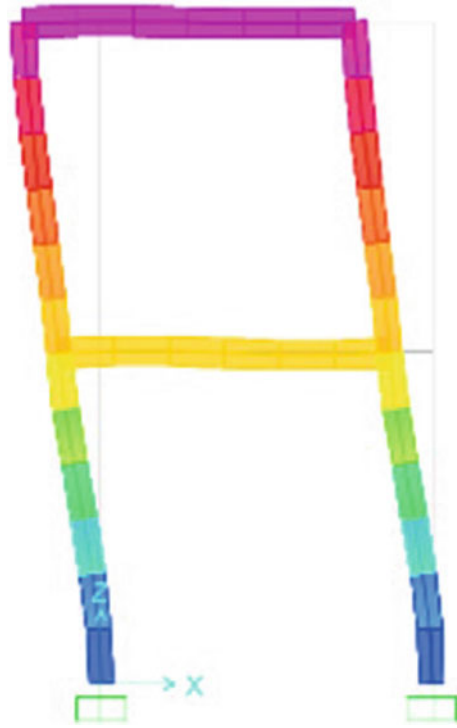
Fig. 19 Load—displacement for bottom storey (push) of analytical frame
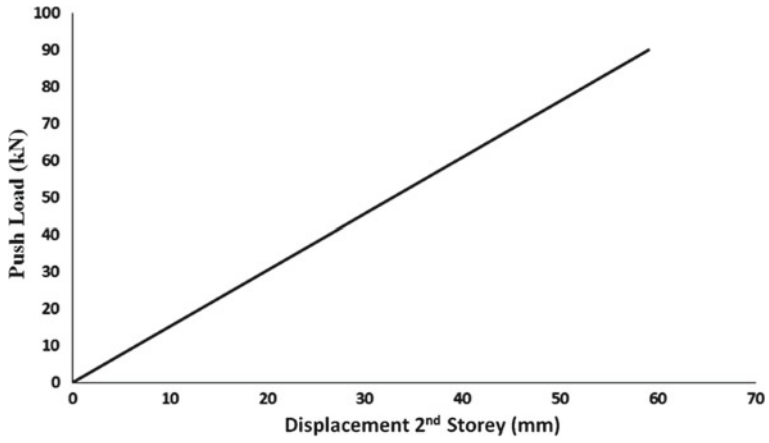
Fig. 20 Load—displacement for second storey (push) of analytical frame

Fig. 21 Load—displacement profile for bottom storey (pull) of analytical frame
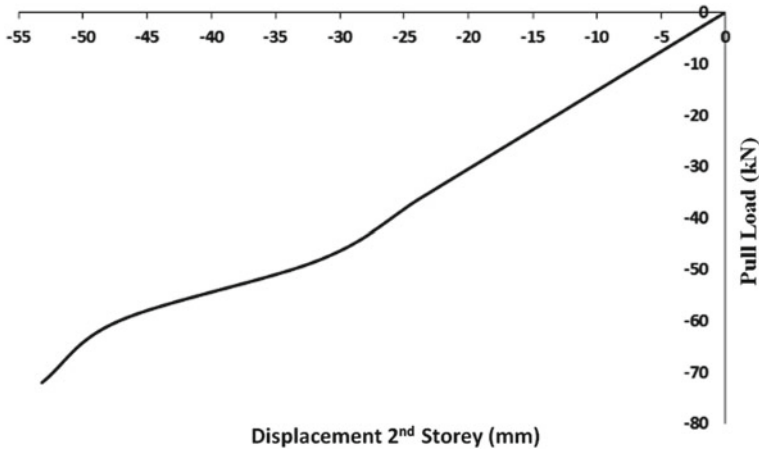
Fig. 22 Load—displacement profile for second storey (pull) of analytical frame

Table 2 Load—deflection values for experimental frame

No.	Load (kN)		Deflection (mm)			
	Forward push	Reverse pull	First storey		Second storey	
			Push	Pull	Push	Pull
1	0	0	0	0	0	0
2	15	12	5.69	−5.60	9.12	−8.12
3	30	24	11.54	−12.39	20.58	−17.13
4	45	36	17.2	−18.25	30.1	−25.96
5	60	48	22.58	−24.28	40.23	−33.98
6	75	60	28.12	−29.38	51.32	−42.36
7	90	72	35.45	−35.50	61.32	−51.14
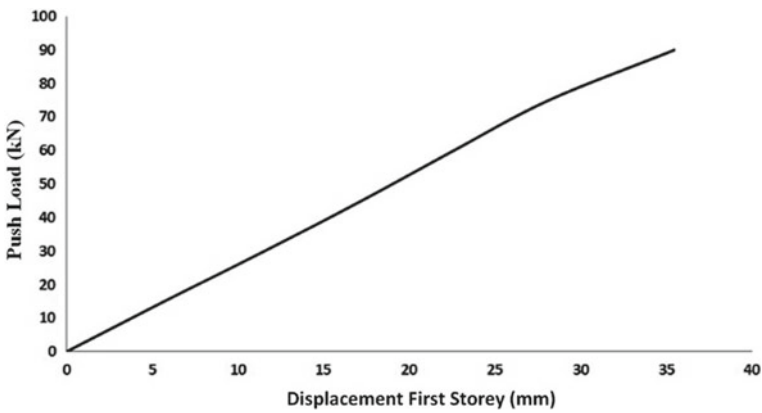
Fig. 23 Load—displacement for bottom storey (push) of experimental frame
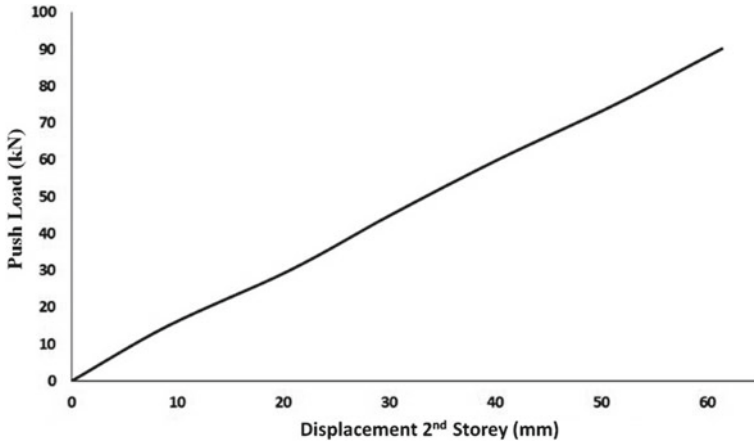
Fig. 24 Load—displacement for second storey (push) of experimental frame

Fig. 25 Load—displacement for bottom storey (pull) of experimental frame
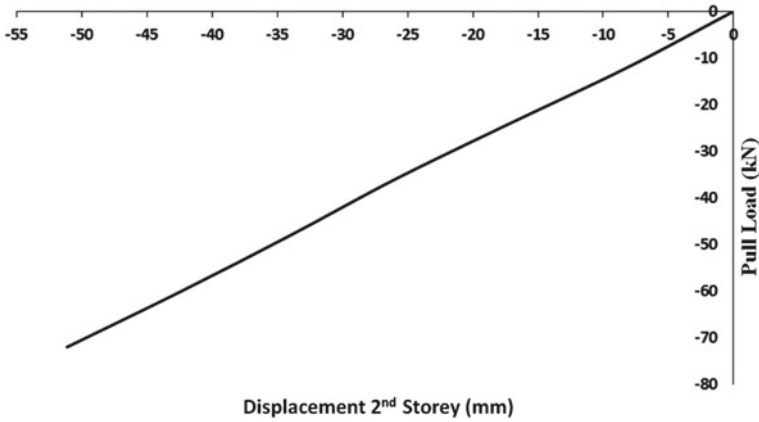
Fig. 26 Load—displacement for second storey (pull) of experimental frame

Fig. 27 Stiffness of reinforced geopolymer concrete (analytical frame)
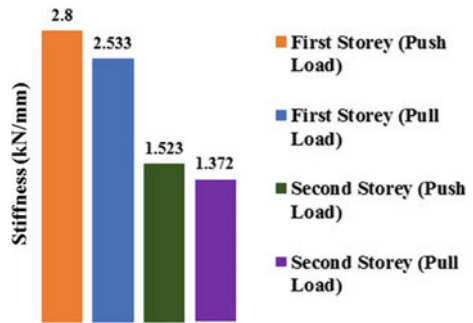
Fig. 28 Stiffness of reinforced geopolymer concrete (experimental frame)
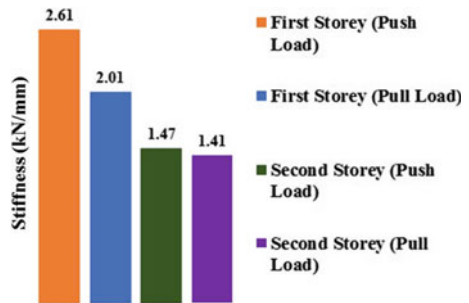
Fig. 29 Ductility factor of reinforced geopolymer concrete (analytical frame)
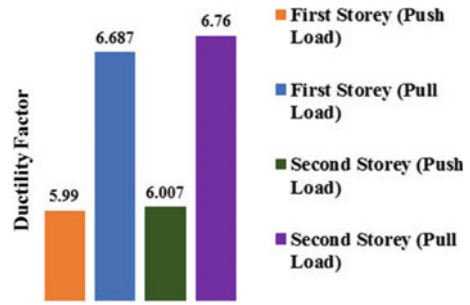
Fig. 30 Ductility factor of reinforced geopolymer concrete (experimental frame)
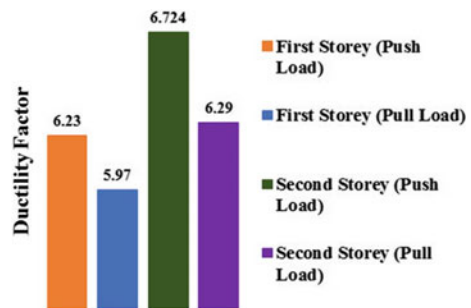
Fig. 31 Energy absorption capacity of reinforced geopolymer concrete (analytical frame)
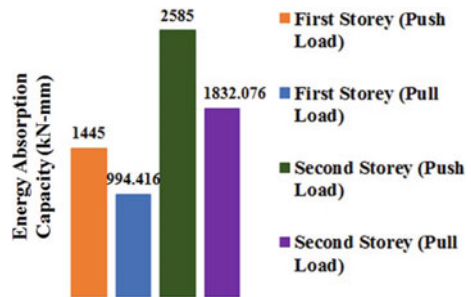
Fig. 32 Energy absorption capacity of reinforced geopolymer concrete (experimental frame)

References

1. Lazarescu AV, Szilagyi H, Baera Loani A (2017) The effect of alkaline activator ratio on compressive strength of fly ash-based geopolymer paste. IOP conference series: materials science and engineering 209:1–6
2. Vora PR, Dave UV (2013) Parametric studies on compressive strength of geopolymer concrete. Proced Eng 51:210–219
3. Malhotra VM (1999) Making concrete 'greener' with fly ash. ACI Concr Int 21:61–66
4. Kumar R, Naik T (2010) Sustainable concrete with industrial and post-consumer by-products. In: 2nd international conference on sustainable construction materials and technologies, Ancona, Italy, June 28–30, 1899—1910
5. Rakesh Kumar (2014) Greener concrete using industrial by-products. Indian Concr J 88:29–40
6. Pithadiya PS, Nakum AV (2015) Experimental study on geopolymer concrete by using GGBS. Int J Res Eng Tech 4:185–187
7. Davidovits J (1999) Chemistry of geopolymeric systems, terminology. 99 Geopolymer international conference proceeding, Saint-Quentin, France, June 30–July 02, 9–40
8. Davidovits J (2013) Geopolymer cement, a review. Geopolymer Science and Technics, Geopolymer Institute Library, pp 2–11
9. Davidovits J (2008) Geopolymer chemistry and applications. ed. Institut Geopolymere, France
10. Provis John L (2018) Alkali—activated materials. Cem Concr Res 114:40–45
11. Provis John L, Palomo A, Cai Jun S (2015) Advances in understanding alkali-activated materials. Cement Concr Res 78:110–125
12. Provis JL, Van Deventer JSJ (2014) Alkali-activated materials: state-of-the-art reports, XIV edn. Springer, Netherlands, Dordrecht
13. Provis JL, Bernal Susan A (2014) Geopolymers and related alkali-activated materials. Ann RevMater Res 44:299–327
14. Hardjito D, Rangan BV (2005) "Development and properties of low-calcium fly ash-based geopolymer concrete", Research Report GC-2. Curtin University of Technology, Perth, Australia
15. Humayun BS, Kaushik Hemant B (2016) Behaviour and failure mechanisms of masonry-infilled RC frames (in low-rise building) subject to lateral loading. Eng Struct 111:233–245
16. Huang Q, Guo Z, Kuang JS (2016) Designing infilled reinforced concrete frames with the 'strong Frame-weak infill' principle". Eng Struct 123:341–353
17. Jayaramappa N (2015) Study on the behaviour of RC frame for lateral load. Int J Eng Res Tech 4(5):781–788
18. Kalaipandian K, Amuthaselvakumar R (2016) Sesmic behaviour of RC frame with and without masonry infill. Int J Eng Tech 3(5):2139–2144

Evaluation of Rapid Chloride Permeability Test on Concrete Containing Steel, E-Waste Copper Wire and E-Glass Fibres

Ganesh Naidu Gopu and A. Sofi

Abstract The main cause of reinforced concrete deterioration is chloride attack. Chloride ions penetrated into the concrete can destroy the passive layer around steel reinforcement provided by the high alkalinity and low pH of cement paste, activating electrochemical corrosion. Durable concrete gives more corrosion resistance of embedded steel that continuously ensures a stronger long life of the reinforced concrete structure. The concrete structures within the seashore areas allow chloride ions to easily penetrate into the concrete and reduce the life span of the structure. In this paper, the rapid chloride permeability test (RCPT) as per ASTM C1202 is presented to determine the chloride profile, concrete chloride resistivity and rate of corrosion. The specimens were prepared with concrete incorporating three different type fibres including steel, E-waste copper wire and E-glass fibres of 1.0% by volume of concrete. The RCPT was conducted for time period of 28 days, 56 days and 90 days. The final RCPT results of fibre-reinforced concrete mix with control mix concrete were compared. The test result shows that the E-glass fibre-reinforced concrete was more durable than the other concrete mixes.

Keywords Rapid chloride permeability test · E-waste copper wire fibre · E-glass fibre · Corrosion · Durability

1 Introduction

Corrosion of embedded steel bars is a serious durability problem in reinforced concrete structures. It is well established that the chloride ions can destroy the passive layer around steel reinforcement provided by low pH of cement paste, thus activating the electrochemical corrosion [1]. The reinforced concrete structures exposed to coastal environment exhibit problems of durability because of chloride ion penetration into the concrete [2]. To overcome these weaknesses, fibres are introduced in concrete mix [3] to increase the strength and durability of concrete. The rapid

G. N. Gopu (✉) · A. Sofi
School of Civil Engineering, Vellore Institute of Technology, Vellore, India
e-mail: gopuganeshnaidu@gmail.com

chloride permeability test (RCPT) is used to estimate the chloride ion resistance of various concrete mixes. In the RCPT (ASTMC1202-97 or AASHTO T277-96), 60 V potential is continuously applied to the concrete specimen up to 6 h, and the current passing is measured at every 30 min time duration based [4]. The rapid chloride penetration test is used to find out the resistance of the chloride ion permeability using various types of mineral admixture. The size of aggregates influences the charge passing through the specimen, and the method of curing and void ratio of materials affect the permeability of chloride ion into the specimen [5]. Zongjin and Baoguo (1999) have investigated the depth of chloride ion permeability relation and determined the chloride diffusivity coefficient of the concrete sample using rapid chloride non steady-state migration test method. RCPT test does not measure permeability of concrete; however, it measures the concrete resistivity [6]. The concrete resistivity is found by passing current through the specimen.

This study presents the results of rapid chloride permeability test (RCPT) to determine the chloride profile, concrete chloride resistivity and rate of corrosion. Different types of fibre include steel fibre, E-waste copper wire fibre and E-glass fibre were used in reinforced concrete, and the effect of chloride ion permeability, resistivity and rate of corrosion in the specimen was measured using RCPT.

2 Experimental Investigation

2.1 Materials

2.1.1 Cement

The ordinary Portland cement of 53 Grade was used in this study. The cement was tested as per IS 12269-2013 to determine the specific gravity (SG) of cement which is 3.15. The initial and final setting time of cement was 200 and 280 min, respectively. Other properties are shown in Table 1.

2.1.2 Fine Aggregates

The regionally available stream sand was used as fine aggregate (FA) in this study. The sand was tested as per IS 2386-3 (1963). The fine aggregate is confirming to zone II. The aggregate passing through 4.75 mm sieve and retained on the 0.25 mm sieve was used. The specific gravity (SG) of FA is found to be 2.66 shown in Table 2.

Table 1 Properties of cement

Properties	Results
Fineness	227 m^2/kg
Soundness	10 mm
Setting time	
Initial	200 min
Final	280 min
Compressive strength	
7 days	28 N/mm^2
14 days	39 N/mm^2
28 days	56 N/mm^2

Table 2 Properties of aggregates

Physical properties	Coarse aggregates Aggregate	Fine aggregates Aggregate
Specific gravity	2.58	2.66
Fineness modulus	4.32	2.32
Bulk density (kg/m^3)	1540	1780

2.1.3 Coarse Aggregates

The crushed granite stone was used as coarse aggregate. The maximum coarse aggregate size of 20 mm was used, and specific gravity (SG) of the coarse aggregate is 2.58 as shown in Table 2.

2.1.4 Steel Fibres (SF)

Steel fibres confirming to ASTM A820/A820M-4 were used in this study. The steel fibres (see Fig. 1a) used in concrete mix could improve the flexural strength, elasticity

Fig. 1 Types of fibres

Table 3 Properties of steel, E-waste copper wire and E-glass fibres

Properties of fibre	Steel fibres	E-waste copper wire fibre	E-glass fibre
Shape	Straight	Straight	Straight
Length (mm)	40	30	6
Diameter (mm)	0.8	0.6	0.12
Aspect ratio (L/D)	50	50	50
Tensile strength (N/mm^2)	1220	1366	1950

and toughness of concrete containing steel fibres. The properties of steel fibres are shown in Table 3.

2.1.5 E-Waste Copper Wire Fibres

E-waste consists of all waste from electronic gadgets and electrical appliances. The length of E-waste copper wire fibre used is 30 mm (see Fig. 1b).The properties of E-waste copper wire fibres are shown in Table 3.

2.1.6 E-Glass Fibres

E-glass fibres confirming according to ASTM D3517-14 were used. The dried fibres were then cut to the required lengths to attain the desired aspect ratio of 50 (shown in Fig. 1c). The properties of E-waste glass fibres are shown in Table 3.

3 Mix Proportions

This study used a concrete grade of M40. The proportion of concrete mix was designed in accordance with BIS 10264-2009, and the proportion is shown in Table 4. A w/c of 0.45 was used to implement the codal requirements for exposure condition of concrete in saline environment. Ordinary Portland cement is used as binding material, and 20 mm maximum size stone chips and river sand with fineness modulus of

Table 4 Mix proportions of concrete

Materials (kg/m^3)					w/c ratio
Water	Cement	Fine aggregate	Coarse aggregate	Fresh density	
190	422	725	1008	2345	0.45

2.8 were used as coarse aggregate and fine aggregate in concrete, respectively. The water used in this study has a chloride ion concentration of 1200 mg/L and pH 7.5.

4 Test Procedures

The specimens were prepared and tested as per ASTM C192 recommendations. The concrete mix adopted was M40 concrete with percentage of fibres ranging from 1.0% of volume of concrete. All the specimens were de-moulded after 24 h and moist cured at 23 °C and 95% RH for 27 days. The concrete discs of 100 mm in diameter and 50 mm in thickness were sliced from the top portion of 100 mm × 200 mm cylinders for the RCPT test (see Fig. 2).

Three specimens were prepared for all three different types of mix with steel, E-glass and E-waste copper wire fibres. The specimens were pre-conditioned according to the ASTM C 1202 standard procedure. The anolyte solution NaOH concentration was kept at 0.3 N as per the ASTM C 1202 guidelines, and the concentration of the catholyte solution (NaCl) was used 3% to comply with the standard procedure.

4.1 Rapid Chloride Permeability Test (RCPT)

According to ASTM C1202, test specimen casted with dimensions 100 mm diameter and 50 mm thickness. The test speciment coated with epoxy. After coated with epoxy, specimens were placed in a vacuum chamber for 3 h in order to remove the air from the voids evantually voids filled with water. The specimen was saturated by vacuum

Fig. 2 Concrete disc samples

left hand cell   Right hand cell   60 Volts DC source   Vacuum Chamber
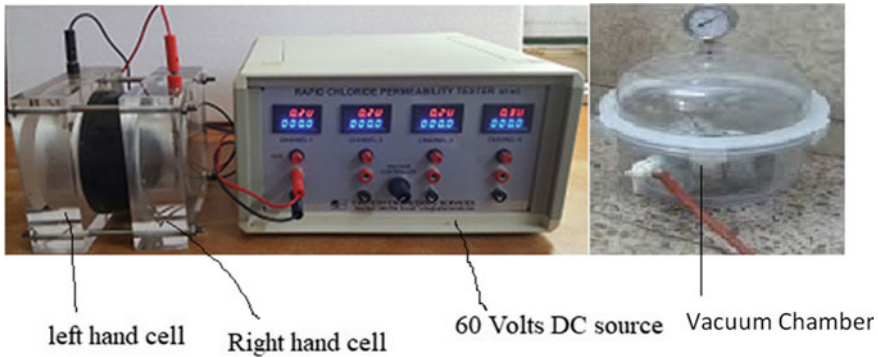
Fig. 3 Rapid chloride penetration test set-up

Table 5 RCPT ratings for concrete (as per ASTM C1202)

Charge passed (coulombs)	Chloride ion permeability
>4000	High (H)
2000–4000	Moderate (M)
1000–2000	Low (L)
100–1000	Very low (V)
<100	Negligible (N)

for 1 h and soaked for 18 h in RCPT test chamber. 3% Nacl solution filled by left-hand cell (−) will act as catholyte, and 0.3 N concentration NaOH solution filled by right-hand cell (+) will act as anolyte. The system was connected with 60 V potential applied for 6 h; however, for every 30 min, the current was measured (mA) using the ammeter and the cell arrangement as shown in Fig. 3.

RCPT ratings are shown in Table 5. Three cylindrical specimens were prepared for each mix. A total 36 cylinders were prepared, and 72 disc samples were tested. A series of six disc specimens for each mix were tested, and the average value can be determined.

4.1.1   Passing Charges

The specimen was placed in the chamber, and 60 V potential DC was connected. For every 30 min, the current passing through the specimen was measured. The average current flowing through one cell (I) in coulombs was calculated by using Eqs. (7)–(2).

$$I = 900 * 2 * I_{\text{cummulative}} \tag{1}$$

$$I_{\text{cummulative}} = I_0 + I_{30} + I_{60} + I_{90} + I_{120} + I_{150} + I_{180} + I_{210}$$

Table 6 Chloride permeability charge passed (Coulombs)

Grade of concrete	Type of concrete	Charge passed in Coulombs			
		7 days	28 days	56 days	90 days
M40	Control concrete mix	5200	2790	1795	730
	Steel fibre-reinforced concrete mix	4310	2454	1400	296
	E-glass fibre-reinforced concrete mix	3990	2322	1210	285
	E-waste copper wire fibre-reinforced concrete mix	4365	2565	1750	325

$$+ I_{240} + I_{270} + I_{300} + I_{330} + I_{360} \qquad (2)$$

where

I_0 = Initial current reading in mA	I_{30} = At 30 min current reading in mA
I_{60} = At 60 min current reading in mA	I_{90} = At 90 min current reading in mA
I_{120} = At 120 min current reading in mA	I_{150} = At 150 min current reading in mA.
I_{180} = At 180 min current reading in mA	I_{210} = At 210 min current reading in mA
I_{240} = At 240 min current reading in mA	I_{270} = At 270 min current reading in mA
I_{300} = At 300 min current reading in mA	I_{330} = At 330 min current reading in mA
I_{360} = At 360 min current reading in mA	

The total charge passing through the specimen was calculated using Eqs. [7] and [2] at all ages, and the results are given in Table 6

From the results, it was observed that the charge passing in initial days was high in earlier stages and gradually decreased at later stages. The charge passing was less in fibre-reinforced concrete compared to control specimen. The fibres used in concrete reduce the cracks, which makes the interconnecting voids to be minimum, and permeability resistance is good [3]. The charge passing through E-glass fibre inclusion concrete specimen was very low when compared to steel and E-waste copper wire fibre concrete mixes as shown in Fig. 4. It was observed that the chloride ion permeability is proportional to charge passage [8].

4.1.2 Electrical Resistivity

The E-resistivity for all mixtures corresponding to electrical current measurements at 30 min from the start of the RCPT was recorded. The values were calculated using Eq. [8].

$$\rho = \frac{VA}{IL} \qquad (3)$$
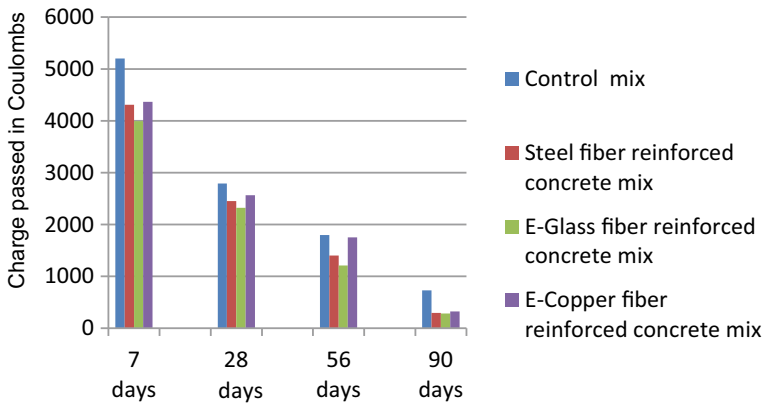
Fig. 4 Comparison of total charge passed versus number of days

where

ρ Resistivity (Ω m)
V Applied voltage (V)
A Cross-sectional area of the specimen (m^2)
I Current (A)
L Thickness of the specimen (m)

The previous investigations [9, 10] recommended the calculation of 1-min resistivity to avoid temperature effects (up to 40 °C) that could happen even at 30 min from the start of the test. Nevertheless, no such temperature rise was observed in the present study for all tested mixtures, and the maximum temperature gradient at 30 min did not exceed 6 °C. Also, there was a marginal difference between the initial and 30-min currents resulting in comparable resistivity values at 1 and 30 min. Thus, only the 30-min resistivity was considered herein conforming to passing charge extrapolations.

Electrical resistivity of concrete can be measured for the first 30 min from the start of the RCPT by using the Eq. (8), and the results are shown in Table 7. Electrical resistivity of the steel fibre, E-glass fibre and E-waste copper wire fibre-reinforced concrete is compared with the control concrete mix. It was observed that electrical resistivity increased for the specimens incorporated with steel and E-glass fibres compared to control concrete mix at all ages. E-copper wire fibre-reinforced concrete reduces the electrical resistivity at 56 and 90 days as shown Fig. 5. As electrical resistivity increased, eventually, chloride ion permeability decreases in concrete containing fibres [7].

Table 7 Electrical resistivity of concrete (Ω m)

Type of concrete mix	30-min current (m A)				Resistivity of concrete (Ω.m)			
	7 days	28 days	56 days	90 days	7 days	28 days	56 days	90 days
Control concrete mix	175	85	50	25	53.86	110.88	188.5	376.99
Steel fibre-reinforced concrete mix	145	75	45	20	65	125.66	209.44	471.24
E-glass fibre-reinforced concrete mix	145	70	40	15	65	134.64	235.62	628.32
E-waste copper fibre-reinforced concrete mix	170	85	55	25	55.44	110.88	171.36	376.99
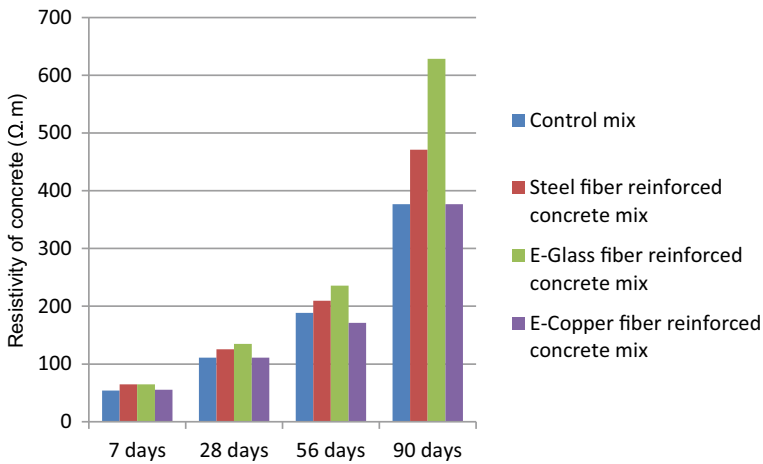
Fig. 5 Comparison of resistivity of concrete (Ω m) versus number of days

4.1.3 Corrosion Rate of Steel Rebar

The resistivity of concrete calculated from the RCPT can be used to estimate the length of corrosion propagation stage until spalling of concrete. Generally, a linear correlation between the inverse of concrete resistivity and the steel corrosion rate has been established. For instance, when concrete resistivity exceeds 70 Ω m, the corrosion rate of steel rebar is expressed by Eq. (11).

$$C_R = 1000/\rho_{\text{concrete}} \qquad (4)$$

where

Table 8 Corrosion rate (μm Fe/yr)

Type of concrete mix	Resistivity of concrete (Ω·m)				Corrosion rate (μm) Fe/yr			
	7 days	28 days	56 days	90 days	7 days	28 days	56 days	90 days
Control mix	53.86	110.88	188.5	376.99	0	9.02	5.31	2.65
Steel fibre-reinforced concrete mix	65	125.66	209.44	471.24	0	7.96	4.77	2.12
E-glass fibre-reinforced concrete mix	65	134.64	235.62	628.32	0	7.43	4.24	1.59
E-copper fibre-reinforced concrete mix	55.44	110.88	171.36	376.99	0	9.02	5.84	2.65

C_R Corrosion rate (μm Fe/yr)

ρ_{concrete} Concrete resistivity (Ω m)

Then, the duration of corrosion propagation stage can be calculated by dividing the amount of corrosion that causes cracking by the corrosion rate [11, 12]. In addition to resistivity, by considering oxygen availability and the concentration of hydroxide ions (OH$^-$), a more accurate estimation of the corrosion rate can be obtained. Although by taking measurements from the RCPT at short time, the intervals can eliminate the temperature effect on the RCPT passing charge and resistivity results; however, such procedure may not correctly assess the chloride ion penetrability in concrete. The concrete with low resistivity (i.e. high passing charges) does not necessarily have a high chloride ion diffusivity. When the concrete resistivity exceeds 70 Ω m, the corrosion rate of steel rebar's is measured and given in Table 8 using Eq. [11]. From the result, it was observed that the corrosion rate in initial days is low, and it was increased gradually as shown in Fig. 6. The RCPT test results could not predict the corrosion rate exactly [13, 14].

5 Conclusion

It was concluded that all the test specimens casted with and without fibres exhibited very low permeable resistance during 7,28 and 56 days. But after 90 days these specimens exhibited good permeable resistance. Especially fibre-reinforced concrete gives excellent resistance compared to control concrete mix.

- It was observed that for 90 days, the charge passing through the concrete with steel fibre, E-glass fibre and E-waste copper wire fibre decreased by 59.4%, 60.12% and 55.35%, respectively, when compared to the control concrete mix.
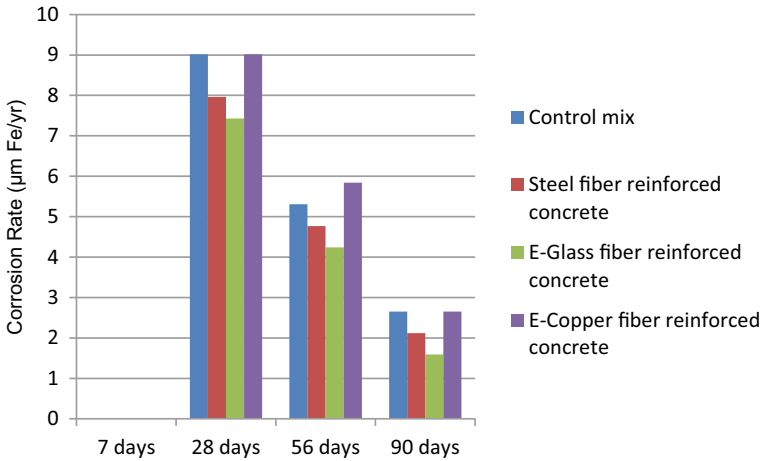
Fig. 6 Comparison of corrosion rate (μm Fe/yr) versus number of days

- For 90 days, the chloride resistivity of the concrete with steel fibre, E-glass fibre and E-waste copper wire fibre increased by 19.94%, 39.9% and 0%, respectively, when compared to the control concrete mix for the first 30 min.
- For 90 days, the corrosion rate of the concrete with steel fibre, E-glass fibre and E-waste copper wire fibre decreased by 19.94%, 39.9% and 0% respectively when compared to the control concrete mix for the first 30 min.

Hence, it can be concluded that the charge passed through concrete containing fibres in concrete was lesser than the control concrete. From, the RCPT test, it was observed that less charge passed through the E-glass fibre compared to the steel fibre and E-waste copper wire fibre-reinforced concrete.

References

1. Pyo S, Koh T, Tafesse M, Kim H-K (2019) Chloride-induced corrosion of steel fiber near the surface of ultra-high performance concrete and its effect on flexural behavior with various thickness. Constr Build Mater 224:206–213
2. Berrocal CG, Lundgren K, Löfgren I (2016) Corrosion of steel bars embedded in fibre reinforced concrete under chloride attack: State of the art. Cem Concr Res 80:69–85
3. Mangat PS, Gurusamy K (1988) Corrosion resistance of steel fibres in concrete under marine exposure. Cem Concr Res 18(1):44–54
4. Aldea CM, Young F, Wang K, Shah SP (2000) Effect of curing conditions on properties of concrete using slag replacement. Cem Concr Res 30(3):465–472
5. Feldman RF, Chan GW, Brousseau RJ, Tumidajski PJ (1994) Investigation of the chloride permeability test. ACI Mater J 91(2):246–255
6. Tang L, Nilsson L (1992) Rapid determination of the chloride diffusivity in concrete by applying an E- field. ACI Mater J 89(1):49–53

7. Atewi YR, Hasan MF, Güneyisi E (2019) Fracture and permeability properties of glass fiber reinforced self-compacting concrete with and without nanosilica. Constr Build Mater 226:993–1005

8. Song QL, Yu R, Shui ZH, Rao Suduan, Wang XP, Sun M, Jiang CY (2018) Steel Fibre content and interconnection induced electrochemical corrosion of ultra-high performance fibre reinforced concrete (UHPFRC). Cement Concr Compos 94:191–200

9. Selvi MT, Thandavamoorthy TS (2013) Studies on the properties of steel and polypropylene fibre reinforced concrete without any admixture. Int J Eng Innov Technol (IJEIT), 3(1):411–416

10. Bassuoni MT, Nehdi ML, Greenough TR (2006) Enhancing the reliability of evaluating chloride ingress in concrete using the ASTM C 1202 rapid chloride penetrability test. J ASTM Int 3(3):1–13

11. Ganesh Naidu G, Sri Durga Vara Prasad M, Venkata Kishore N, Hari Prasad R (2019a) Influence of pet waste on mechanical properties of concrete. Int J Eng Adv Technol 9(1):2605–2607

12. Kuder KG, Shah SP (2010) Processing of high-performance fiber-reinforced cement-based composites. Constr Build Mater 24(2):181–186

13. Ganesh Naidu G, Sri Durga Vara Prasad M, Venkata Sai Pavani A (2019b). Impact of chloride attack on basalt fibre reinforced concrete. Int J Innov Technol Explor Eng 8(12):4467–4469

14. Li Z, Baoguo Ma JP (1999) Investigation of chloride diffusion for high-performance concrete containing fly ash, Microsilica, and chemical admixtures ACI Mater J 96(3):53–62

15. IS:12269-2013 (2013) Ordinary Portland Cement, 53 grade specification (First Revision). Bureau of Indian Standards, New Delhi, India

16. BIS:10262 (2009) Indian Standard Guidelines for concrete mix design proportioning. Bureau of Indian Standards, New Delhi, India

17. IS 2836-Part 3 (2005) Indian standard methods of test for aggregates for concrete. Bureau of Indian Standards, New Delhi, India

18. ASTM C1202-19 (2019) Standard test method for electrical indication of concrete's ability to resist chloride ion penetration. American Society for Testing and Materials, ASTM International

19. ASTM A 820/A820M (2013) Standard Specification for Steel fibres for concrete mix. American Society for Testing and Materials, ASTM International

20. ASTM D3517-14 (2014) Code for Glass fibre specifications and testing. American Society for Testing and Materials, ASTM International

21. ASTM C192-19 (2019) Standard practice for making and curing concrete test specimens in the laboratory. American Society for Testing and Materials, ASTM International, p 2019

22. AASHTOT277-86 (1996) Standard method of test for rapid determination of the chloride permeability of concrete. American Association of State Highway and Transportation Officials, Washington, DC

Role of NaOH Concentration on Kinetic Ratios of Eco-friendly Geopolymer Concrete Cured Under Ambient Temperature

Srinivasreddy Kuunreddy and S. Bala Murugan

Abstract Ordinary Portland Cement has a negative impact on the environment due to the consumption of available natural resources and high energy during production. The use of industrial by-products as a supplementary cementitious material in geopolymer concrete could reduce the CO_2 emissions, loss of energy, land fillings, and natural resources can be protected. The paper presents effect of increase in sodium hydroxide concentration from 0.5 to 10 M in the alkaline solution on the strength properties of ternary blended geopolymer concrete specimens cured at ambient temperature. It was found that the compressive strength increases significantly with an increase in the NaOH concentration due to the decrease in the kinetic ratios. The compressive strength of geopolymer concrete with manufactured sand (M-Sand) was varied in the range of 39.3–65.3 MPa at 28 days. The increase in cost of ternary blended geopolymer concrete mixes is less with an increase in the NaOH concentration.

Keywords Compressive strength · Kinetic ratios · NaOH concentration · Ambient temperature curing

1   Introduction

Cement is widely used construction material throughout the world because of its ease in operation, mechanical properties, and durability aspects. The cement industries are facing challenges to meet the demand, due to limited natural resources (limestone) and carbon emissions during the combustion of fossil fuels and de-carbonation of limestone [1–3]. Cement is the most energy-intensive material and associated with environmental pollution issues [4]. On the other hand, the industries require a vast area of land for the safe disposal of the industrial by-products. The industrial by-products that are rich in aluminates and the silicates such as flyash, Ground

S. Kuunreddy (✉) · S. Bala Murugan
School of Civil Engineering, Vellore Institute of Technology, Vellore, India
e-mail: kunnreddy.123@gmail.com

Granulated Blast furnance Slag (GGBFS), and alccofine can be used as supplementary cementitious materials in green concrete (Mehta and Siddique) [5]. By utilizing these industrial by-products in geopolymer concrete will find a viable solution to meet the future demand for concrete, to overcome the issues caused by the Ordinary Portland Cement (OPC) and to unregulate the disposal of industrial by-products by reusing in geopolymer concrete [6, 7]. Geopolymer concrete is emerging cementless concrete with environmental sustainable characteristics [8]. Flyash was used as primary precursors in the geopolymer concrete because of its chemical composition and ease of availability throughout the world Davidovits [9]. The alumina and silica present in the industrial by-products react with the alkaline solution to form a three-dimensional polymeric chain of Si–O-Al-O ring structure [8, 10]. The reactivity of flyash alone in the presence of alkaline solution is slow at ambient temperature [11]. The reactivity of flyash and the alkaline solution was effective in the presence of initial temperature curing, which leads to attaining high early compressive strength of geopolymer concrete [12]. The limitation for flyash-based geopolymer concrete at in situ application is high-temperature curing around 40–60 °C to attain the required strength parameters which is not feasible [5]. To overcome this drawback, several researchers focused on the synthesis of geopolymer concrete by adding calcium-based materials. These calcium-based materials can liberate the required heat to the geopolymer system and helps in attaining the required strength to the geopolymer system at ambient temperature [13, 14]. The compressive strength and fresh properties of the geopolymer concrete depend on the source of the materials, the molarity of the NaOH and the ratio of the Na_2SiO_3 to NaOH, alkaline liquid to binder, curing conditions and type of admixtures [15].

To enhance the reactivity of the geopolymer concrete at ambient temperature, flyash is replaced with GGBFS and alccofine. Ternary binders are used to study the influence of varying the NaOH concentrations on the compressive strength and the kinetic reactions at ambient temperature. The ratio of Na_2SiO_3 to NaOH used is 2.5 in all the mixes. M-sand is used as fine aggregates in all the geopolymer mixes to overcome the problems faced due to the river sand.

2 Materials

The binder materials are subjected to scanning electron microscopy (SEM) and energy-dispersive X-ray spectroscopy (EDS) to identify the particle shape and elemental composition.

2.1 *Flyash*

Low-calcium class F flyash is the by-product obtained from the thermal power plants by combustion of pulverized coal during the power generation. The source
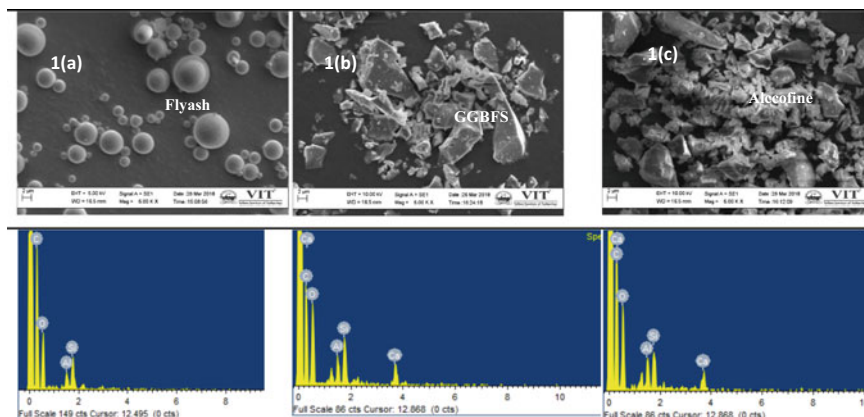
Fig. 1 SEM and EDS of binder materials

Table 1 Weight percentages of elements in binder materials

Binder/Element	C (%)	O (%)	Al (%)	Si (%)	Ca (%)
Flyash	59.19	31.99	2.75	6.07	–
GGBFS	38.52	36.19	3.84	8.36	13.09
Alccofine	45.69	35.26	4.01	6.38	8.66

of flyash may vary the chemical composition of material. The flyash used in this work is obtained from the KTPP Telangana. These industrial by-products can be used as supplementary cementitious material because of high silica ($SiO_2 > 60\%$) and alumina ($Al_2O_3 > 30\%$). From Fig. 1(a), it can be seen that the shape of the flyash particle is spherical. The percentages of different elements present in the flyash are shown in Table 1.

2.2 Ground-Granulated Blast Furnace Slag

Ground-granulated blast furnace slag is a by-product obtained from iron ore industries. In this study, GGBFS used is supplied by the local distributor in Chennai, Tamil Nadu. Manufacturing process plays a key role such as temperature in the furnace, granulation of slag, and viscosity of slag liquid in attaining the required parameters for the processed slag. From Fig. 1(b), it can be seen that the particle shape of the GGBFS is angular. The percentages of different elements present in the flyash are shown in Table 1.
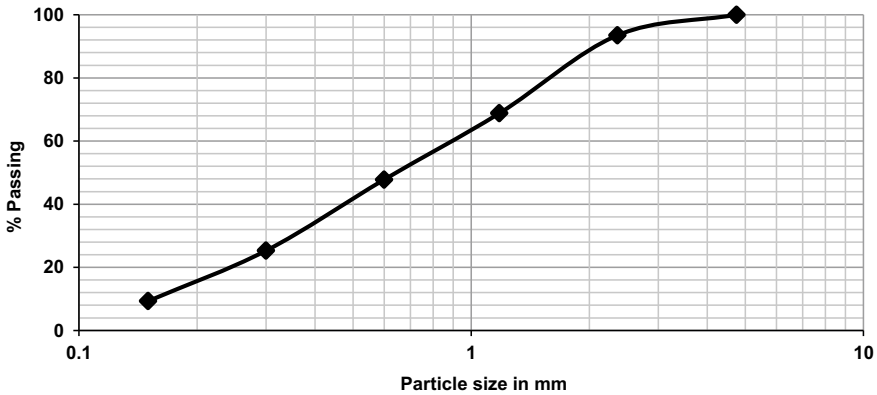
Fig. 2 Sieve analysis graph of M-sand

2.3 Alccofine

Alccofine is a low calcium silicate material produced by controlled granulation of slag. Ultrafine alccofine is purchased from the Counto Microfine products Pvt. Ltd India confirming to (ASTM C989-99). The high reactivity and the unique chemistry of alccofine make the concrete workable by reducing the water content. Alccofine can either be used as an additive or in replacement to cement and flyash to produce high-strength concrete. The angular particle shape of alccofine is shown in Fig. 1(c), the percentages of different elements present in the flyash are shown in Table 1.

2.4 Aggregates

Finding the good quality of fine aggregates is a challenging situation for the construction industry to substitute the natural river sand. The natural river sand is completely replaced by the manufactured sand. The sieve analysis was conducted for the M-sand, and it falls under ZONE–II and the fineness modulus is 3.2 as per IS 383 [16]. The sieve analysis graph is shown in Fig. 2. The coarse aggregates used are in the range from 12.5 to 20 mm. The aggregate used is free from dust and the aggregates are in surface saturated dry condition at the time of use in geopolymer concrete.

2.5 Alkaline Solution

The alkaline solution is the combination of the sodium hydroxide (NaOH) and sodium silicate (Na_2SiO_3) solution. For effective polymerization reactions with aluminates and silicates present in the binder material, the alkaline solution was prepared 24 h

before mixing with the dry materials. The ratio of Na_2SiO_3 to NaOH was taken as 2.5 for all the mixes. NaOH used in this study is in the form of pellets (Industrial Grade). The required quantity of NaOH was calculated based on the molarity and dissolve the pellets in pure water. The NaOH solution is free from impurities and crystals. The sodium silicate is purchased from a local distributor in Chennai. The molar ratio of SiO_2/Na_2O is 2.2 in the sodium silicate.

2.6 Superplasticizer and Water

Naphthalene-based Conplast SP430 was used as superplasticizer in the geopolymer concrete to improve the workability. Pure water was used for mixing and to improve the workability of geopolymer concrete.

3 Experimental Program

3.1 Preparation, Casting, and Testing of Geopolymer Concrete Specimens

Mix design of geopolymer concrete was prepared based on the previous studies of Lloyd and Rangan [17]. Mixing and sample preparation method is similar to preparation of conventional concrete as per IS 516 [18]. The mix proportion details are shown in Table 2. For each mix of geopolymer concrete, nine cubes were cast. Flyash, GGBFS, and alccofine were mixed homogenously; then, the fine aggregates and the coarse aggregates were added to the binder material and mix continued for five minutes. The calculated quantities of pre-mixed alkaline solution, water and superplasticizer was mixed with the dry mix proportions. The mix continued for another five minutes until the mix attains the uniformity. The fresh geopolymer concrete was free from the segregation and bleeding. The prepared geopolymer concrete was poured into cube mould of size $100 \times 100 \times 100$ mm in three different layers, and the concrete was vibrated using the vibrating table for 20–40 s to remove the entrapped air in the concrete. After 24 h of rest period, the concrete cubes were cured at ambient temperature for 7, 28, and 56 days. The concrete cubes were tested using the compressive strength testing machine of capacity 2000 kN, and the load of 2.5 kN/s was applied till the failure of specimen.

Table 2 Details of mix proportions

Mix ID	Flyash (kg/m³)	GGBS (kg/m³)	Alccofine (kg/m³)	Aggregates (kg/m³)		Molarity NaOH	Alkaline solution (kg/m³)	Water (kg/m³)	Superplasticizer (kg/m³)
				Coarse	Fine				
0.5	137.9 (35)	197 (50)	59.1 (15)	1108	739	0.5	157	59	5.9
1	137.9 (35)	197 (50)	59.1 (15)	1108	739	1	157	59	5.9
2	137.9 (35)	197 (50)	59.1 (15)	1108	739	2	157	59	5.9
4	137.9 (35)	197 (50)	59.1 (15)	1108	739	4	157	59	5.9
6	137.9 (35)	197 (50)	59.1 (15)	1108	739	6	157	59	5.9
8	137.9 (35)	197 (50)	59.1 (15)	1108	739	8	157	59	5.9
10	137.9 (35)	197 (50)	59.1 (15)	1108	739	10	157	59	5.9

4　Results and Discussion

4.1　Compressive Strength

A series of seven ternary blended geopolymer concrete mixes synthesized with different NaOH molarity were prepared to determine the compressive strength of geopolymer concrete. For each mix, three cubes were tested and the average of the three cubes was taken as crushing strength. The details of the compressive strength results are mentioned in the Table 3. From the results of compressive strength, it can be seen that the mix having 0.5 M of NaOH attained a low compressive strength of 39.3 MPa at 28 days due to the weak chemical reactions. The obtained results were similar to that of previous researcher Puertas et al. [11]. The mix with 10 M NaOH attained the highest compressive strength of 65.3 MPa at 28 days due to the effective leaching of silica, and alumina. From these results, it can be concluded that the compressive strength of ternary blended geopolymer concrete is influenced by the molarity of NaOH in the alkaline solution. NaOH molarity controls the release rate of silicates and aluminates in the initial dissolution [8]. At higher molarity of NaOH, the leaching of silica and alumina enhanced the compressive strength of geopolymer concrete [19]. The percentage increase in compressive strength of geopolymer mixes with 0.5–10 M NaOH is 66%. It is suggested from the results, the mixes having more than 50% slag low molarity are sufficient to produce the high compressive strength of 60 MPa. Later, age compressive strength at 56 days was observed for the geopolymer concrete mixes with different molarity of NaOH. The compressive strength of ternary blended geopolymer concrete increased in the range of 42.2–67.2 MPa at 56 days with increase in the molarity of NaOH from 0.5 to 10 M. It is observed in all the geopolymer mixes that with an increase in the age of the geopolymer concrete compressive strength also increased. The percentage increase in compressive strength of ternary blended geopolymer concrete mixes from 28 to 56 days was relatively less, upon comparing with 7–28 days strength.

Table 3 Compressive strength and kinetic ratios of geopolymer concrete

Mix Id	7 days (MPa)	28 days (MPa)	56 days (MPa)	SiO_2/Na_2O	Al_2O_3/Na_2O	H_2O/Na_2O
0.5	38.7	39.3	42.2	11.85	2.54	20.36
1	47.6	49.5	50.4	11.43	2.45	19.51
2	55.1	60	63.5	10.62	2.27	16.04
4	54.16	64.9	67.8	9.5	2.03	15.68
6	55.5	58.4	61	8.65	1.84	13.94
8	58.6	65.1	65.8	7.99	1.71	12.6
10	66	65.3	67.2	7.46	1.60	11.54

4.2 Comparing the Compressive Strength of Different Mixes with Kinetic Ratios of Geopolymer Mixes

It was observed from the Table 3 and Fig. 3, with the increase in NaOH concentration, Na_2O content in the mixes increased, these are responsible for dissolution of aluminates and silicates in the binder materials. In the slag-based mixes, Na_2O content is partly absorbed by the calcium silicate hydrate gel (C–S–H) and the Na_2O helps in balancing the OH^- anions during the hydration of slag [20]. With the increase in NaOH concentration, there is a considerable decrease in H_2O content in the mixes. The decrease in H_2O content is responsible for the increase in compressive strength of the geopolymer mixes with higher molarity of NaOH. In addition to that, increasing NaOH molarity in the ternary blended geopolymer mixes, the compressive strength was increased due to a decrease in the kinetic ratios of SiO_2/Na_2O, Al_2O_3/Na_2O and H_2O/Na_2O. It is observed that with increase in the molarity of NaOH from 0.5 to 10 M the SiO_2/Na_2O ratio decreased by 4.39, Al_2O_3/Na_2O ratio decreased by 0.94 and $H2O/Na_2O$ decreased by 8.82. The decrease in kinetic ratios is responsible for increase of compressive strength with increase in molarity of NaOH.
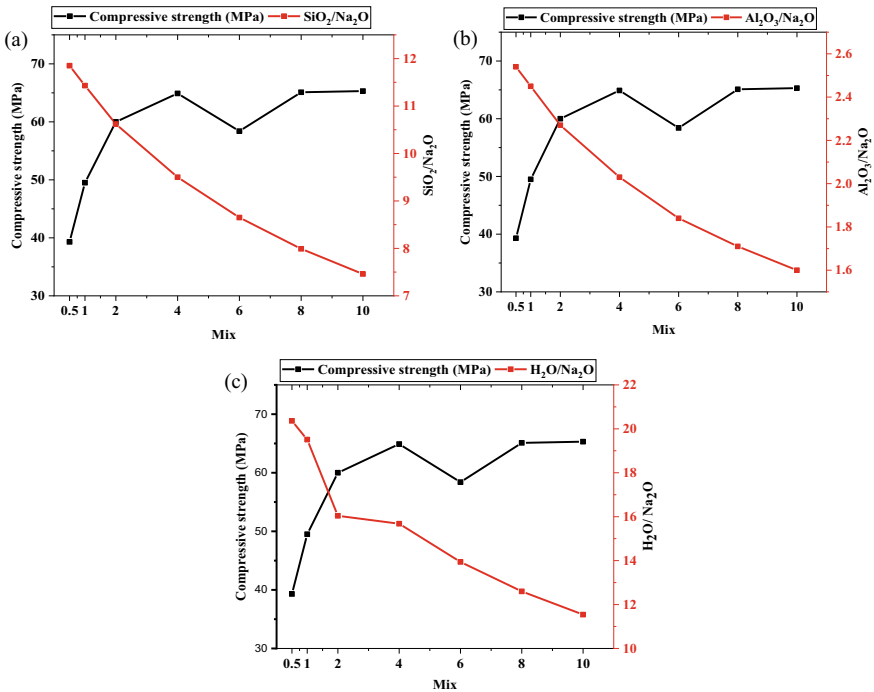
Fig. 3 Comparing the 28-day compressive strength with kinetic ratios. **a** SiO_2/Na_2O ratio, **b** Al_2O_3/Na_2O ratio, **c** $H2O/Na_2O$ ratio

5 Cost Analysis of Ternary Blended Geopolymer Concrete

The cost analysis of geopolymer concrete with different molarities of NaOH in the alkaline solution was carried out to find the economic feasibility to the construction industries. The rates of the material are taken from the standard schedule rates. The rates of the different materials are mentioned in Table 4.

From Table 5, the cost analysis of ternary blended geopolymer concrete with different molarities of NaOH in the alkaline solution was calculated for 1m^3 of concrete. It is depicted from the cost analysis that by varying the NaOH concentration from 0.5 to 10 M, the marginal difference in the production cost of geopolymer concrete is less. The percentage increase in the production cost from 0.5 to 10 M molarity geopolymer concrete is 8.3%; however, the increase in compressive strength is about 66%.

Table 4 Details of rates of materials

Material	Rupees	Unit
Flyash	72	m^3
GGBFS	2	kg
Alccofine	5	kg
Coarse aggregate	1065	m^3
Fine aggregate (M-sand)	600	m^3
Sodium silicate	9	kg
Sodium hydroxide	25	kg
Superplasticizer	200	kg

Table 5 Cost analysis of ternary blended geopolymer concrete with different NaOH molarity

Materials	Quantity (kg/m^3)	0.5 (₹)	1 (₹)	2 (₹)	4 (₹)	6 (₹)	8 (₹)	10 (₹)
Flyash	137.9	8.256	8.256	8.256	8.256	8.256	8.256	8.256
GGBFS	197	394	394	394	394	394	394	394
Alccofine	59.1	295.5	295.5	295.5	295.5	295.5	295.5	295.5
CA	1108	808.8	808.8	808.8	808.8	808.8	808.8	808.8
FA	739	295.6	295.6	295.6	295.6	295.6	295.6	295.6
SS	112.5	1012.5	1012.5	1012.5	1012.5	1012.5	1012.5	1012.5
SH	45	22.35	43.67	84.57	160.97	232.35	296.42	356
SP 430	5.9	1180	1180	1180	1180	1180	1180	1180
Total cost (₹)		4017	4038	4079.2	4155.6	4227	4291	4350.6

6 Conclusion

- Effective utilization of industrial by-products can replace the OPC completely and helps in making the concrete eco-friendly material.
- Incorporating alccofine in the ternary blended geopolymer concrete attained high strength concrete at ambient temperature. The presence of high glass content and ultrafine size helps in attaining the early strength of 95% in 7 days.
- Blending flyash with GGBFS and alccofine, low molarity NaOH is suggested to attain the required strength properties at ambient temperature. The production cost increases with increase in the NaOH concentration.
- Higher molarities of NaOH in geopolymer concrete attained high strength, when compared with the lower NaOH molarities due to the difference in the leaching of aluminates and silicates from the binder material.
- With the increase in the NaOH concentration, Na_2O content in the mix is increased and the H2O content is decreased in the geopolymer matric, and these are responsible for the strength gain and strength reduction concerning for NaOH molarity.
- With an increase in the NaOH molarity from 0.5 M to 10 M molarity, SiO_2/Na_2O, Al_2O_3/Na_2O and H2O/Na_2O decreased considerably. The reduction in the kinetic ratios improved the compressive strength from 0.5 to 10 M NaOH concentration.

References

1. Singh B, Ishwarya Gupta GM, Bhattacharyya SK (2015) Geopolymer concrete: a review of some recent developments. Constr Build Mater 85:78–90
2. McLellan BC, Williams RP, Lay J, Van Riessen A, Corder GD (2011) Costs and carbon emissions for geopolymer pastes in comparison to ordinary Portland cement. J Clean Prod 19:1080–1090
3. Chuah, Duan WH, Pan Z, Hunter E, Korayem AH, Zhao XL, Collins F, Sanjayan JG (2016) The properties of flyash based geopolymer mortars made with dune sand Mater Des 92:571–578
4. He P, Wang M, Shuai Fu, Jia D, Yan S, Yuan J, Jia Huan Xu, Wang PF, Zhou Yu (2016) Effects of Si/Al ratio on the structure and properties of metakaoline based geopolymer. Ceram Int 42:14416–14422
5. Mehta A, Siddique R (2016) An overview of geopolymers derived from industrial by-products. Constr Build Mater 127:183–198
6. Akcaozoglu S, Atis CD (2011) Effect of granulated blast furnace slag and fly ash addition on the strength properties of lightweight mortars containing waste PET aggregates. Constr Build Mater 25(10):4052–4058
7. Islam A, Alengaram UJ, Jumaat MZ, Bashar II (2014) The development of compressive strength of ground granulated blast furnace slag-palm oil fuel ash-fly ash based geopolymer mortar. Mater Des 56:833–841

8. Duxson P, Fernandez-Jimenez A, Provis JL, Lukey G, Palomo A, Van Deventer J (2007) Geopolymer technology: the current state of the art. J Mater Sci 42(9):2917–2933
9. Davidovits J (2008) Geopolymer Chemistry and Applications, 2nd edn. Geopolymer Institute, Saint-Quentin, France
10. Hardjito D, Cheak CC, Ing CHL (2008) Strength and setting times of low calcium flyash based geopolymer mortar. Modern Appl Sci 2(4):3–11
11. Puertas F, Martinez-Ramirez S, Alonso S, Vazquez T (2000) Alkali-activated fly ash/slag cement strength behaviour and hydration products. Cem Conc Res 30:1625–1632
12. Bakharev T (2005) Geopolymeric materials prepared using class F fly ash and elevated temperature curing. Cem Conc Res 35:1224–1232
13. Nath P, Sarker PK (2012) Geopolymer Concrete for Ambient Curing Condition. In: The Australasian structural engineering conference. Perth, Western Australia
14. Palomo A, Fernandez-Jimenez A, Kovalchuk G, Ordonez LM, Naranjo MC (2007) OPC fly ash cementitious systems: study of gel binders produced during alkaline hydration. J Mater Sci 42:2958–2966
15. Sathonsaowaphak A, Chindaprasirt P, Pimraksa K (2009) Workability and strength of lignite bottom ash geopolymer mortar. J Hazard Mater 168(1):s44-50
16. IS 383 (2002) Specifications for coarse and fine aggregates from natural sources for concrete. Bureau of Indian Standards, New Delhi, India
17. Lloyd NA, Rangan BV (2010) Geopolymer concrete with fly ash. In: Second international conference on sustainable construction materials and technologies. Ancona, Italy.
18. IS 516 (2004) Methods of tests for compressive strength of concrete. Bureau of Indian Standards, New Delhi, India
19. Rattanasak U, Chindaprasirt P (2009) Influence of NaOH solution on the synthesis of fly ash geopolymer. Min Eng 22(12):1073–1078
20. Wang SD (2000) The role of sodium during the hydration of alkali-activated slag. Adv Cem Res 12(2):65–69

Low-Velocity Impact Behaviour of Novel Steel Fibrous Grouted Aggregate Concrete

T. Abirami, M. Loganaganandan, and G. Murali

Abstract This investigation explores the impact behaviour of novel steel fibrous grouted aggregate concrete (SFGAC) subjected to falling mass impact. The making of SFGAC comprises high fibre and coarse aggregate content with respect to conventional fibre-reinforced concrete (CFRC). Initially, the steel fibres and coarse aggregates were thoroughly mixed and filled into the moulds; subsequently, a cement slurry injection is prepared with cement, fine aggregate and water. All samples were tested using drop mass impact in conformity with ACI Committee 544. Ten concrete mixes were formulated with 3D and 5D hooked end steel fibres, where fibre content differs between 1.0% and 5% for CFRC and SFGAC. The number of blows to induce crack initiation and ultimate crack, energy absorption capability at crack initiation and ultimate crack, failure patterns and compressive strength are examined and conferred. The result shows that the specimen with SFGAC attained better impact strength than the CFRC specimen. Consequently, based on the annotations, a novel SFGAC is a tough competitor for various applications owing to effortlessness production technique with higher impact strength.

Keywords Impact · Fibres · Impact energy · Failure · Grout

1 Introduction

In worldwide, concrete is a versatile civil building material, and it is widely used in both civilian and military infrastructure (Asrani et al., [1]. However, the plain concrete possesses high rigidity, relatively low tensile strength, weak crack resistance; as a result, it exhibits brittle failure [2]. Incorporation of steel fibres into concrete matrix mitigates its brittleness and increases the impact strength up to fifteen times [3–5],Qian and Stroeven, [6] by delayed crack formation [7] and limited crack propagation [8] and reduced crack tip opening displacement inside the concrete [7]. The enlargement and growth of micro-scale cracks produced in concrete makes it

T. Abirami · M. Loganaganandan · G. Murali (✉)
School of Civil Engineering, SASTRA Deemed To Be University, Thanjavur, India
e-mail: murali@civil.sastra.edu

unable to overcome the internal stress within the material [9]. The fibres themselves bear some of these internal stresses while the excessive stresses are imparted to the vicinity in the matrix, and this behaviour attributes to the FRC being remarkable over the non-fibrous concrete [10],Nystrom et al., [11].

SFGAC is a novel type of concrete, and its impact response is superior as compared with CSFC. Therefore, SFGAC can be rated as an improved fibre rein-forced composite that owns exceptional mechanical properties, ductility and high energy absorption capacity [8, 12, 13]. Mostly, CSFC holds [8, 13–15] 0.5–2.0% of steel fibres, while SFGAC holds 2–6% of fibres [13–15]. Due to the combined effect of increased steel fibre content, manufacture of SFGAC with conventional mixing process becomes impossible [17]. To alleviate such complications, a novel manufacturing procedure has been developed by the investigators. The manufacture of SFGAC includes high fibre and coarse aggregate content with respect to CSFC. Firstly, the fibres and coarse aggregates are mixed together thoroughly and filled into the moulds,subsequently, a cement slurry prepared with cement, fine aggregate and water is injected. The gravity method of grouting was adopted to inject the cement slurry with light vibration [18]. SFGAC holds 50% more volume of coarse aggregate with respect to CSFC Abdelgader [19].

Therefore, SFGAC is an innovative concrete with greater compressive strength and showed higher toughness [12]. Due to the high fibre content, fibre bridging micro-cracks can alleviate the stress concentration, thereby postponing the crack proliferation [20]. The crack path of SFGAC is crooked due to random fibre orientation and higher fibre content, resulting in greater energy requirement for fibre de-bonding and pull-out Ostertag and Yi [21]. SFGAC can offer excellent substitute for conventional fibrous concrete owing to its advanced manufacture method that leads to the broad implementation in current building of infrastructure.

2   Research Significance

Numerous studies[22, 23] are existing in literature relevant to the impact response of CFRC, while there are only limited studies reporting the impact behaviour of SFGAC subjected to falling mass impact. Despite a plethora of the previous researches, the impact behaviour of novel steel fibrous grouted aggregate concrete under falling mass collision was not examined so far and the full potential of SFGAC under falling mass impact is still not entirely explored. The research in this field of study was limited over the last decade, since it was not given major importance. In this work, an effort was made to evaluate the impact response of SFGAC under falling mass impact.

Fig. 1 Appearance of hooked end steel fibres **a** 3D and **b** 5D

3 Experimental Program

3.1 Raw Materials

Ordinary Portland Cement (OPC) of grade 53 cement was used in accordance with IS:8112 [24]. M-sand was used as fine aggregate owing to the insufficiency of river sand. M-sand exhibited equal mechanical performance to that of river sand. Coarse aggregate of nominal size 16 mm was used with the specific gravity of 2.65 inconformity with IS 383–1970 [25]. Two different steel fibres were used,3D and 5D hooked end fibres. The geometry of the both steel fibres is shown in Fig. 1. The tensile strength of 3D and 5D fibres was 1150 and 2350 MPa, respectively.

3.2 Mix Proportioning

Ten mixes were prepared using the 3D and 5D steel fibres, the water–binder ratio (w/b) and sand–binder ratio (s/b), in case of SFGAC, were kept constant as 0.45 and 1, respectively. In order to increase the workability and to make the grout flowable, a high-performance superplasticizer (Master Glenium 8233) was utilized. The grout was prepared to meet the efflux time as per ASTM C939/C939M—16a [26]. Figure 2a shows the production technique of conventional fibre-reinforced concrete. The steel fibre of 1 and 1.5% in both 3D and 5D was mixed randomly, and concreting was done by conventional method. For the SFGAC mixtures, 4% and 5% fibre content was used. Figure 2b demonstrates the production technique of SFGAC, fibres and coarse aggregate are filled into the moulds, thereby cement slurry prepared with cement, fine aggregate and water is injected to fill the voids. Table 1 shows the details of the mix proportion.

Fig. 2 Production technique **a** CFRC **b** SFGAC

Table 1 Composition of mixes

Mix ID	s/b ratio	w/b ratio	Cement (kg/m^3)	FA (kg/m^3)	CA (kg/m^3)	Fibre dosage (%)	SP (%)
PC	–	0.45	345	888	1131	0	0.3
F-1-5D	–		345	888	1131	1.5	0.5
F-1.5-5D	–		345	888	1131	1.5	0.9
F-0–0	1.0		–	–	–	0	0.4
F-4-5D			–	–	–	4	0.4
F-5-5D			–	–	–	5	0.4
F-1-3D	–		345	888	1131	1.0	0.4
F-1.5-3D	–		345	888	1131	1.5	0.4
F-4-3D	1.0		–	–	–	4	0.4
F-5-3D			–	–	–	5	0.4

3.3 Testing Set-Up for Specimens

To assess the compressive strength and impact strength, 150 mm size cubical specimens and cylindrical specimen of 150 mm diameter and 65 mm height, respectively, were employed. The mould is properly gutted, and oil was applied on all sides of the mould for ease of removal of concrete after fabrication. After casting, the specimens were allowed for standard curing around 20–22 °C for a period of 28 days before testing.
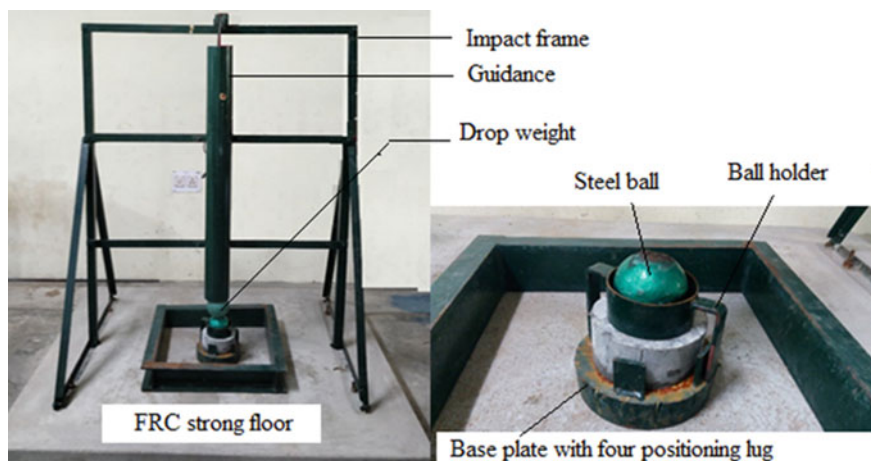
Fig. 3 Falling mass impact test set-up

3.4 Test Arrangements

The compression strength test was performed on 150 mm cubes in conformation with IS: 516–1959 [27]. The impact resistance of the specimens were evaluated based on the ACI Committee Guidelines [28]. As per the recommendations of ACI Committee 544, impact loading is imparted by a steel ball having a mass of 4.45 kg released repeatedly from a height of 457 mm on the specimen's top surface of the specimen. The number of impact inducing initial crack (X_1) and number of impact inducing failure (X_2) were observed as strength at initial crack and ultimate strength, respectively. Figure 3 illustrates the test set-up for the falling mass impact. The delivered impact energy per impact was evaluated from Eq. (1)

$$\text{Impact energy} = n \times m \times g \times h \tag{1}$$

where n, number of impact; m, mass of steel ball; g, acceleration due to gravity; and h, drop height.

4 Results and Discussion

4.1 Influence of Fibre on Compressive Strength

The strength under compression of CFRC specimens (F-1-5D, F-1.5-5D, F-1-3D, F-1.5-3D) and SFGAC specimens (F-4-5D, F-5-5D, F-4-3D, F-5-3D) was shown in Table 2. The compressive strength of CFRC specimens (F-1-5D, F-1.5-5D, F-1-3D,

Table 2 Summary of falling mass impact test results

Mix ID	Compressive strength (MPa)	Number of impact		Impact energy (J)		IDI
		X_1	X_2	X_1	X_2	
PC	34.24	21	36	427	732	1.71
F-1-5D	39.18	147	305	2991	6205	2.07
F-1.5-5D	43.25	172	374	3499	7609	2.17
F-0–0	40.85	29	58	590	1180	2.00
F-4-5D	53.85	383	1175	7792	23,905	3.07
F-5-5D	58.43	428	1358	8708	27,629	3.17
F-1-3D	37.23	128	285	2604	5798	2.23
F-1.5-3D	41.17	151	348	3072	7080	2.30
F-4-3D	52.03	362	1096	7365	22,298	3.03
F-5-3D	56.72	401	1263	8158	25,696	3.15

F-1.5-3D) was found to be 39.18, 43.25, 37.23 and 41.17 MPa, respectively. These values were 14.4%, 26.3%, 8.7% and 20.2% higher as associated with PC. Similarly, the compressive strength of SFGAC specimens (F-4-5D, F-5-5D, F-4-3D, F-5-3D) was found to be 53.85, 58.43, 52.03 and 56.72 MPa, respectively. These values were 31.8%, 43.0%, 27.3% and 38.8% higher compared to non-fibrous grouted specimen (F–0–0). From the obtained results, it is clear that SFGAC specimens containing high fibre content exhibited superior performance over CFRC specimens and the same trend was observed in the earlier research [29] (Fig. 4).
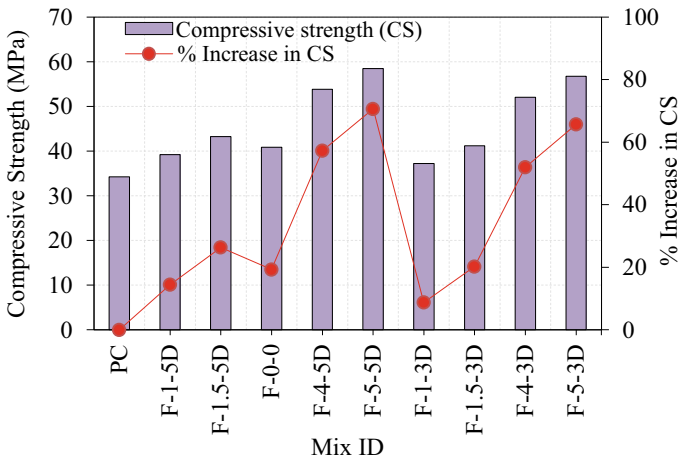
Fig. 4 Compressive strength of plain and fibrous concrete
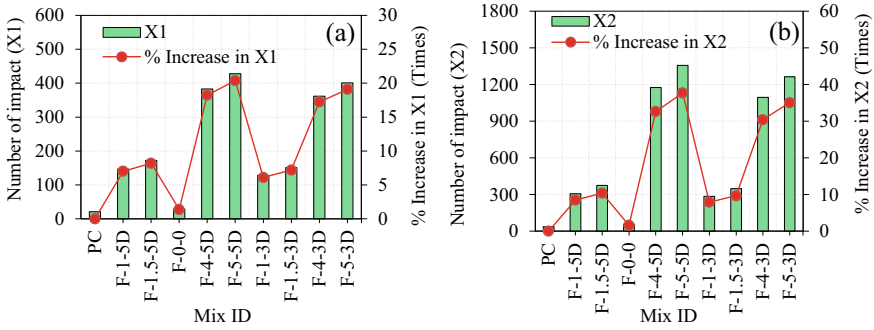
Fig. 5 Number of impact **a** X_1 **b** X_2

4.2 Influence of Fibre on Impact Strength

The ability of concrete to withstand the repeated blows and energy absorption defines its impact strength, and the X_1 and X_2 values were shown in Table 2. Also, the impact energy for all the specimens was calculated and shown in Table 2.

From Fig. 5a X_1 values for the F-1-5D, F-1.5-5D, F-1-3D and F-1.5-3D specimens (CFRC) were 147, 172, 128 and 151, respectively. There is a slight increase in X_1 by 7, 8.2, 6.1 and 7.2 times with respect to PC. Likewise, from Fig. 5b, the X_2 values of the CFRC specimens occurred at 305, 374, 285 and 348, respectively. An increment in X_2 values was observed by 8.5, 10.4, 7.9 and 9.6 times, respectively, with respect to PC. Therefore, F-1.5-5D specimen exhibited the superior performance among over all mixes. This is due to the high fibre content which helps in preventing propagation of cracks [29].

X_1 values for the F-4-5D, F-5-5D, F-4-3D and F-5-3D specimens were 383, 428, 362 and 401, respectively. By comparing with F–0–0 specimen, X_1 values were increased by 13.2, 14.8, 12.5 and 13.8 times for the F-4-5D, F-5-5D, F-4-3D and F-5-3D specimens, and it is illustrated in Fig. 5a. Similarly, X_2 values observed were 1175, 1358, 1096 and 1263 for the F-4-5D, F-5-5D, F-4-3D and F-5-3D specimens, respectively. The value of X_2 was enhanced by 20.2, 23.4, 18.9 and 21.7 times for the SFGAC specimens, respectively. It is clearly noted from Fig. 5, the F-5-5D specimen showed the highest impact strength as compared with other grouted specimens. This can be attributed to the higher fibre content and coarse aggregate, thereby the fibre balling effect is avoided completely in case of the novel production technique of SFGAC.

4.3 Comparison with CFRC Specimen and SFGAC Specimen

From the obtained results, the SFGAC specimens exhibit a significant increase in impact strength as compared to CFRC specimens. Also, the impact strength of
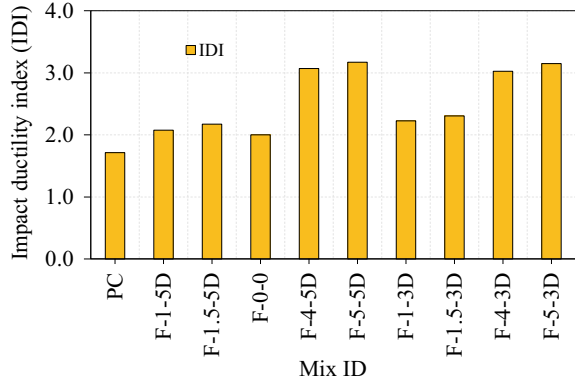
5D fibres shows superior strength characteristics in comparison with 3D fibre. The highest impact strength was attained in F-5-5D specimens owing to its higher fibre dosage and coarse aggregate content. On the other hand, the CFRC specimens also tend to possess some increase in the compressive strength but because of the limitations of fibre dosage and difficulty in distribution of fibres, achieving higher strength is difficult in case of CFRC.

4.4 Impact Ductility Index (IDI)

IDI is defined as the ratio of impact energy at failure and impact energy at initial crack. Figure 6 represents the IDI of CFRC and SFGAC specimens. IDI values of F-1-5D, F-1.5-5D, F-1-3D and F-1.5-3D specimens (CFRC) were 2.07, 2.17, 2.23 and 2.3, respectively. These values were much higher when compared with PC specimen which has the value of 1.71. Likewise, the IDI values for F-4-5D, F-5-5D, F-4-3D and F-5-3D specimens (SFGAC) were 3.07, 3.17, 3.03 and 3.15, respectively. These values have an immense increase when compared with non-fibrous grouted specimen (F–0–0). According to the results obtained, the SFGAC specimens exhibited superior performance in the post initial crack as compared with CFRC specimens. The graph clearly depicts the influence of fibres in post-crack resistance.

4.5 Cracking Pattern

Two distinct types of cracking patterns were observed in PC and fibrous concrete. The mode of failure observed in non-fibrous concrete was brittle which is shown in Fig. 7a, through d. Furthermore, the crack growth cannot be restricted in PC specimens, and thus cracks develop and made the specimen to break into pieces Asrani et al. [1, 2]. In case of fibrous concrete specimens, the failure pattern turned

(a) PC   (b) F-1-5D   (c) F-1.5-5D

(d) F-0-0   (e) F-4-5D   (f) F-5-5D

(g) F-1-3D   (h) F-1.5-3D   (i) F-4-3D

(j) F-5-3D
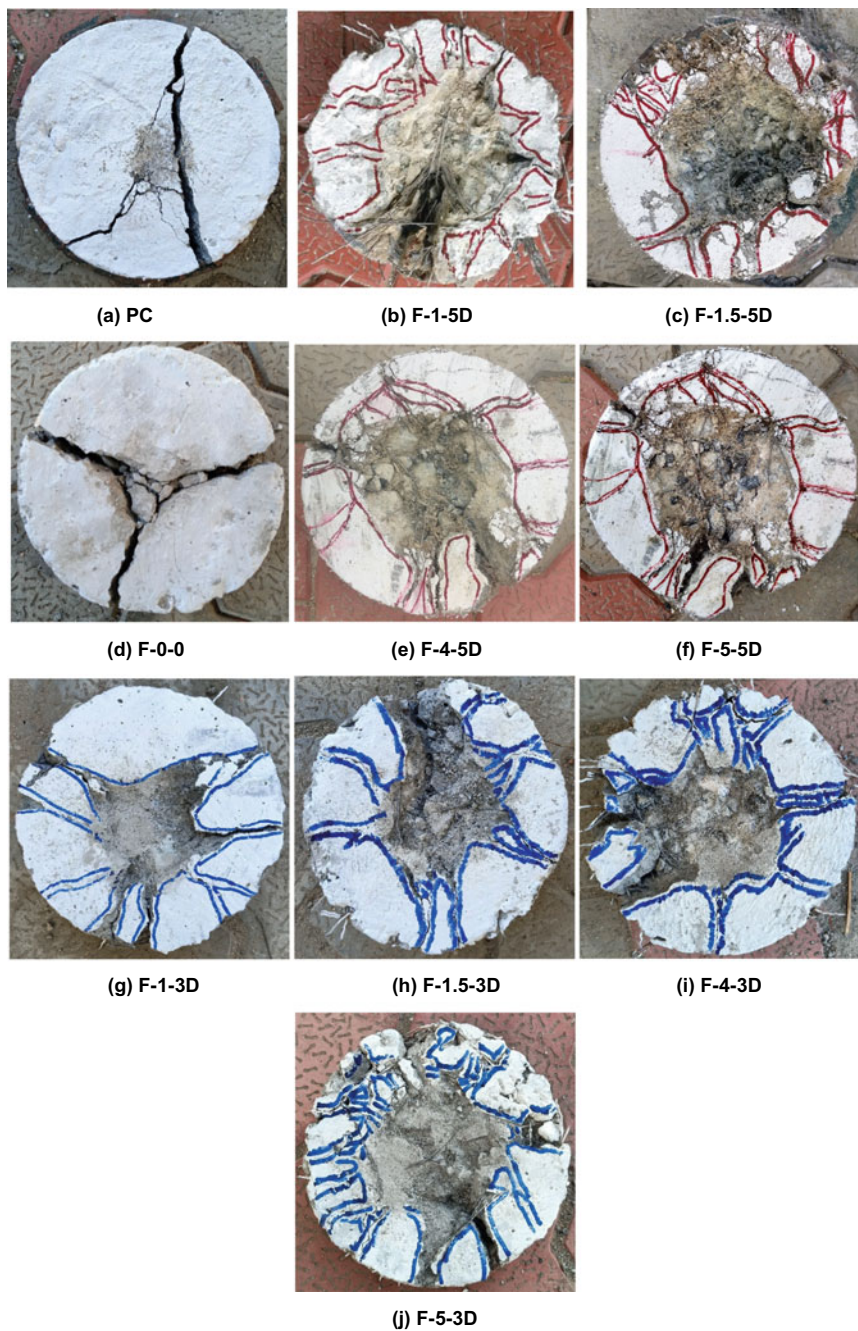
Fig. 7 Failure and cracking configuration under falling mass impact

from brittle to ductile is shown in Fig. 7b, c, e to j. This is attributed to the fact that fibres possess good tensile strength and has good energy absorbing capacity. By assessing the cracking pattern under falling mass impact, it is clear that ductile failure is best suited as it gives an ample warning before failure by yielding [7] and [30]. Also, the fibres make the concrete to sustain more amount of impact load after the initiation of first crack [31].

5   Conclusions

The following conclusions were derived from the experimental test results.

1. In spite of steel fibre cost, SFGAC can provide cost effective since it contains about 50% additional coarse aggregate with reference to CFRC.
2. The compressive strength of SFGAC specimens was observed to be much greater with respect to CFRC specimens. The maximum compressive strength was found in F-5-5D specimen. This strength is increased by 70.6% with respect to PC specimen and 43.03% with respect to F–0–0 specimen.
3. In conventional method of fibre reinforcement, the maximum dosage of fibre is limited to 2% since higher fibre dosage causes fibre balling and difficulty in fibre placement. In contrast to CFRC, the SFGAC, the maximum fibre dosage is 6%, and it can be made without any placement difficulties. The increase in fibre content exhibited an enhancement in both compressive and impact strength.
4. There was a huge inflation in the number of impact inducing initial crack and failure in 5D fibres, which clearly depicts that incorporation of 5D fibres results in increased impact strength as compared to 3D fibres.
5. By incorporating steel fibres into the concrete, ductile type of failure is achieved which is very much preferable as it gives an ample warning before failure. Also the post-crack resistance and toughness get improved.

References

1. Asrani Neha P, Murali G, Parthiban K, Surya K, Prakash A, Rathika K, Chandru U (2019) A feasibility of enhancing the impact resistance of hybrid fibrous geopolymer composites: experiments and modelling. Constr Build Mater 203(13):56–68
2. Murali G, Santhi AS, Mohan Ganesh G (2014) Impact resistance and strength reliability of Fiber-reinforced concrete in bending under drop weight impact load. Int. J. Technol. 5(2):111–120
3. Song PS, Hwang S, Sheu BC (2004) Statistical evaluation for impact resistance of steel fibre-reinforced concretes. Mag. Conc. Res. 56(8):437–442
4. Dancygier AN, Yankelevsky DZ, Jaegermann C (2007) Response of high performance concrete plates to impact of non-deforming projectiles. Int J Impact Eng 34(11):1768–1779
5. Zhang X, Ruiz G, Elazim AMA (2015) Loading rate effect on crack velocities in steel fibre-reinforced concrete. Int J Impact Eng 76:60–66

6. Qian CX, Stroeven P (2000) Development of hybrid polypropylene-steel fibres reinforced concrete. Cem. Conc. Res. 30:63–69
7. Murali G, Muthulakshmi T, Nycilin Karunya N, Iswarya R, Hannah Jennifer G, Karthikeyan K (2017) Impact response and strength reliability of green high performance fibre reinforced concrete subjected to freeze-Thaw cycles in NaCl solution. Mater Sci Medziagotyra 23(4):384–388
8. Murali G, Venkatesh J, Lokesh N, Reddy NT, Karthikeyan K (2018) Comparative experimental and analytical modeling of impact energy dissipation of ultra-high-performance fibre reinforced concrete. KSCE J Civil Eng 22(8):3112–3119
9. Semsi Y, Hasan SA, Volkan T (2013) The effects of impact loading on the mechanical properties of the SFRCs. Constr Build Mater 41:68–72
10. Yazici S, Inan G, Tabak V (2007) Effect of aspect ratio and volume fraction of steel fibre on the mechanical properties of SFRC. Constr Build Mater 21:1250–1253
11. Nystrom U, Gylltoft K (2011) Comparative numerical studies of projectile impacts on plain and steel-fibre reinforced concrete. Int J Impact Eng 38:95–105
12. Nehdi ML, Najjar MF, Soliman AM, Azabi TM (2017) Novel steel fibre-reinforced preplaced aggregate concrete with superior mechanical performance. Cement Concr Compos 82(10):242–251
13. Sudarsana Rao H, Ghorpade VG, Ramana NV, Gnaneswar K (2010) Response of SIFCON two-way slabs under impact loading. Int J Impact Eng 37(4):452–458
14. Tuyan M, Yazıc H (2012) Pull-out behavior of single steel fiber from SIFCON matrix. Constr Build Mater 35(7):571–577
15. Sengul O (2018) Mechanical properties of slurry infiltrated fiber concrete produced with waste steel fibers. Constr Build Mater 186(10):1082–1091
16. Murali G, Ramprasad K (2018) A feasibility of enhancing the impact strength of novel layered two stage fibrous concrete slabs. Eng Struct 175(9):41–49
17. Kumar GS, Rajasekhar K (2017) Performance analysis of Levenberg-Marquardt and steepest descent algorithms based ANN to predict compressive strength of SIFCON using manufactured sand. Eng Sci Technol Int J 20(10):1396–1405
18. Najjar MF, Soliman AM, Nehdi ML (2014) Critical overview of two-stage concrete: properties and applications. Constr Build Mater 62(12):47–58
19. Abdelgader HS (1996) Effect of quantity of sand on the compressive strength of two stage concrete. Mag Concr Res 48(177):353–360
20. Magnusson J (2006) Fibre reinforced concrete beams subjected to air blast loading. Int J Concr Res 35(16):18–34
21. Ostertag CP, Yi CK (2007) Crack/fiber interaction and crack growth resistance behavior in microfiber reinforced mortar specimens. Mater Struct 40(7):679–691
22. Jeon S-J, Jin B-M (2016) Improvement of impact-resistance of a nuclear containment building using fiber reinforced concrete. Nucl Eng Des 304:139–150
23. Yoo D-Y, Banthia N (2019) Impact resistance of fiber-reinforced concrete—a review. Cem Concr Compos 104:103389
24. IS 8112–2013. Ordinary portland cement, 43 grade—specification, (second revision). Bur. Indian Stand, New Delhi
25. IS:383–1970. Specifications for coarse and fine aggregates—specification, (second revision). Bur. Indian Stand, New Delhi
26. ASTM C939, C939M—16a (2016) Standard test method for flow of grout for preplaced aggregate concrete (flow Cone Method). ASTM International, USA
27. IS 516 1959 Indian standard methods of tests for strength of concrete Bur. Indian Stand, New Delhi
28. ACI 304.1 (2005) Guide for the use of preplaced aggregate concrete for structural and mass concrete applications American Concrete Institute, USA
29. Murali G, Poka L, Parthiban K, Haridharan MK, Siva A (2019) Impact response of novel fibre-reinforced grouted aggregate rubberized concrete. Arabian J Sci Eng 44:8451–8463

30. Murali G, Santhi AS, Mohan Ganesh G (2016) Loss of mechanical properties of fiber-reinforced concrete exposed to impact load. Romanian J Mater 46(4):491–496
31. Murali G, Asrani NP, Ramkumar VR, Siva A, Haridharan MK (2019) Impact resistance and strength reliability of novel two-stage fibre-reinforced concrete. Arabian J Sci Eng 44(13):4477–4490

Compressive Strength of TBC at Elevated Temperatures with Different Cooling Regimes

Kunkulagunta Varun Teja and Thiruvadi Meena

Abstract It is a foregone conclusion that the manufacturing process of cement adds 5% of the annual anthropogenic global carbon footprint. Researchers have extensively used different types of mineral admixture include ground granulated blast slag, silica fume, metakaolin and fly ash in concrete to reduce the carbon footprints. This study used the sugar cane bagasse ash (SCBA) and silica fume (SF), a mineral admixture as partial replacements for cement, thereby resulting in the formulation of ternary blended concrete. The replacement of SF was maintained at a constant percentage of 10%, and the percentage of SCBA was varied between 0 and 30%, with an increment of 5%. The concrete cubes were prepared with different proportions of SCBA along with 10% of SF and exposed to elevated temperatures 200, 300, 500 and 700 °C and cooled using two cooling regimes, viz. water and air cooling. It was noticed that SCBA15SF10 TBC replacement of OPC had shown better performance at all temperatures when subjected to both air and water cooling.

Keywords Sugarcane bagasse ash · Silica fume · Elevated temperatures · Air cooling · Water cooling

1 Introduction

Ordinary Portland Cement (OPC) is the most desirable and widely used as a binding material in the preparation of concrete for several decades in civil engineering applications. The demand for cement is more than likely to increase still further. This results in a drastic increase in carbon footprint; hence, the consumption of cement in the construction industry must be reduced by partially replacing pozzolanic materials in place of cement. The pozzolanic materials need to be not only cost-effective but also should provide increased workability, better strength characteristics and excellent durability of concrete. Aldred et. al. [1] the Chairperson of American Concrete Institute (ACI), laid down the guidelines for the use of SF in concrete. In SF, most

© The Editor(s) (if applicable) and The Author(s), under exclusive license to Springer Nature Singapore Pte Ltd. 2021

227

of its particles should be smaller than 1 mm having an average diameter of 0.1 μm, which is just about one of the hundredth size of an average cement particle. SF in fresh concrete reduces the bleeding and enhances the cohesiveness. Calcium ion present in SF combines to form calcium-silicate-hydrate (C–S–H) through pozzolanic reaction. Cement replaced with 5–10% of SF gives better results in strength. Uchikawa et. al. [2] proved that 10% by mass replacement of SF bonded up almost three times more alkali in C–S–H. Bache [3] demonstrated that the use of silica fume reduced the water content because the space between cement particles is occupied by silica fume instead of water. Bhanja and Sengupta [4] have concluded that SF replacement of cement gives better compressive strength results and as well as tensile strength over the concrete without any cement replacement. Vishal and Pranita [5] have investigated the effect of SF on concrete to determine the ideal replacement percentage evaluation between consistent concrete and concrete containing SF. It was reported that when cement was replaced by 10% of SF gave better results, but further replacement of cement by SF gave lesser strength. From the above results, it was obvious that the substitution of cement with SF in the range of 5–15% could give better results in terms of compressive strength.

Ganesan et. al. [6] have carried out an experimental investigation on the use of SCBA as additional cementitious material. The authors investigated the mechanical properties of TBC (i.e. compressive and split tensile strength of concrete) and assessed the durability tests (i.e. sorptivity, water absorption and chloride diffusion test) of concrete containing different percentages (0, 5, 10, 15, 20 and 25%) of SCBA. It was concluded that the concrete containing 20% of SCBA could give better results in terms of compressive and split tensile strength of concrete. Replacing bagasse ash with cement gives early strength and exhibits a reduction in water permeability. This is due to the fineness of bagasse ash that led to an increase in water consumption too. Fairbairn et. al. [7] have studied the thermal and mechanical properties of replacing cement by SCBA with 5 to 20%, indicating that SCBA can be used as an admixture for cement manufacturing. Corderio et. al. [8, 9] have investigated the effect of calcination temperature on the pozzolanic activity of SCBA and presented the outcomes of the process of SCBA under organized calcination temperature conditions to obtain ingredients with ideal pozzolanic activity. Ribeiro and Marcio [10] demonstrated that sugarcane samples were burnt in an exposed electric oven at a heating rate of 10 °C/min at 350 °C for three hours, and at varying temperatures in the range from 400 to 800 °C for additional three hours. At all the temperatures, the pozzolanic action, loss on ignition of the vestiges and structural state of silica were determined. Bahurudeen and Manusanthanam [11] have studied the performance evaluation of SCBA-based cement for durable concrete and found that SCBA, in concrete, ominously enriched its durability performance. This was confirmed by conducting several tests such as chloride conductivity test, rapid chloride penetration test, sorptivity test and torrent air permeability test. They showed that prominent reduction in concrete permeability with an increase in SCBA replacement was due to the pozzolanic effect of SCBA and augmentation in pore structure as a result of pore refinement. From the past literature reviews, it can be seen that the SCBA has good pozzolanic activity and identified as the replacement material for cement. Moreover,

SCBA is burnt in kilns usually at a temperature of 600 °C and sometimes at high temperatures that depends upon the moisture content, and later, it is taken to mill in order to make it on par with of fineness of the cement.

Arioz [12] studied the properties of concrete under elevated temperatures. The author explained the loss of weight and the variations of the surface of concrete specimens at different elevated temperatures. The results showed that increasing the temperature increased the damage level of the specimen. It was also observed that more numbers were observed on the surface of concrete specimens at 600 °C. Chan et.al. [13] have studied the compressive strength and pore structure of high performance concrete exposed at a high temperature of up to 800 °C. They concluded that the high-performance concrete attained higher residual strength than the conventional concrete. The similarity of pore structure, together with porosity and pore size distribution, had shown the deprivation of mechanical properties of high-performance concrete subjected to high temperatures.

The authors identified sugar cane bagasse ash (SCBA), which is obtained as a surplus product from the sugarcane industry, as one of the replacement materials. Furthermore, silica fume (SF) was selected as the other mineral admixture to enhance the strength and durability of concrete. It also serves as a partial replacement for cement as well [14]. The resultant concrete mix is termed as ternary blended concrete (TBC). This study focused on exposing the TBC specimens to different higher temperature levels and subsequently cooling them down to room temperature under two different regimes, i.e. air cooling (normally leaving to air) and water cooling (by jetting with water pumps).

2   Materials

Ordinary Portland Cement with 53 grade cement was used for the entire research work, and special care has been taken to preserve it by tightening the bags to prevent it from getting affected by humidity and atmospheric moisture. Tests include specific gravity [21], fineness [22], soundness [23] and setting time [24] of cement were conducted to determine the physical properties of cement. The physical properties of cement material are listed in the following Table 1.

Table 1 Physical properties of ordinary Portland cement

Test		Value
Specific gravity		3.15
Fineness of cement		8.53%
Soundness test (Le Chatelier)		4 mm
Setting time	Initial	180 min
	Final	396 min

Table 2 Physical properties of SCBA

Tests	Value
Density	$575Kg/m^2$
Specific gravity	2.2
Mean size particle	0.1–0.2 μm
Mean specific area	2500 m^2/kg
Particle shape	Spherical

Table 3 Chemical properties of SCBA (obtained from NCS Sugar Ltd.)

Chemical composition	Composition (%)
SiO_2	72
Al_2O_3	16
K_2O	4.1
Na_2O	3.2
MgO	1.8
CaO	1.5
Fe_2O_3	0.5
TiO_2	0.5
Free moisture	0.4

The SCBA was obtained from NCS Sugar Limited located at Bobbili, Vizianagaram District of Andhra Pradesh State, India. The ash was intended to operate with a boiler of travelling gate type with outlet steam parameters of 87 kg/cm^2 and 515 °C using bagasse ash as a main fuel. After that, the ash was grounded in a mill in order to make it as finer than cement fineness. The following Tables 2 and 3 depict the physical and chemical properties of SCBA.

Silica fume is a non-crystalline polymorph of silicon dioxide. The size of the powder is ultrafine which obtained as a by-product of the ferrosilicon alloy and silicon production; the particles comprised of spherical in shape with an average diameter of 150 nm. The physical and chemical properties of silica fume are taken from Astra chemicals, Chennai, and the properties are listed in Tables 4 and 5.

The locally available crushed granite was used as the coarse aggregate in the preparation of concrete. The course aggregate was sieved with a 20 mm size sieve and washed to remove dirt and dust. Table 6 depicts the physical properties of the coarse aggregates.

Table 4 Physical properties of silica fume

Tests	Value
Specific surface area	20 cm^2/gm
Bulk density	600–50 kg/m^3
Specific gravity	1.9

Table 5 Chemical properties of silica fume

Chemical properties	Composition in %
Silica (SiO_2)	93.04
Alumina (Al_2O_3)	0.0430
Ferric oxide (Fe_2O_3)	0.44
Titanium oxide (TiO_2)	0.0011
Sodium oxide (Na_2O)	0.003
Loss on ignition	2.24
Calcium oxide (CaO)	0.001

Table 6 Physical properties of coarse aggregate

Tests conducted	Value
Specific gravity	2.64
Water absorption	3.72%
Fineness modulus	7.3

The river sand compliance to Zone-II was used as a fine aggregate. It was confirmed that the fine aggregate was inert, clean and free from organic matters such as clay and silt. All the tests were carried out according to IS-2386(Part 3):[25]. The physical properties of fine aggregates are depicted in Table 7.

Superplasticizer, namely Conplast SP-430 from FOSROC Company, was used in order to attain good workability of the mix for the chosen water–cement (w/c) ratio of 0.48. The specific gravity of SP was varied between 1.221 and 1.224 at 30 °C in the absence of chloride. Air entrained in the mixes was approximately taken as 1.0%. The physical properties of Conplast SP-430 are depicted in Table 8.

Table 7 Physical properties of fine aggregates

Properties	Value
Specific gravity	2.62
Fineness modulus	2.69

Table 8 Physical properties of Conplast SP-430 as per the suppliers

Description	Property
Appearance	Brown liquid
Specific gravity [BSEN 934–2]	1.179 @ 22 °C + 2 °C
Alkali content [BSEN 934–2]	Typically lesser than 55 g. Na_2O equivalent/litre of admixture

3   Experimental Program

The mineral admixtures SCBA and SF, in this study, were replaced with cement at different replacements. The concrete grade of M30 was prepared using IS: 10262:2009, and the mix proportions used to cast were shown in Table 9. A total of 7 series of $150 \times 150 \times 150$mm specimens were prepared with different percentage replacements of mineral admixtures along with control concrete, and the mixes were named as shown in Table 10.

After collecting all the ingredients required for the mix, the ingredients such as cement, SCBA and SF were mixed for half an hour with hand in order to make a homogeneous mix and were cast and placed in the moulds. After 24 h, the specimens were demoulded and placed in curing tank for a period of 28 days. Then, the cured specimens were dried well before exposed to elevated temperatures of 200, 300, 500 and 700 °C up to the time period of 1 h after reaching the target temperature.

The specimens obtained from the furnace were cured in two different ways namely air cooling and water cooling. Air cooling is carried out by leaving the specimens in the air for gradually cooling up to room temperature, and water cooling is made by forcing water on to the specimens. Later, the compressive strength test was conducted according to Indian Standard IS: 516 [23–26]. The compressive strength of concrete can be determined by load obtained divided by the area of specimen.

Table 9   Mix proportion of ternary blended concrete as per IS: 10262:2009

OPC (kg)	SCBA (kg)	Water (L)	Fine aggregate (kg)	Coarse aggregate (kg)
340	–	163	736.2	1231.2

Table 10   Mix proportion of TBC with SCBA and SF

Series	SCBA replacement for OPC (%)	SF replacement for OPC (%)
SCBA0SF0	0	0
SCBA5SF10	5	10
SCBA10SF10	10	10
SCBA15SF10	15	10
SCBA20SF10	20	10
SCBA25SF10	25	10
SCBA30SF10	30	10

4 Results and Discussions

4.1 Weight Loss

The specimens were weighed prior to placing in the furnace. After exposed to temperature, the specimens were weighted and cooled at different cooling regimes. The difference in weight loss was measured. Figures 1 and 2 show the weight loss of specimens for air and water-cooling regimes. The percentage of weight loss at temperature 700 °C was relatively greater than control specimen at room temperature. It shows that increasing the temperature leads to the loss of weight in concrete specimen. This is due to the loss of water present in the cement matrix. Compared to water-cooling specimens, there is a 20% more loss at air-cooling specimens at the temperature rate of 700 °C. At 500 °C, the weight loss for the mix SCBA10SF10, SCA20SF10 at air cooling is almost same. This indicates that the loss of water for those mixes is low even at high temperatures.
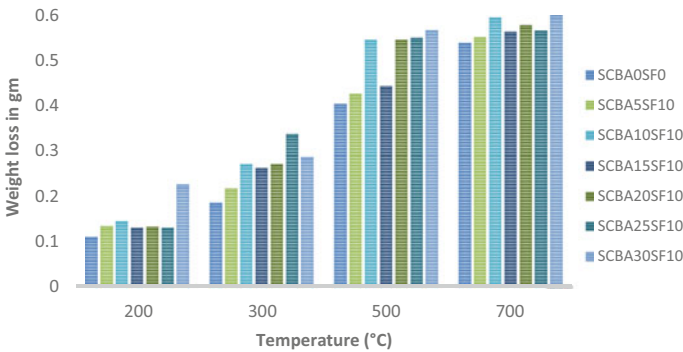

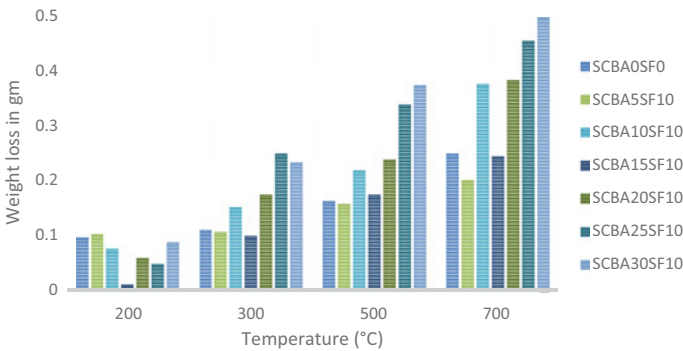**Fig. 1** Weight loss in air-cooled specimens

Fig. 2 Weight loss in water-cooled specimens

Normal Concrete   Air Cooling Specimen   Water Cooling Specimen

Fig. 3 Colour change of specimens (specimen SCBA15SF10)

- From the above Figs. 1 and 2, it is observed that the weight loss of the specimen increased as the exposure temperature increased.
- The results also show that reduction of weight loss for the case of 15% SCBA and SF10% replacement of OPC is lesser than the other mixes.
- It seems that for the mix SCBA15SF10, the densification of concrete was improved, and hence, the chances for the discharge of moisture were lesser compared to other mixes.
- At different percentage replacements, it is clearly observed the weight loss is more in 700 °C. This is due to the total disintegration of C-S–H gel [15] (Fig. 2).

Figure 3 shows the colour change of SCBA15SF10 mix specimens of room temperature, air-cooled and water-cooled specimen. At low temperatures, the change of colour of specimens is mild, whereas at high temperatures there is a drastic change in colour which can be clearly observed with the naked eye. The specimens heated at 500 and 700 °C were turned to blackish colour while quenching it with water. After drying, the colour of the specimen has changed into grey colour. This is due to the sudden change in temperature effect in the concrete specimen. For air-cooled specimens, the colour of the specimen turned into white due to the evaporation of water from internal layers of concrete.

4.2 Compressive Strength

Figures 4 and 5 show the 28-day compressive strength of air-cooled specimens and water-cooled specimens, respectively.

The compressive strength of concrete depends on the degree of hydration of cement, rate and time of exposure and moisture content. From Fig. 5, it was observed that the strength decreased with an increase in temperature when subjected to immediate water cooling for all the cases of TBC. From Fig. 4, it can be seen that the phenomenal strength was decreased at 300 °C and sudden increase in strength at 500 °C when subjected to air cooling for all the cases of TBC. It was noticed

that SCBA15SF10 exhibited better performance compared to other percentages of TBC when subjected to elevated temperatures followed by air and water cooling. At SCBA30SF10, the strength was significantly decreased at all the temperatures both in air cooling and water cooling because of replacing the more percentage of SCBA.

From Fig. 5, it is identified that at 200 °C the ternary blended concrete of SCBA15SF10 performed well when subjected to elevated temperatures followed by sudden cooling. This is due to the sudden thermal shock existence in the specimens [13, 16, 17]. From Fig. 5, it is seen that the compression strength was higher in SCBA15SF10 for temperature 500 °C at all replacement's levels of TBC. This increased strength in SCBA concrete is due to the presence of high silica. Silica present in these materials could react with lime which was released during hydration of cement, and it forms additional silicate hydrate (C–S–H) as new hydration products. The change in unit length of specimen per degree at high temperatures takes place is known as coefficient of thermal expansion. This expansion leads to the internal stress of the specimen, and it results in the form of cracks and weakening of
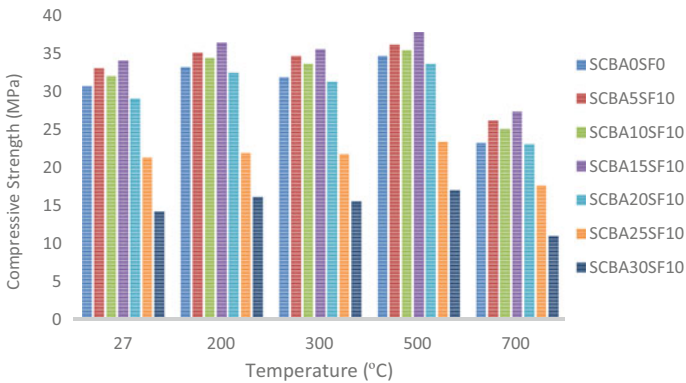

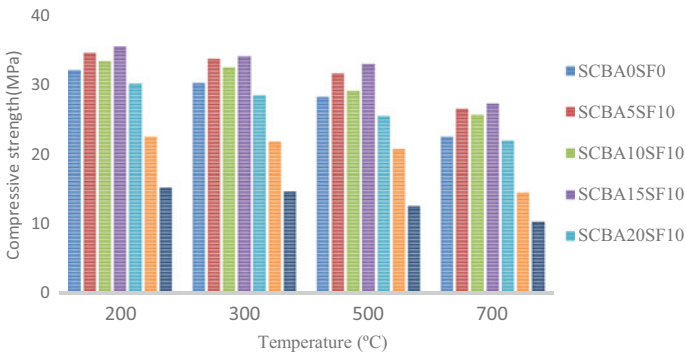**Fig. 4** Compressive strength of air-cooled specimens

Fig. 5 Compressive strength of water-cooled specimens

Table 11 Minerals present in SCBA15SF10 specimens

P—Portlandite	AS—Anorthite sodium	C—Calcite
Q—Quartz low	AL—Albite	E—Ettringite
LA—Larnite	M—Mullite	G—Gypsum
F—Fayalite	V—Vaterite	W—Wollastonite

building structure. At higher temperatures, a very steep drop in compressive strength was observed for all percentage replacements in TBC with SCBA and SF indicates poor endurance properties at 700 °CC due to the complete deterioration of C–S–H gel after 500 °C. The reasons for the loss of strength at high temperatures are explained as follows: After 200 °C, the water present in the internal layer of CSH-gel and some chemically combined water from both CSH-gel and sulfo-aluminate hydrates could be lost. Further, after 400 °C, the strength decreases due to the loss of non-evaporable water from the gel pores. At about 600 °C and beyond that, the dehydration of cement paste starts and causes loss of strength. It implies that the TBC after 700 °C shows very poor strength [18–20].

4.3 XRD Analysis

X-ray diffraction (XRD) is an exceptional method to find out the crystallinity of a compound present in the material. This test was carried out on SCBA15SF10 in a diffractometer measuring instrument at University of Hyderabad, Hyderabad district of Telangana, India. The minerals found by the XRD analysis are given in Table 11 (Fig. 6).

XRD analysis was conducted to notice changes in the hydration process due to the presence of SCBA and SF at elevated temperatures. Figure 8 shows the period compositions in air-cooled concrete specimen SCBA15SF10 exposed to 500 °C temperature and water cooled of SCBA15SF10 specimens after exposure to 200 °C temperature. Due to their crystal-like nature, portlandite (P), wollastonite, ettringite, silica and mullite peaks appear clearly in the XRD analysis.

In air-cooling SCBA15SF10 concrete specimen, the chemical composites like quartz (26%), anorthite (20%), mullite (10%), ettringite (10%), wollastonite (14%) and vaterite (4%) contents are higher which lead to develop the amount of compressive strength of SCBA15SF10 TBC at 500 °C. In water-cooling SCBA15SF10 concrete specimen, the chemical compounds like quartz low (30%), anorthite (18%), mullite (6%), vaterite (17%), quartz (30%) and albite (13%) contents are higher which lead to improve the compressive strength, interlinking nature and temperature resistance at 200 °C.

In air cooling after exposure to 500 °C and in water cooling at 200 °C, no significant changes in the peaks were observed and only a slight decrease in the calcium hydroxide and mullite peaks were observed for the SCBA + SF specimens. New phases like fayalite and gehlenite are formed at those temperatures and found to be
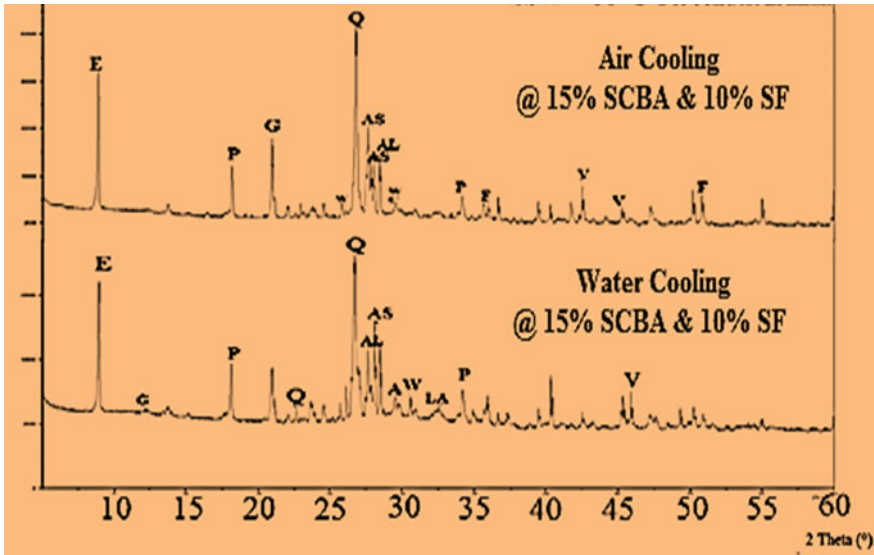
Fig. 6 XRD analysis of air and water-cooled specimens SCBA15SF10 exposed to 400 °C temperature

very minute. Due to this very minute percentage, they are not mentioned in Fig. 7. This is the reason why SCBA15SF10 replacement gives high strength for both water cooling and air cooling.
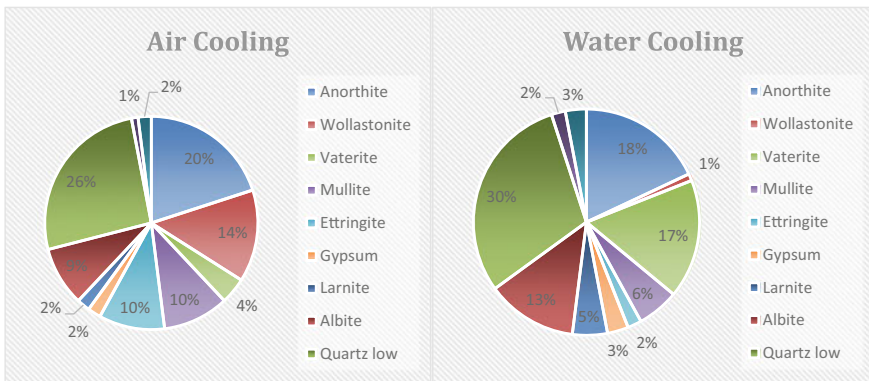
Fig. 7 Percentage of minerals present in the TBC specimens

5   Conclusions

- From the present study, it was noticed that SCBA15SF10 TBC replacement of OPC has shown better performance at all temperatures when subjected to both air and water cooling.
- Results show that the rate of loss in strength depends on the type of cooling regimes. The loss of compressive strength was minimum under air cooling as the heat gradient is gradual, whereas the loss was maximum under sudden cooling due to sudden thermal shock.
- For both the cooling regimes, it was found that the weight loss in concrete containing SBCA and SF was more when subjected to temperature of 700 °C.
- For air cooling, the maximum compression strength was gained at 500 °C at all replacement levels of SF and SBCA in TBC.
- For water cooling, the maximum compressive strength was gained at 200 °C at all replacement levels of TBC.
- Formation of new phases at high temperatures was the reason for the increase in strength of the specimen SCBA15SF10 at 500 °C for air cooling and 200 °C for water cooling.

References

1. Aldred JM, Holland TC, Morgan DR (2006) Guide for the use of silica fume in concrete. Reported by ACI–American Concrete Institute–Committee, 234
2. Uchikawa H, Uchida S, Hanehara S (1989) Relationship between structure and penetrability of Na Ion in hardened blended cement paste. Mortar Conc J Res Onoda Cem Company 41(121):71–84
3. Bache HH (1981) Densified cement/ultra fine particle based materials. In: Presented at second international conference on superplasticizers in concrete. Ottawa, Ontario, Canada
4. Bhanja S, Sengupta B (2005) Influence of silica fume on the tensile strength of concrete. Cem Concr Res 35(4):743–747
5. Vishal SG, Pranita SB (2014) Influence of silica fume on concrete. IOSR J Mech Civil Eng (IOSR-JMCEPP) 44–47
6. Ganesan K, Rajagopal K, Thangavel K (2007) Evaluation of bagasse ash as supplementary cementitious material. Cement Concr Compos 29(6):515–524
7. Fairbairn EM, Americano BB, Cordeiro (2010) Cement replacement by sugar cane bagasse ash: CO_2 emissions reduction and potential for carbon credits. J Environ Manage 91(9):1864–1871
8. Cordeiro GC, Toledo RD Filho LM, Tavares LM, Fairbairn EMR (2008) Pozzolanic activity and filler effect of sugar cane bagasse ash in Portland cement and lime mortars. Cement Concr Compos 30(5):410–418
9. Cordeiro GC, Toledo Filho RD, Fairbairn EMR (2009) Effect of calcination temperature on the pozzolanic activity of sugar cane bagasse ash. Constr Build Mater 23:3301–3303
10. Ribeiro DV, Marcio RM (2014) Effect of calcination temperature on the pozzolanic activity of Brazilian sugar cane bagasse ash (SCBA). Mater Res 17(4):974–981
11. Bahurudeen A, Santhanam M (2015) Influence of different processing methods on the pozzolanic performance of sugarcane bagasse ash. Cement Concr Compos 56:32–45

12. Arioz O (2007) Effects of elevated temperatures on properties of concrete. Fire Saf J 42(8):516–522
13. Chan SYN, Xin L, Sun W (2000) Effect of high temperature and cooling regimes on the compressive strength and pore properties of high-performance concrete. Constr Build Mater 14(5):261–266
14. Varun Teja K, Purnachandra Sai P, Meena T (2017) Investigation on the behaviour of ternary blended concrete with scba and sf. IOP Conf Series Mater Sci Eng 263(3)
15. Xie Q, Zhang L, Yin S, Zhang B, Wu Y (2019) Effects of high temperatures on the physical and mechanical properties of carbonated ordinary concrete. Adv Mater Sci Eng
16. Ferhat B, Gül R (2009) Effect of elevated temperatures and cooling regimes on normal strength concrete. Fire Mater 33(2):79–88
17. Yaragal CS, Ramanjaneyulu S (2016) Exposure to elevated temperatures and cooled under different regimes-a study on polypropylene concrete. Adv Mater Res 5(1):21–34
18. Varun Teja K, Meena T (2019) Experimental exploration of perlite concrete under elevated temperatures. Indian Conc J 93:27–33
19. Varun Teja K, Meena T (2020) An insight into temperature characteristics of ternary blended concrete with perlite powder. Asian J Civil Eng 21:41–48
20. Teja KV, Meena T (2020) Performance of ternary blended concrete and binary concrete made with perlite powder at elevated temperatures. Jordan J Civil Eng 14(2)
21. IS: 2720-part 3–1980. Methods of test for soils, determination of specific gravity, fine, medium and coarse grained soils. Bur. Indian Standard, New Delhi.
22. IS 4031–11 (1988) Methods of physical tests for hydraulic cement, determination of Density Bur Indian Standard New Delhi
23. IS 5513:1996. Vicat apparatus-specification, (Second Revision). Bur. Indian Standard New Delhi.
24. IS 5514:1996. Apparatus used in 'le-Chatelier' test -specification, (first revision). Bur. Indian Standard New Delhi.
25. IS 2386(part 3):1963. Methods of test for aggregates for concrete, Specific gravity, density, voids, absorption and bulking. Bur. Indian Standard, New Delhi.
26. IS:516–1959. Methods of tests for strength of concrete. Bur. Indian Stand. New Delhi.

A Review on the Mechanical Properties and Resistance of Blended Fibrous Concrete Composite Towards Impact

S. Janani and A. S. Santhi

Abstract Concrete is subjected to sudden impact loads in water-controlled structures like dams, tunnels; airport terminal asphalts; structures used for military and industrial purposes. When subjected to extreme load conditions and aggressive environments, plain concrete which is already brittle in nature fails suddenly. Fibre-reinforced concrete is a rapidly developing construction technique which can be used for almost all structural systems. Fibres enhance the ductility of concrete structure by improving their mechanical properties. This paper presents a review on the behaviour of fibre-reinforced concrete under normal as well as impact loads and also identifies the materials that can be used for blending cement in concrete as cost-effective means of construction is one of the challenging aspects in these industries.

Keywords Concrete · Impact · Fibre-reinforced concrete · Mechanical properties

1 Introduction

Concrete is the principal building material used extensively in the construction industry. The structural performance of concrete becomes an indigenous factor to be considered for any type of construction. Unlike the static loads, the concrete exhibits a highly complicated behaviour under impact loading condition. The major problem of impact is its dynamic conduct and nonlinear deformation. Plain concrete has little or no impact resistance. Most of the studies [1] on impact have been associated with military and nuclear sectors, where a smaller size impactor hits a massive sized target. The impact loading occurs for a very short interval of time, and the material fails locally either by punching or in the form of bell-shaped ejected cone [2].

The areas where impact loads can be applied to concrete structures include, ice impact on marine and offshore structures; projectile or aircraft impact on protective structures and the structures experiencing blast or explosive loads [3]. Shock absorbing areas like machine foundation pads, railway buffers concrete need to have

S. Janani · A. S. Santhi (✉)
School of Civil Engineering, Vellore Institute of Technology (VIT), Vellore, India
e-mail: as_santhi@vit.ac.in

high resistance towards impact and good energy absorption capacity [4]. In hilly and mountainous regions, the roadways face a greater threat because of frequent rock falls and massive stone break-up. Hence, the study on impact and development of safety structures to resist extreme loads has become a serious issue. The critique can be divided into three main forms: analysis of shock wave propagation, exploring the experiments related to impact and examining the methods to improve resistance of concrete material towards impact [5].

2 Types of Fibres and Their Role in Concrete

Concrete is known for its increased strength, durability and high rate of strain hardening. The main disadvantage is its brittleness which is characterized by relatively low strength in tension and very low resistance towards opening of cracks and its propagation. Fibres can be classified into steel fibres with variety of shapes and sizes and microfibers; alkali-resistant glass fibres; synthetic fibres made by adding polyethylene, polypropylene, polyvinyl alcohol and so on; and the last category is carbon, pitch, polyacrylonitrile fibres (PAN fibres). Natural vegetable fibres can only be applied to ordinary concrete, and asbestos fibres are not used in construction because of their negative effect on human health. Fibres help in avoiding the formation of single large cracks. The large cracks are replaced with dense system of microcracks in fibres for ensuring proper safety and durability aspects. Fine fibres restrict the opening as well as the propagation of microcracks because of their compact dispersion in the cement matrix. Longer fibres of 50 or 80 mm length stop the occurrence of larger cracks and contribute to increased final strength of FRC [6].

2.1 Onset of Fibre Reinforcement

In early 1900s, cement paste is reinforced with asbestos fibres and applied to produce plates for roofing and piping. Later on, glass fibres were used as a reinforcement to cement mortar [7]. In case of adverse environmental conditions, alkaline Portland cement pastes were suitable, but its compatibility with E-glass fibres is not that good, addition of zircon oxide (Zr O) helps to overcome this and makes the concrete compatible with alkali-resistant glass fibres [8]. In this manner, fibres have been applied to concrete with combination of one or more materials till date.

2.2 Fibre Types and Their Use in Concrete

2.2.1 Steel Fibres

Concrete reinforced with steel fibres absorb energy under dynamic loadings [9]. Figure 1 shows the different types of steel fibres employed in the construction industry. The main perspective of using steel fibres as a reinforcement system in concrete is its performance in post-cracking stage. Fibre volume and efficiency are the two principal parameters to be considered in identifying the stress and the corresponding strain behaviour of concrete. A distinctive phenomenon which is predominant in this system is softening branch, where a linear increase in stress is observed and beyond the first crack opening there is a decrease in stress. With the provision of sufficient quantity of steel fibres, considerable amount of energy is absorbed (phase of softening branch followed by strain-hardening phase with consecutive multiple cracks). Steel fibres of different sizes in hybrid reinforcement control microcracks enhance the tensile strength and improve workability because the fine microfibres govern compressive strength and slightly affect the tensile strength; longer steel fibres affect strength and toughness characteristics [6]. This depends on type of fibre material, application methodology, element geometry, and matrix properties [10–12].

Steel fibres reduce localized damage and prevent brittle failure. Reinforcement in concrete can be carried out in two ways: conventional steel bar mesh usually applied for global bending stiffening and closed spaced wires for providing local stiffening. With relatively low but denser reinforcement, fibres give good scabbing resistance [13]. Due to "wall-effect" between long and short steel fibres in hybrid steel fibres, the workability is comparatively better than homogenous fibre reinforcement [14]. During freeze and thaw cycles with 3% NaCl solution, steel fibres have little or no effect on loss in weight of concrete. The freeze thaw cycles is observed to have
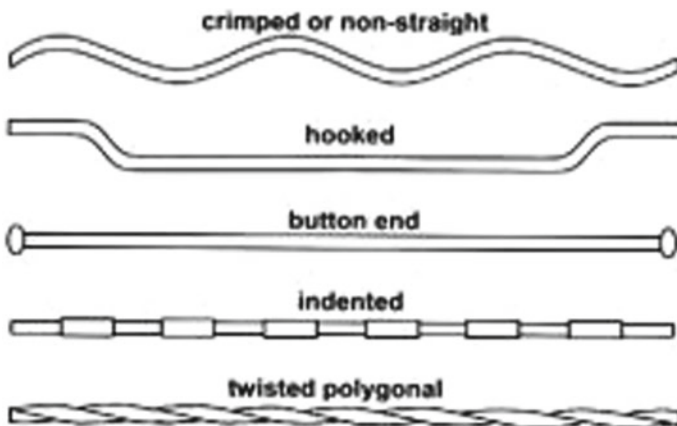

Fig. 1 Types of steel fibres [6]

no significant effect on impact strength of steel fibre-reinforced concrete as impact energy is in good correlation with residual strain [15]. Steel fibres rarely modify the strength in compression and elastic modulus of concrete with drastic variation with peak stress and strain graph. Increase in fibre content increases the strength and ductility in which fracture energy and crack width are calculated from inverse analysis [16]. Under quasi-static loads, fibre content has a quantitative effect on increased strength and elastic modulus. The fibres disturb post-peak response and increase the potential energy and strength under impact [17]. Their applications lie in air and water transportations, structures related to storage of armaments in military services and in overlays of industrial floors [18–22].

2.2.2   Polypropylene Fibres

Polypropylene fibres (in small amounts up to 1 kg/m^3) are responsible for arresting shrinkage cracks at early stage during its initial hours of setting. Different types of polypropylene fibres are shown in Fig. 2. These fibres (either monofilament or fibrillated) with a maximum volume of 2%, increase compressive strength, toughness, impact and fatigue strength of concrete. The unique aspect is that the modulus of elasticity of concrete is same as that of the fibres used in it. Polypropylene fibres find its application in fire and high-temperature exposures by melting and paving the way for the release of internal pressure and delay the destruction of the existing structure [24]. The reason behind the refinement of mechanical properties is their build-up strength and toughening feature. In reality, the dynamic performance is entirely different from static. The typical aspect is that the peak stress and peak strain are inversely proportional, furthermore, when the strain rate intensifies, dynamic strength of concrete gets upgraded [25].

A semblance to steel fibres is HPP (synthetic macrofibre material, a type of polypropylene fibre—in appearance and function) did not have good response on the strength of lightweight aggregate concrete in compression. This recommends a certain limit of 9 kg/m^{3}beyond which the strength of concrete in compression
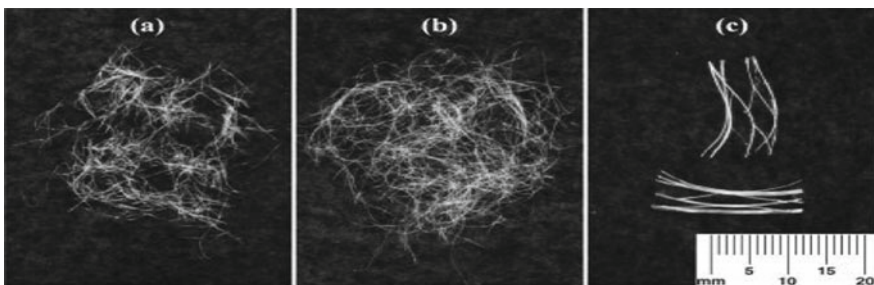
Fig. 2 **a** 6 mm monofilament, **b** 12 mm multifilament and **c** 20 mm fibrillated polypropylene fibres [23]

reduced. The other mechanical properties—split tensile, flexural toughness and impact strength—were increased to a greater extent with respect to fibre content. Bonding between fibres and cement paste is affected and cracks can be formed due to relative weak link. Though significant strength increase is observed, random dispersion of fibres causes weak link at the interfaces [26]. Polypropylene fibres help to create a proper channel for the pressure to release and prevent the formation of cracking and spalling. 0.1–0.25% of polypropylene fibres minimize spalling. Polyethylene fibres in high density form have relatively greater elastic modulus and higher tensile strength [27].

2.2.3 Secondary Fibres—Carbon, Wool and Textile Fibres

Carbon fibre composites are responsible for improved flexural strength, toughness, reduced drying shrinkage and voltage-sensitive effect in electrical applications. These fibres can be employed for building claddings, bridges and other engineering structures. The fibres along with their carriers are shown in Fig. 3. Carbon fibres are the best for structures in marine environments where corrosion is frequent and dangerous than the steel fibres because of its durability [29].

Wool fibres combined with earthen material intensify flexural strength and give better performance at post-cracking stage. Fibres of longer lengths provide good strength when the deformations are larger [30]. Instead, when Hemp fibres are used, they boost up ductility, fracture resistance under static and dynamic loading [31]. Compared to unidirectional fibres, fibres in textile forms commonly called fibre

Fig. 3 Carbon tows and fibre samples settled on specific carriers [28]
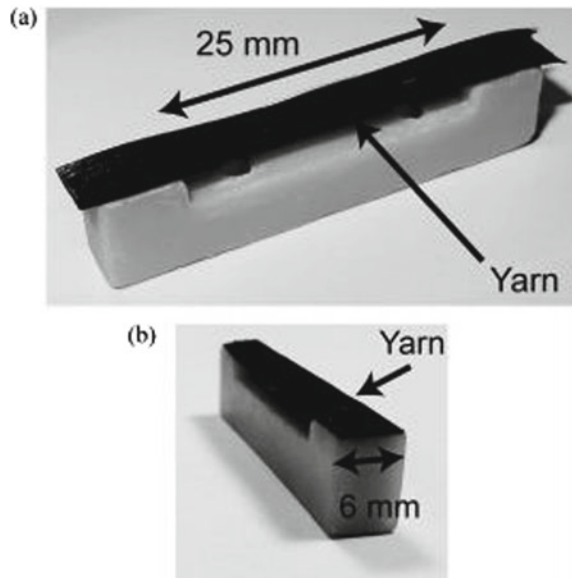
composites are very effective in resisting impact damage [32]. These fibres have high impact resistance due to their dimensional stability, indistinct conformability and extreme mould ability [33].

2.2.4 Fibre-Reinforced Polymer

Fibre-reinforced polymers are advantageous in enhancing the infrastructure because of its non-corrosiveness, lightweight and better strength development. One of the serious issues in cement concrete sleepers is the sound produced due to the vibration or noise absorption from the high-speed fast-moving trains [34–36]. Polymer concrete helps in tremor or noise absorbtion, resistance to corrosion and quick curing time [37, 38]. The advantageous characteristics of carbon fibre-reinforced polymer are its corrosion-less characteristic, ease at handling and transportation, high specific strength and specific stiffness [39]. In case of hazardous environments, electrical and magnetic fields, steel fibres may cause durability issues [40–42]. Irrespective of type of fibre to be used, there has been many issues to be noted like material constituent, amount of fibres, mortar–fibre interface characteristics, geometry and so on [43, 44].

3 Blended Materials on Concrete

The waste materials removed from industries not only reduce the pollution due to Co_2 emissions but also increase the energy consumption to a greater extent [45]. Fly ash can be partially used to replace cement in normal and high-strength concrete [46]. When fly ash is mixed with cementitious materials, pozzolanic reaction starts where it chemically reacts with calcium hydroxide and generates secondary C–S–H gel [47]. This is followed by hydration and strength gain in the concrete structure. Silica fume, a similar kind of material, contributes to enhanced tensile strength at optimum dosage. These materials are responsible for high early compressive strength, tensile, flexural strengths, modulus of elasticity, increased toughness and greater bond strength [48]. Silica fume has also become an important ingredient in high strength concrete because of its bonding in interfacial zone of cement paste aggregate. These microparticles make the interfacial zone denser subsequently increase the uniformity [49–51]. With the help of ultra-fine pozzolans like silica fume and fly ash, chemical admixtures like superplasticizers and fibres, normal concrete can be converted to ultra-high strength; they decrease brittleness and alter the material constituents by reducing the water–cement ratio, increasing the cementitious content and change the mixing time [52]. In actual fact, these supplementary cementitious materials—fly ash, silica fume, blast furnace slag and natural pozzolans—are both technically and economically advantageous too [53].

4   Combination of Fibres and Blends in Concrete

Steel fibres in concrete reduce the workability by providing rich mix. When silica fume is combined with steel fibre, steel fibres increase compressive strength and decrease modulus of elasticity. On contrary, silica fume compensates it by increasing the elastic modulus of concrete but also increases the brittleness which in turn overcomes by steel fibres. Thus, the ductility of concrete is greatly improved [54]. Polypropylene fibres combined with silica fume on natural pozzolan cements, fibres were responsible for controlled cracking, enhanced early age drying shrinkage and reduced permeability and silica fume increase compressive strength, early age cracking, permeability and carbonation depth. Short discrete fibres were recommended to decrease the impact of long-term early age damage and durability of concrete Flores [55]. Fibres with natural pozzolans like silica fume and fly ash decrease workability. With increased volume of fibres, slump flow gets reduced gradually. The drying shrinkage in concrete also gets influenced.

5   Improvement of Mechanical Properties and Impact Resistance of Concrete Containing Fibres and Blends

ACI 544 gives recommendations on identifying the resistance of concrete specimens towards impact by using moulds of 152 mm diameter and 63.5 mm thick. A hammer of weight 4.54 kg is allowed to fall from a standard height of 457 mm onto the steel ball which is placed on the top of the concrete specimen. The number of blows that the specimen can resist gives the resistance towards impact. This method of identifying impact resistance has been used by many researchers.

The properties of fly ash concrete reinforced with steel fibres were studied by [56]. This included workability and unit weight of fresh concrete, mechanical properties (strength of concrete in compression, split tension, flexure and modulus of elasticity); durability properties, such as freeze–thaw resistance, drying shrinkage and sorptivity coefficient. Class F fly ash was used as a partial replacement to cement at 15 and 30%. Hooked-end steel fibre was employed at levels 0.25, 0.5, 1 and 1.5%. The test results showed that the unit weight of fresh concrete was increased with every unit increase in fibre content and decreased with a unit increase in fly ash content. The steel fibre addition reduced the workability of concrete. It was also perceived that the VeBe time measurement for workability was more appropriate than the slump. Steel fibre addition did not greatly influence the strength of concrete in compression. Furthermore, the strength loss due to fly ash was not compensated by the steel fibre addition. Till 0.5% steel fibre addition, the flexure strength of concrete remained unchanged. At 1%, the enhancement in strength was observed to be from 0 to 15%. and at 1.5%, the enhancement in strength was observed to be in the range of 30 and 60%. The strength of concrete in split tension was increased at all percentages of fibres. Modulus of elasticity was not prominently affected by the fibre addition. It

has to be noted that the behaviour of fly ash concrete is similar to that of normal concrete. Fibre-reinforced fly ash concrete also showed better performance under durability aspects of concrete, such as sorptivity, drying shrinkage and freeze–thaw resistance.

Evaluation of mechanical properties and resistance of concrete towards impact by combining silica fume with steel fibres was made by Nili and Afroughsabet [57]. Silica fume was replaced to cement at 8% by its weight. Steel fibres were of hooked-end type with length 60 mm and aspect ratio 80 and were employed at 0.5 and 1%. The test results were evaluated for 7, 28 and 91 days. The mechanical properties and impact resistance were evaluated using the tests on compression, split tension, flexure and impact (as per ACI 544). Two types of water/cement ratio were incorporated 0.46 and 0.36, and correspondingly, the results were evaluated. It was perceived that the steel fibres enhanced the strength of concrete in compression. The increase in strength was identified to be 19 and 13.6% for water/binder ratio of 0.46 and 0.36, respectively, with 1% volume fraction of steel fibres. It is also emphasized that the incorporation of silica fume improved the strength of concrete in compression both in fibrous and non-fibrous states. In the concrete mix containing both silica fume and steel fibres, the strength of concrete in split tension was affected by fibres rather than silica fume. Concrete mix with 1% steel fibre content and silica fume showed highest strength in flexure in comparison to all other mixes. The steel fibre-reinforced concrete showed enhanced resistance towards impact by prolonging the number of blows between the occurrence of first crack and final failure. The silica fume addition not only increased the impact energy absorption capacity but also intensified the brittleness of concrete. The combination of silica fume and steel fibres strengthened the ductility of concrete, where the silica fume acted as pozzolanic material and steel fibre acted as crack arrestors. This also improved the energy absorption capacity of concrete towards impact.

Boulekbache et al. [58] studied the behaviour of steel fibre-reinforced concrete under flexure when subjected to cyclic loading. This test was conducted on standard prisms of size 150 mm × 150 mm × 700 mm. Three strengths of concrete 30 (ordinary), 60 (self-compacting) and 80 MPa (high) were taken into consideration. Hooked-end steel fibres of two different aspect ratios 65 and 80 were considered at volume fractions 0.5% and 1%. A standard quantity of silica fume was incorporated (i.e. 10% by weight of cement) in high-strength concrete. It was perceived that the addition of steel fibres enhanced the flexure strength of concrete. Fibres were effective in providing good bond in concrete mix owing to their compatibility with the concrete matrix. The strength enhancement of fibrous concrete of aspect ratio 80 was found to be 242, 174 and 150% in self-compacting, high and ordinary strength concrete, respectively. Under cyclic loading, the volume fraction and aspect ratio of fibres were responsible for the enhancement of reversible displacement in the post-cracking zone. The volume fraction of fibres had a significant effect on the improvement of cumulative energy of FRC, and it was vice versa for aspect ratio consideration.

Karthikeyan and Dhinakaran [59] evaluated the combined use of ultra-fine TiO_2 ($UFTiO_2$) and silica fume (SF) on the enhancement of mechanical and durability

characteristics of concrete. The silica fume was replaced to cement at 4.5, 9.5 and 14.5%. The UFTiO$_2$ was employed at a constant percentage of 0.5% to the concrete mix. Crimped steel fibres were also used at 0.5% to elevate the above-mentioned properties of concrete. Steel fibres were of 12.5 mm length, 0.45 mm diameter with an aspect ratio 27.78. The tests conducted to predict the response of concrete include compression, water absorption, sorption, split tension, flexure and impact. The impact resistance of concrete was identified using drop weight impact test conducted as per the recommendations of ACI 544, wherein a hammer of weight 44.70 N was dropped from a standard height of 1120 mm onto a steel ball of diameter 64 mm placed at the top of the cylindrical specimens. It was observed that the plain and fibre-reinforced concrete with 10% replacement of cement (9.5% SF + 0.5% UFTiO$_2$) had attained better mechanical properties by improving the compressive strength, split tension and flexure strengths. Even though the fibre content was constant and distribution of fibres in fibre-reinforced concrete was also uniform, there observed a change in strength owing to the combined addition of ultra-fine TiO$_2$ and silica fume. The 10% replacement of cement with SF and UFTiO$_2$ proved to be the optimum mix, whereas the other mixes showed a decrease in strength. Excess replacement of cement did not provide better bonding properties. The impact resistance of concrete was enhanced but did not alter due to a constant percentage of fibre was employed. The durability properties of concrete were also improved. The results observed in mechanical properties were inversely proportional to the sorption coefficient. This was perceived to be a desirable phenomenon in the performance of concrete.

AbdelAleem et al. [60] studied the combined effect of using synthetic fibres and crumb rubber on the resistance towards impact of self-consolidating concrete (SCC). Cement was replaced by fly ash at 30% and metakaolin at 20%. Crumb rubber was partially replaced with fine aggregate from 0 to 30%; as every 5% increment. The mix comprised of three parts; first, fly ash and metakaolin with crumb rubber at replacement levels from 0 to 30%; second, crumb rubber employed at 5–20% with the synthetic fibre addition at 0.2% or steel fibre at 0.35%; third, crumb rubber at 30% mixed with 1% synthetic fibre or 1% steel fibre. The performance of the mixes was identified using their mechanical properties and resistance towards impact. The impact resistance of concrete was discerned using two different methods; drop weight test as per ACI 544 and three-point flexure loading test (for energy absorption capacity of concrete identification). The crumb rubber addition had reduced the mechanical properties and enhanced the impact resistance of concrete. Though synthetic fibre addition to SCC exhibited poor performance in compression, their best performance was observed in split tension and flexure. Varying the fibre length also determined the behaviour of concrete. Length of fibre ranging between 19 and 38 mm decreased the strength of concrete in compression and increased the strength in split tension and flexure. Steel fibre addition to concrete improved both the mechanical properties and resistance of concrete towards impact. In SCC, synthetic fibres were found to be comparatively more advantageous than steel fibres. Thus, the combination of fibres with blends not only improved the mechanical properties but also improved the resistance of concrete towards impact.

6   Conclusion

This paper reviews the previous works carried out on concrete composites made from blends and fibres; their properties, behaviour and resistance towards impact. Although there have been a vast study related to this area already, this paper mainly concentrates on behaviour towards mechanical properties and impact resistance. The remarks of this literature review are summarized as follows:

- There are two main perspectives to safeguard the structure against loading. One is to shield it with proper covering, and the other is to strengthen it. The former is costly and time consuming than the latter. The strengthening of concrete can be done in various forms; one such aspect is addition of certain materials which can make the concrete sustainable as well as durable in nature.
- Addition of fibres provides a rich mix thereby causing lesser workability. These fibre composites have greater load carrying capacity because of greater surface area achieved on drying. In actual fact, fibres bridge the gap and create a homogeneous matrix mix subsequently preventing crack formation and its propagation.
- The most commonly used fibres in construction industry are steel and polypropylene fibres. Steel fibres are responsible for energy absorbing capacity when subjected to dynamic loading; polypropylene fibres are thermally stable with high melting point and can be suited in alkaline environment at extreme temperature conditions.
- Impact load has not been calculated with a desired formula till now. The load is identified in terms of its kinetic energy where hammer (weight) drops from a certain desired height (The only codal procedure available is ACI 544.2R-1989, and this can be modified by varying height of drop, weight of hammer and size of the specimen apparently based on the requirement).
- Fibres are advantageous in enhancing the impact resistance of concrete because fibrous concrete does not exhibit brittle failure. Fibre type, content and orientation are to be considered in ensuring desirable behaviour of fibrous concrete composites.
- Fly ash and silica fume blends when used in combination, the disadvantage of the former (less early strength and good later strength) is overcome by the later because silica fume helps in providing good early strength. They also enhance workability due to their smaller particle sizes; minimize cracks due to thermal and drying shrinkage and finally improves the mechanical properties of concrete.
- More studies have to be encouraged on concrete composites made with blends and fibres to exhibit better performance and safeguard the structure against aggressive environment; by reducing pollution through lesser cement consumption and upgrade the desired service life of structure.

In order to obtain an eco-friendly environment, the wastes have to be removed and utilized either as an alternative or additive to concrete. This method of utilizing the waste is advantageous in terms of both cost and improving the quality of concrete

in terms of their mechanical properties and impact resistance. Plastic waste is one such hazardous and dangerous waste polluting the environment. Some studies have already been started on utilizing this plastic waste as fibres in concrete. In a similar manner, the materials causing hazardous effect on environment have to be identified and utilized appropriately in order to provide green environment for the present as well as future generation.

References

1. Shill SK, Al-Deen S, Ashraf M (2019) Saponification and scaling in ordinary concrete exposed to hydrocarbon fluids and high temperature at military airbases. Constr Build Mater 215:765–776
2. Othman H, Marzouk H (2016) An experimental investigation on the effect of steel reinforcement on impact response of reinforced concrete panels. Int J Impact Eng 88:12–21
3. Zineddin M, Krauthammer T (2007) Dynamic response and behaviour of reinforced concrete slabs under impact loading. Int J Impact Eng 34:1517–1534
4. Gupta T, Sharma R-K, Chaudary S (2015) Impact resistance of concrete containing waste rubber fiber and silica fume. Int J Impact Eng 83:76–87
5. Mougin J-P, Perrotin P, Mommessin M, Tonnelo J, Agbossou A (2005) Rock fall impact on reinforced concrete slab: an experimental approach. Int J Impact Eng 31:169–183
6. Brandt A-M (2008) Fibre reinforced cement-based (FRC) composites after over 40 years of development in building and civil engineering. Compos Struct 86:3–9
7. Biryukovich KL, Biryukovich Y, Biryukovich DL (1964) Glass-fibre-reinforced cement. CERA Translation. Budivelnik, Kiev.
8. Majumdar A-J, Ryder J-R (1968) Glass fibre reinforcement of cement products. Glass Technol 9(3):78–84
9. Haido J-H, Abu Bakar B-H, Abdul-Razzak A-A, Jayaprakash J, Choong K-K (2011) Simulation of dynamic response for steel fibrous concrete members using new material modeling. Constr Build Mater 25:1407–1418
10. Larenjeira F (2010) Design oriented constitutive model for steel fiber reinforced concrete. Doctoral diss., Polytechnic university of Catalonia, Barcelona, Spain.
11. Cucchiara C, Mendola L-L, Papia M (2004) Effectiveness of stirrup and steel fibers as shear reinforcement. Cem Conc Compos 26:777–786
12. Cunha VMCF (2010) Steel fibre reinforced Self-compacting concrete. Doctoral diss., University of Minho, Guimaraes, Portugal
13. Dancygier A-N, Yankelevsky D-Z (1996) High strength concrete response to hard projectile impact. Int J Impact Eng 18(6):583–599
14. Yu R, Spiesz P, Brouwers HJ-H (2014) Static properties and impact resistance of a green ultra-high performance hybrid fibre reinforced concrete (UHPHFRC): experimental and modeling. Constr Build Mater 68:158–171
15. Zhang W, Chen S, Zhang N, Zhou Y (2015) Low-velocity flexural impact response of steel fiber reinforced concrete subjected to freeze-thaw cycles in NaCl solution. Constr Build Mater 101:522–526
16. Yoo D-Y, Yoon Y-S, Banthia N (2015) Flexural response of steel-fiber-reinforced concrete beams: effect of strength, fiber content and strain rate. Cem Concr Compos 64:84–92

17. Yoo D-Y, Banthia N, Yoon Y-S (2016) Flexural behaviour of Ultra-high-performance fiber reinforced concrete beams reinforced with GFRP and Steel rebars. Eng Struct 111:246–262
18. Dey V, Bonakdar A, Mobasher B (2014) Low-velocity flexural impact response of fiber-reinforced aerated concrete. Cem Conc Comp 49:100–110
19. Rao M-C, Bhattacharyya S-K, Barai S-V (2011) Behaviour of recycled aggregate concrete under drop weight impact loads. Constr Build Mater 25(1):69–80
20. Rahmani T, Kiani B, Shekarchi M, Safari A (2012) Statistical and experimental analysis on the behaviour of fiber reinforced concretes subjected to drop weight test. Constr Build Mater 37:360–369
21. Wang H-T, Wang L-C (2013) Experimental study on static and dynamic mechanical properties of fiber reinforced light weight aggregate concrete. Constr Build Mater 38:1146–1151
22. Yazici S, Arel H-S, Tabak V (2013) The effects of impact loading on the mechanical properties of SFRCs. Constr Build Mater 41:68–72
23. Maluk C, Bisby L, Terrasi GP (2017) Effects of polypropylene fibre type and dose on the propensity for heat-induced concrete spalling. Eng Struct 141:584–595
24. Ramakrishnan V, Zellers R, Patnaik AK (2007) Plastic reduction potential of a new high tenacity monofilament polypropylene fiber. In: Malhotra VM (ed) 9th CANMET/ACI international conference on recent advances in concrete technology. ACI SP-243, 49–62
25. Zhang H, Liu Y, Sun H, Wu S (2016) Transient dynamic behaviour of polypropylene fiber reinforced mortar under compressive impact loading. Constr Build Mater 111:30–42
26. Li J-J, Niu J-G, Wan C-J, Jin B, Yin Y-L (2016) Investigation on mechanical properties and microstructure of high performance polypropylene fiber reinforced light weight aggregate concrete. Constr Build Mater 118:27–35
27. Kodur, V.K.R (1999). "Fire Performance of high-strength concrete structural members." Research report, National Research Council of Canada, Institute for Research in construction, 1206–20.
28. Tourlonias M, Bueno M-A, Poquillon D (2017). Friction of Carbon tows and fine single fibres. Composites Part A 116–23
29. Kucharska L, Brandt AM (1997) Pitch-based Carbon fibre reinforced cement composites, a review. Arch Civil Eng 43(2):165–187
30. Aymerich F, Fenu L, Meloni P (2012) Effect of reinforcing wool fibres on fracture and energy absorption properties of an earthen material. Constr Build Mater 27(1):66–72
31. Aymerich F, Fenu L, Francesconi L, Meloni P (2016) Fracture behaviour of fibre reinforced earthen material under static and impact flexural loading. Constr Build Mater 109:109–119
32. Chou TW, Ko F (1989) Textile structural composites. Elsevier Science Publishing, New york
33. Naik KN (1994) Woven fabric composites. Technomic publishing, Lancaster
34. Mellet C, Letourneax F, Poisson F, Talotte C (2006) High speed train noise emission: Latest investigation of the aerodynamic/rolling noise contribution. J Sound Vib 293:535–546
35. Barsikow B, King W, Pfizenmaier E (1987) Wheel/rail noise generated by a high speed train investigated with a line array of microphones. J Sound Vibr 118:99–122
36. Krylov VV (2001) Noise and vibration from high-speed trains. Thomas Telford
37. Rebiez K (1996) Precast use of polymer concrete using unsaturated polyester resin based on recycled PET waste. Constr Build Mater 10:215–220
38. Orak S (2000) Investigation of vibration damping on polymer concrete with polyester resin. Cem Concr Res 30:171–174
39. Xie J, Huang P, Guo Y (2012) Fatigue behaviour of reinforced concrete beams strengthened with prestressed fiber reinforced polymer. Constr Build Mater 27:149–157
40. Granju JL, Balouch SU (2005) Corrosion of steel fibre reinforced concrete from the cracks. Cement Concrete Research 35(3):572–577
41. ACI: 544.2R (1989) State-of-the-art report on fiber reinforced concrete. ACI. Reapproved, 1996 and 2009.
42. El-Dieb AS (2009) Mechanical, durability and microstructural characteristics of ultra-high-strength self-compacting concrete incorporating steel fibres. Mater Des 30(10):4286–4292
43. Shah SP, Rangan BV (1971) Fiber reinforced concrete properties. Proc ACI J 68(2):126–135

44. Nawy E (2008) Construction Engineering Handbook, 2nd edn. Taylor & Francis Group, FL (USA)
45. Li ZJ (2011). Advanced concrete technology. Wiley
46. Hu C (2014) Microstructure and mechanical properties of fly ash blended cement pastes. Constr Build Mater 73:618–625
47. Taylor HFW (1997) Cement chemistry, 2nd edn. T. Telford
48. Bhanja S, Sengupta B (2005) Influence of silica fume on the tensile strength of concrete. Cem Concr Res 35:743–747
49. Aitcin PC (1983) Condensed silica fume. Editions de L'Universite de Sher brooke, Sherbrooke, Quebec, Canada
50. Aitcin PC (1998) High strength concrete. Spon Press, London, UK
51. Tasdemir MA, Bayramov F (2002) Mechanical behaviour of cement based composite materials. ITU J/d Eng 1(2):125–144 ((In Turkish with English abstract))
52. Rahman S, Molyneaux T, Patnaikuni I (2005) Ultra high performance concrete, recent applications and research. Australian J Civil Eng 2(1):13–20
53. Baghabra Al-Amoudi OS, Maslehuddin M, Ibrahim M, Shameem M, Al-Mehthel MH (2011) Performance of blended cement concretes prepared with constant workability. Cem Concr Compos 33:90–102
54. Koksal F, Altun F, Yigit I, Sahin Y (2008) Combined effect of silica fume and steel fiber on the mechanical properties of high strength concretes. Constr Build Mater 22:1874–1880
55. Flores Medina N, Barluenga G, Hernandez-Olivares F (2015) Combined effect of Polypropylene fibers and Silica fume to improve the durability of concrete with natural pozzolans blended cement. Constr Build Mater 96:556–566
56. Atis CD, Karahan O (2007) Properties of steel fiber reinforced fly ash concrete. Constr Build Mater 23:392–399
57. Nili M, Afroughsabet V (2010) Combined effect of silica fume and steel fibers on the impact resistance and mechanical properties of concrete. Int J Impact Eng 37:879–888
58. Boulekbache B, Hamrat M, Chemrouk M, Amziane S (2016) Flexural behaviour of steel fibre-reinforced concrete under cyclic loading. Constr Build Mater 126:253–262
59. Karthikeyan B, Dhinakaran G (2018) Influence of ultrafine TiO_2 and silica fume on performance of unreinforced and fiber reinforced concrete. Constr Build Mater 161:570–576
60. AbdelAleem BH, Ismail MK, Hassan AAA (2018) The combined effect of crumb rubber and synthetic fibres on impact resistance of self-consolidating concrete. Constr Build Mater 162:816–829

Performance of Novel Magnesium Phosphate Cement Using Sodium Dihydrogen Phosphate

P. Kathirvel, R. Lakshmi, and J. Jacob

Abstract Magnesium phosphate cements (MPC) are formed by reacting dead burned magnesia with soluble phosphates at room temperature, which are found to be quick setting with significant strength. The reaction is a highly exothermic process with fast hardening process. It is an acid–base reaction to form insoluble phosphate binder. It acts as an alternate binding material to normal Portland cement concrete. MPC is mostly prepared with a retarder, such as borax, to slow down the quick setting of the binder. Dead burned magnesia reacts with phosphate in the hydration of MPC produces struvite which attach onto the MgO particles which have not reacted, leading to the formation of solid particles. The strength and durability of MPC depend on the quantity and characteristics of the ingredients, water to binder ratio and admixtures. In most case of MPC, the phosphates used are dihydrogen phosphates of ammonium and potassium. This study used phosphate of sodium dihydrogen phosphate instead of phosphates of ammonium and potassium. Novel magnesium phosphate cement using dead burnt MgO and sodium dihydrogen phosphate (NaH_2PO_4) has been developed. Chemically inactive dead burnt MgO used was produced by sintering raw MgO at a controlled temperature of 1750 °C in rotary kiln. The MgO to NaH_2PO_4 ratio adopted was from 4:1 to 1:4. The study involved the mechanical properties including compressive and split tensile strength, durability and microstructure properties including scanning electron microscope and EDAX, for various proportions. The optimum mix for magnesium sodium dihydrogen phosphate cement (MNPC) was arrived as 70% dead MgO and 30% sodium dihydrogen phosphate which gave the better result in terms of strength and durability.

Keywords Magnesium phosphate cement · Sodium dihydrogen phosphate · Magnesia · Phosphate binder

P. Kathirvel (✉) · R. Lakshmi · J. Jacob
Department of Civil Engineering, Kamaraj College of Engineering & Technology, Madurai, India
e-mail: kathirvel_p@yahoo.com

1 Introduction

Magnesium phosphate cement is formed by the reaction between magnesia and soluble phosphate. There are two forms of magnesium oxide cement, namely magnesium oxysulfate (MOS) and MPC. MPC develops larger mechanical strength compared to OPC. MPC, though being high performance, is a fast-setting cement binder that contains a large amount of useful properties in comparison with normal OPC binder systems. MPC provides a fast-setting, sturdy and resilient binder system for a construction merchandise applications. The magnesia utilized in this technique may be an unreactive MgO, either arduous or dead burnt MgO. Boric acid or borax is employed as retarder to obtain sufficient time for even mixing before set. Magnesium-based cement normally delivers better compressive strength of 60–300 MPa and tensile strength of over 5.5 MPa, very much stronger than that of standard concrete. MgO cements are thermally and electrically non-conductive. MPC has low shrinkage and high bond strength. The most common initial setting times are ten to twenty minutes, which may be increased from 45 to 60 min by adding retarders. An early strength of about 14 MPa is developed within 2 h of mixing. The general application of magnesium potassium phosphate cement (MKPC) is in rapid restoration of civil structures and prevention of corrosion of metals.

MPC can be prepared by mixing magnesium oxide (MgO) with either dihydrogen phosphates of ammonium or sodium or both [1]. The setting time in MPC is short, and process is highly exothermic, when MgO immediately reacts with the orthophosphate acid [2]. Xiang and Yang [3] have observed that the increase in the pH value of MKPC paste resulted in heat-absorbing reactions. From the study by Kandeel et al. [4], the usage of the seawater in the production of masonry units increased the strength properties of magnesium oxychloride (MOC) specimens. As per the work of Ribeiro et al. [5], the compressive strength of 28 and 365 days mortar decreased by 17% for sand with 50% by weight of MgO and 25% for sand with 100% by weight of MgO. The MPCs which possess sodium, which have alkaline pH, possess antibacterial activity. The study on microstructure of the MPC shows that the phosphates result in dissolution of Si and Al from the fly ash (FA) and ground-granulated blast furnace slag (GBFS). Potassium aluminosilicate is formed as a secondary product in FA and GBFS blended magnesium potassium phosphate cement (MKPC) enhanced in Si and Al [6]. MKPC paste specimens cured under seawater gave more than double the compressive strength, mass increase and drying shrinkage [7]. When MPC-based substances are immersed in water or 3% NaCl solution for a long time, loss in strength takes place [7]. The splitting and flexural strength of MKPC restored specimens' shows better bonding property with the old concrete, same as that of the initial specimen before rupture [8]. Chau et al. [9] showed that with increase in M/K ratio, the reaction rate of MKPC system increases.

Hau et al. [10] found that the magnesium sodium phosphate cement (MNPC) attained quicker setting time than the MKPC because of high solubility and fast dissolving rate. MKPC shows higher compressive strength and water resistance ability than the MNPC. The optimal ratios of magnesium/phosphate for sodium

and potassium MPC were 9.5 and 5.9. Andrzej and Karin [11] indicated that magnesium oxide reduced micro-cracking of the binder matrix, showed good bond with cellulose materials and gave early strength, as compared with OPC. Ma and Xu [12] have investigated the properties of MKPC depending upon M/P proportion and W/C ratio. MKPC is a type of binary cement. Liu and Chan [13] also found that the substitution of magnesium oxide by aluminium oxide up to 10% increased the compressive strength of MPC. Lu and Bing [14] have concluded that by addition of metakaolin, MPC increases the setting time about 52 min and compressive strength to about 66 MPa. In this paper, a new MNPC was prepared by the combination of MgO and sodium dihydrogen phosphate (NaH_2PO_4) in certain ratios. Its hardening properties and microstructure were investigated for the varying mixes.

2 Experimental Programme

2.1 Materials

The dead burnt MgO powder is obtained by grinding magnesia as shown in Fig. 1, produced in TANMAG, Salem, India. It was produced by sintering the raw MgO at a controlled temperature of 1750 °C in a rotary kiln. The specific gravity and bulk density of dead burnt MgO were 3.44 and 3.14 g/cm^3, respectively. Table 1 shows the chemical composition of dead burnt MgO. The sodium dihydrogen phosphate used was white powder of laboratory grade quality. The dry MKPC in the current research

Fig. 1 Dead burnt MgO

Table 1 Chemical composition of dead burnt MgO

Ingredients/Grade	MgO %	CaO %	Al_2O_3%	Fe_2O_3%	SiO_2%	LOI %
Grade VII	85.00	1.75	0.75	1.50	10.50	0.50

Table 2 Mix proportions

Mix id	Dead burnt MgO (%)	NaH$_2$PO$_4$ (%)
MPN2080	20	80
MPN3070	30	70
MPN4060	40	60
MPN5050	50	50
MPN6040	60	40
MPN7030	70	30
MPN8020	80	20

was prepared in the laboratory by mixing the magnesium oxide powders and sodium dihydrogen phosphate. Dirt-free river sand with fineness modulus of 2.6 conforming to grade of Zone II of IS 383–1970 (R2011) was used. The specific gravity of fine aggregates used was 2.65. The water used was ordinary potable water.

Based on the literature, MgO to sodium dihydrogen phosphate was adopted in the ratios of 1:4 to 4:1, with change of 10% of material for each specimen. Therefore, mix proportions as given in Table 2 were adopted for the experiments. The MNPC was mixed with sand in the ratio 1:3 with 0.3 water/binder ratio, to form mortar in which all the mix specimens were tested. All the MPC mortar mixes hardened within a period of one hour. The work involved the strength test including compressive strength and split tensile strength, durability test by sulphate attack and microstructure study by scanning electron microscopy (SEM) and energy-dispersive X-ray analysis (EDAX).

2.2 Test Methods

The compressive strength test of concrete was conducted as per IS516-1959. The test was carried out using compression testing machine (CTM) of 2000kN capacity to find the maximum load till the failure. Various mixes were placed in moulds of size 70 mm × 70 mm × 70 mm after mixing for two minutes. The samples were de-moulded in twenty-four hours. The samples were water cured for 28 days and tested for compressive strength. The split tensile strength on concrete was carried out in accordance with per IS5816-1999. The samples for split tensile strength testing 75 mm diameter and 150 mm height were prepared for the above mixes, cured for 24 h, de-moulded and tested after 28 days of water curing. The durability of the specimens was tested by checking for weight loss and reduction in compressive strength after placing the specimens in magnesium sulphate solution with 5% concentration for 120 days. The SEM analysis and EDX were made to study the microstructure of the specimens. The SEM images revealed the information about the sample including external morphology while the EDX technique was used to categorize the elemental composition of the materials.
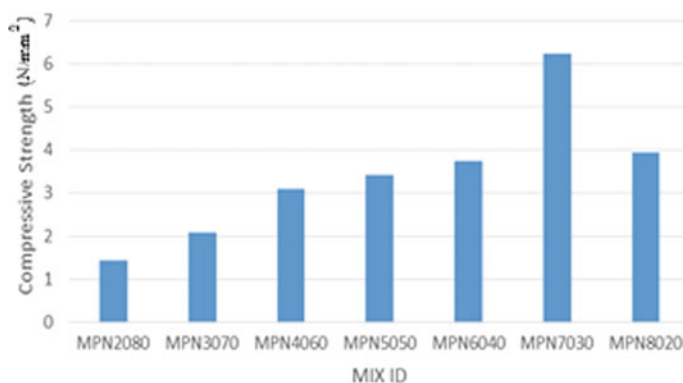
3 Results and Discussions

3.1 Compression Strength Test

Table 3 and Fig. 2 show the compressive strength of the MNPC mortar at 28 days for various mixes with MgO to NaH_2PO_4 in the ratio 1:4 to 4:1 with 10% variation of material in each mix. For the mix MPN2080 (1:4) mortar, the compressive strength was 1.44 N/mm^2, and it increased to 2.1, 3.08, 3.42, 3.74 and 6.24 N/mm^2 for mixes MPN3070, MPN4060, MPN5050, MPN6040 and MPN7030, respectively. However, for MPN8020 (4:1), the compressive strength decreased to 3.94 N/mm^2. The MPN7030 mix which is 70% MgO and 30% NaH_2PO_4 gave the maximum compressive strength of 6.24 N/mm^2, which is 82% more than that of MPN5050 which is equal mix of MgO and NaH_2PO_4 at 50:50.

Table 3 Compressive strength test results for varying proportions of MPN

| Mix id	Dead burnt MgO (%)	NaH_2PO_4 (%)	Compressive strength N/mm^2
MPN2080	20	80	1.44
MPN3070	30	70	2.1
MPN4060	40	60	3.08
MPN5050	50	50	3.42
MPN6040	60	40	3.74
MPN7030	70	30	6.24
MPN8020	80	20	3.94

Fig. 2 Compressive strength for varying proportions of MPN

3.2   Split Tensile Strength Test

The split tensile strengths of the MNPC mortar at 28 days for various mixes MPN2080 to MPN8020 with MgO to NaH_2PO_4 in the ratio 1:4 to 4:1 with 10% variation of material in each mix are shown in Table 4 and Fig. 3. For the mix MPN2080 (1:4) mortar, the split tensile strength was 0.29 N/mm^2, and it increases to 0.54 N/mm^2, 0.69 N/mm^2, 0.84 N/mm^2, 0.93 N/mm^2 and 1.03 N/mm^2 for mixes MPN3070, MPN4060, MPN5050, MPN6040 and MPN7030, respectively. However, for MPN8020 (4:1), the strength decreased to 0.87 N/mm^2. The MPN7030 mix which is 70% MgO and 30% NaH_2PO_4 gave the maximum split tensile strength of 1.03 N/mm^2, which is 22% more than that of MPN5050 which is equal mix of MgO and NaH_2PO_4 at 50:50. The increase in split tensile strength was also the same trend as seen in compressive strength.

Table 4 Split tensile strength for varying proportions of MPN	Mix id	Dead burnt MgO (%)	NaH_2PO_4 (%)	Split tensile strength N/mm^2
	MPN2080	20	80	0.29
	MPN3070	30	70	0.54
	MPN4060	40	60	0.69
	MPN5050	50	50	0.84
	MPN6040	60	40	0.93
	MPN7030	70	30	1.03
	MPN8020	80	20	0.87
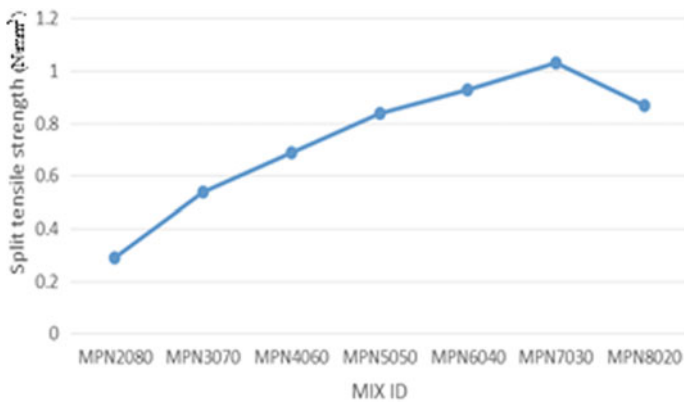
Fig. 3   Split tensile strength for varying proportions of MPN

3.3 Durability Test (Sulphate Attack)

The specimens were kept in 5% $MgSO_4$ solution for 120 days to check the durability of the mixes by observing the loss in mass and strength. The percentage loss in mass is given in Table 5 and Fig. 4, which was from 0 to 5%. There was a loss of 1.2% in the mass of the specimen, compared to the initial value, for MPN7030 which is relatively lesser. Compared to the other mix specimens, the dense packing of the particles in MPN7030 which resulted in the increase in strength had resulted in improved durability with lesser loss of mass under sulphate attack.

Table 6 and Fig. 5 show the compressive strengths of the MNPC mortars at 120 days for various mixes kept in 5% $MgSO_4$. For the mix MPN2080 (1:4) mortar, the compressive strength was 0.4 N/mm^2, and it increased to 1.34 N/mm^2, 2.28 N/mm^2, 4.27 N/mm^2, 3.93 N/mm^2 and 4.59 N/mm^2 for mixes MPN3070, MPN4060, MPN5050, MPN6040 and MPN7030, respectively. However, for MPN8020 (4:1) the compressive strength decreased to 3.25 N/mm^2. The MPN7030 mix which is 70% MgO and 30% NaH_2PO_4 gave the maximum compressive strength of 4.59 N/mm^2, which is 8% more than that of MPN5050 which is

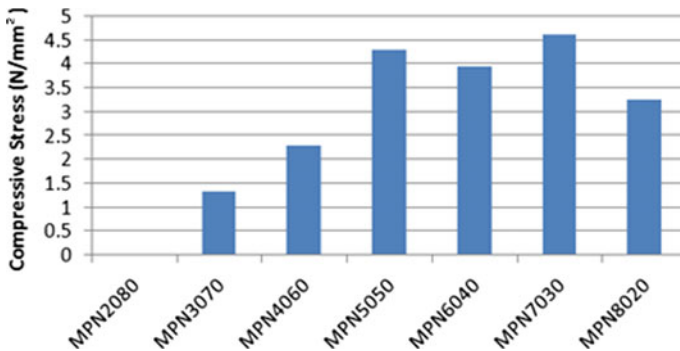Table 5 Weight loss after 120 days in 5% $MgSO_4$ (durability test for varying proportions of MPN)

Mix id	Initial mass of specimen (g)	Mass of specimen after 120 days (g)	Loss of mass (%)
MPN2080	590	560	5.0
MPN3070	640	640	0
MPN4060	730	710	2.7
MPN5050	630	630	0
MPN6040	740	720	2.7
MPN7030	830	820	1.2
MPN8020	790	780	1.3
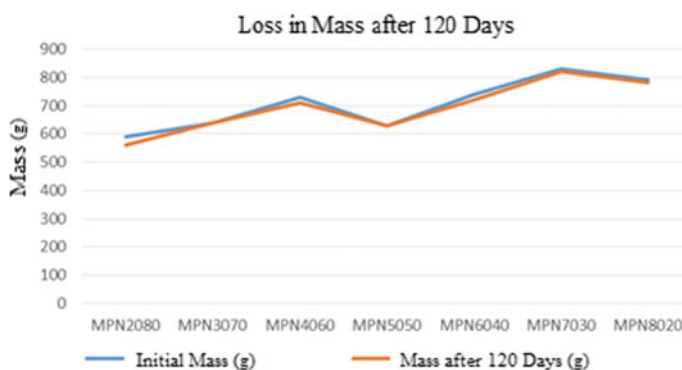
Fig. 4 Loss in mass after 120 days in 5% $MgSO_4$ solution

Table 6 Compressive strength loss after 120 days in 5% MgSO$_4$ (durability test for varying proportions of MPN)

| Mix id	Compressive strength at 120 days in 5% MgSO$_4$ (N/mm^2)
MPN2080	0.40
MPN3070	1.34
MPN4060	2.28
MPN5050	4.27
MPN6040	3.93
MPN7030	4.59
MPN8020	3.25

Fig. 5 Loss in compressive strength in 5% MgSO$_4$ solution for 120 days

equal mix of MgO and NaH$_2$PO$_4$ at 50:50. The trend of loss in compressive strength was in line with the loss in mass of the specimen when placed under 5% MgSO$_4$ solution, thereby showing consistent results.

3.4 Microstructure of Hardened MNPC Mortar

The microstructure of the MNPC mortars at 28 days was investigated by SEM, coupled with energy-dispersive spectroscopy (EDX), which has been shown in Fig. 6a–e for various mixes. In general, all the MNPC mortars exhibit a dense microstructure. Moreover, EDX analysis on these mixes shows that the secondary reaction products share a major proportion of the common elements such as Mg, P, Al, Si, Na and O.

The microstructure study by SEM and EDAX shows that the crystalline bonding is more in MPN7030, thereby increasing the strength and durability of the mix compared to the other mixes. It shows a more complicated and denser microstructure. Backscattered electron images pertaining to MPN7030 show that increase in the percentage of magnesium phosphate enhances the sealing efficiency when
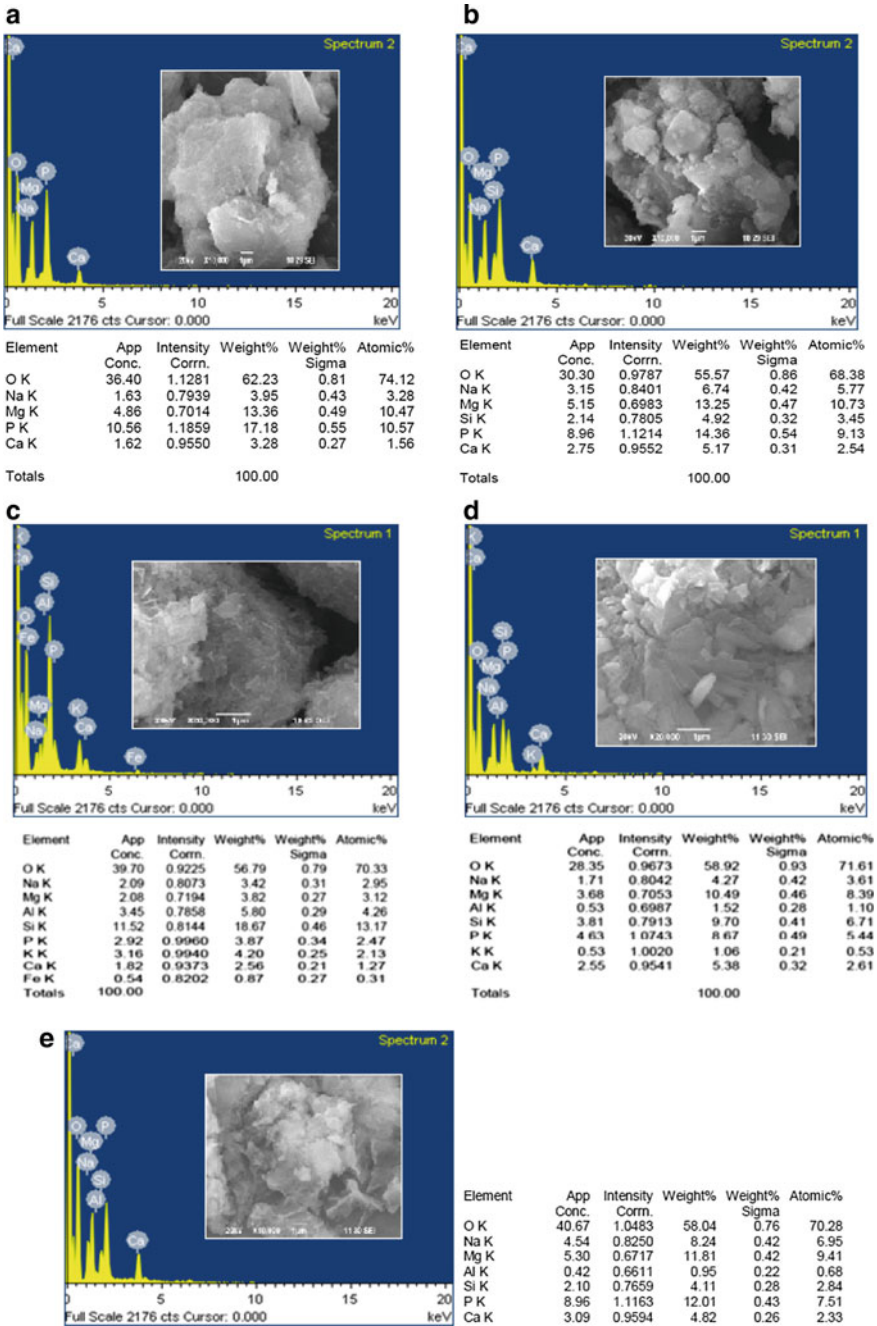
Fig. 6 **a** SEM and EDAX image of magnesium, **b** SEM and EDAX image of magnesium phosphate cement using $MgO:NaH_2PO_4 = 30:70$phosphate cement using $MgO:NaH_2PO_4 = 40:60$, **c** SEM and EDAX image of magnesium, **d** SEM and EDAX image of magnesiumphosphate cement using $MgO:NaH_2PO_4 = 50:50$ phosphate cement using $MgO:NaH_2PO_4 = 60:40$, **e** SEM and EDAX image of magnesium phosphate cement using $MgO:NaH_2PO_4 = 70:30$

compared to other combination containing magnesium phosphate and sodium dihydrogen phosphate. Moreover, MPN7030 mix has low alumina content (0.42% by weight) when compared to other mixes, contributing higher strength development. Since the samples have uneven surfaces, EDX analysis does not provide accurate molar ratios. Hence, chemical reactions of the secondary products shall be found in further study.

4   Conclusions

This paper investigates the variation in proportions of dead burnt MgO and NaH_2PO_4 with respect to mechanical properties of MNPC mortars. Finally, the microstructures of representative specimens were examined by SEM and EDAX techniques to confirm the experimental results. The conclusions arrived from this work is that magnesium phosphate cement made with dead burnt MgO and sodium dihydrogen phosphate hardened within a period of one hour for various mix proportions and showed significant mechanical properties. The maximum compression and split tensile strength were observed in the mix MPN7030 which is 70% MgO and 30% NaH_2PO_4. Durability results and the microstructure of MPN7030 were also in line with the strength properties, where it performed better than all the other mixes. Though the strength was not in par with concrete made with Portland cement, the mix may be used in the manufacture of bricks and building blocks. This study demonstrates the need of optimum design of magnesium sodium dihydrogen phosphate cement. Optimal phosphate/magnesium ratio of 3:7 is required for better strength and durability of MPC.

References

1. Mestres G, Maria-Pau G (2011) Novel magnesium phosphate cements with high early strength and antibacterial properties. Acta Biomater 7:1853–1861
2. Orlov AA, Chernykh TN (2016) Research of water resistance and heat resistance of magnesium phosphate cements. Procedia Engineering 150:1623–1626
3. Chun X, Jian-Ming Y (2011) Effect of disodium hydrogen phosphate on hydration and hardening of magnesium potassium phosphate cement. J Mater Civil Eng 23(10):1405–1411
4. Kandeel AM, El-Mahlrawy MS, Hassan HA (2012) Effect of type of mixing water and sand on the physico-mechanical properties of magnesia cement masonry units. Hous Build Natl Res Centre 8:8–13
5. Ribeiro DV, Agnelli JAM, Morelli MR (2013) Study of mechanical properties and durability of magnesium phosphate cement matrix containing grinding dust. Mater Res 16(5):1113–1121
6. Gardner LJ, Bernal SA, Walling SA (2015) Characterization of magnesium potassium phosphate cements blended with flyash and ground granulated blast furnace slag. Cem Concr Res 74:78–87
7. Yang Q, Zhu B, Wu X (2000) Characteristics and durability test of magnesium phosphate cement-based material for rapid repair of concrete. Mater Struct 33:229–234

8. Yue Li, Bai WL, Shi TF (2017) a study of the bonding performance of magnesium phosphate cement on mortar and concrete. Constr Build Mater 142:459–468
9. Chau CK, Qiao F, Li Z (2012) Potentiometric study of the formation of magnesium potassium phosphate hexahydrate. J Mater Civil Eng 24(5):586–591
10. Hau DS, Yan H, Zhang J (2016) experimental and computation investigation of magnesium phosphate cement mortar. Constr Build Mater 112:331–342
11. Cwirzen A, Habermehl Cwirzen K (2013) Effects of reactive magnesia on microstructure and frost durability of Portland cement-based binders. J. Mater. Civil Eng. 12:1941–1950
12. Ma HY, Xu BW (2017) Potential to design magnesium potassium phosphate cement paste based on an optimal magnesia-to-phosphate ratio. Mater Des 112:331–342
13. Liu N, Chan B (2016) Experimental research on magnesium phosphate cements containing alumina. Constr Build Mater 121:354–360
14. Lu X, Bing C (2016) Experimental study of magnesium phosphate cements modified by Metakaolin. Constr Build Mater 123:719–726

Identification of Crystalline Mineral Phases of Ornamental Latticed Jallies of Madras High Court Building, Tamil Nadu

M. Shivakumar, Thirumalini Selvaraj, Eleonora Odelli, and Rajan

Abstract Stones surfaces and elevated architectural grillworks of historic buildings, due to their predominantly outdoor location, suffer from deterioration factors, including air pollution, soluble salts, relative humidity (RH)/temperature, biodeterioration and by shelling in 1914. The durability and longevity of the structure can be enhanced on proper restoration techniques are adopted in order to arrest the degradation, contaminants, damages and environmental forces. The mineralogical identification and organic substrates were evaluated using X-ray diffraction (XRD), Fourier transformation-infrared spectroscopy (FT-IR), optical microscopy (OM) and Munsell colour chart for rock identification. Presence of silicates, feldspar, calcite and hornblende confirmed the rock to be sandstone on agreement with Munsell colour specifying the pale soft yellow (quartzose sandstone) and inorganic binding agent of calcite as cementing material was also confirmed through FT-IR analysis. Reduced feldspar peaks affirmed the rock has weathered for ages. The results provided the base for the formulation of repair and restoration work of high court building and for modern conservationist.

Keywords Red sandstone · Material characterization · Munsell chart · Indo saracenic architecture

M. Shivakumar · T. Selvaraj (✉)
School of Civil Engineering, Vellore Institute of Technology, Vellore, India
e-mail: Thirumalini.selvaraj@vit.ac.in

E. Odelli
Department of Earth Science, University of Pisa, Pisa, Italy

Rajan
Padmanabhapuram, Thuckalay, India

1   Introduction

Ancient structures built across India have various architectural styles and its cultural importance, which retrieves back the historic information and production technology adopted during the construction of the structure. The tangible structures exposed to environmental and catastrophic change the needs, protection and preservation to safeguard the historic importance to the future generations [1]. Monuments constructed in medieval India used sandstone slabs and blocks for centuries, some of the finest sandstone structures, namely Amer Fort-Rajasthan, Jama Masjid-Delhi, Laxmi Nivas Palace-Bikaner, Humayan Tomb-Delhi and Nilakanteshwarar Temple-Gujarat finished with locally available geoearth materials. Sandstone is a sedimentary rock which is derived from pre-existing sedimentary, igneous or metamorphic rocks, which is mainly composed of rock grains and silt-sized particles [5]. Sedimentary rocks are usually laid down in layers, one on top of the other, which differ to a more or less well-marked degree in composition, grain size, colour or some other properties. Such layers are called beds or strata. The separation planes between the beds are bedding planes, and the whole set of beds shows stratification. A group of beds is called the formation. Sedimentary rocks are geologically classified as mechanically formed, chemically formed and organically formed. Being a widespread aggregate across the country, it has been used in ancient monuments and ornamental works from many centuries due to its mechanical strength and durability. Sandstone is being classified into rudaceous or pebbly, arenaceous or sandy, argillaceous or clayey based on its mineral composition. A sandstone consisting 25% of feldspar clasts is termed as arkose, 90% quartz termed as quartzose [4].

One such finest structure that was built in nineteenth century which is 125 years old is Madras high court building (Indo Saracenic style) as shown in Fig. 1. It is a

Fig. 1   Madras high court building, Chennai, Tamil Nadu [9]

fine example of classical style of European architecture covering an area of 30 acres. The building is prone to ageing and biodegradation due to natural environmental factors [6]. Combination with splendid domes, turrets, pillars, columns and grand arches finished with bricks, marble, sandstone and curved plaster works is added to the beauty of the building. The main aim of this study is to extract the high court red sandstone samples for mineralogical characterization by XRD, FTIR and optical microscopy (OM) to replicate the degraded and deteriorated ancient ornamental latticed stones of the high court building. The scientific results obtained could be used to suggest the possible type of classification of stones utilized during the construction.

2 Materials and Methods

2.1 Sampling of Stone

Madras high court building is a protected monument under the state archaeology department, Chennai. The 127-year-old structure has undergone many changes during its lifetime to various reasons, and its recent research is to restore the original deteriorated ornamental stone works of the building. As shown in Fig. 2, specific locations were identified under the governance of state archaeology and conservators to extricate the ornamental latticed jallies stone samples without altering or damaging the heterogeneity of the samples. Moreover, the samples were collected from the respective heights to avoid the capillary rise and water dampness.

2.2 Analytical Methods

Munsell rock chart describes the colour from medium to fine-grained rocks but it is also helpful in working with coarse-grained rocks. The Munsell chart is designed to cover the range of chief rock-forming minerals such as feldspar, quartz, mica and hornblende. Similarly, the rocks colour pattern was found with three attributes such as hue, value and chroma. The hue has the colour patterns of red, orange and yellow, etc., value denotes the lightness or darkness of a colour (ex 7R), and chroma indicates the saturation or brilliance of the respective colours [7]. Xray diffraction (XRD) analyses of fine samples were carried out using Bruker desktop diffractometer working with the Cu K-alpha radiation ($k = 1.54182$) and graphite monochromator in the diffracted beam, at 1.5 kW and interpretation by Bruker DIFFRAC. SUITEEVA software. It gives qualitative result on the possible presence of minerals in the mortar samples [10]. The test was performed at a 2-theta range from 5° to 90° with a step of 0.2° and a dwell time of four seconds. The resulting diffraction patterns were analysed using X-Pert high score software. Fourier transformation-infrared spectroscopy analyses were performed using a Perkin–Elmer spectrometer, equipped with a global
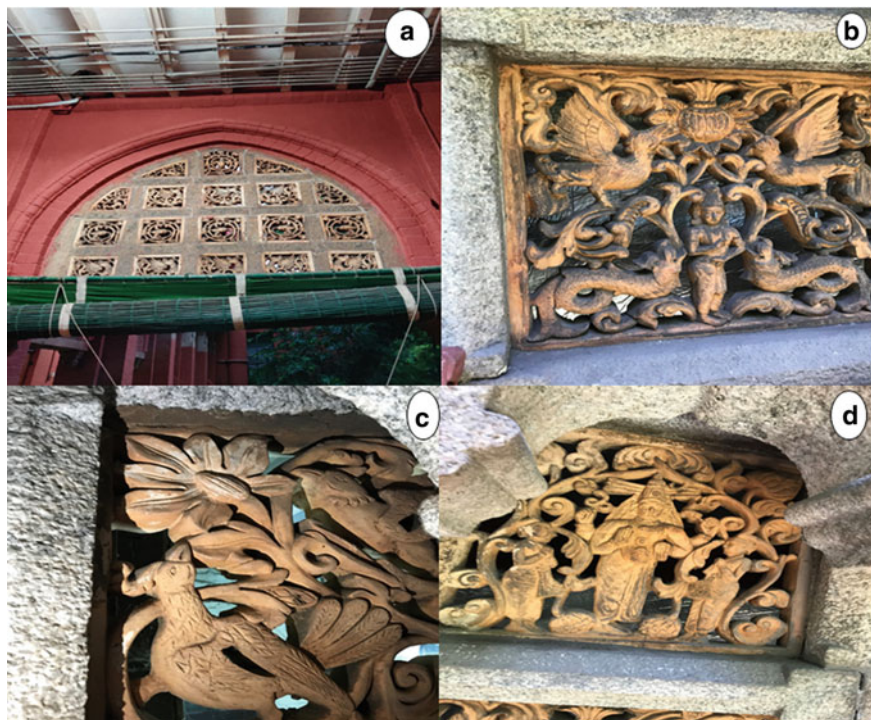
Fig. 2 Sampling locations **a** high court ornamental lattice jallies, **b–d** sandstone ornamental designs

source and a deuterated triglycine sulphate (DTGS) detector. Pellets were prepared by gently grounding pottery sample with KBr in the 1:20 ratio. Spectra were recorded in the 400–4000 cm^{-1} range with a resolution of 4 cm^{-1}, averaging 100 scans [8]. Preliminary morphological observations were carried out on collected ornamental latticed micro-fragments using Zeiss M420 stereomicroscope. Thin Section (30 μm) thick samples was polarized using a Nikon Eclipse E400 with digital image capture system.

3　Sandstone Overview

As shown in Fig. 3, the classification of sedimentary rocks can be made on the basis of origin, namely mechanically formed, chemically formed and organically formed.
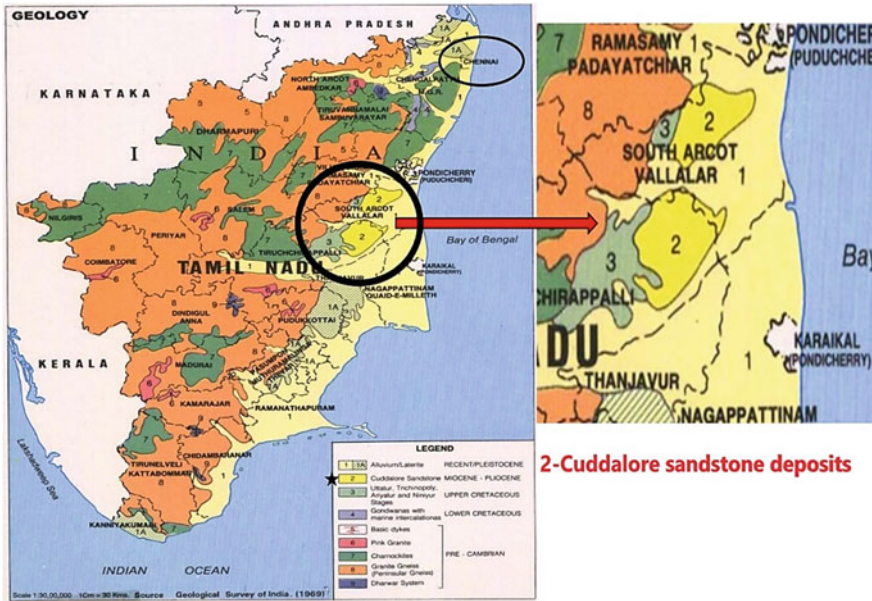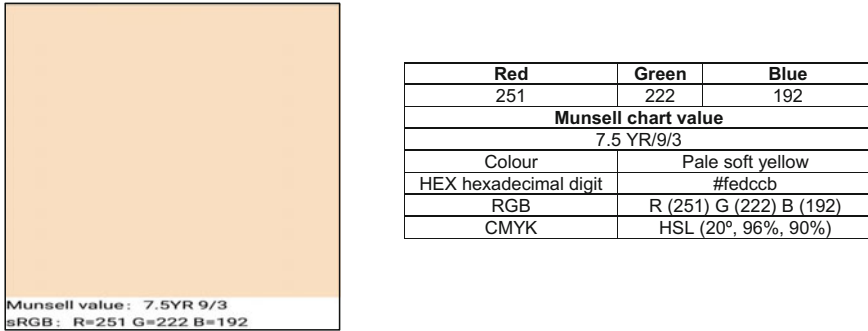
Fig. 3 Geological map on sandstone deposits in Cuddalore, Tamil Nadu

3.1 Mechanically Formed Sedimentary Rocks

This class of sedimentary rocks is formed from fragments of pre-existing rocks, which have been transported into their new position by mechanical means. As examples of such means may be instanced movement by wind or water or glacier ice. These rocks can be classified into the following three groups: (a) rudaceous or pebbly, (b) arenaceous or sandy and (c) argillaceous or clayey.

a. **Rudaceous or pebbly** sedimentary rocks are consolidated gravels of various types. The constituent pebbles are large; if they are angular, the rock is called a breccia; if they are rounded, a conglomerate. It must be noted that breccias might be formed in various ways, for instance by the fracturing and re-cementing of a rock during faulting.

b. **Arenaceous or sandy rocks** consists of small grains, mostly of quartz, cemented by a scanty bond of silica, iron oxide, calcium carbonate, clayey material, etc. The main type is sandstone. Grit is an arenaceous rock made up of angular fragments.

c. **Argillaceous or clayey rocks** consist of the finest fragments worn from older rocks. Examples are clay, retaining enough moisture to be plastic; mudstone, containing little moisture and not plastic, however, still not fissile; shale, a nonplastic clay–rock splitting along its bedding planes. To this series may here be added slate, which is a rock of clay composition with a well-developed cleavage—slaty cleavage—not often coincident with the original bedding planes. Slate is

Red	Green	Blue
251	222	192
Munsell chart value		
7.5 YR/9/3		
Colour	Pale soft yellow	
HEX hexadecimal digit	#fedccb	
RGB	R (251) G (222) B (192)	
CMYK	HSL (20º, 96%, 90%)	

Fig. 4 Munsell chart representing sandstone colour attributes [7]

really a metamorphic rock, and its slaty cleavage results from the parallel orientation of flaky minerals formed when a shale has been subjected to considerable pressure.

4 Analytical Test Results

### 4.1 Munsell Rock Colour Interpretation

From Fig. 4, the Munsell rock chart indicates that sandstone is pale soft yellow, usually the sandstone is available in tan, brown, yellow, red, grey, pink, white and black. However, according to the availability of sandstone, chemical compositions and weathering conditions, the colour of the rock changes. The colour of the sandstone depends on its grains and bonding materials, with abundance of potassium feldspar often gives a pink colour called as feldspar-rich sandstone. Iron oxide (Fe_2O_3) combined with cementitious materials like fractions of calcite imparts tones of yellow, orange, brown or red [2]. A clay matrix results in a greenish black colour and extreme hardness called as wackes. This study confirms the sandstone with high range of quartz and feldspar called as quartzose sandstone.

4.2 XRD Interpretation

XRD spectrum in Fig. 5 reveals the 2⊖ position between 10 and 90° confirming the mineral peaks of sandstone rock. The XRD peaks of sandstone show the major peak of quartz at 2⊖ positions (26.58, 20.83, 50.37 and 68.42°) with deflection angle 3.03Å confirming to international centre of diffraction data file (ICDD) JCPDS (003–0427). The crystalline grain distribution in sandstones is usually of quartz. Moreover, the quartz content of these sands can be very high up to 90% or more are called
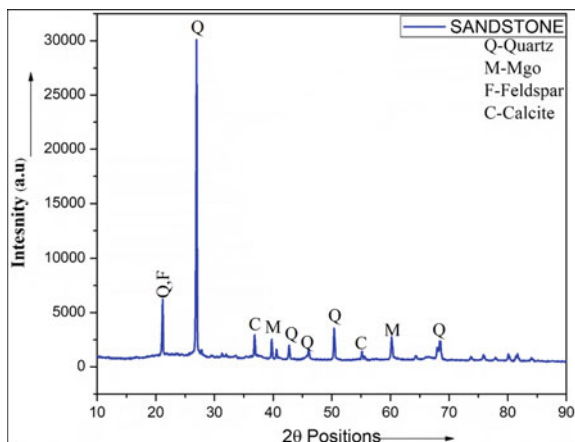
as mature quartzose sandstone. But, if the composition of the rock is with higher amount of feldspar content its considered to be immature arkosic sandstone with high weathering property [3]. Further the XRD graph revealed the minor range of peaks of calcite $2\ominus$ positions at 37.4° and 53.85° with deflection 2.39 and 1.69 Å confirming diffraction file (037–1497). The calcite peak confirms the interaction mechanism due to the dispersion of cementing material [5]. The minor peaks of magnesium oxide in sandstone revealed in the graph at 41.25° and 61.36° indicating that it provides the resistance and plasticity to the rock [10].

4.3   FT-IR and Optical Microscopy Analysis

From Fig. 6, it affirmed the strong spectral band at 1060 and 457 cm^{-1} confirms the presence of alumina-silicate and si–o stretching. Further the high ranged feldspar peak is depicted at 353 cm^{-1} with minor ranged hornblende calcite (C–H) asymmetric peak stretching exhibited at 775 cm^{-1}, respectively [11]. The reduced feldspar (plagioclase) spectral peaks substantiate the weathered conditions of the sampled sandstone from the high court building. The mineralogical characterization of the stone samples is performed by comparing the results achieved with XRD and FT-IR with polarized microstructural observations confirming the widespread brown spots of quartz and white to grey patchy regions of calcite depositions and red patches of feldspar as shown in Fig. 6b [4].
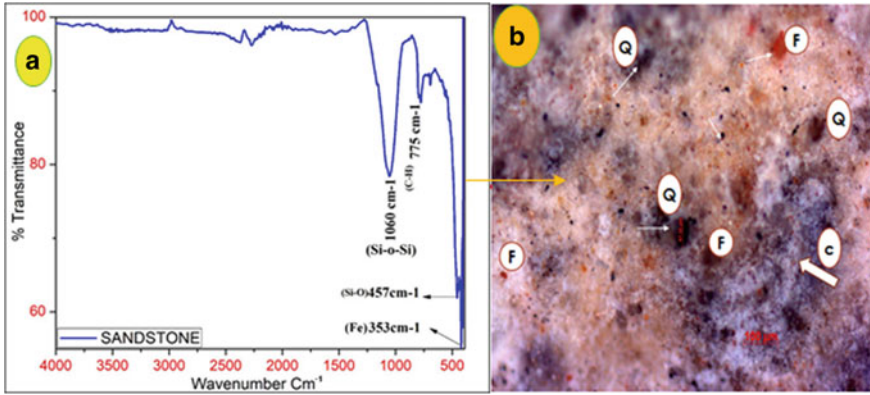
Fig. 6 FT-IR analysis of high court sandstone sample

5 Discussion

Qualitative mineralogical identification of high court sandstone samples revealed the presence of quartz, ferric oxide, magnesia, feldspar and few calcite peaks. FT-IR results reveal the quartz and feldspar spectral peaks at 353, 457 and 1060 cm^{-1} with minor spectral peak of calcite ranged at 775 cm-1 indicates the material property and better understanding on the presence of minerals. The ancient stone samples of high court building showed the presence of siliceous particle distribution around 60–70% along with feldspar, and iron oxide ranging around 30–35% reveals the red colouration on the sandstone through the polarized optical microstructural thin section confirming the rock as quartzose sandstone, in agreement with local geological sandstone rock deposition at Cuddalore region. Presence of high range of silica and reduced feldspar percentage may be the reason behind the deterioration. Sandstones are competent and sometimes brittle during deformation resulting in a highly fractured rock with a high hydraulic conductivity compared with more plastic materials. Comparing the analytical interpretations, the quartzose sandstone can be used for the restoration of the latticed jallies of the building.

6 Conclusion

The mineralogical and visual characterization of sampled ornamental latticed jallies of high court building has confirmed the raw material to be quartzose sandstone, upon the XRD and FT-IR analysis. The visual characterization through the Munsell colour chart indicated the pale soft yellow shade with chart value of 7.5 YR/9/3, indicating the presence of quartz and feldspar. The high range quartz and feldspar act as a resilience to weathering, and fractions of calcite act as a cementing material to bind the minerals. The microstructure provided the widespread quartz and reduced

feldspar indicates that the rock is weathered in correlation with FT-IR results on exposure to the external environmental conditions. Since all the modern analytical test methods are confirmatory, FESEM-EDX can be further analysed as futuristic study to analyse the conditions. Thus, the results of the characterization studies provided good observation on the presence of minerals and its interaction properties, which work as base of restoring the high court latticed ornamental jallies. Further, this database guides the public works department, state archaeology and modern conservators to protect the national integrity of the structure.

References

1. Rodrigues JD, Charola AE, Henriques F (2016) Conservation and restoration of the Don José I monument in Lisbon, Portugal. Part I: stone components. Restorat Build Monum 2–3(22):75–80
2. Bratitsi M, Liritzis I, Vafiadou A, Xanthopoulou V, Palamara E, Iliopoulos Y (2018) Critical assessment of chromatic index in archaeological ceramics by Munsell and Rgb: novel contribution to characterization and provenance studies. Mediterran Archaeol Archaeome 18(2):175–212
3. Hussain A (2018) XRD and petrographic analysis of rose sandstone. Report on Postgraduate Grant Scheme, Italy
4. Medini HK, Arbi M (2018) Chemical and physical analysis of sandstone and relationship with weathering damage of Madâin Sâlih monuments. J Taibah Univ Sci 12(1):37–45
5. Mounia B, Merzoug B, Chaouki B, Djaouza AA (2013) Physico-chemical characterization of limestones and sandstones in a complex geological context, examplenorth-east constantine: preliminary results. Int J Eng Technol 5(1):114–118
6. Mukuna Mubiayi P (2013) Characterisation of sandstones: mineralogy and physical properties. Lect Notes Eng Comput Sci 3:2171–2176. LNECS
7. Color M (1994) Munsell soil color charts, Rev. Macbeth Division of Kollmorgen Instruments, New Windsor, NY
8. RILEM TC 167-COM, 'COM-(2001).Assessment of mix proportions in historical mortars using quantitative optical microscopy. Mater Struct 34(241):387–388
9. Sivarajan (2017) Heritage makeover for Madras High courts Domes. Heritage walk through the Madras High Court, Chennai. 16021448/1042033
10. Middendorf B, Hughes JJ, Callebaut K, Baronio G, Papayianni I (2005) Investigative methods for the characterisation of historic mortars. Part 1: mineralogical characterisation. Mater Struct 38:771–780
11. Li S, Huo R, Wang B, Ren ZZ, Ding Y, Qian M, Qiu T (2018) Experimental study on physicomechanical properties of sandstone under acidic environment. Adv Civil Eng 5784831:1–15

Durability Properties of Geopolymer Concrete Containing Ground-Granulated Blast Furnace Slag and Black Rice Husk Ash

Tata Sravani and Prasanna Venkatesan Ramani

Abstract Concrete production requires a large amount of Ordinary Portland Cement (OPC) which contributes to enormous carbondioxide emission leading to serious environmental problems. Geopolymer concrete (GPC) is one of the innovative solutions to overcome such environmental issues concerning OPC usage. It is produced by mixing mineral admixtures rich in silica and alumina with alkaline activators resulting in binders due to the polymerization reaction. In this study, GPC was produced using the mineral admixture ground-granulated blast furnace slag (GGBS) as a primary binder which was replaced with black rice husk ash (BRHA) in different proportions of 10, 20 and 30% by weight. A mixture of sodium hydroxide (NaOH) and sodium silicate (Na_2SiO_3) was used as the alkaline activators. After the application of oven curing, the specimens were exposed to acid and seawater resistance tests for 30, 60 and 90 days to evaluate the durability properties of geopolymer concrete. The experimental results showed that the addition of BRHA to geopolymer concrete specimens (GPR1 and GPR2) showed better resistance against acid and seawater as the weight and strength losses were lower for 10 and 20% replacement levels than the control specimens (GP).

Keywords Geopolymer concrete · Ground-granulated blast furnace slag · Black rice husk ash · Acid resistance · Seawater resistance

1 Introduction

Concrete, the widely most used construction material in the world, has gained its popularity because of its several benefits like relatively low cost of production, ease of handling, capacity to be moulded into the desired shape, desired strength ranging from low to very high, serviceability and durability. The principal component of concrete is cement, generally, Ordinary Portland Cement (OPC) which acts as the binder and holds the aggregates intact. However, during the production of OPC, it is found to be

T. Sravani (✉) · P. V. Ramani
Assistant Professor (Senior), School of Civil Engineering, Vellore Institute of Technology, Vellore, India
e-mail: tata.sravani2019@vitstudent.ac.in

277

associated with some unfavourable effects to the environment. The manufacturing of OPC is highly energy intensive and produces a high amount of CO_2 into the ambiance which contributes significantly to the 'greenhouse' effect. Bhanumathi das and Mehta [1] have stated that the production of one tonne of cement consumes nearly about 1.5 tonnes of earth minerals, and also one tonne of CO_2 is released into the atmosphere. The raw materials required for cement production are non-renewable and are depleting at a rapid rate. However, at the same time, several industrial and agro-wastes with inherent cementitious properties are produced abundantly. They are mostly disposed into landfills. Employing such by-products as alternates for cement has various benefits including conservation of the environment, the sustainability of resources and solving the disposal problem of by-products. Varadan Vivek et al. [2] pointed out that as per the central statistical organization, there is a drastic change in the increase of industries every year due to the population demand which leads to huge construction and infrastructure projects development. They have highlighted that the manufacturing of cement is a key ingredient in producing the concrete which can be minimized by adding by-products as an admixture to enhance the strength and durability properties of concrete.

Geopolymer concrete, primarily, is introduced by Davidovits [3]. It has recognized that to develop geopolymer concrete, 60% less energy is essential, and it also has 80% less CO_2 emissions than the production of Ordinary Portland Cement Duxson et al.. [4]. Sarath and Ramesh [5], showed the test data of geopolymer concrete achieved by mixing GGBS and metakaolin indicate that on exposure to 5% Na_2SO_4, H_2SO_4 and NaCl, the losses in weight and strength are significantly less than the cement concrete. Several researchers [6], Piyaphanuwat et al. [7] have reported that the addition of BRHA in concrete has improved its durability properties. Naresh Babu et al. [8] have conducted investigation on geopolymer concrete blended with GGBS and phosphogypsum which showed less weight loss in H_2SO_4. Kim et al. [9] have developed the geopolymer concrete based on alkali-activated rice husk ash (RHA) by adding sodium hydroxide with sodium silicate. Durability studies were carried out in acid and sulphate solutions and initiated that geopolymer concrete showed very less weight loss when compared to steam-cured mortar specimens.

The present investigation aims to study the durability properties of GPC usage as an alternative for conventional concrete. The performance of GGBS and BRHA used in the GPC is assessed. The strength and weight loss of GPC prepared with GGBS and BRHA when immersed in acid and seawater solutions are to be found.

2 Materials and Methods

2.1 *Ground-Granulated Blast Furnace Slag (GGBS) and Black Rich Husk Ash*

GGBS is obtained from JSW Cements Ltd., Bellari, India. GGBS is one of the primary binders to produce geopolymer concrete (GPC) conforming to the specifications of BIS: 12089–1987 [16]. BRHA is obtained from the rice mill near Karaikudi. The BHRA binder was used in percentages of 0, 10, 20 and 30% along with GGBS. The size of the material should pass from 75 μ sieve. The test data (as per ASTM-D: 3682–01) properties are collected from SGS Laboratories, Chennai, and are shown in Table 1. Figures 1 and 2 show the SEM results of the particle distribution of GGBS and BRHA.

Table 1 Results of GGBS and BRHA

Properties	Test results	
	GGBS	BRHA
Silicon dioxide (SiO_2)	31.25%	93.96%
Aluminium trioxide (Al_2O_3)	14.06%	0.56%
Ferric oxide (Fe_2O_3)	2.80%	0.43%
Calcium oxide (CaO)	33.75%	0.55%
Magnesium oxide (MgO)	7.03%	0.40%
Loss on ignition	1.52%	9.79%
Specific gravity	2.61	2.14
Blaine fineness	4550 cm^2/g	5673 cm^2/g

Fig. 1 SEM image of GGBS

CEG 5 00kV 11 1mm x30 SE   1 00mm

Fig. 2 SEM image of BRHA

CEG 5 00kV 10 8mm x30 SE   1 00mm
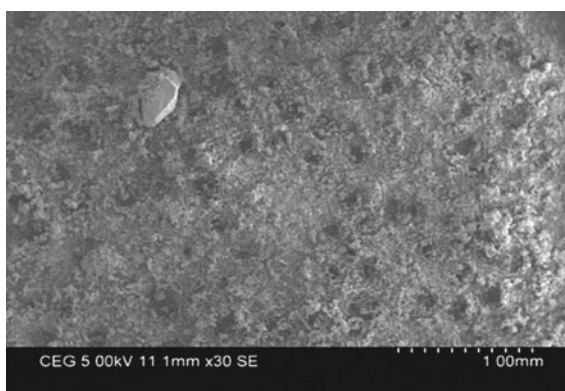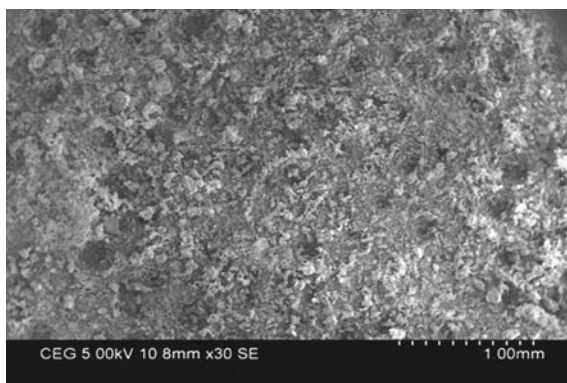
Table 2 Experimental results of coarse and fine aggregates

Experiments	Test results	
	Coarse aggregate	Fine aggregate
Fine modulus	6.29	3.54
Specific gravity	2.72	2.61
Zone	I	II
Size of aggregate	20 mm	<4.75 mm
Surface texture	Smooth	Smooth
Particle shape	Angular	Angular

2.2 Aggregates

The tests on physical properties of coarse and fine aggregates were conducted as per BIS: 2386–1963 [17] and BIS: 383–1987 [18]. The test results are given in Table 2. The fineness modulus of aggregates represents the average size of the particles by an index number which is calculated by performing sieve analysis. The specific gravity of aggregates is in the range of 2.5–3.0. The aggregates size, texture and shape are selected as per IS:456–2000, which prescribes that the nominal size of coarse aggregates should be 20 mm and fine aggregates to be chosen <4.75 mm size with a smooth texture and angular shape for bonding purpose.

2.3 Alkaline Solution

The alkaline solution was prepared using sodium hydroxide and sodium silicate. The purity of NaOH is maintained between 97 and 100%, and the composition of Na_2SiO_3 is prepared by adding Na_2O (14.7%), SiO_2 (29.4%) and water (55.6%) by mass. The ratio of alkaline liquid to binder was taken as 0.4. The concentration of

sodium hydroxide was taken at 8M, and the ratio of NaOH to Na_2SiO_3 was taken as 2.5.

2.4 Superplasticizer

The superplasticizer of 2% (Naphthalene) was added to reduce the usage of water, attaining early strength and enhancing the workability of fresh properties of geopolymer concrete.

2.5 Water

Water also plays an important role in the preparation of GPC. 15% of extra water was also added to the binder content to amplify the workability of the geopolymer concrete.

3 Methodology

To produce the GPC mix, it is essential that it requires careful selection and proportioning of the ingredients which are almost the same as the conventional concrete. The GPC mix design process is developed for low calcium-activated geopolymers using alkaline activator solutions. The density of geopolymer concrete was assumed as 2400 kg/m^3, and 30 MPa was assumed as a minimum targeted strength due to the lack of availability of codal provisions. The calculations were made based on the density of concrete as per the mix design given by Lloyd and Rangan [10]. Based on that method, by withholding the total aggregates content from the density, the total mass of GGBS and alkaline activator solution was attained. The combined total volume occupied by the coarse and fine aggregates was assumed to be 77%. The alkaline liquid to binder ratio was taken as 0.40. The targeted compressive strength and workability were determined using water to geopolymer solid ratios. In this investigation, GGBS was used as the control specimen for preparing geopolymer concrete (GPC), and the BRHA was varied in terms of GPR1-10%, GPR2-20% and GPR3-30%. Table 3 shows the mix proportions in terms of quantities.

4 Preparation of Test Specimens

All the ingredients, in dry condition, were weighed and mixed thoroughly in pan mixer up to 3–4 min. The alkaline solution was prepared by combining the sodium

Table 3 Mix proportions of GPC

Raw materials	Proportions (kg/m^3)			
	GP	GPR1	GPR2	GPR3
GGBS	394	355	315	276
BRHA	0	39	79	118
Coarse aggregate	1201	1201	1201	1201
Fine aggregate	647	647	647	647
Sodium hydroxide	45	45	45	45
Sodium silicate	113	113	113	113
Superplasticizer	8	8	8	8
Water	59	59	59	59

hydroxide and sodium silicate solutions in the ratio of 1:2.5. Subsequently, this solution was added to the dry mix. For improving the workability, 15% of extra water was added by the weight of the binder in addition to 2% of superplasticizer. For each test, nine specimen samples of each mix were prepared and cured at a temperature of 60 °C constant temperature for 24 h to sustain the rate of polymerization and setting of GPC. After de-moulding, the cubes were again placed in the oven with the same temperature for another 24 h. The specimens were then allowed to room temperature until the day of testing.

5 Results and Discussion

5.1 Acid Resistance Test

The GPC cubes of 100 mm × 100 mm × 100 mm were cast and tested for acid resistance after 28 days. At the outset, the weight of each specimen was measured, and for assessing the loss in compressive strength, the initial characteristic compressive strengths of the respective mixes were measured. Then the specimens were immersed separately in 3% hydrochloric acid (HCl) and 3% sulphuric acid (H_2SO_4) solutions for a period of 30, 60 and 90 days from the day of immersion. On the day of the testing, the specimens were taken out, cleaned and measured the weight. Subsequently, the specimens were tested using the compression testing machine of 2000 kN capacity at a uniform rate of loading of 140 kg/cm^2/min as per BIS: 516-1959 [19] test procedure. The losses in weight and the compressive strength of the GPC were then determined. The results of strength and weight losses of H_2SO_4 and HCl are shown in Tables 4 and 5. Figures 3 and 4 show the performance of weight loss and % compressive strength loss of GP and GPR specimens exposed to H2SO4 and HCl for a period of 30, 60 and 90 days.

Table 4 Weight and compressive strength loss of GPC specimens exposed to H2SO₄

(a)

Mix	Initial Weight at 28 days (kg)	Weight loss after immersion (%)		
		30 days	60 days	90 days
GP	2.53	0.25	3.45	6.1
GPR1	2.51	0.1	2.85	4.9
GPR2	2.48	0.1	3.1	5.2
GPR3	2.44	0.4	5.6	10.8

(b)

| Mix	Initial Characteristic Compressive Strength at 28 days (kg)	% Compressive strength loss after immersion		
		30 days	60 days	90 days
GP	69.3	3.3	10.25	15.2
GPR1	70.7	2.9	9.6	13.4
GPR2	51.5	3.2	10	13.9
GPR3	24.5	9.8	24	39.5

Table 5 Weight and compressive strength loss of GPC specimens exposed to HCl

(a)

Mix	Initial Weight at 28 days (kg)	Weight loss after immersion (%)		
		30 days	60 days	90 days
GP	2.53	0	1.8	4
GPR1	2.51	0	1.15	3.1
GPR2	2.48	0	1.4	3.5
GPR3	2.44	0.2	3.8	8.6

(b)

Mix	Initial Characteristic Compressive Strength at 28 days (kg)	% Compressive strength loss after immersion		
		30 days	60 days	90 days
GP	69.3	2.1	8.8	12.4
GPR1	70.7	1.8	8.5	11.5
GPR2	51.5	1.9	9.1	12.1
GPR3	24.5	7.1	16.3	24.6

The exposure of GPC specimens to 3% H_2SO_4 solution reveals that, in terms of both weight and strength losses at 30, 60 and 90 days, the control specimens showed higher losses at all three testing periods. GPR1 and GPR2 specimens showed lower losses than the control specimen GP, which indicates that the addition of BRHA had a positive effect on the acid resistance of GPC. For instance, at 90 days of exposure to H_2SO_4, there was a 12% lesser weight loss for GPR1 specimens and 9% for GPR2 specimens while comparing the control GPC specimens. The strength
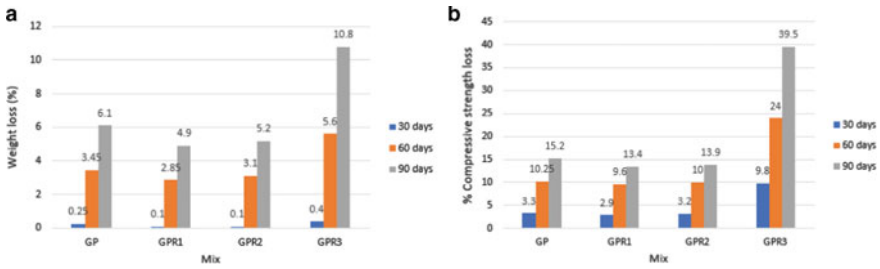
Fig. 3 **a** Weight loss of GPC on exposure to H_2SO_4. **b** Strength loss of GPC on exposure to H2SO4
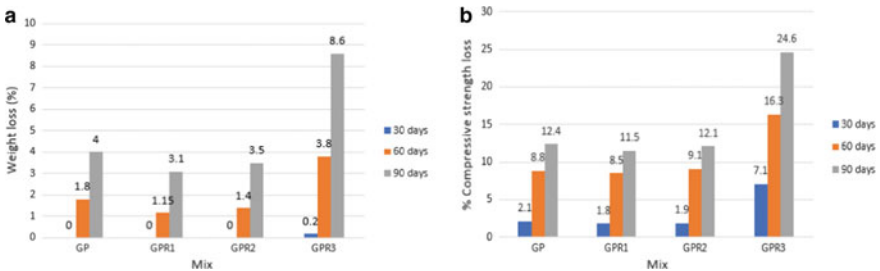
Fig. 4 **a** Weight loss of GPC on exposure to HCl. **b** Strength loss of GPC on exposure to HCl

losses are 18 and 13% lower for GPR1 and GPR2 against the control specimens at 90 days of exposure. The finer BRHA particles enhanced the dissolution of silica and alumina ions to form a stronger geopolymer matrix resulting in more resistive passive layer against the attack of sulphate ions. However, when the BRHA addition was increased to 30%, the losses suddenly amplified. This effect can be possibly due to the irregular silica–alumina ratio resulting with excess BRHA [11], which can also be inferred from the material property of BRHA where the silica content is as high as 93.96% while the alumina content is only 0.56%. The results are comparable with Rajamane et al. [12] *where the GGBS-based GPC specimens showed compressive strength losses of* 3.7, 10 and 11.1 *after exposure to* 2% H_2SO_4 at 30, 60 and 90 days, *respectively.* Exposure to HCl also showed a similar trend with addition of BRHA lowering the weight and strength losses. But the losses are less severe than that of H_2SO_4 which seemed to have cause more aggressive attack on concrete than HCl. The action of H2SO4 on concrete is more aggressive due to the combination of acid and sulphate attack Barbhuiya and Kumala, [13].

5.2 *Seawater Resistance Test*

For evaluating the seawater resistance, the test procedure was similar to that of the acid resistance test. The prepared specimens were cured for 28 days and immersed in the

seawater mediate obtained from the shore of the Bay of Bengal near Thiruvanmiyur, Chennai, for periods of 30, 60 and 90 days. Prior to immersion in seawater, the weight of specimens and the characteristic compressive strength were measured. After 30, 60 and 90 days of immersion in seawater, the specimens were taken out, and the surfaces were cleaned, weighed, and subjected to axial load at a rate of 140 kg/cm^2/min. The weight loss and compressive strength loss measurements were calculated for each period of immersion. The results of strength and weight losses of GPC exposed to seawater are shown in Table 6. Figure 5 shows the variation in weight loss and % compressive strength loss of GP and GPR specimens exposed to seawater for periods of 30, 60 and 90 days.

From the obtained results, no significant weight losses were observed in all mixes at 30 days of exposure. With continued exposure to seawater, the specimens suffered significant weight loss at 60 and 90 days. The weight and compressive strength losses of GPR1 were, respectively, 12 and 32% lower than that of a control specimen GP

Table 6 Weight and compressive strength loss of GPC specimens exposed to seawater

(a)

Mix	Initial Weight at 28 days (kg)	Weight loss after immersion (%)		
		30 days	60 days	90 days
GP	2.53	0.2	4.7	8.8
GPR1	2.51	0.15	4.1	7.6
GPR2	2.48	0.2	5.2	9.3
GPR3	2.44	0.3	8.8	17.1

(b)

Mix	Initial Compressive Strength at 28 days (kg)	% Compressive strength loss after immersion		
		30 days	60 days	90 days
GP	69.3	6.5	13.4	22.7
GPR1	70.7	5.9	11.3	19.4
GPR2	51.5	6.8	14.6	25.6
GPR3	24.5	9.2	26.5	42.6
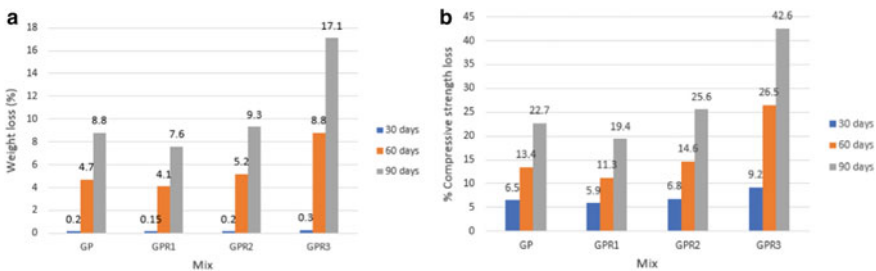
Fig. 5 a Weight loss of GPC on exposure to Sea water. **b** Strength loss of GPC on exposure to seawater

at 90 days of immersion. But the weight losses were slightly higher (around 5%) for GPR2, in comparison with control GP specimens at 60 and 90 days. Strength losses too exhibited a similar increasing trend for the GPR2 mix against GP control mix. GPR3 specimens showed maximum losses in weight and compressive strength at all the three different exposure periods. This was due to the interconnectivity of the increased pores allowed rapid chloride ion movements from the outer to the inner side of concrete resulting in deterioration and weight loss [14]. The surface of the GPC specimens showed visible stains at 30 days and continued to deteriorate with time. Significant surface erosion was observed after 90 days of exposure to seawater. Similar results were reported by Omer et al. [15]. By comparing the acid resistance test, the reduction in compressive strength of GPC was relatively greater at 60 days and 90 days. Under the action of seawater, the higher leaching of alkalis in the specimens altered the integrity of the geopolymer alumino-silicate network which contributed to the higher losses Olivia and Nikraz, [14].

6   Conclusions

Based on the experimental investigation, it can be concluded that GPC made with GGBS and BRHA could perform remarkably well in the durability criteria. The addition of BRHA improves the durability of GPC. After 90 days of exposure to H_2SO_4, the weight and strength losses of GPR1 and GPR2 were 12 and 9% lesser than control GP specimens, respectively. Similar behaviour was observed for the specimens exposed to HCl, where the addition of BRHA in proportions of 10 and 20% showed better resistance than the control GP specimens in terms of strength and weight losses. Against the action of seawater, the addition of BRHA upto 10% exhibited beneficial effect of minimizing the strength and weight losses in GPC. However, beyond 20% BRHA proportion, the specimens performed poorly in all the tests owing to poor structural compatibility from inappropriate silica–alumina ratio. It can be concluded that GPC can be highly useful as an alternative durable construction material. Besides minimizing the CO_2 emission, GPC production utilizes industrial wastes like GGBS and BRHA for generating the binding system in concrete, which will also alleviate their disposal problem.

References

1. Bhanumathidas N, Mehta PK (2001) Concrete mixtures made with ternary blended cements containing fly ash and rice-husk ash. In: 7th CANMET/ACI international conference on fly ash, silica fume, slag and natural Pozzolans in concrete. Chennai, India, pp 22–27
2. Vardhan Vivek CM, Anitha A, Sravani T (2015) Use of partially treated wastewater of battery industry in cement mortars. J Environ Res Develop 9(3A):933–943
3. Davidovits J (1999) Chemistry of geopolymeric systems, terminology. Geopolymere '99 conference. Saint-Quentin, France, pp 9–22

4. Duxson P, Provis JL, Lucky GC, Van Deventer IS (2007) The role of inorganic polymer technology in the development of green concrete. Cem Concr Res 37(12):1590–1597
5. Sarath CKB, Ramesh (2017) Durability studies of GGBS and metakaolin based geopolymer concrete. Int J Civil Eng Technol 8(1):17–28
6. Chatveera B, Lertwattanaruk P (2009) Evaluation of surface resistance of cement mortars containing black rice husk ash. J Environ Manage 9(3):1435–1441
7. Piyaphanuwat R, Asavapisit S, Buddhawong S (2005) Effects of elevated temperature curing on strength and leachability of the solidified wastes using lime and BHA as solidification binder. Suranaree J Sci Technol 91–97
8. Naresh Babu Y, Sudarsana Rao H, Ghorpade VG (2017) Strength and durability studies on geopolymer concrete blended with GGBS and phosphogypsum. Int J Chem Tech Res 10(6):987–994
9. Kim YY, Lee BJ, Saraswathy V, Kwon SJ (2014) Strength and durability performance of alkali-activated rice husk ash geopolymer mortar. Hindawi Publishing Corporation, The Scientific World Journal, pp 1–10
10. Lloyd NA, Rangan BV (2010) Geopolymer concrete with fly ash. In: Second international conference on sustainable construction materials and technologies. Ancona, Italy
11. Rajesh M, Chachithanantham S, Ramaswamy A (2016) Performance and behaviour of GGBS imparted to geopolymer concrete structural elements and analysed with ANSYS. Adv Mater Sci Eng 7023897:1–9
12. Rajamane NP, Nataraja MC, Dattatreya JK, Lakshmanan N, Sabitha D (2012) Sulphate resistance and eco-friendliness of geopolymer concretes. Indian Concr J 86:13–21
13. Barbhuiya S, Kumala D (2017) Behaviour of a sustainable concrete in acidic environment. Sustainability 9:1556–1568
14. Olivia M, Nikraz H (2013) Properties of fly ash geopolymer concrete in seawater environment. In: Proceedings of the 13th east asia-pacific conference on structural engineering and construction. Sapporo, Japan
15. Omer SA, Demirboga R, Khushefati WH (2015) GGBFS based geopolymer mortars immersed in sodium and magnesium sulphate solutions and sea water. Int J Eng Res Technol 4:377–384
16. BIS 12089–1987 Specification for granulated slag for the manufacture Portland slag cement. Bureau of Indian Standard, New Delhi
17. BIS 2386–1963 Methods of testing for aggregates for concrete, specific gravity, Density, absorption and organic impurities. Bureau of Indian Standard, New Delhi
18. BIS: 383–1987, Specification for coarse and fine aggregate from natural sources for concrete. Bureau of Indian Standard, New Delhi
19. BIS: 516–1959 Methods of test for strength of concrete. Bureau of Indian Standard, New Delhi

Correction to: Identification of Crystalline Mineral Phases of Ornamental Latticed Jallies of Madras High Court Building, Tamil Nadu

M. Shivakumar, Thirumalini Selvaraj, Eleonora Odelli, and Rajan

Correction to:
Chapter "Identification of Crystalline Mineral Phases of Ornamental Latticed Jallies of Madras High Court Building, Tamil Nadu" in: J. Jayaprakash et al. (eds.),
***Advances in Construction Materials and Structures*,**
Lecture Notes in Civil Engineering 111,
https://doi.org/10.1007/978-981-15-9162-4_21

In the original version of the book, the misspelt co-author name "Eleonora Regattieri" has been changed to read as "Eleonora Odelli" in Chapter 21. The erratum chapter and the book have been updated with the change.